H24/3051

MONASH UNIVERSITY
THESIS ACCEPTED IN SATISFACTION OF THE
REQUIREMENTS FOR THE DEGREE OF
DOCTOR OF PHILOSOPHY
ON.................... 5 October 2001 ....
..............██████████████████████.
        Sec. Research Graduate School Committee

Caldera Collapse and the Generation of Waves

Thesis submitted for the degree of
Doctor of Philosophy

by

James Paul Peter Gray
B.Sc. (Hons)

Department of Mathematics and Statistics
Monash University
May 2001

Addendum

Page 32: Figure 2.12: Replace "ξ" with "v"

Page 56: Paragraph 3: After "*implementations respectively.*" insert:

"*The colours in figures 4.4 and 4.5 (as well as figures 4.9 - 4.12) refer to the speed of the particle, similar to the figures presented in chapter 3.)*"

Page 60: Figure 4.6: After "*In these experiments*" insert "$W = 40cm$,"

Page 72: Figure 4.13: Replace full stop after "*the experimental results in section 4.1*" with "*, allowing for the factor of two difference in the definition of W.*"

Page 77: Paragraph 1: Replace "*The north eastern inlet*" with "*The north western inlet*".

Page 79: Equation 5.3: Replace "x_b" by "y_b" in the second partial derivative.

Page 85: At the end of paragraph 4 insert:

"*The artificial viscosity used in the solid body calculations is the same as that used in the incompressible fluid calculations (2.16), except that a larger value of the artificial viscosity parameter $\alpha = 0.5$ is used in the solid body calculations.*"

Page 138: Figure 6.20: Replace "$V_f = 1 \times 10^{-4}$" with "$V_f = 1 \times 10^{-3}$"

" As far as the laws of mathematics
refer to reality, they are not certain,
and as far as they are certain,
they do not refer to reality."

Albert Einstein (1879-1955)

i

Contents

Summary

This thesis begins with an historical survey of caldera collapse events and their effects. We then review a range of numerical methods which are suitable for the solution of the Navier-Stokes equations. We discuss the suitability of Smoothed Particle Hydrodynamics (SPH) because of the ease with which it can handle complicated free surface motions, and also because it can be extended to include the physics required for the computation of problems in rock mechanics and fracture for the modelling work in this thesis.

In chapter two we describe the SPH method and detail its application to free surface fluid mechanics. We discuss the implementation of boundary conditions in SPH and show that ghost particle formulations are superior to the use of boundary particle forces.

We validate our code and boundary conditions on a range of test problems in chapter three. We find good agreement for our SPH calculations with experimental and theoretical results, we also compare to the results of other numerical methods.

Different forms of caldera collapse are reviewed in chapter four. A simplified model for piston subsidence is introduced and we present wavetank experiments for the generation and runup of waves produced using this piston model. We compare these experiments to SPH calculations and discuss extensions of our calculations to gain an understanding of wave generation in the more realistic case.

Having considered calculations for the generation of waves from caldera collapse we alter course to investigate the modelling of stresses and fault formation around magma chambers and the relation of these faults to collapse structures. We outline the addition of a deviatoric stress tensor to our numerical equations in chapter five. The deviatoric stress tensor is introduced to provide resistance to material deformation, consistent with Hooke's law. The formulation of a damage model suitable for the simulation of brittle materials is described.

SPH calculations are known to be affected by a crippling short wavelength instability when particles are acted upon by large tensile stresses. Artificial stress terms are introduced into the SPH equations to combat this instability. Dispersion

relations for stress waves are derived, the SPH equations are shown to agree with the continuum equations in the long wavelength limit. The short wavelength limit of the dispersion relation is found and used to calculate the stability properties of SPH under the application of tensile stresses when the artificial stress terms are implemented.

Various test problems of solid body dynamics are presented in chapter six. These problems demonstrate the effect of artificial stress terms to remove the numerical fracturing caused by the tensile instability. Simulations of elastic, plastic, ductile and brittle materials are shown. The concentration of stress around a circular cavity is described.

Chapter seven begins with a review of the physical processes involved in crack formation in rock surrounding magma chambers and caldera collapse. Basic calculations illustrate the effects of the important physical processes and conditions. More realistic calculations illustrate possible fracture regimes and the suitability of SPH as a useful tool for the further analysis of these problems.

Concluding remarks are made in chapter eight with a summary of results and a discussion of areas in which further investigation should proceed. Three appendices are provided, outlining that thermodynamic effects can be neglected in the study of wave generation, a detailed derivation of the dispersion relation of chapter five, and conclude with a commentary on the animations of simulations contained on the accompanying CDROM.

Candidate's Statement

This is to certify that the work presented in this thesis has been carried out in the Department of Mathematics and Statistics, Monash University, Australia and has not been previously submitted to any university or technical institution for a degree or award. This thesis is comprised of only my original work, except where due acknowledgement is made in the text. The length of this thesis is less than 100,000 words, exclusive of figures, tables, appendices and references.
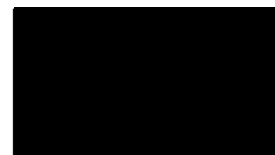
James P. P. Gray

Acknowledgements

Publications

During the course of my candidature two refereed articles relating to the contents of this thesis were published:

- Gray, J. P., and Monaghan, J. J., (1998), "A Study of Waves Developed by Caldera Collapse", proceedings of the *Thirteenth Australiasian Fluid Mechanics Conference* , **Vol 1**, 279-283.

The contents of this paper are presented in sections 3.1, 3.2 and 4.1 of this thesis.

- Gray, J. P., Monaghan, J. J. and Swift, R. P., "SPH Elastic Dynamics". *Computer Methods in Applied Mechanics and Engineering, accepted.*

The contents of this paper are presented in sections 5.6, 6.1, 6.2 and 6.4 of this thesis. Due reference to the contributions of my collaborators is made in the text.

"I'm a Cork on the Ocean,
Floating Over the Raging Sea,
How Deep is the Ocean?
How Deep is the Ocean?

I'm a Rock in a Landslide,
Rolling Over the Mountain Side,
How Deep is the Valley?
How Deep is the Valley?"

Brian Wilson

Chapter 1

Introduction

The aim of thesis is to investigate the modelling of events associated with caldera collapse eruptions and examine if these collapse events can lead to tsunami production. Caldera collapse occurs when the ejection of magma from a volcano leads to the rock overlying a partially empty magma chamber to become unstable and collapse into the chamber. Tsunamis or *tide waves* are large, fast moving, long wavelength waves and are typically caused by undersea earthquakes or landslides. Though tsunamis can be produced by any displacement of a significant amount of water. Tsunamis carry vast amounts of energy and can be very destructive when they come into contact with land.

1.1 Physical Motivation

Latter (1981) outlines ways that events associated with volcanic eruptions can lead to tsunami generation. A proposed mechanism is that the collapse of a volcano in a marine environment leads to the formation of a cavity into which an influx of water can flow and generate waves. This thesis focuses on this mechanism, though the techniques used would be equally applicable to modelling production of tsunamis from volcanically initiated earthquakes or landslides.

One question we wish to understand is how waves form when a caldera in contact with the sea collapses. In chapter four we consider how waves are produced in simplified models of caldera collapse, using both numerical simulations and wave tank experiments. We then progress to examining the effects of altering the geometry of the cavity on the waves produced.

The initial motivation for this study (on the connection between caldera collapse and tsunami production) is the theory that the Bronze Age eruption ($\sim 1,500BC$) of the Mediterranean island of Santorini led to the demise of the Minoan civilisation in nearby Crete (Marinatos 1939). The island of Santorini lies in the sea between

Greece and Crete and possesses a rich history. It has been linked to tales in Greek mythology (Jason and the Argonauts (Luce 1970) and the legend of the lost city of Atlantis) and has been the site of many volcanic eruptions including a large eruption in the Bronze Age. Some of the eruptions on Santorini have led to caldera collapse events (chapter four). The subsidence of large parts of the island into the sea has led to the creation of large cliffs which has meant that not only has the island been transformed into a region of extreme beauty, it has also led to the creation of an area of extensive scientific interest.

In figure 1.1 we present a recent map of the island[1]. The island complex is approximately $14km$ in diameter with interior cliffs up to $300m$ high. The northern section of the interior basin is almost $370m$ deep, with the southern section having depth around $275m$. The present day caldera was formed in a series of distinct eruptions and collapse events (Druitt and Francaviglia 1992). A flooded caldera existed before the Bronze Age eruption which increased the area and depth of the depression. There has been extensive geological research into the volcanology of the island (Sparks and Wilson (1990), Heiken and McCoy (1984) and references therein).

The Greek archaeologist Marinatos proposed a theory that the Bronze Age eruption of Santorini led to the demise on the Minoan civilisation on Crete (Marinatos 1939). The Minoan civilisation was one of the earliest European civilisations and lies at the roots of Western culture (Graham 1967). Marinatos' motivation was that the Minoans seemed to mysteriously disappear soon after the eruption of Santorini.

Page (1970,1978) and Luce (1970) have examined the effects the eruption may have had on life on Minoan Crete. The dumping of volcanic ash may have rendered Crete uninhabitable for some years, or a damaging earthquake may have been initiated by the eruption. Komlós, Hédervári, and Mészáros (1978) discuss a correlation between earthquakes in the months both preceding and following volcanic eruptions of Santorini. This connection is found to be consistent with research into other volcanoes.

Archaeological digs at the town of Akrotiri on Santorini, failed to uncover the remains of human skeletons. Heiken and McCoy (1990) attribute this to the residents being pre-warned of impending disaster and fleeing before the eruption. There are

---

[1] "Santorin Island Ancient Thera Surveyed by Captain Thomas Graves F.R.G.S. H.M.S. Volage 1848" from The Journal of the Royal Geographical Society, Volume 20, 1850. obtained from the Perry-Castañeda Library Map Collection at "http://www.lib.utexas.edu".
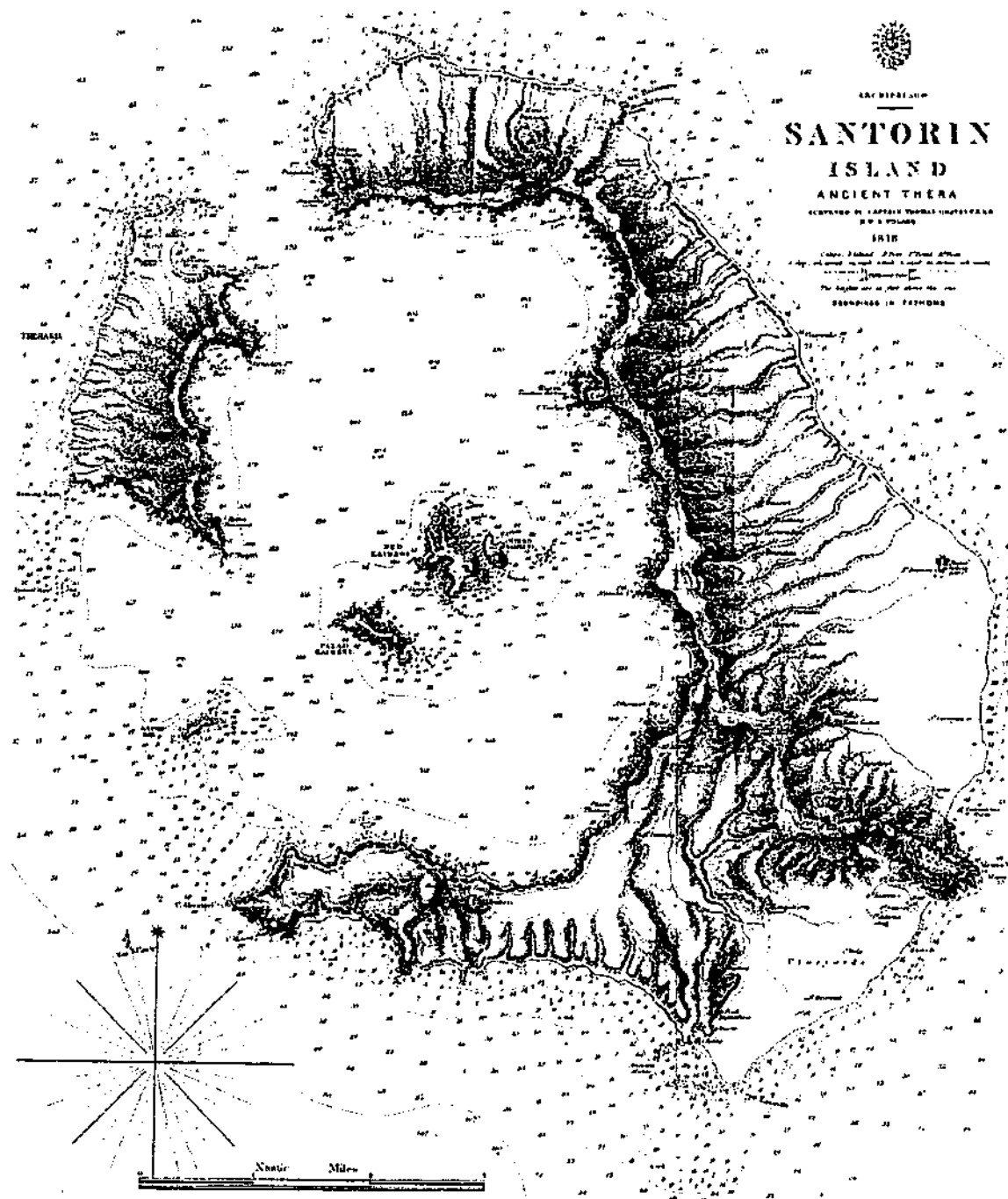
Figure 1.1: *Recent map of Santorini. The bays in the centre of the island were formed by caldera collapse. Small islands in the middle were formed by recent volcanic activity.*

signs of buildings being repaired after an earthquake, covered by a small ash deposit which is thought to have come from volcanic activity a few weeks or months prior to the beginning of the major eruption. The presence of ash in the air could have made breathing difficult and possibly frightened inhabitants into leaving.

An alternative way that volcanic eruptions can lead to destruction is through the initiation of tsunamis (Mészáros 1978; Yokoyama 1978). The 1972 eruption of Ritter island (Papua New Guinea) picked up seismic signals which may have been caused by either caldera-collapse or an explosive eruption. An eruption which led to tsunami production (Cooke et al. 1976). The original report into the 1883 eruption of Krakatau (Indonesia) (Verbeek 1884) attributed the collapse of the northern part of the mountain as the origin of a large *tide wave*.

The 1883 eruption of Krakatau produced tsunamis which killed 36,000 people on surrounding islands. There are many similarities between the 1883 eruption of Krakatau and the Minoan eruption of Santorini. Both occurred in island settings that had pre-existing calderas and involved caldera collapse of large sections of the centre of an island, though the Minoan eruption of Santorini was larger. Using the recorded events at Krakatau (Verbeek 1884) as a guide we expect a complicated eruption sequence at Santorini with many tsunamis generated. Thornton (1996) reviews how the eruption is thought to have occurred and examines the way the ecosystem on Krakatau was rebuilt after the 1883 eruption.

Even though a tsunami may not be responsible for the downfall of the Minoan society, the possibility that a similar eruption in some other situation could cause significant damage is not precluded. Decker (1990) estimates that an eruption at least as big as the Minoan eruption on Santorini is likely to occur somewhere on earth every 300 years or so. It is therefore important that we are able to predict the possible effects of such an eruption.

Thermodynamic effects in the event of caldera collapse are undoubtedly important if one is to gain a complete understanding of the problem. The possible interactions between molten lava and sea water must be considered, along with the effects that different temperatures have on rock properties and fracture mechanisms. However, in this thesis the focus will be on the mechanical effects rather than the thermodynamic effects. We feel that there are interesting fluid dynamics problems that need to be solved before including the complications of thermodynamics.

In appendix A we show that over the short time scale for which caldera collapse

may lead to significant wave production the thermodynamic effects have only a small effect on the mechanics of the wave generation and flow. The thermodynamic effects are important and can lead to the dynamic mixing of lava and water and explosions in situations where equal volumes of lava and water are present (Colgate and Sigurgeirsson 1973).

A distinct (yet related) factor we examine is the way in which fracture of the rock surrounding the magma chamber occurs. The issue of the origin of calderas in controversial (McBirney 1990; Lipman 1997). Numerical modelling provides a method to investigate how different magma chamber geometries, rock types and loading conditions affect where faults occur and how calderas form. An understanding of the mechanism of collapse is scientifically interesting and vital for the determination of possible effects from caldera collapse eruptions.

Furthermore, the numerical modelling of rock mechanics is important in other areas. Applications of rock mechanics in geophysics can be found in the review by Sammonds (1999) who investigates deformation of the earth's crust and the break-up of ice sheets. The fracture and break-up of rocks and metals are also important in many, astrophysical, engineering, material science and mining applications. Rock mechanics is a relatively new discipline, a review of the history of rock mechanics is found in Jaeger (1979).

1.2 Numerical Method

Many factors have to be considered when choosing a numerical method which is suitable for a particular application. Primarily one must ensure that the numerical method is capable of computing the particular task, the accuracy, speed and ease of use of the method must also be examined.

In this thesis there are two areas we wish to investigate. The first involves the computation of complex free surface flows of water, the second area is the computation of the dynamics and fracture of solid bodies. It is in many ways preferable that the same method be employed for both areas as this then makes it much easier to eventually combine the two areas.

Free surface flow reviews have been given by Scardovelli and Zaleski (1999) and Ferziger and Perić (1996) (pg.321-335) discussing many of the numerical methods

used for multiphase and free surface flows. Yeung (1982) presents a review for the solution of free surface flow problems using a potential (stream function) approach to solve the governing equations of fluid dynamics. Raad (1995) looks at the use of computational fluid dynamics in the solution of water wave problems with particular emphasis on Marker and Cell (MAC) techniques. The methods we discuss are concentrated on primitive variable techniques (pressure, velocity) as they lead to fewer dependent variables and therefore are better for three dimensional calculations (Fletcher 1988) (pg.387).

Finite element methods have many attractive features, although we base the discussion in this section more on the use of particle methods. Lyard and Genco (1994) and Xing et al. (1998) discuss the use of finite element methods in the computation of water waves. Curnier (1993) outlines the use of finite elements in solid body mechanics.

When using finite differences free surface flows are more difficult to model than standard confined flows as they involve a moving boundary (the free surface) the shape and position of which is previously unknown. The difficulty in computing free surface motion lies in how to track free surfaces. One possibility is to fit a grid along the free surface, then adjust and regrid the problem as the free surface moves. These techniques are known as boundary fitting, they are fully Eulerian but can be difficult to regrid for complicated surface motions.

A way to remove the problems of regridding is to remove the grid from the simulation. The Particle In Cell (PIC) method (Harlow 1964) was the first step in this direction. PIC was originally developed to model fluid problems with large distortions and/or colliding interfaces. It is a hybrid method, taking features of Lagrangian and Eulerian approaches.

In the Eulerian approach a fluid is divided up into a number of computational *cells* which are fixed in space. The fluid then passes through the *cells* subject to the governing partial differential equations. Large fluid motion and distortion are easily handled. The major disadvantage of these schemes in modelling free surface flows is that they handle material interfaces poorly.

The Lagrangian approach divides the computational fluid into *cells* which move with the fluid. In the limit of extremely high resolution, one can imagine each computational cell representing a molecule of the fluid. As the computational domain is following the fluid Lagrangian techniques are better at tracking interfaces, though

can breakdown when the fluid has undergone large distortions.

The PIC method involves a stationary grid of points on which the filed variables are calculated. These variables are then interpolated onto a Lagrangian mesh of particles which represent the fluid and its motion. As the variables are calculated on a stationary grid, large distortions of the fluid are possible without the grid becoming tangled. As the fluid is represented by a set of Lagrangian particles, interface tracking is simple.

The approach used by the MAC and Volume of Fluid (VOF) methods is to define a fixed grid over which the simulation is to be computed and then track the movement of the interface around this grid. The MAC method (Harlow and Welch 1965) does this by using a series of marker particles which define the free surface and are followed to track movement of the free surface. There is Lagrangian tracking of marker particles which rely on an Eulerian grid for the velocities. The VOF method Hirt and Nichols (1981) tracks the free surface by solving an equation for the void fraction of liquid in each cell. In this case the free surface is found from the Eulerian tracking of a colour function representing whether or not a particular cell contains a fluid fully, partially or not at all.

The method we choose to use is the Lagrangian particle method Smoothed Particle Hydrodynamics (SPH) (Monaghan 1992). The major difference between SPH and the other methods we have discussed is that it doesn't require the use of a grid in its computations. Instead particles consist of interpolating functions, which interact with surrounding particles, in this way it can be considered intuitively similar to the interactions between particles in a real fluid. The advantage of not having a grid is that there are no grid tangling problems when fluid deformations are large. As a bonus the method is simple, easy to use and complicated physics can be easily incorporated.

An example of the ease with which physics can be incorporated is that solid body problems can be handled by essentially only adding a resistive term to the stress tensor. The size these resistive stress terms is found from a version of Hooke's law. The addition of these terms to the stress tensor was first proposed by Wilkins (1964) and Petschek and Hanson (1968) in a finite difference context. It was later examined by Libersky and Petschek (1991) and Benz and Asphaug (1994) in the SPH framework.

The calculations that we perform are two dimensional, the main reason for this

being that the computational effort involved in three dimensional calculations would require programming in parallel. Also the experiments that we perform and compare to are two dimensional. Axisymmetric calculations can be performed using SPH (Petschek and Libersky 1993; Coleman and Bicknell 1985). Though the problems that we are investigating are not axisymmetric problems, and are better performed in two dimensions as there are both interesting two dimensional problems and an obvious extension into the third dimension.

1.3 Thesis Outline

This thesis began with an introduction of it's primary motivation, the eruption of Santorini and an outline of our reasons for choosing the SPH numerical method for the numerical modelling of the production of water waves and rock fracture.

Chapter two outlines the SPH technique as it applies to the modelling of hydrodynamic flows. The chapter begins with a brief introduction of the method and a derivation of the appropriate equations. It concludes with a discussion on the use of boundary conditions in SPH.

In the third chapter, the SPH code is validated against simple test problems. The problems that are presented have both a connection to the flows that are generated in the caldera collapse of an island volcano, but more importantly they have either experimental or theoretical solutions to which we can compare our results. The purpose of this chapter is that once we are confident that the numerical models behave suitably for a series of simple test cases, we can be confident that they can correctly model more complicated situations that cannot be replicated by experiment or theory.

A review of caldera collapse is given in chapter four. Wave tank experiments for a simple model of the waves produced due to piston subsidence are presented and replicated by numerical simulations. Effects of changes to the geometry of the cavity are studied. The application of these experiments and simulations to the realistic case of Santorini is discussed.

In chapter five the hydrodynamic equations are extended to model elastic-plastic media by the addition of a deviatoric stress tensor. The equations used for the modelling of ductile (plastic) materials and a damage model for brittle fracture are

introduced. A method to combat the SPH tensile instability is implemented and a dispersion analysis is undertaken to study the stability of the method.

We follow the lead of Libersky and Petschek (1991), Benz and Asphaug (1994) in using SPH to model the deformations and fracturing of solid materials in chapter six. We begin by looking at the collision of elastic balls and the oscillations of elastic and plastic plates, the concentration of stress around a circular hole is calculated. We also present simple tests of our fracture model by simulating the fracture of plates in tension. The simulations that we present are two dimensional, this allows us to obtain the fundamental results without the extra computational effort and geometry complications of three dimensional calculations.

In chapter seven we present SPH calculations which examine the stress fields and formation of fractures around magma chambers, we compare SPH results with the surface stress fields of Gudmundsson (1998). The effects of important physical processes are examined and computations illustrate possible fracture regimes and the suitability of SPH in the further analysis of these problems. This chapter applies to the formation of calderas in both inland and marine environments.

We conclude in chapter eight with a brief review of the work conducted and areas in which further investigations should be concentrated.

Chapter 2

Smoothed Particle Hydrodynamics

n this chapter we outline the equations of Smoothed Particle Hydrodynamics (SPH). We begin by describing the method, showing how it is applied to the modelling of hydrodynamic media. We then discuss boundary conditions and their implementation in SPH.

The SPH method originated in the late seventies with papers by Lucy (1977) and Gingold and Monaghan (1977) as a means of solving gas dynamics problems in astrophysics. Since then the method has been used to solve many astrophysical problems with modern reviews given by Benz (1990) and Monaghan (1992).

SPH can be modified to handle incompressible fluids such as water (Monaghan 1994) and used to simulate free surface flows such as a breaking dam and waves on a beach. SPH is a gridless, Lagrangian method which is ideal for computing free surface flows, as particles are free to move wherever they please without the restrictions of a grid.

The problems associated with a grid in finite difference type calculations restrict their ability in solving free surface problems, for example breaking waves, that involve large grid movements and distortion.

Other methods have been able to simulate the travelling motions of waves, but it is only recently that overturning waves have been simulated beyond the stage where they hit the water. Chen et al. (1999) use a Volume of Fluid (VOF) variant to model plunging breakers and wave splash-up. Variations of the finite difference Marker and Cell (MAC) method (Miyata 1986; Mader 1986) are able to handle breaking waves but are complicated to code. The fully nonlinear potential flow model of Grilli et al. (1997) is capable of handling the breaking and overturning of waves but cannot simulate flow once the overturning wave has rejoined the body of the fluid.

2.1   The SPH Method

The SPH method involves approximating a function, say A, by a summation of the values of A at a set of disordered points (the particles),

$$A_s(\mathbf{r}) = \sum_{b=1}^{n} m_b \frac{A(\mathbf{r}_b)}{\rho(\mathbf{r}_b)} W(\mathbf{r} - \mathbf{r}_b, h) \tag{2.1}$$

where, n is the number of particles and W is the kernel. An SPH kernel is a function that is an approximation to a δ-function,

$$\lim_{h \to 0} W(\mathbf{r} - \mathbf{r}', h) = \delta(\mathbf{r} - \mathbf{r}'). \tag{2.2}$$

It is also important that the kernel is normalised,

$$\int W(\mathbf{r} - \mathbf{r}', h) \mathrm{d}\mathbf{r}' = 1. \tag{2.3}$$

In theory the summation is over all particles involved in the calculation, but in practice the kernels used are non-zero only near the particle, and the summation is only carried out over particles in each others neighbourhoods. Early calculations used a Gaussian for the kernel although Monaghan and Lattanzio (1985) define a spline based kernel.

Cubic spline kernels are used as they have compact support (that is they have non zero value within a finite domain), they also have a continuous second derivative so that minor perturbations to particle positions give only minor variations to the resulting summation. In two dimensions a cubic spline kernel is,

$$W(r) = \frac{10}{7\pi h^2} \begin{cases} 1 - \frac{3}{2}\left(\frac{r}{h}\right)^2 + \frac{3}{4}\left(\frac{r}{h}\right)^3 & \text{if } 0 \le \frac{r}{h} \le 1 \\ \\ \frac{1}{4}(2 - \frac{r}{h})^3 & \text{if } 1 \le \frac{r}{h} \le 2 \\ \\ 0 & \text{if } 2 \le \frac{r}{h} \le \infty. \end{cases} \tag{2.4}$$

The kernel is a differentiable function and $A(\mathbf{r}_b)$ is just the value of A at the point $\mathbf{r}_b$ so that the derivative of A can be calculated exactly as,

$$\nabla A(\mathbf{r}) = \sum_{b=1}^{n} m_b \frac{A(\mathbf{r}_b)}{\rho(\mathbf{r}_b)} \nabla W(\mathbf{r} - \mathbf{r}_b, h). \tag{2.5}$$

In SPH the spatial derivatives are exact derivatives of approximate interpolating functions.

2.2 Equations for Fluid Dynamics

Like many fluid dynamics calculations we wish to solve the full Navier Stokes equations. These are the momentum equation (for constant viscosity, μ),

$$\frac{d\mathbf{v}}{dt} = -\frac{1}{\rho}\nabla P + \frac{\mu}{\rho}\nabla^2\mathbf{v} + \mathbf{F}_{ext}, \tag{2.6}$$

where, $\mathbf{v}$ is velocity, P is Pressure, ρ is density and $\mathbf{F}_{ext}$ is any external forces such as gravity, and the continuity equation,

$$\frac{d\rho}{dt} = -\rho\nabla \cdot \mathbf{v}. \tag{2.7}$$

To use equations (2.6) and (2.7) in the SPH technique we must use equations (2.1) and (2.5) to convert them into SPH form. We take a simplified momentum equation (neglecting viscosity and external forces),

$$\frac{d\mathbf{v}}{dt} = -\frac{1}{\rho}\nabla P. \tag{2.8}$$

This could be converted straight into SPH form although the resulting equation would be unsymmetric in particles a and b meaning that momentum will not be accurately conserved. Instead we make use of the relation,

$$\nabla\left(\frac{P}{\rho}\right) = \frac{\nabla P}{\rho} - \frac{P}{\rho^2}\nabla\rho. \tag{2.9}$$

So that (2.8) becomes,

$$\frac{d\mathbf{v}}{dt} = -\nabla\left(\frac{P}{\rho}\right) - \frac{P}{\rho^2}\nabla\rho. \tag{2.10}$$

In SPH interpolation form equation (2.10) becomes,

$$\frac{d\mathbf{v}_a}{dt} = -\sum_b m_b \left(\frac{P_a}{\rho_a^2} + \frac{P_b}{\rho_b^2}\right)\nabla_a W_{ab}. \tag{2.11}$$

To account for viscosity, the one dimensional momentum equation with viscosity,

$$\frac{dv}{dt} = -\frac{1}{\rho}\frac{\partial P}{\partial x} + \frac{1}{\rho}\frac{\partial}{\partial x}\left(\mu\frac{\partial v}{\partial x}\right) \tag{2.12}$$

can be rewritten as,

$$\frac{dv}{dt} = -\frac{1}{\rho}\frac{\partial}{\partial x}\left(P - \mu\frac{\partial v}{\partial x}\right). \tag{2.13}$$

It is clear from (2.13) that the viscosity term is acting as an artificial pressure term. When particles are moving together ($\partial v/\partial x < 0$) density is increasing, the artificial pressure also increases to resist the density increase. Using this idea a symmetric viscosity term Π_{ab} is added to equation (2.11) such that,

$$\Pi_{ab} \sim \frac{\mu}{\rho^2}\frac{\partial v}{\partial x}. \tag{2.14}$$

Leading to a suitable SPH viscosity term,

$$\Pi_{ab} = \alpha h\frac{\overline{c}_{ab}}{\overline{\rho}_{ab}}\frac{\mathbf{v}_{ab}\cdot\mathbf{r}_{ab}}{\mathbf{r}_{ab}^2 + \eta^2} \tag{2.15}$$

where $\overline{c}_{ab} = (c_a + c_b)/2$, $\overline{\rho}_{ab} = (\rho_a + \rho_b)/2$ and $\mathbf{r}_{ab} = \mathbf{r}_a - \mathbf{r}_b$. The symmetry of this term ensures conservation.

The idea of using an artificial viscosity term is taken from Von Neumann and Richtmyer (1950) who used it to model hydrodynamic shocks by smearing out the shock front to remove discontinuities in the system.

There is also a kinetic pressure term in the viscosity which is used to handle penetration in the case of high Mach number collisions. This term is usually negligible in the incompressible form of SPH where small Mach number flows are considered. In low Mach number flows the velocity of bulk fluid motion, v is much less than the soundspeed, c_s. The second term of (2.16) scales like $\beta h\frac{\mathbf{v}_{ab}\cdot\mathbf{r}_{ab}}{\mathbf{r}_{ab}^2 + \eta^2}$ compared to the first term which is like $\alpha\overline{c}_{ab}$, as $v \ll \overline{c}_{ab}$ the term involving alpha will usually be larger.

$$\Pi_{ab} = \alpha h\frac{\overline{c}_{ab}}{\overline{\rho}_{ab}}\frac{\mathbf{v}_{ab}\cdot\mathbf{r}_{ab}}{\mathbf{r}_{ab}^2 + \eta^2} + \frac{\beta h^2}{\overline{\rho}_{ab}}\left(\frac{\mathbf{v}_{ab}\cdot\mathbf{r}_{ab}}{\mathbf{r}_{ab}^2 + \eta^2}\right)^2 \tag{2.16}$$

Artificial viscosity was introduced into SPH gas dynamics problems to stabilise the calculations by limiting the motions of particles which are moving together, this is the reason we use artificial viscosity. The flows we are computing are fast moving and often turbulent, viscous boundary layers do not form. That we obtain good agreement with experiment indicates that the neglect of a realistic viscous term does not seriously effect these calculations. Morris, Fox, and Zhu (1997) introduce a realistic viscous term in their low Reynolds number computations.

Note that there is no change in the way the viscous term is calculated when the boundary particles (to be introduced in section 2.4) are involved in the summation. So the final momentum equation is,

$$\frac{d\mathbf{v}_a}{dt} = -\sum m_b \left(\frac{P_a}{\rho_a^2} + \frac{P_b}{\rho_b^2} + \Pi_{ab} \right) \nabla_a W_{ab} + \mathbf{F}_a. \tag{2.17}$$

We take typical values of $\alpha = 0.01$ and $\beta = 3\alpha$, so that,

$$\Pi_{ab} = -\frac{\alpha h}{\bar{\rho}_{ab}} \left(\bar{c}_{ab} + 3h \left| \frac{\mathbf{v}_{ab} \cdot \mathbf{r}_{ab}}{\mathbf{r}_{ab}^2 + \eta^2} \right| \right) \frac{\mathbf{v}_{ab} \cdot \mathbf{r}_{ab}}{\mathbf{r}_{ab}^2 + \eta^2}. \tag{2.18}$$

For compressible flows in SPH density is determined by the simple summation,

$$\rho = \sum_b m_b W_{ab}. \tag{2.19}$$

Although as pointed out by Monaghan (1994), this is unsatisfactory when dealing with fluids such as water where the density falls discontinuously to zero at the surface. If (2.19) is used to calculate the density the smoothing performed by the kernel means that the density drops to zero over the smoothing distance $2h$, instead of instantaneously, leading to an incorrect pressure being calculated from the equation of state.

Instead density is determined via the continuity equation,

$$\frac{d\rho}{dt} = -\nabla \cdot (\rho \mathbf{v}) + \mathbf{v} \cdot \nabla \rho, \tag{2.20}$$

or in SPH summation form,

$$\frac{d\rho_a}{dt} = \sum_b m_b (\mathbf{v}_a - \mathbf{v}_b) \cdot \nabla_a W_{ab}. \tag{2.21}$$

Monaghan (1989) noted that it is not necessary for the velocity at which a particle is moved to be equal to the actual velocity of the particle. In the XSPH variation of SPH particles are moved at an average velocity of neighbouring particles, to keep an orderly arrangement of particles in non-viscous compressible flows.

Particles are moved according to,

$$\frac{d\mathbf{r}_a}{dt} = \mathbf{v}_a + \xi \sum_b \frac{m_b}{\bar{\rho}_{ab}} (\mathbf{v}_b - \mathbf{v}_a) W_{ab}, \tag{2.22}$$

where, typically, $\xi = 0.5$.

Monaghan (1994) proposes a way to model incompressible flows by modifying the compressible SPH technique. The idea makes use of the artificial compressibility method used by Chorin (1967) (see also Hirt and Nichols (1980) who use a similar idea to model compressible flows with an incompressible code). Chorin uses the fact that fluids such as water are actually slightly compressible. Usually water is modelled as an artificial fluid that is more incompressible than it actually is. Incompressible SPH takes a different path, modelling water with an equation of state that gives a higher compressibility than the actual fluid.

It can be shown from the momentum equation that,

$$\frac{\delta\rho}{\rho} \sim \frac{vL}{\tau c_s^2} \tag{2.23}$$

for bulk fluid motions $v \sim L/\tau$ so that,

$$\frac{\delta\rho}{\rho} \sim \frac{v^2}{c_s^2} = M^2. \tag{2.24}$$

If we wish to keep density variations down to 1% we need to choose a Mach number $M = 0.1$. The best way to do this is to choose a soundspeed much greater than a typical velocity. A good compromise between small density variations and a large timestep ($\delta t \sim h/c_s$) is to take $c_s = 10V_o$ where V_o is the largest (or typical) velocity expected.

The equation of state used is (Batchelor 1973),

$$P = B\left(\left(\frac{\rho}{\rho_0}\right)^\gamma - 1\right) \tag{2.25}$$

where $B = \rho_o c_s^2$. For most of the cases considered we take $c_s^2 = 200gh$ where H is a measure of the depth of the fluid. B is therefore a problem dependent constant. We take $\gamma = 7$.

An alternative approach for the modelling of incompressible flows using SPH is the projection technique of Cummins and Rudman (1999), in which a pressure Poisson equation is solved, ensuring the incompressibility condition ($\nabla \cdot \mathbf{v} = 0$) is met. Here pressure is not used as a thermodynamic variable, and sound waves are not present. This technique has the advantage of allowing larger timesteps, though there is an increase in the amount of work required per timestep.

2.3 Fluid Dynamics Implementation

Finding Particles   Although the SPH algorithm doesn't require the use of a grid for computing derivatives, it has long been established that a grid can be of use in determining particle positions (Monaghan 1985). SPH requires that particles within a distance $2h$ of each other are included in the summations. Linked lists (Hockney and Eastwood 1981) (pg.278) are an efficient way of determining which particles are within the smoothing distance.

The idea is to place a grid of square cells (with sides of length $2h$) around the particles in the simulation. Each cell then has a pointer (Head of Chain) that gives either the identifying number for the first particle in the cell, or zero if the cell contains no particles. The first particle in the cell then contains a pointer (link) to the second particle in the cell and so forth.

At the start of each timestep. The grid is constructed and the Head of Chain (HOC) array is initialised to zero. Each particle is tested to see in which cell it belongs. The particle is then placed at the Head of Chain for that cell with its link (LL) pointing to the previous particle at the Head of Chain. To illustrate this we use the setup in figure 2.1. Cells B and F do not contain any particles so we find $HOC(B) = 0$ and $HOC(F) = 0$. Cell G contains particles 3 and 4. This cell will have $HOC(G) = 4$, a pointer to particle 4. The link list of particle 4 then has a pointer to the next particle in the cell, $LL(4) = 3$ and $LL(3) = 0$ to signify that there are no more particles in the cell.
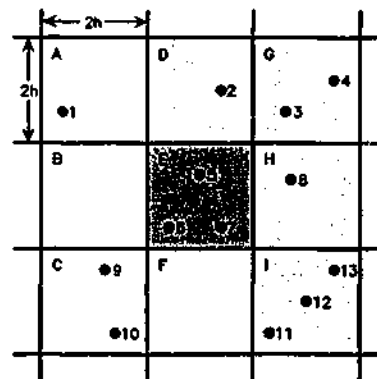
Figure 2.1: Diagram to illustrate the use of a grid and linked lists in determining which particles are neighbours and will contribute to a summation.

When we wish to find the particles required for summations we traverse each cell and treat it as the *homecell*. We examine particles in the *homecell* with all the particles in the *neighbouring* eight cells, and include them in the summations if they are within the $2h$ smoothing distance. However we only need to include half the neighbouring cells if we make use of the symmetry of the interactions between particles. Taking cell E of figure 2.1 as an example, we only treat the lightly shaded cells as neighbouring cells, as interactions between cell B and E would have been accounted for when cell B was the homecell and similarly for other cells.

Integration Scheme In this section the SPH summations that give the rate of change of force, position and density are written as $\mathbf{F}$, $\mathbf{v}$ and D. A subscript of o indicates a quantity at the beginning of a timestep, a p indicates a predicted quantity and no superscript refers to the value after the timestep integration has been completed.

Position is integrated using a leap frog integrator (Lattanzio et al. 1985).

$$\mathbf{r} = \mathbf{r}_o + \Delta t \mathbf{v}_o + \frac{1}{2}(\Delta t)^2 \mathbf{F}_o \tag{2.26}$$

Velocity and density are then integrated by a predictor-corrector scheme (Monaghan 1989). We have a predictor step,

$$\begin{aligned} \mathbf{v}_p &= \mathbf{v}_o + \Delta t \mathbf{F}_o \\ \rho_p &= \rho_o + \Delta t \mathbf{D}_o. \end{aligned} \tag{2.27}$$

We now calculate new values of $\mathbf{F}$ and $\mathbf{D}$ before using a corrector step,

$$\begin{aligned} \mathbf{v} &= \mathbf{v}_p + \tfrac{1}{2}\Delta t(\mathbf{F} - \mathbf{F}_o) \\ \rho &= \rho_p + \tfrac{1}{2}\Delta t(\mathbf{D} - \mathbf{D}_o). \end{aligned} \tag{2.28}$$

Damping As described later in section 2.4 we require for our system to be damped down at the start of the calculation to remove any energy inherent in the initial setup. This energy is due to external forces (gravity, boundary forces) not being in equilibrium with the initial set up and an adjustment of particle positions is required to bring these forces into equilibrium.

Damping is conducted by reducing the particle velocities by the factor Γ during the damping period. Γ is a factor typically equal to 0.998 during damping, otherwise

$\Gamma = 1$. The Predictor and Corrector steps for velocity then become,

$$
\begin{aligned}
\mathbf{v}_p &= \Gamma(\mathbf{v}_o + \Delta t \mathbf{F}_o) & \text{Predictor Step} \\
\mathbf{v} &= \Gamma(\mathbf{v}_p + \tfrac{1}{2}\Delta t(\mathbf{F} - \mathbf{F}_o)) & \text{Corrector Step}
\end{aligned}
\tag{2.29}
$$

Time Stepping   The size of the timestep (δt) is limited by the Courant condition and a gravitational condition. The timestep used being the minimum of the two. The gravitational timestep is calculated from the speed of sound and the typical velocity that the fluid can reach due to the gravitational force. The Courant condition (Monaghan 1989) is based on the speed of sound and particle viscosity.

$$
\begin{aligned}
\Delta t_{grav} &= \frac{1}{2} MIN \left(\frac{h}{\bar{c} + \sqrt{gh}} \right) \\
\Delta t_{cour} &= MIN \left(\frac{h}{2\bar{c} + 3 \left| h\frac{\mathbf{v}\cdot\mathbf{r}}{r^2+\eta^2} \right|} \right) \\
\delta t &= MIN(\Delta t_{grav}, \Delta t_{cour})
\end{aligned}
\tag{2.30}
$$

In the current case of (nearly) incompressible fluids where the soundspeed is high ($c \gg \sqrt{gh}$) and the timestep is essentially determined by the Courant condition.

2.4   Boundary Conditions

In order to be able to determine the flow of fluid in a specified domain, one is required to know the initial state of variables in the domain and boundary conditions on the spatial edge of the domain (the spatial edge of the domain also includes any obstacles that may be in the interior of the fluid). Different conditions are required to account for the different effects that boundaries can have on a fluid.

There are generally two ways that boundary conditions can be imposed in a numerical computation. Dirichlet conditions where the value of a variable is given on the boundary, and Neumann conditions where the derivative is specified at the edge of the domain.

2.4.1   Types of Boundary Conditions

Solid Boundaries   The major feature of solid boundaries such as the bottom and sides of a tank is that they do not allow the fluid to pass through them. Another

way of expressing this is that the normal component of the velocity of the fluid is zero at the boundary. A nonzero normal velocity near the boundary must decrease to zero at the boundary. Mathematically this condition is expressed that on the boundary,

$$\mathbf{v} \cdot \mathbf{n} = 0, \tag{2.31}$$

where, $\mathbf{v}$ is the fluid velocity and $\mathbf{n}$ is the direction normal to the boundary.

For moving boundaries, such as a plate being lifted through a fluid, this condition must be generalised. The normal component of fluid velocity must now match the normal velocity component of the boundary. The condition is now,

$$(\mathbf{v} - \mathbf{v}_B) \cdot \mathbf{n} = 0, \tag{2.32}$$

where, $\mathbf{v}_B$ is the velocity of the boundary.

We now consider the tangential component of velocity on the boundary.

No-Slip Boundary   On a no-slip boundary the tangential velocity component on the boundary is zero. On the boundary we take,

$$\mathbf{v} \cdot \mathbf{t} = 0, \tag{2.33}$$

where, $\mathbf{t}$ is the direction tangential to the boundary.

No-slip boundaries are important in cases of viscous boundary layers. At the interface between boundary and fluid friction holds the fluid to the boundary, both the normal and tangential components of velocity are zero.

Free-Slip Boundary   If we were to study the flow of low viscosity fluids across boundaries we would notice that the boundary layers are much thinner and the majority of the fluid is allowed to freely slip along the boundary/fluid interface. At a free-slip boundary viscous effects are ignored and the tangential component of velocity can be non-zero at the boundary.

Inflow Boundary   Inflow and outflow boundaries occur at points where fluid is entering or leaving the domain respectively. At an inflow boundary the velocity of the flow is specified with a Dirichlet condition. That is on an inflow boundary,

$$\mathbf{v} = A(t), \tag{2.34}$$

where $A(t)$ can either be a constant or vary with time.

Outflow Boundary For an outflow condition, the velocity at which the fluid leaves is in general dependent on the flow inside the domain and an outflow velocity cannot be defined similar to the inflow condition. In this case there is zero acceleration of the flow at the boundary, so that on an outflow boundary,

$$\frac{\partial \mathbf{v}}{\partial t} = 0. \tag{2.35}$$

Free Surface Boundary Free surface boundaries can be complicated as their position is not previously known. The usual condition at a free surface is that the pressure at the surface is equal to the atmospheric pressure. We denote atmospheric pressure to be P_a and at a free surface boundary take,

$$P = P_a. \tag{2.36}$$

In practice we find $P \gg P_a$ for the interface between water and the atmosphere and it is sufficient to take,

$$P = 0. \tag{2.37}$$

We do not consider the effects of surface tension as our length scales are large and curvatures are usually small. The reviews of Dias and Lharif (1999) and Perlin and Schultz (2000) consider the effects of surface tension on waves.

2.5   Solid Boundaries in SPH

In the astrophysical applications of SPH (Gingold and Monaghan 1977; Lucy 1977) to stars explicit boundary conditions were not required. However, the problems considered in the extension of SPH to model fluid flows (Monaghan 1994), require that solid boundaries be included. Originally boundary conditions were treated by assuming that the effect of a boundary was to provide a force to the fluid to ensure that the fluid is unable to pass through the boundary.

The early SPH fluid calculations employed a Lennard-Jones type boundary force, Monaghan (1994) develops a force that was based on an idea of Peskin (1977) which allowed for calculations of irregular boundary shapes and complex geometries.

Problems of disorder near boundaries suggest boundary prescriptions based on ghost particles. These methods are in someways analogous to a Neumann boundary

condition, where properties near a boundary are found by mirroring the properties across the boundary.

There are two different ways of incorporating ghost or imaginary particle boundary techniques into SPH simulations. Obviously it can be done by actually incorporating the ghost particles into the SPH simulation (Morris, Fox, and Zhu 1997). Or alternatively by altering the SPH equations to include the boundary effects in the simulation without storing boundary particle properties (Takeda, Miyama, and Sekiya 1994; Randles and Libersky 1996). Randles and Libersky give a good discussion of the problems of modelling boundary conditions in SPH.

There are many different ways of employing boundary conditions in SPH. Here we look at three of them, Lennard-Jones forces, boundary particle forces, and ghost particle boundary implementations.

Lennard-Jones Forces The Lennard-Jones form for a boundary particle force is based on known forces between molecules (Lennard-Jones 1931), (Baker 1963) (pg.7).

$$f(r) = D \left(\left(\frac{r_o}{r} \right)^{p_1} - \left(\frac{r_o}{r} \right)^{p_2} \right) \frac{\mathbf{r}}{r^2} \tag{2.38}$$

The Lennard-Jones force is purely repulsive and is set to zero if $r > r_o$, where r_o is the initial particle spacing. The p constants must satisfy $p_1 > p_2$, and D has dimensions of velocity squared. D is chosen depending on the physical situation being considered. We take $p_1 = 12$, $p_2 = 6$ and $D = gh$ for our Lennard-Jones calculation.

Boundary Particle Forces Peskin (1972,1977) studied the flows associated with blood transfer through the heart. These flows become complicated as the boundaries (heart walls, valves) interact and move with the fluid (blood). Peskin introduced the idea of having boundary forces consisting of a force at the boundary, which could be approximated by a delta function (a similar technique is used by Sulsky and Brackbill (1991) to study the effects of a suspension of particles in a fluid). This leads to a natural implementation in SPH where all fluid particles are smoothed out by an approximation to a delta function. A boundary force based on the SPH kernel would seem appropriate because the pressure forces involve the gradient of

the kernel. A suitable form is,

$$
f(r_\perp) = v c_s{}^2
\begin{cases}
2/3h & \text{if} \quad 0 < r_\perp/h < 2/3 \\[2mm]
(r_\perp/h^2)(2 - \tfrac{3}{2}r_\perp/h) & \text{if} \quad 2/3 < r_\perp/h < 1 \\[2mm]
(1/2h)(2 - r_\perp/h)^2 & \text{if} \quad 1 < r_\perp/h < 2 \\[2mm]
0 & \text{if} \quad 2 < r_\perp/h < \infty
\end{cases}
\tag{2.39}
$$

where $r_\perp$ is the perpendicular distance between the fluid particle and the boundary particle and v is a free parameter which determines the strength of the boundary force, typically $v = 0.01$.

Monaghan (1995) introduces a way for such a boundary force to be used which also allows for a constant force to be given to a particle moving parallel to the boundary and can be easily extended to complicated geometries. It is important for the boundary to apply a smooth force, otherwise a fluid particle travelling parallel to the boundary would notice differences in the force (disorder in the flow) as it passes from being directly over the top of a particle, to between two particles and then over the top of a particle again. The method consists of assigning each boundary particle a normal direction $\mathbf{n}$ and then calculating the perpendicular $r_\perp$ and tangential $r_\parallel$ distances to interacting fluid particles.

The boundary force F_{bnd}, is then calculated as,

$$
F_{bnd} = f(r_\perp) P(r_\parallel) \mathbf{n},
\tag{2.40}
$$

where,

$$
P(r_\parallel) =
\begin{cases}
\tfrac{1}{2}(1 + \cos(\pi r_\parallel/\Delta p)) & \text{if} \quad |r_\parallel| < \Delta p \\
0 & \text{if} \quad |r_\parallel| > \Delta p.
\end{cases}
\tag{2.41}
$$

Ghost Particle Methods   The major problem with the above boundary prescriptions is that they produce disorder near the boundaries. The boundary force is only dependent on the distance a fluid particle is away from the boundary with no (or little) consideration of the velocity or pressure of the fluid near the boundary. A stationary fluid particle with low pressure is given the same boundary force as a

fluid particle with a high velocity and pressure, even though it is clear that the second case requires a higher force to keep the fluid particle from passing through the boundary. This inconsistency leads to higher disorder and particle movement away from the boundary (see figure 2.2) near the free surface than at the bottom of the tank.
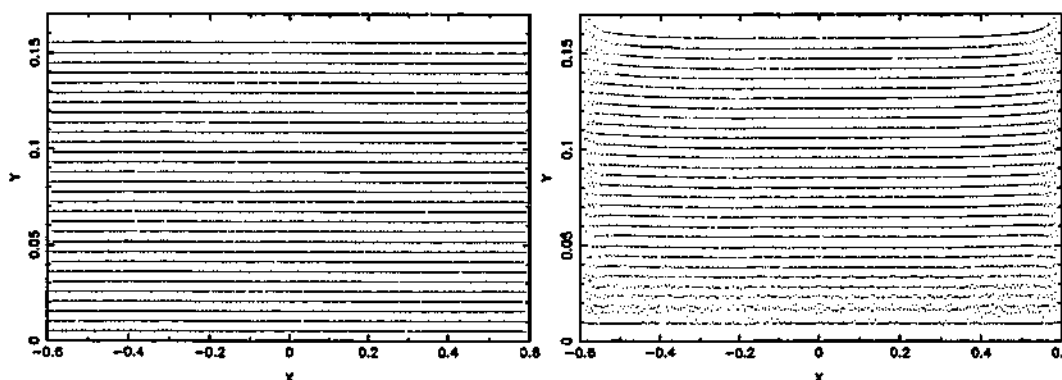
Figure 2.2:   *How the use of boundary particle forcing alters the positioning of particles from an initially ordered state to the raised and disordered state in the second frame.*

The boundary force methods also employ the use of a free parameter (v in (2.39)) which determines the strength of the boundary force. Whilst it would be possible to have a variable parameter which is dependent on the pressure and velocity of fluid particles the best way to handle these contributions is unknown.

Randles and Libersky (1996) give a review of ghost particle boundary conditions. One way to approach the problem is to add terms in the integration by parts when the equations are being derived that are only used when boundary particles are present. Takeda, Miyama, and Sekiya (1994) model the boundaries in their viscous flow calculation by using imaginary particles outside the domain which contribute to the density and viscous force terms of their equations.

The alternative to this is to model boundaries using SPH particles which supply a viscous term to ensure that fluid particles do not pass through the boundary. This idea was used by Morris, Fox, and Zhu (1997) in their modelling of low Reynolds number flows which require a no-slip boundary condition. Libersky and Petschek (1991) implement boundaries by reflecting the properties of particles near a boundary to ghost particles across the boundary. The general idea is that when a boundary

and fluid particle interact the boundary particle is given a *mirror velocity* from the fluid particle. The *mirror velocity* is then used in the calculation of the viscosity term.

In the following examples the ghost particle boundaries of Morris, Fox, and Zhu (1997) have been implemented. Our examples only deal with straight boundaries and right angles although it is possible to easily extend to more complex topography.

Each boundary consists of several lines of boundary ghost particles, the number of lines is kernel dependent. We ensure that we have ghost boundary particles within the $2h$ smoothing length. The lines of ghost particles are aligned on a Cartesian grid.

The mirror velocity of a boundary particle is found by taking a linear extrapolation across the boundary to give a zero velocity at the boundary. This is done by calculating the perpendicular distance between the boundary particle and the boundary D_b, and the distance between the fluid particle and the boundary D_f.

$$\beta = 1 + \frac{D_b}{D_f} \tag{2.42}$$

There is a limit, $\beta_{max} = 1.5$ placed on β to ensure that large velocities do not arise when a fluid particle approaches very close to a boundary. The velocity of the ghost particle is assigned by,

$$V_b = (1 - \beta)V_f. \tag{2.43}$$

This velocity is then used in the calculation of the SPH viscosity term. Although not in the XSPH term and determination of densities. The mirror velocity of the boundary particles V_b and the actual velocity of the fluid particle are placed into the equation for the viscous term (2.16). The calculation for the density of boundary particles is conducted in exactly the same way as that for fluid particles.

It is not altogether clear or intuitive as to how one should handle the corners of a boundary. The problem is how does one work out which boundary or part of a boundary should interact with a fluid particle. The approach taken by Monaghan (1995) for a single row of particles is to assign a normal to each boundary particle with a 45° normal being given to the particle at the intersection of two boundaries.

The situation becomes more difficult when one is dealing with several rows of ghost particles, as one has to decide which particles should be given a 45° normal
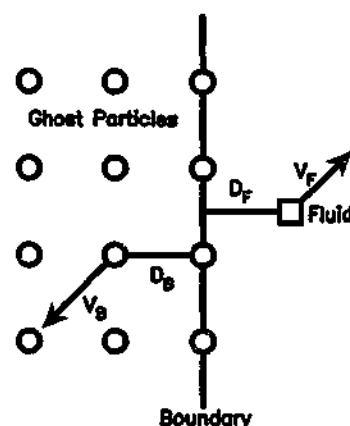
Figure 2.3: *Relation between the actual velocity of a fluid particle and the mirror velocity assigned to an interacting boundary particle. The boundary is the solid black line. The circles denote the 'ghost boundary particles', with the open square representing a fluid particle. The number of lines of ghost particles is dependent on the smoothing length.*

when a corner is encountered. The approach taken in this investigation is to break the boundary up into three regions as seen in figure 2.4. Those boundary particles found in region 1 are given a horizontal normal, those occurring in region 3 are said to have a vertical normal, with those in region 2 deemed to be those having a 45° normal. However, it must be pointed out that this may not necessarily be the best solution to this problem.

Problems would arise in our prescription if one wished to model a boundary that contained sharp edges such as the spike in figure 2.5. It is unlikely that the tip of the spike would contain enough ghost particles to prevent fluid particles on opposite sides of the boundary from interacting, so care must be taken in the case of sharp boundaries.

2.5.1 One Dimensional Boundary Conditions

The easiest way to study boundary conditions is to look at a one dimensional problem where complications associated with corners do not occur. The simulations shown in this section are conducted with a cubic kernel and a smoothing length $h = 1.2\Delta p$. Similar results were found when using a quartic kernel with smoothing length $h = 1.4\Delta p$.
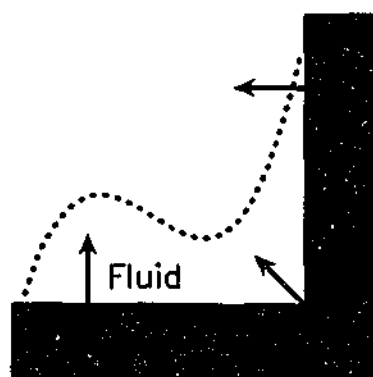
Figure 2.4: How the normal direction associated with a corner is assigned. Area 1 is assigned a normal which is horizontal. Particles in area 2 are assigned to have a 45° normal. The boundary particles in area 3 have a vertical normal.
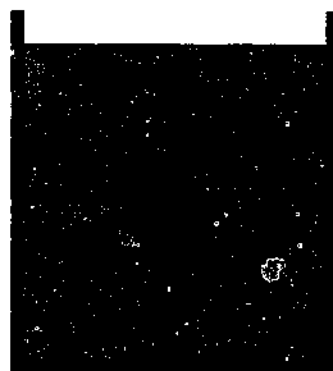
Figure 2.5: An example of a sharp boundary that could cause problems with our ghost particle boundary treatment as the tip of the boundary is unlikely to contain enough ghost particles to fill the smoothing length of fluid particles adjacent to the boundary.

We consider the one dimensional problem of water under gravity g, with damping, to produce a steady state for which $P = \rho_o g(D - y)$ where D is the depth of fluid of density ρ_o.

In general our SPH computations start with particles initially laid out on a Cartesian lattice. This is not the most stable configuration and the particles slowly adjust themselves to preferred positions. Also, because the fluid is treated as being compressible and relies on sound waves to transport information, we do not end up with instantaneous hydrostatic balance in our system. For these reasons we allow most of our simulations to settle down by damping for a few thousand timesteps before beginning our simulations. As the timestep is very short, sound waves are probably allowed to travel the domain back and forth in the order of fifty times in the damping period. We introduced a damping factor in section 2.3 which reduces the velocity at which particles are allowed to move in the damping period, allowing them to slow down and reach a stable state.

Figure 2.6 shows the pressure against distance for the steady state of an SPH simulation with Lennard-Jones boundary forces (2.38). A density of water of $\rho_o = 1.0 kg/m^3$ is used, the acceleration due to gravity is taken to be $g = 1.0 m/s$, and the initial fluid height was $0.15 m$. The peak pressure is and should be $150 Pa$. The gradient is also correct although there is an amount of disorder introduced into the pressure and density profiles near the bottom boundary. This disorder does not affect the profile near the free surface.

As illustrated in figure 2.7 a large amount of disorder is introduced when a boundary force based on an SPH kernel is employed. This simulation is conducted with fifty particles. Figure 2.8 is the same calculation but with ten times the amount of particles. It is clear that the disorder is reduced at the free surface, although spurious pressures are still found down towards the boundary. Again the pressure towards the boundary fluctuates around the correct value of $150 Pa$. The calculation took $2,000$ steps when fifty particles were used which corresponds to a time of 0.66 seconds, the five hundred particle simulation took $7,000$ steps to reach an equilibrium, but it must be pointed out that this corresponds to a time of 0.23 seconds.

Even though there is a *zig-zag* pressure variation between adjacent particles we still find that the total force on a particle $(-\nabla P/\rho + g)$ is small, in the vertical direction. The term associated with the pressure gradient balances with the gravitational

Figure 2.6: *Pressure P, against distance y, using Lennard-Jones boundary forces after 2,000 steps of damping (0.663 seconds). The calculation uses 50 particles, h = 1.2 and a cubic kernel.*

force. Forces in the horizontal direction are also small.

Figure 2.9 is a graph of steady state pressure versus distance when ghost particle boundary conditions are used. The pressure variation is much smoother than in the other two cases. There is only a minor variation in pressure near the boundary with the pressure clearly reaching the correct value at the boundary.

2.5.2 Two Dimensional Boundary Conditions

While it is important to know that we can correctly model boundaries in one dimension it is much more interesting and important that we can handle boundaries in two dimensions, as these are the situations which we are modelling.

Figure 2.10 illustrates the settling down of the specific kinetic energy over time for the two dimensional case of kernel based boundary force boundaries. As our calculations are in two dimensions we define the specific energy as the energy per unit thickness with units of J/m. The initial stationary particles quickly gain a large amount of kinetic energy as they move to their preferred conditions. The specific kinetic energy then settles down in a rather ragged fashion until most of the kinetic energy has been dissipated.
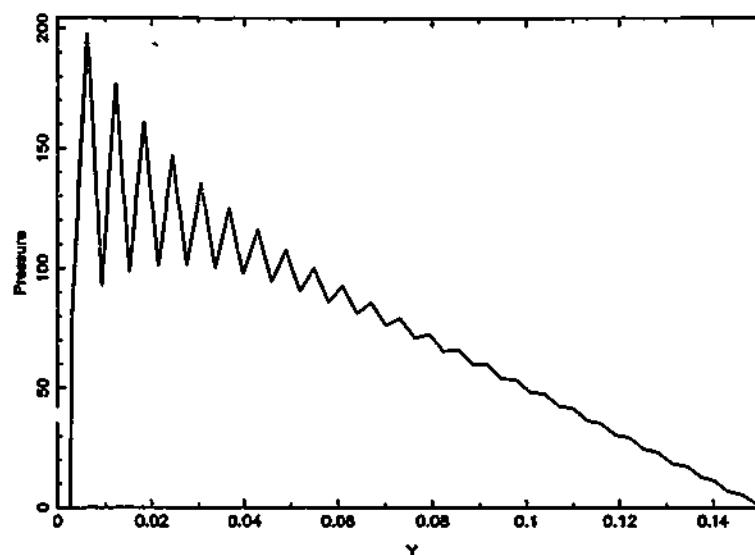
Figure 2.7: *Pressure against distance using kernel boundary forces after* 2,000 *steps of damping (0.663 seconds). The calculation uses* 50 *particles,* $h = 1.2$ *and a cubic kernel. Notice that there is a much larger amount of disorder at the left hand boundary than in the Lennard-Jones case (figure 2.6).*

Figure 2.11 is a plot of specific kinetic energy versus time for the damping period of a tank of water modelled using a ghost particle boundary implementation. The major point to notice is that the ghost particle boundaries provide a smoother damping down of the fluid than that obtained with boundary forces. The specific kinetic energy decrease is reminiscent of a decaying oscillatory solution for a damped forced simple harmonic oscillator. Note also that the maximum kinetic energy is one tenth of that reached in the case of kernel boundary forces (figure 2.10).

Figure 2.12 shows the pressure profile for hydrostatic balance after 10,000 steps of damping for a simulation of a tank of water using a boundary force boundary implementation. The first thing to notice is that particles are pushed away from the bottom boundary. It should also be observed that all the particles have experienced a vertical shift with the initial water depth of 15 cm increased to 16 cm. There is also a large amount of disorder towards the bottom boundary. The pressure variation at each depth is due to effects caused by the side boundary meaning that there is a variation of pressure as one moves across the tank, but like the one dimensional example the variation in the total force is small.
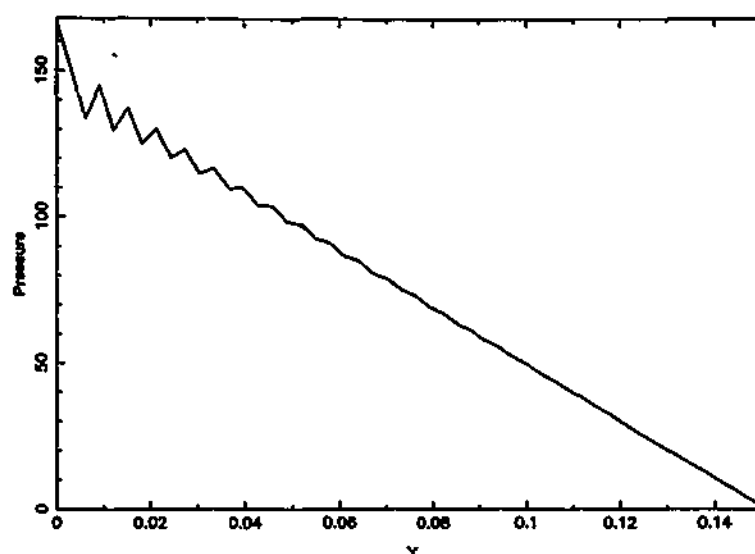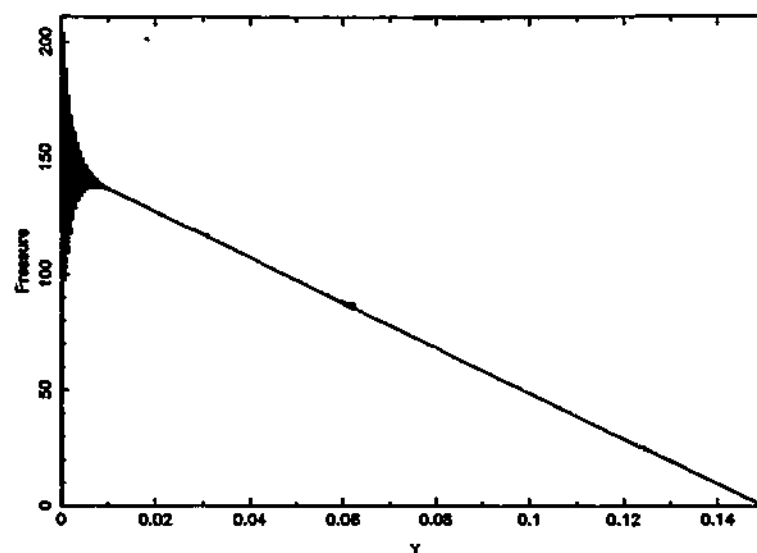
Figure 2.8: Pressure against distance using kernel boundary forces after 7,000 steps of damping (0.23 seconds). This calculation uses 500 particles, $h = 1.2$, and a cubic kernel. Note that the higher resolution brings the disorder closer to the boundary and evens out once the interactions don't reach the free surface.
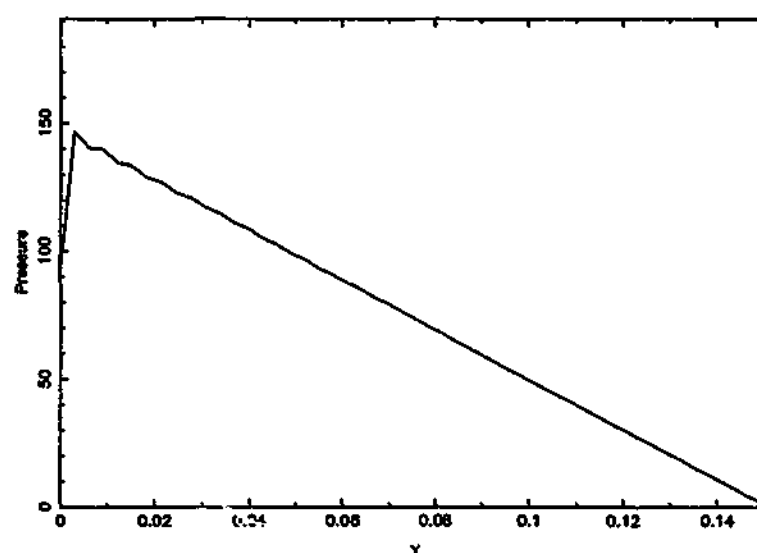
Figure 2.9: Pressure against distance using a ghost particle boundary implementation after 2,000 steps (0.663 seconds). The calculation employs 500 particles, $h = 1.2$ and a cubic kernel. It is clear that this type of boundary condition gives a significantly less varied pressure profile.
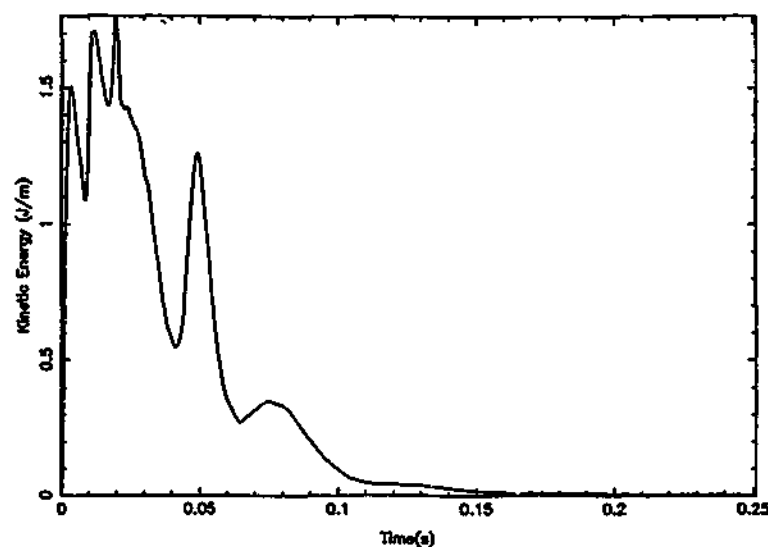
Figure 2.10: Damping for 1,500 steps using a kernel based boundary implementation. Note the 'random' way in which the particle velocities settle down.
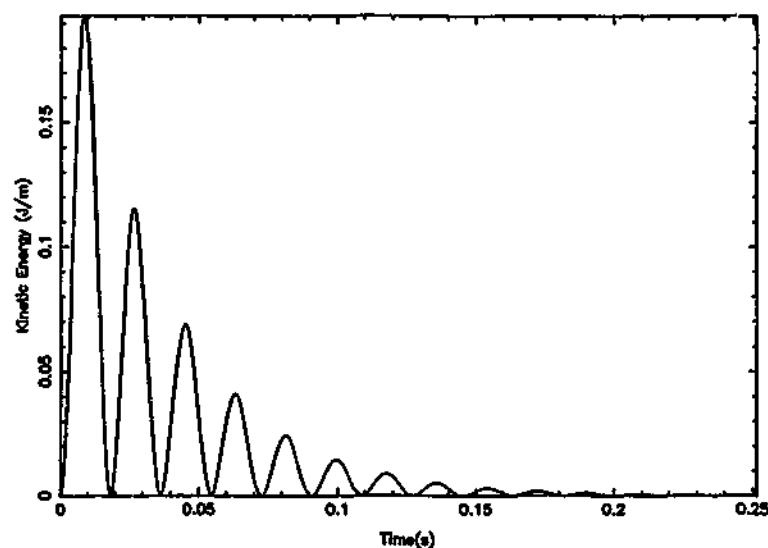
Figure 2.11: Damping for 1,500 steps using a ghost particle boundary implementation. Here the settling period occurs in a more ordered and structured way than for the case of boundary force boundary conditions.
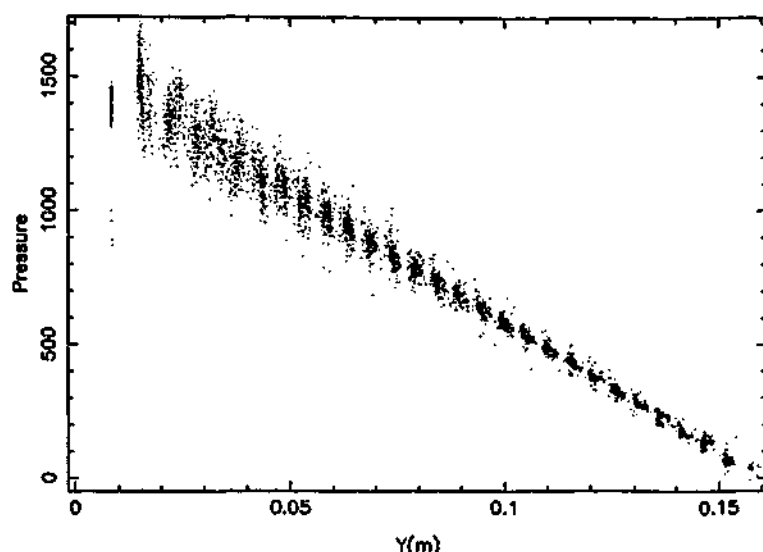
.Figure 2.12: Pressure against vertical distance in a two dimensional simulation
after 10,000 steps using kernel based boundary forces. The simula-
tion has 30 particles in the vertical direction with equal horizontal
resolution. The smoothing length $h = 1.2\Delta p$, with the viscosity pa-
rameter $\alpha = 0.01$ and the parameter which controls the size of the
boundary force $\xi = 0.02$. The simulations use a cubic kernel.
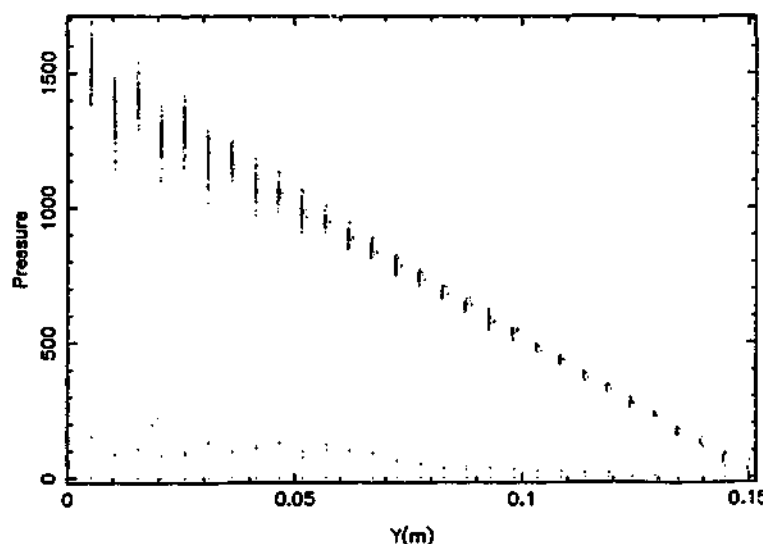
Figure 2.13: Pressure against vertical distance in a two dimensional simulation
after 10,000 steps using a ghost particle boundary implementation.
All other details of the simulation are as for figure 2.12.

Figure 2.13 shows the case of two dimensional ghost particle boundaries with a graph of pressure against distance, again as in the one dimensional case a two dimensional ghost particle boundary produces less disorder in the simulation. The y positions of the the particles are not overly changed, and the water depth stays at the initial depth ($15cm$). There is a slight variation in the pressure values towards the bottom boundary, again this is caused by the side boundaries. The problem is less pronounced near the surface as the particles there are more able to change their positioning to remove the disorder. The shift in the horizontal direction is always less than 10% of the particle spacing in the ghost particle case. In the boundary force case the shift is as large as 100% near the side boundaries though it is typically 20% away from the side boundaries.

Chapter 3

Water Wave Code Validation

efore modelling complex flows we must first validate our SPH code by comparing computations for simple flows with experimental and analytic solutions. These test cases have been chosen as they involve similar phenomena to those we expect to find in the production of waves by caldera collapse.

The first case we present is the propagation and run up of solitary waves. We then consider SPH models for the generation of waves via a moving piston. The problem of a breaking dam has been simulated to show that we can correctly model the collapse of a column of water and its motion as it surges across a boundary. Some simple undular bores have been used as test cases as they highlight some features of the flows that we will consider later in the caldera collapse case. Finally, we consider weir flow in the case of zero gravity. Other authors have carried out similar tests using SPH (Monaghan 1994; Morris, Fox, and Zhu 1997; Monaghan and Kos 2000) though we present this section as we use a different version of the SPH code of Monaghan (1994) and implement the boundary conditions differently.

3.1 Solitary Wave Propagation

Simulations were performed to see how accurately SPH modelled the extent of runup of a solitary wave against a wall, with the results compared to similar computations using a MAC method and experiments (Chan and Street 1970). The agreement with experiment is excellent.

Our initial test is to compare the runup of a solitary wave on a vertical wall. Solitary waves are known to satisfy the Kortweg de Vries (KdV) equation (Lighthill 1980),

$$\eta_t + 6\eta\eta_x + \eta_{xxx} = 0. \tag{3.1}$$

Where subscripts denote derivatives so that $\eta_t = \partial\eta/\partial t$, $\eta_x = \partial\eta/\partial x$ and $\eta_{xxx} = \partial^3\eta/\partial x^3$. The standard solution to this equation has the form,

$$\eta = \frac{H}{\cosh^2\left(\sqrt{\frac{3}{4}\frac{H}{D^3}}(x - Ut)\right)}. \tag{3.2}$$

Where H is the wave amplitude, D is the depth of water on which the wave is propagating and U is the wave speed. The theory of this solution is based on small amplitude waves, so that $H \ll D$.

In the simulations the particles were initially set up on a Cartesian lattice with those fluid particles above the free surface of the wave omitted. Because the particles are set up with a constant density, the equation of state (2.25) means that the particles in the simulation will also have a constant pressure, and a readjustment is required to attain a hydrostatic pressure profile.

The usual SPH technique is to damp the system for a time to remove some of this excess energy, allowing the particles to arrange themselves in a stable configuration. This is not suitable in this case as the initial set up contains a position and velocity profile of the particles which is not preserved through the damping process, so that the profile at the end of damping, would be vastly different to the initial profile. An alternative is to damp down the system and allow particles to arrange themselves with particles above the free surface of the wave present. Then remove those particles that do not make up the wave or base of water on which the wave is to propagate, and assign the velocity profile to the particles. Though the creation of a new free surface when the particles are removed introduces a different pressure profile and the problem reappears. For this reason the simulations of solitary waves (with initial profile given by (3.2)) presented in this section do not use damping.

It was found that when particles were set up on a Cartesian grid there was a tendency, especially for particles near the free surface to band together, giving a poorly resolved wave. This can be overcome by applying a small sinusoidal perturbation to the initial x and y positions of the particles. This gave an initial setup which was less prone to the problem of particles banding together.

Boundaries were modelled by the use of boundary particles (section 2.5), which provide a boundary force dependent on the distance a particle is from the boundary. As already outlined this leads to fluid moving away from the boundaries, and is more

pronounced for particles near the surface as they don't have large pressure forces above them to force them back towards the boundary. As this only occurs over a distance $O(h)$ from the boundary, it has minimal effect on the final computation of these free surface waves.

0   **0.5**   **1**
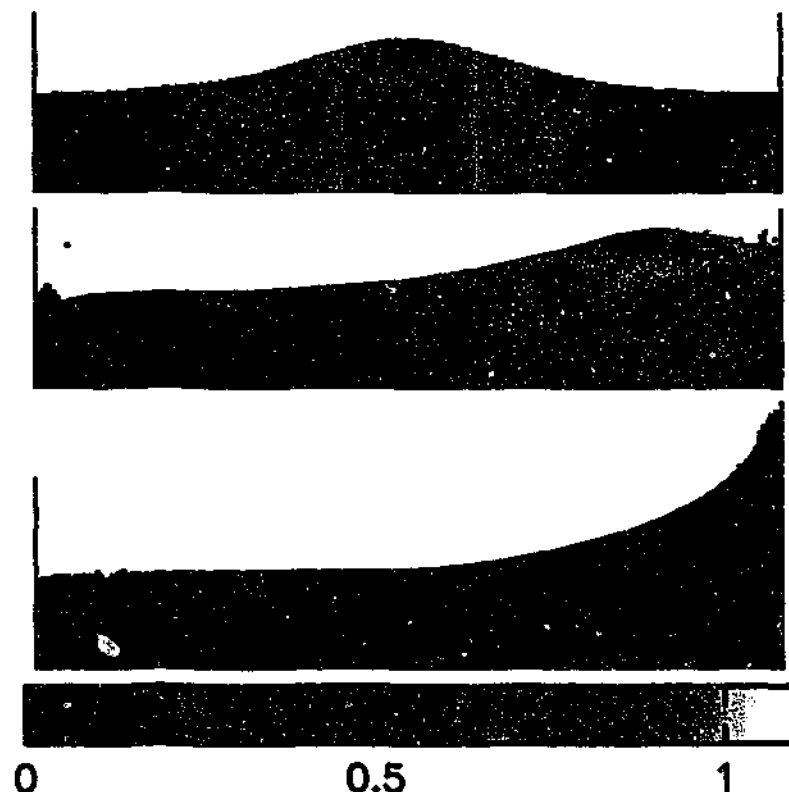
Figure 3.1: Solitary wave running up a wall. The tank is 1.68m long with the same scale being employed in the vertical direction. The wave propagates on water of depth 21cm, with the wave amplitude being half the undisturbed depth. Particles are coloured according to their speed, with the key at the bottom referring to all three frames. The times of each of the above frames are 0.0, 0.28 and 0.55 seconds from top to bottom respectively.

Figure 3.1 shows a sample simulation of the initial state and the wave running up the wall. The horizontal length scale of these waves is found by $\sqrt{(4D^3)/(3H)}$, this quantity decreases as the amplitude is increased. The smallest amplitude wave we modelled was $H = 2cm$, the depth of water on which our waves propagate was

$D = 21cm$ and the length of the tank was $168cm$. The horizontal length scale in this case is $79cm$ or approximately half the length of the tank. It is important that the tank remains longer than the horizontal length scale of the waves for correct simulation.

We can see the wave moving towards the right and running up the wall of the tank in figure 3.1. The small disturbance near the left boundary is due to the fluid initially moving away from the left boundary and forming a small return wave. Particles are coloured according to their speed, with lighter colours denoting higher speeds. The lower velocities (darker colours) found in the third frame of figure 3.1 are due to the loss of kinetic energy of the wave as it climbs the wall, gaining in gravitational potential energy.

Figure 3.2 compares a series of SPH results for the extent of run up against a wall to those obtained by Chan and Street (1970). It is clear that both numerical methods are in excellent agreement for low amplitude waves $H/D \leq 0.3$ (H is the wave amplitude and D is the depth of water underneath the wave), with good agreement for higher amplitudes with the SPH simulations being in better agreement with the experimental results. The minor differences for larger amplitudes reflect the non linearity of the higher amplitude waves.

The initial setup used by Chan and Street (1970) is based on a power series expansion given by Laitone (1960), which is different to the initial setup used for the present computations. Because the SPH simulations are in excellent agreement with experiment even though the initial state (3.2) is only an approximation, it is clear that the wave in the simulation quickly adjusts to a form consistent with the equations of motion.

It is to be expected (for small amplitude waves) that after the interaction with the wall the wave will reform with the same profile as before although travelling in the opposite direction. When $H/D = 0.2$ the agreement between the incident and reflected waves was good, this is also in agreement with the method of Chan and Street (1970). As expected large amplitude waves produced a reflected wave with a different profile to the incident wave.
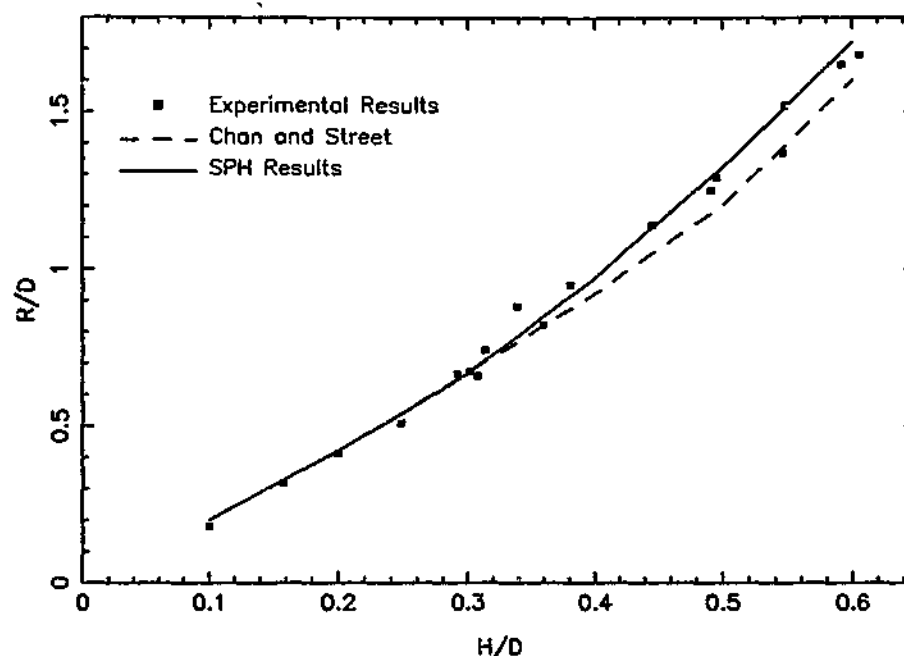
Figure 3.2:   *Comparison of SPH results for the run up against a wall to those of Chan and Street (1970) and the experimental results of Camfield and Street (1968). H is the amplitude of the wave, D is the depth of water on which the wave propagates and R is the maximum extent of run up on the wall.*

3.2   Wave Generation

A weakness in the previous test was that the initial state was not consistent with the exact equations. One of the advantages of SPH is that it is possible to simulate actual experiments, where the fluid is initially at rest and the wave is initiated by moving part of the boundary or other solid surface (see Monaghan and Kos, 2000).

We simulate runup experiments where the solitary wave is generated by moving the left boundary into a fluid at rest. This has the advantage that the fluid can be damped into hydrostatic equilibrium before the wave is initiated. We specify the velocity of the left hand boundary as follows. Taking g as the acceleration due to gravity, for $0 \leq t \leq t_* \sqrt{D/g}$ we (constantly) accelerate the velocity to $V = (1/10)t_* \sqrt{gD}$, for $t_* \sqrt{D/g} \leq t \leq (3/2)t_* \sqrt{D/g}$ we set $V = (1/10)t_* \sqrt{gD}$. We then (constantly) decelerate the wall velocity down to rest for $(3/2)t_* \sqrt{D/g} \leq t \leq (5/2)t_* \sqrt{D/g}$ after which the wall is stationary, $V = 0$. The non dimensional

parameter t_* was chosen in the domain $1 \leq t_* \leq 5$ to generate waves of different amplitude.
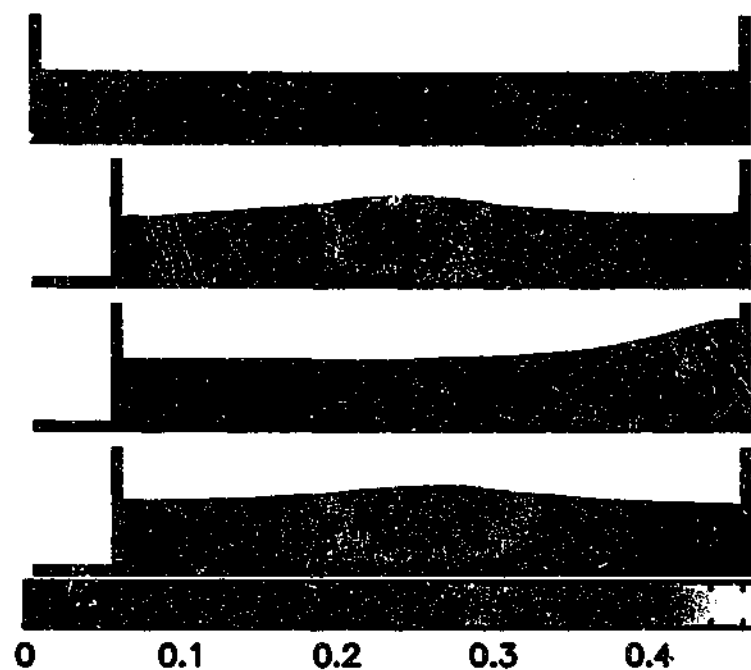
Figure 3.3: *Wave generated by a moving left hand boundary in a 1.8m long tank. The times of the frames are 0.0, 1.06, 1.72, 2.31 seconds from top to bottom respectively. Particles are coloured according to their speed, with 10,937 particles being used in the simulation. This is the case of $t_* = 3$, $\alpha = 0.01$ and water depth $D = 0.16m$, we take $h/\Delta p = 1.2$.*

It is important that the velocity is decelerated back down to zero as it was found that if the motion of the wall was instantaneously stopped (at $t = (3/2)t_*\sqrt{D/g}$) the water close to the wall retained the velocity of the wall. This led to a gap as the fluid moved away from the wall and the production of a smaller secondary wave as water curled back towards the wall.

In figure 3.3 we illustrate the wave generated by a moving left hand wall in a tank 1.8m long, 0.16m deep, with $t_* = 3$ at four times; the initial setup before the wall motion has begun, the incident wave at midtank, the wave running up the wall and finally the reflected wave at midtank. One notices in the case depicted in figure 3.3 that the wave is reflected without significant change. The only major difference between the reflected and incident waves is a small amount of dispersion.

All cases except for $t_* = 5$ were conducted with a tank length of $1.8m$. The length was doubled (to $3.6m$) in the $t_* = 5$ case as the wave did not have enough time to properly form and propagate in the smaller tank.

We find qualitative agreement with the experimental results of Chan and Street for the relation between wave amplitude and runup height. These results are shown in figure 3.4. The three distinct ways of modelling the wall runup of waves (experiment, computer simulation with a given initial condition, and a computer simulation which generates the wave by a moving wall) all produce similar results.
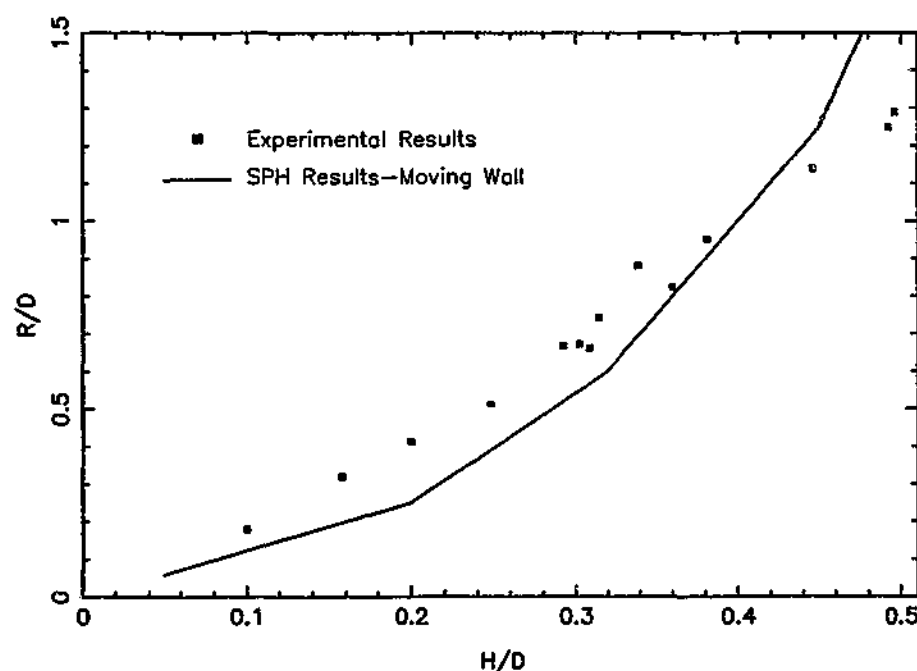
Figure 3.4:   *Comparison of SPH results for the run up against a wall with the experimental results of Camfield and Street (1968).*

The interactions between potential and kinetic energy in a simulation of our generated waves is shown in figure 3.5. During the initial 0.33 seconds damping is applied. The system is allowed to settle down to a steady state characterised by an initial increase in the kinetic and potential energies, the kinetic energy is damped to zero, but the potential energy increase remains due to a raising of the water depth as particles are pushed away from the bottom boundary. Between $0.33 - 0.70$ seconds the wall is accelerating, E_g and E_k steadily increase. For $0.70 - 0.85$ seconds the wall is moved at a constant velocity. The potential energy increase is greater than the
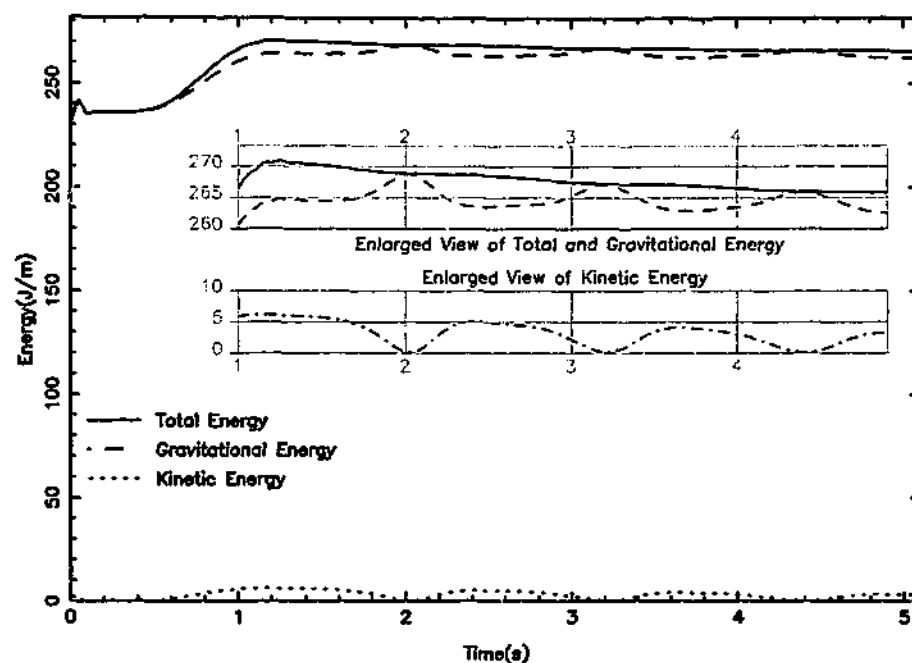
Figure 3.5: *Plot of E_{tot}, E_g and E_g during a simulation of a wave generated by a moving left hand wall. The interchange between E_k and E_g is due to the wave running up and down both walls. Enlarged frames show the total, gravitational and kinetic energies, the scale of the energy is three times the normal scale, scale on the time axis is unchanged.*

increase in the kinetic energy. The increase in energy slows during the time interval $0.85 - 1.27$ seconds as the wall is brought to rest. Work done by the moving wall results in a wave being produced, the interchange between E_k and E_g as the wave runs up and down both the left and right walls is clear.

A few minor energy fluctuations occur as the wall is decelerating, these fluctuations are caused by the body of water attaining a slightly higher velocity than the fluid and a small gap appearing between the wall and the fluid. These variations do not occur when the wall is accelerating as then the wall velocity is always greater than that of the fluid. A small ($\sim 2\%$) total energy loss occurs over the course of the simulation.

To further study the waves we measure the amplitudes and half-widths of the waves that are produced and compare them to solitary waves of the form (3.2) assuming the same amplitudes and half-widths. We study the cross sectional area

and energy of the waves, we do not expect exact agreement between our simulations and these calculations due to the approximations in assuming a waveform and also because the moving wall raises the average water level. We do however expect the results to be similar.

The cross sectional area of a two dimensional wave of the form η (3.2) is given by,

$$A = \int_{-\infty}^{\infty} \eta dx = \int_{-\infty}^{\infty} \frac{H}{cosh^2(x/b)} dx = 2Hb. \qquad (3.3)$$

Table 3.1 compares the area of water displaced by the wall to the equivalent cross sectional area A, calculated from the measured amplitude and half-width of the simulated wave. The differences are typically $10 - 15\%$, except for the smaller waves $t_* = 1, 2$ which produce the weakest waves. This indicates that most of the water displaced by the moving wall appears in the wave. The remainder contributes to an overall increase of the water depth. The larger percentage differences when $t_* = 1, 2$ are due to the waves being small.

t_*	$H\Delta x$ (cm^2)	$2Hb$ (cm^2)
1	27	34
2	108	175
3	242	269
4	430	505
5	672	599

Table 3.1: Comparison of area displaced by the wall and the cross sectional area of the wave. Wave area calculated from measurements of the amplitude and half width assuming the wave to be of the form given by equation (3.2).

If we assume that we have a wave of the form (3.2), we can calculate the gravitational energy of the wave by,

$$E_g = \frac{1}{2} g\rho \int_{-\infty}^{\infty} \eta^2 dx = 2g\rho H^2 b \qquad (3.4)$$

where, $b = 1.135 X_{1/2}$ and $X_{1/2}$ is the half width at half height of the wave. The units of E_g are J/m in these two dimensional calculations.

We analyse the energy of the generated waves in table 3.2. We find that the increase in potential energy in the simulation is (in the order of) twice that found

t_*	ΔE_{pot} (J/m)	$2g\rho H^2 b$ (J/m)	Wall Work (J/m)	ΔE_{tot} (J/m)
1	2.6	0.2	3.0	2.7
2	11.2	5.6	14.0	12.5
3	28.3	13.7	36.7	33.1
4	58.2	36.6	75.2	69.0
5	91.6	66.9	134.7	124.6

Table 3.2: *Comparison of the change in potential energy before and after wave production with the potential energy of the solitary wave solution of the KdV equation (3.2) with the same amplitude and half width as the computed wave. The third column shows the calculated work done by the moving wall compared with the total energy change in the simulations in column four.*

in a wave of the assumed form (3.2) with the same half width and amplitude. The difference is in part due to an overall increase in the water level but also indicates that the waves are of a slightly different form to those given by the solution of the KdV equation.

We also compare the work done by our moving wall with the increase in total energy in our simulation. The work done by the moving wall is given by, the integral $\int F \cdot dx$ on each of the wall particles. The total energy given by the calculated difference in energy between the beginning and end of wave generation in the simulation. We find that 90% of the work done by the wall contributes to our waves with the remainder being lost during the generation mechanism.

Measurements have shown that for a given amplitude, waves generated by this method have comparable (generally within 10%) cross sectional areas to waves of the form (3.2), although the half-widths were different. The waves were of a similar form to the initial wave in the previous section although not strictly the same. The high amplitudes of some of the waves means that they are also likely to have a different waveform as the KdV solution assumes that the waves are of small amplitude.

3.3   Collapsing Column of Water

The problem of a collapsing column of water was investigated experimentally by Martin and Moyce (1952). The experiments involved tracking the amount of surge of the front of a collapsing water column. The experiments were three dimensional, though the behaviour is largely only two dimensional.

The experiments have been simulated using the Marker and Cell (MAC) method (Nichols and Hirt 1971). The results agree within the experimental error to those of the experiments. Morton (1997) uses a finite difference scheme, with a Volume of Fluid (VOF) approach to track the interface. He also obtain good agreement between computations and experiment.

SPH simulations of the collapse of a rectangular column of water have been conducted using two different implementations of ghost particle boundaries. In the first case an *incompressible* boundary was used in which the density of boundary particles was not altered. In the second case the density of boundary particles was changed dependent on the fluid motions near the boundary. We call this the *compressible* boundary approach.

The following graphs for the collapse of a column of water are presented in the scaled units.

$$Z = \frac{z}{a}$$
$$T = nt \left(\frac{g}{a}\right)^{\frac{1}{2}}$$

(3.5)

Where,

$a =$ length of the base of the column,
$z =$ the amount of movement of the surge front,
$n =$ the ratio of column height to length,
$g =$ gravitational acceleration.

In figure 3.6 we show an SPH simulation of the $n^2 = 1$ case of Martin and Moyce (1952). In this case the fluid has a width $a = 0.0572m$ and height $b = 0.0572m =$ with the tank being $0.3432m$ long. In this simulation the resolution is 120×120 particles making up the fluid. The colours represent speed, with lighter colours corresponding to higher speeds.

The best agreement between SPH and experimental results was obtained using the incompressible boundary approach (figure 3.7). The SPH results have the surge
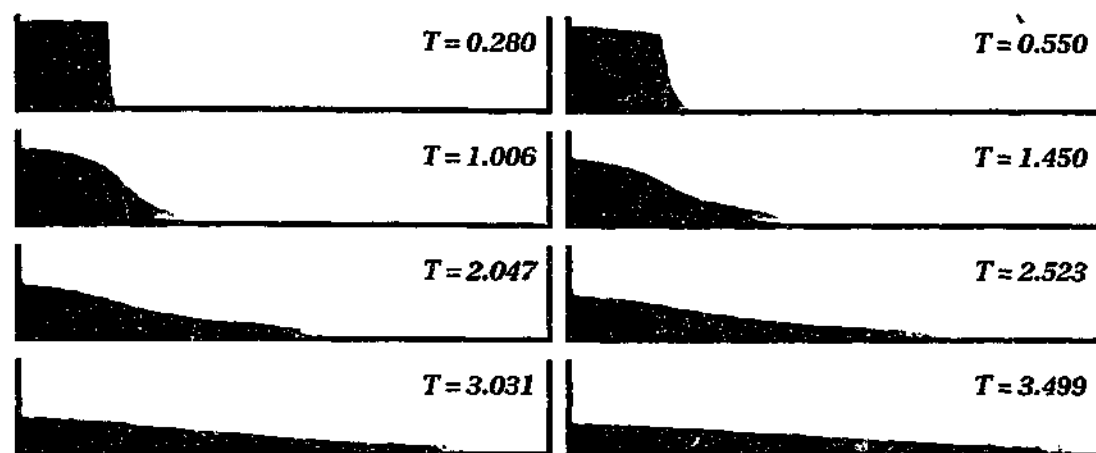
Figure 3.6: *Pictures of collapse of a rectangular column of water. At scaled times*
0.280, 0.550, 1.006, 1.450, 2.047, 2.523, 3.031 *and* 3.499.
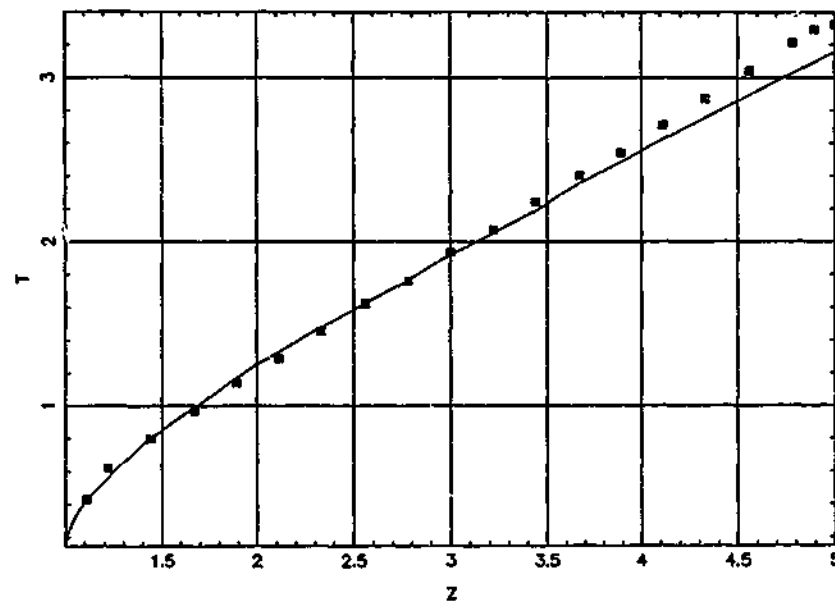
Figure 3.7: *Normalised comparison between the case of 120 particles wide and*
the experimental results of Martin and Moyce (1952) using an incom-
pressible ghost particle boundary. $a = 0.0572m$ *and* $n^2 = 1$. *The dots*
indicate experimental results. The solid line denotes the SPH compu-
tation.
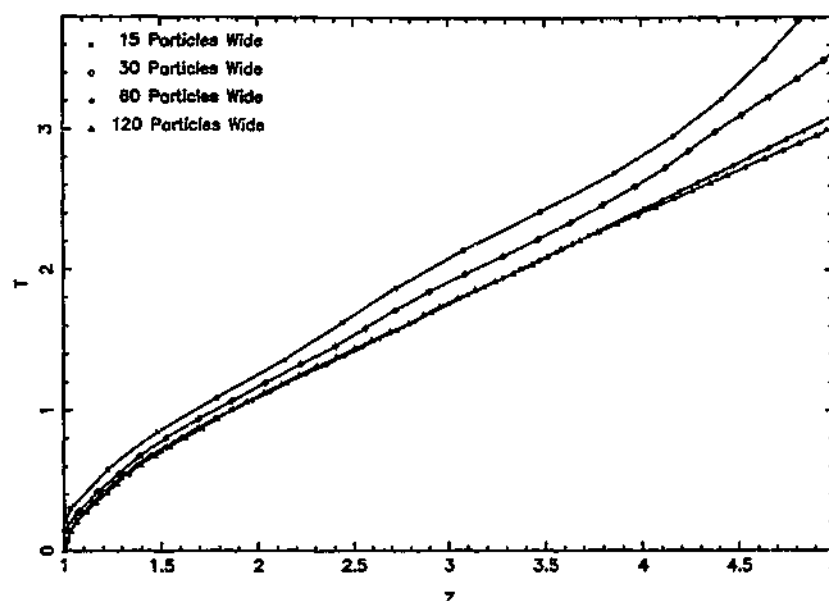
Figure 3.8:   *The convergence for the case of an incompressible boundary. $a =$ $0.0572m$ and $n^2 = 1$. The number of particles refers to both the width and depth of the initial fluid column.*

front travelling faster than that found experimentally. Nichols and Hirt (1971) found a similar error in their computations and thought that it may be due to uncertainty of the time at which motion began in the experiments (Nichols and Hirt 1971), although Martin and Moyce (1952) normalised their data to have the same time $T = 0.8$ at the point $Z = 1.44$. We have also normalised our data in this way, so this should not be a major source of error.

Figure 3.7 shows our results normalised to the same point as the experimental result to remove any uncertainty present in the time of wall removal. Excellent agreement is obtained up until $T = 3.0$ after which a slight divergence occurs. The agreement is within 6% of the experimental results. The convergence to this solution with increasing particle resolution is shown in figure 3.8.

In figure 3.9 we show the motion of the surge front using the compressible boundary approach. In this case particles are less affected by the boundary and the front eventually moves faster than in the incompressible approach.
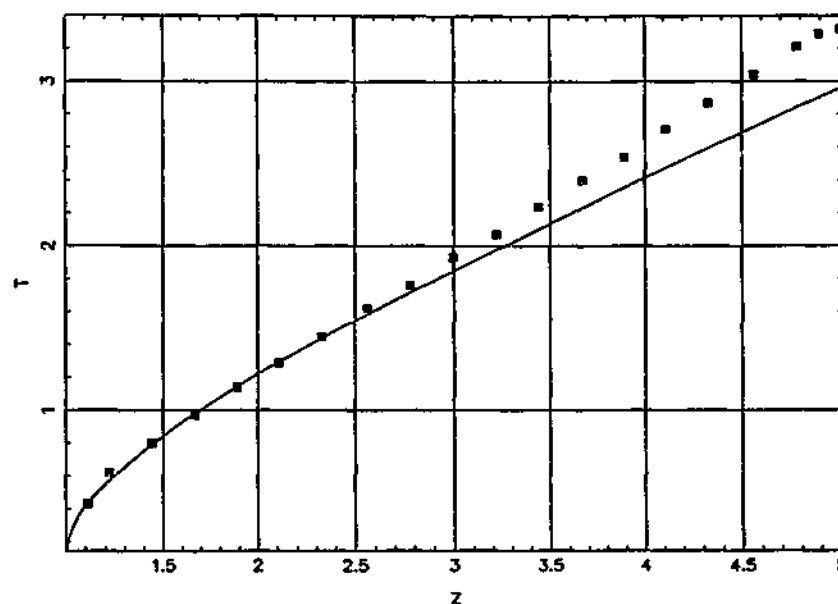
Figure 3.9: *Normalised comparison between the case of 120 particles wide and the experimental results of Martin and Moyce (1952) using a compressible ghost particle boundary approach.* $a = 0.0572m$ *and* $n^2 = 1$. *The dots indicate experimental results. The solid line denotes the SPH computation.*

3.4   Tidal Bores

A bore occurs in situations where there is an abrupt increase in fluid depth associated with an accompanying change in flow rate. In this way they are similar to shocks in gas dynamics. The best known bores are tidal bores which occur in some rivers due to tidal forces of the moon. Rayleigh (1908,1914) first discussed the theory of tidal bores, a description of various bore types is given by Simpson (1997). Undular bores consist of a series of solitary waves associated with a change in the water level. They occur if the change in the water level is less than 0.28 of the undisturbed depth on which the bore is propagating (Peregrine 1966). Bores with depths greater than this are known as turbulent bores and consist of a series of breaking waves.

Hirt and Shannon (1968) used a Marker and Cell method to calculate tidal bores, they were able to correctly model bore heights and velocities. Peregrine (1966) calculate the growth of undular bores using a finite difference technique to solve an equation similar to the KdV equation. Peregrine found that if the difference

between the levels of the bore becomes too large, the pressure profile is no longer hydrostatic because of the vertical acceleration of the water. In the case of a viscous bore a train of uniform waves appear on the bore. In the inviscid case, the leading wave breaks away to form a solitary wave, so that the bore moves into a train of successive solitary waves. The existence of undular bores has also been studied in the atmospheric context (Crook and Miller 1985).

The velocity of propagation of a tidal bore is given by Lamb (1932) (pg.280),

$$V_1 = \sqrt{\frac{gH_2(H_1 + H_2)}{2H_1}}. \tag{3.6}$$
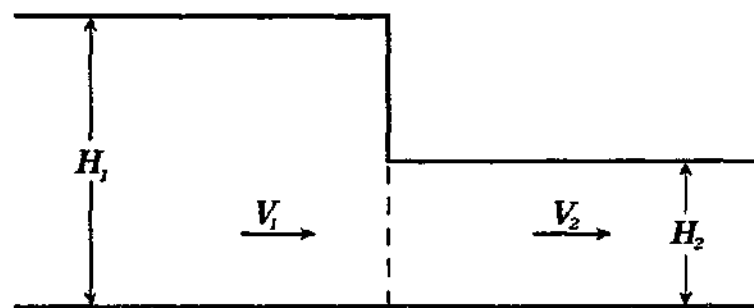
Figure 3.10: *Schematic diagram of a tidal bore. (V_1, H_1) and (V_2, H_2) refer to the water (velocities, depths) before and after the bore respectively.*

The bore in figure 3.11 was simulated by having a $600m$ long tank with water at a depth of $10m$ given a velocity of $8.5m/s$ towards the left hand wall. In this example we took $\alpha = 0.01$, $h = 1.2\Delta p$, with $\Delta p = 0.66m$. To reduce the amount of splash and disorder at the left hand wall the $10m$ of water next to the wall was given a zero velocity and a depth of $20m$.

The theoretical bore speed for a bore of height $H_1 = 18.4m$ and $H_2 = 9.6m$ is $8.46m/s$. This compares with our SPH simulation velocity of $8.58m/s$ (figure 3.11). The bore velocity was calculated by measuring the position of the first peak of the bore $\sim 100m$ apart. The errors involved in the measurements of the position of the peak were small compared to the size of the measurements. Alternatively if we have a viscosity of $\alpha = 0.1$ (figure 3.12) we find that the bore that is produced has heights $H_1 = 14.92m$, $H_2 = 9.86m$. With a corresponding theoretical bore speed of $9.01m/s$. The measured bore speed of the simulation was found to be $8.98m/s$.
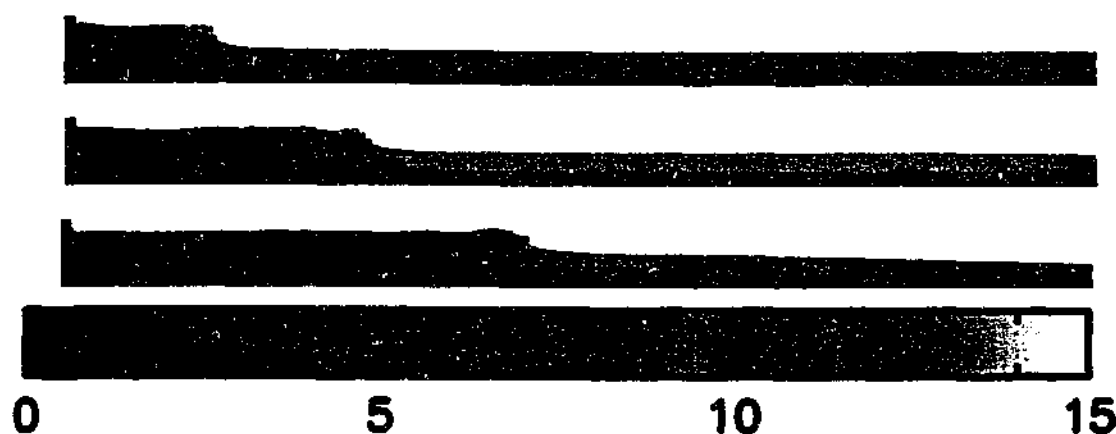
Figure 3.11: SPH simulation of a tidal bore. $H_1 = 18.4m$ and $H_2 = 9.6m$ refer to the water depths before and after the bore respectively. Frames occur at times 5.54 , 11.95 and 19.28 seconds respectively. $\alpha = 0.01$, tank was 600m long. Initial velocity 8.5m/s. The colours refer to the speed of the fluid in m/s

We notice that the simulation with $\alpha = 0.01$ (figure 3.11), was more turbulent than the $\alpha = 0.1$ (figure 3.12) case. Monaghan (1994) shows that the viscosity in the calculation is given by $\mu = (\alpha \rho c_s h)/8$. It is known that the Reynolds number Re is given by, $Re = VL/\mu$, where V and L are typical length scales, it then follows that the Reynolds number is given by,

$$Re = \left(\frac{8}{\alpha}\right)\left(\frac{V}{c_s}\right)\left(\frac{L}{h}\right). \tag{3.7}$$

The quantity V/c_s is the Mach number of the flow which we take as 0.1, a typical value of L/h is 15. so that $Re = 12/\alpha$ and it is to be expected that the $\alpha = 0.1$, $Re = 120$ case is laminar with the $\alpha = 0.01$, $Re = 1,200$ case more turbulent.

In figure 3.13 we show a bore ($\alpha = 0.01$) which was started with a lower initial velocity of $5m/s$. The resulting bore has a lower amplitude, waves are clearly produced at the front of the bore making it undular and consistent with Peregrine (1966).

These results are comparable to those of Monaghan (1994), who used SPH with a boundary force implementation for the boundary conditions.
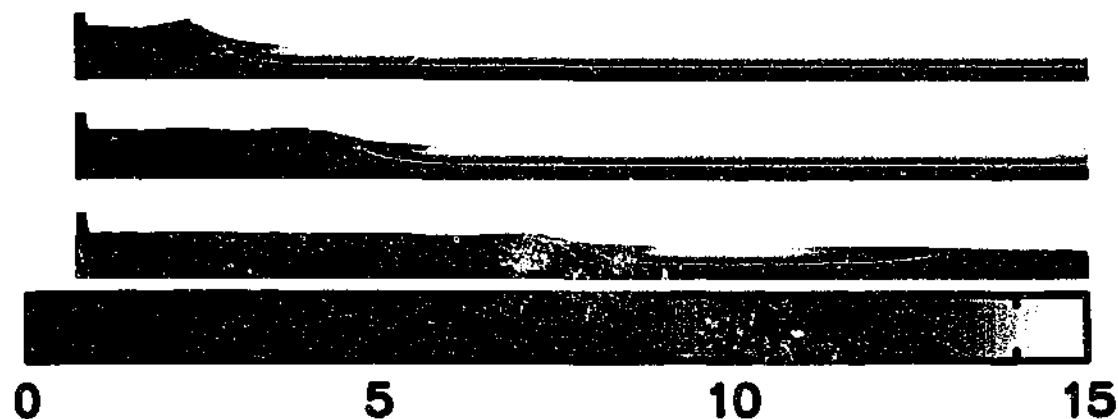
Figure 3.12: SPH simulation of a tidal bore. $H_1 = 14.52m$ and $H_2 = 9.86m$ refer to the water depths before and after the bore respectively. Frames occur at times 5.60, 11.38 and 20.07 seconds respectively. $\alpha = 0.1$. (The tank was 600m long but only the left 400m is shown.) Initial velocity 8.5m/s.
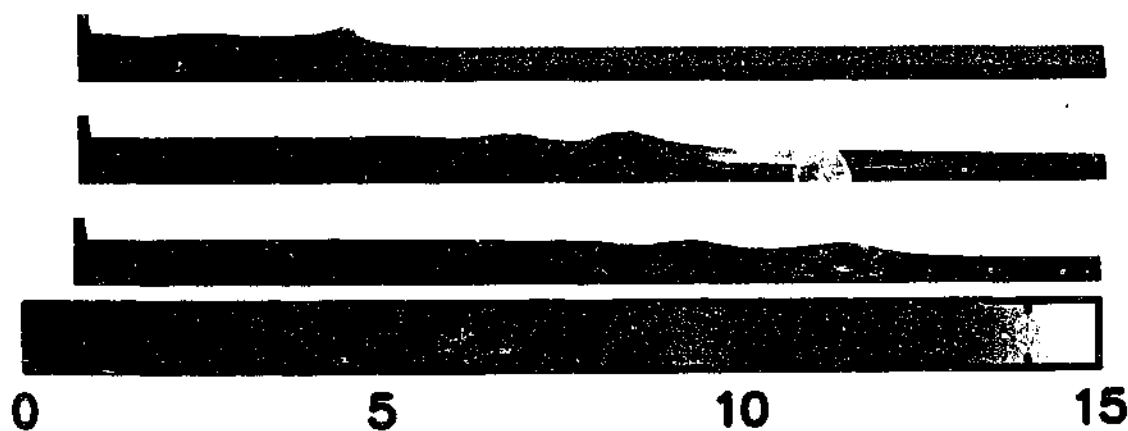
Figure 3.13: SPH simulation of an undular bore in a 600m long tank with the left 300m shown. $\alpha = 0.01$. Times of frames are 11.14, 24.71 and 33.37 seconds respectively. Initial velocity is 5.00m/s

3.5   Weir Flow

Another important class of flows that have been extensively studied both numerically and experimentally are those of weir flow. Weir flows are steady non-uniform flows, where the velocity is constant over time but varies over the spatial extent of the channel due to obstructions (weirs) in the channel. They involve free surfaces which present considerable difficulties for analytic solution (Dias, Keller, and Vanden-Broeck 1988) except for simple geometries and steady flow. Dias and Tuck (1991) present results for a variety of configurations of weir flow, their solutions are found numerically using a series truncation method. They formulate the problem using a potential and stream function approach, transforming to the complex plane (Vanden-Broeck and Keller 1987).

If gravity is neglected Dias and Tuck (1991) show that it is possible to find a solution for the angle θ, of the jet which forms as fluid passes over a weir of different weir heights w. In figure 3.15 we present a comparison between numerical results using our SPH code and the Dias and Tuck solution.

The simulations involve injecting fluid in from the left side at constant velocity and height and measuring the angle that the jet makes with the horizontal after hitting a wall at the opposite end. The angle θ is plotted against the dimensionless wall height w, where $w = W/H$, W is the wall height and H is the downstream fluid height. Obviously the $w = 0$ solution should be a horizontally propagating jet ($\theta = 0$). With the limiting solution for high walls being a perpendicular propagating jet ($\theta = \pi/2$) where the fluid is unable to pass over the boundary.

Simulations were conducted in a tank $4.2m$ long, $0.3m$ high with fluid being input at the left hand side with input velocity $U_{in} = 0.5m/s$. The weir was at the right hand end of the tank with the weir height w varying between 0.25 and 3.0. The downstream flow was input 50 particles high when required, this gives a resolution of $\Delta p = 0.006m$. Calculations proceeded until a steady state was reached at which time the angle of the jet over the weir was measured. There is an amount of scatter in the SPH results due to error in the measurement of the angle θ.
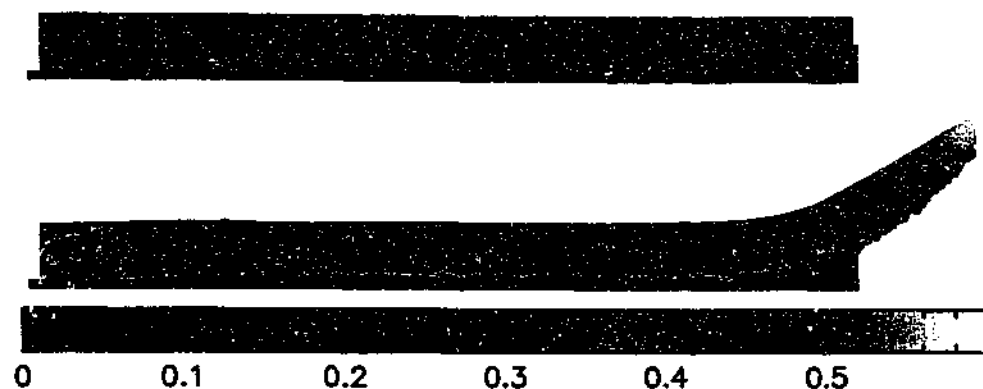
Figure 3.14: *Zero gravity weir with w = 0.5, initial set up and state at t = 1.90 seconds.*
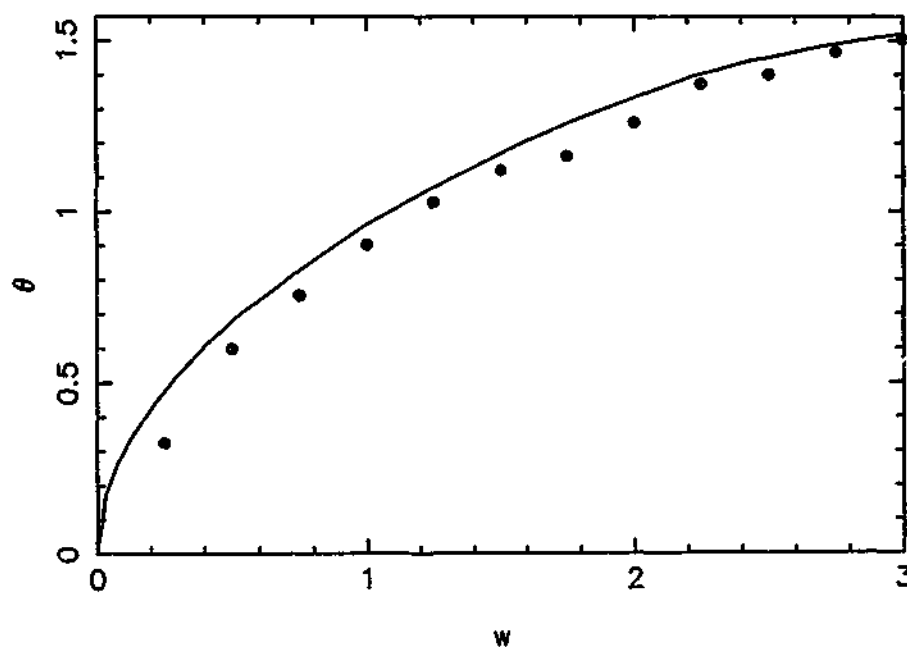
Figure 3.15: *Comparison of the angle θ between the horizontal and the jet moving over a weir of height w in the case of zero gravity. Continuous line is the result of Dias and Tuck, dots represent SPH results.*

3.6   Water Wave Code Summary

In this chapter we have tested our SPH simulations against analytical solutions, experiments and the results of other numerical methods for a range of situations.

We began by looking at the propagation of solitary waves. Initially we set up solitary waves using an analytic solution of the KdV equation and measured the extent to which these waves ran up a vertical wall. The SPH results were in good agreement with experiment and the MAC method.

In section 3.2 we generated waves with the motion of the left hand wall in our computational tank. By varying the motion of the wall we were able to generate waves with a large range of amplitudes. Although the waves were of a different form to those in section 3.1, there was still reasonable agreement between the wave amplitude and the extent of runup with the waves in section 3.1.

The next problem considered was the collapse of a breaking dam. In section 3.3 we found agreement with experimental results and other numerical methods for the horizontal distance moved by the surge front of a collapsing water column.

In section 3.4 we investigated the phenomena of tidal bores. We compared SPH results to the theoretical result for the speed of a bore. We also showed the ease with which SPH can be used to produce different bore types.

The SPH results for the jet angle formed when water passes over a zero gravity weir are compared with the result of Dias and Tuck in section 3.5. Good agreement is found between SPH and the two methods.

We have seen in this chapter that the SPH numerical method is able to accurately model a range of free surface fluid dynamics problems. We can then conclude that the SPH algorithm and our computer program performs satisfactorily. The test problems we have considered are similar to the situations we expect to find in our experiments and simulations of the waves produced during caldera collapse. So we furthermore conclude that the following computations for these waves will also be adequate.

Chapter 4

Waves and Caldera Collapse

caldera is a large bowl shaped crater or depression which is formed during a major explosive volcanic eruption. It is produced by subsidence of the roof of a volcano into its underlying magma chamber. Subsidence occurs when the eruption of magma reduces the pressure in the chamber, so that the chamber is no longer able to support the weight of the volcano roof which collapses into the chamber, much like the downward movement of a piston in a cylinder (figure 4.1).

Caldera volcanoes are responsible for some of the worlds largest volcanic eruptions, with examples being Crater Lake and the islands of Krakatau and Santorini. Calderas can vary from several to ninety kilometres in diameter.

Caldera occurrence is inferred from the similarity between the volume of erupted magma and the volume of the depression resulting from the subsidence. A common feature of calderas is that they are bounded by ring fractures. As the name suggests a ring fracture is a fracture that has a circular (ring) shape. Ring fractures are often the sites of vents from which the magma is erupted as the chamber roof subsides.

Lipman (1997) gives a review of the different types of caldera that can occur. Calderas which are formed in association with a ring fault are known as piston collapse calderas, as they subside as a single coherent block of rock into the chamber. A schematic illustration of piston subsidence is shown in figure 4.1.

There are also more complicated caldera types including piece-meal (non-coherent) calderas which are formed when the subsiding piston breaks up into several different pieces. Trap door calderas occur when the fault only exists on one side of the chamber. In this case collapse occurs in an asymmetric manner with the roof being hinged off the still connected side of the chamber.

Not all calderas are associated with faults. One such type is downsag calderas in which roof flexure allows the rock to subside into the chamber without the occurrence of significant faulting. Funnel calderas (those which have a distinct funnel shape) are associated with explosive eruptions from a single central vent and do not involve the
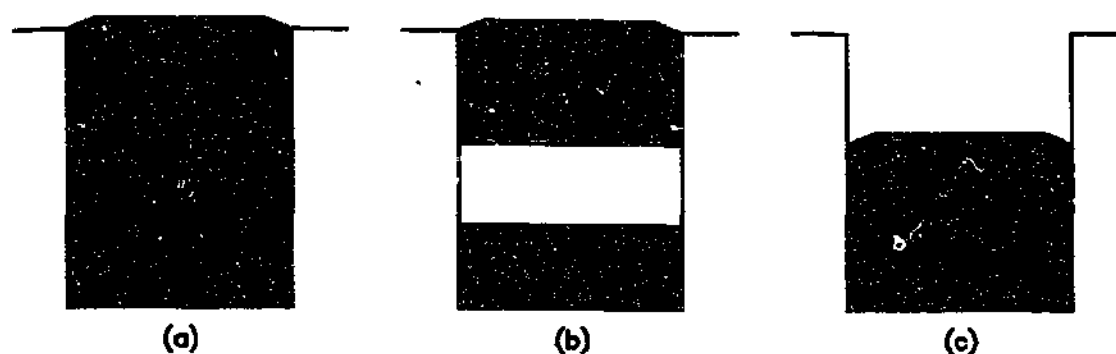
Figure 4.1: *Schematic diagram of caldera collapse. (a) The existence of a magma chamber with an overlying block of rock surrounded by a ring fracture. (b) As the magma erupts it can lead to a partially evacuated chamber. (c) The decrease in pressure due to the evacuated chamber leads to the block subsiding down into the chamber.*

movement of a coherent block, but multiple collapses of slices of rock from the sides of a large circular crater. Walker (1984) presents a study of caldera types, classifying the calderas of various volcanoes around the world, with particular emphasis on calderas that do not fit the previously described ring fault, piston model.

The 1883 eruption of Krakatau and many other caldera forming eruptions have been observed to generate tsunamis. Krakatau produced waves up to $14.5m$ in amplitude (Symons 1888) (pg.96). Tsunamis can be initiated by the sudden displacement of a large volume of water. Latter (1981) discusses the events associated with volcanic eruptions which are possible source mechanisms for tsunami production.

The motion of a pyroclastic flow into the sea can displace water and produce waves (Monaghan, Cas, Kos, and Hallworth 1999). This mechanism is interesting as pyroclastic flows can travel several kilometres from the volcano and may lead to the production of tsunamis from inland volcanoes. Similarly, the motion into the sea of a large amount of rocks and debris during a landslide is a further example of wave production by objects moving into the sea.

Alternatively, the impulse of energy released in a submarine explosions can lead to the production of small tsunamis (Latter 1981). The sudden motion of earth during a volcanically initiated earthquake is another possible cause. In this chapter we investigate tsunamis generated when water flows into the cavity formed by the collapse of a significant portion of an island into the sea.

4.1   Waves Generated by Caldera Collapse

In this section we describe both wave tank experiments and numerical simulations of the waves generated during the collapse of a simple model caldera. The simple model is illustrated in figure 4.2, it consists of a tank of width L, with water in two outer compartments seperated by a central cavity of width W. The walls defining the inner cavity are of height $D = D_1 + D_2$ with the top D_1 of the two walls being removable, this is denoted by the thinner vertical lines in figure 4.2. The caldera collapse is modelled by the removal of these upper sections of the wall which allows water to flow into the cavity and potentially produce waves.
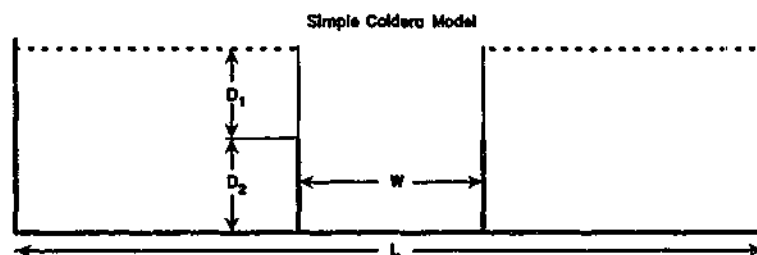
Figure 4.2: Initial setup for our simple caldera model

The experimental results shown in figure 4.3 illustrate a selection of ten frames of our simple caldera model with dimensions $D_1 = 18cm$, $D_2 = 12cm$, $L = 200cm$. and $W = 40cm$. The width (measured perpendicular to the front wall seen in figure 4.3) of the experimental wave tank was $40cm$. The numerical results assume the flow is two dimensional. The experimental setup contained guides to support the removable walls that protruded $2cm$ into the tank (the width of these guides parallel to the front wall was $2.6cm$) and perturb the flow slightly. The effects of the guides are small because the front and back walls of the tank are $40cm$ apart.

Figures 4.4 and 4.5 illustrate SPH simulations with the same dimensions as the experiment shown in figure 4.3 using boundary force and ghost particle boundary implementations respectively. The experimental behaviour is qualitatively the same as the SPH computations. The numerical systems were damped for two thousand steps before the walls were instantaneously removed. As the flow originates from the bottom of the removable walls there are only minor differences in the results if wall movements are included in the calculation. Once the simulation starts water
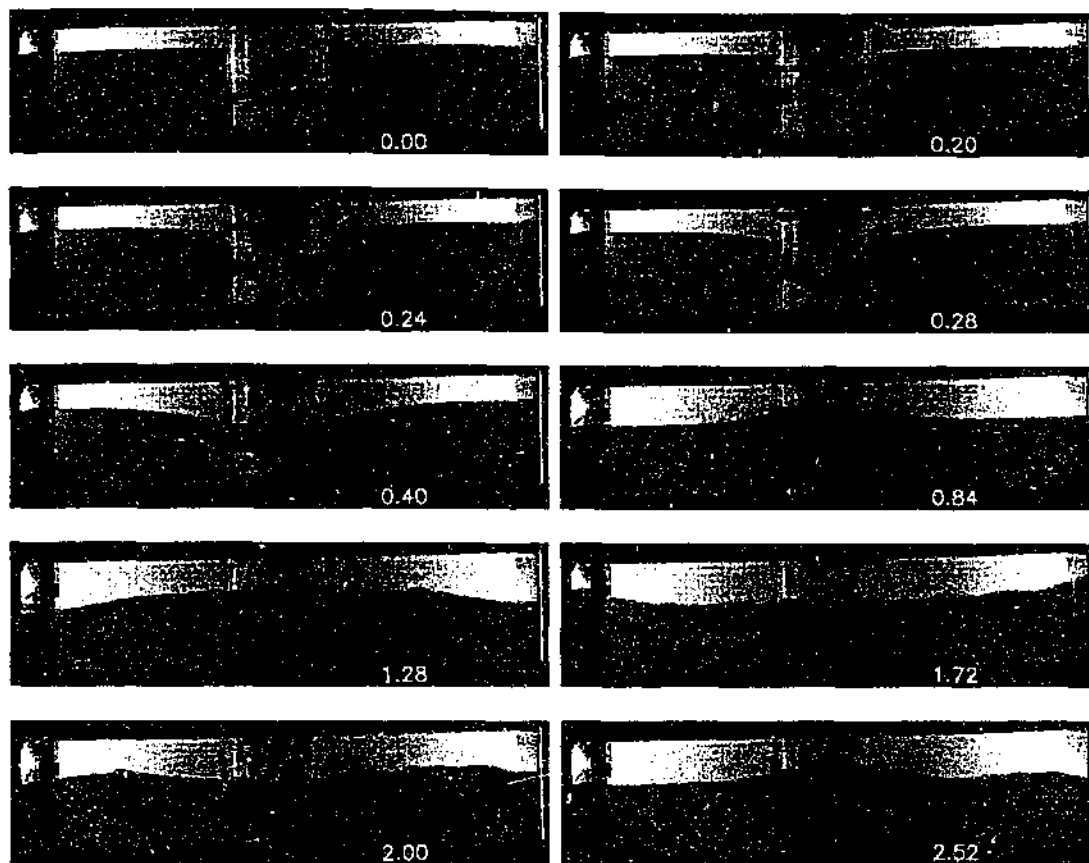
Figure 4.3: *Experimental waves produced by caldera collapse with $D_2 = 12cm$, $D = 30cm$, $W = 40cm$ and $L = 200cm$.*

proceeded to flow into the central cavity splashing up to form a large central column of water. The central column grows, filling up the cavity and increasing in height until the height of the column is greater than that of the surrounding water. The column then breaks up into three parts, two waves emerge travelling left and right, and the central column over the cavity subsides and disperses over time. The two travelling waves reached the end walls and ran up the sides before reforming into two waves reflected off the walls propagating in the opposite direction back towards the caldera centre.

We conducted a series of wave tank experiments to compare with numerical SPH results. Experiments were performed in a tank of $L = 200cm$, $W = 40cm$ and total depth $D = 30cm$. Four different heights for D_2 were employed, these heights being
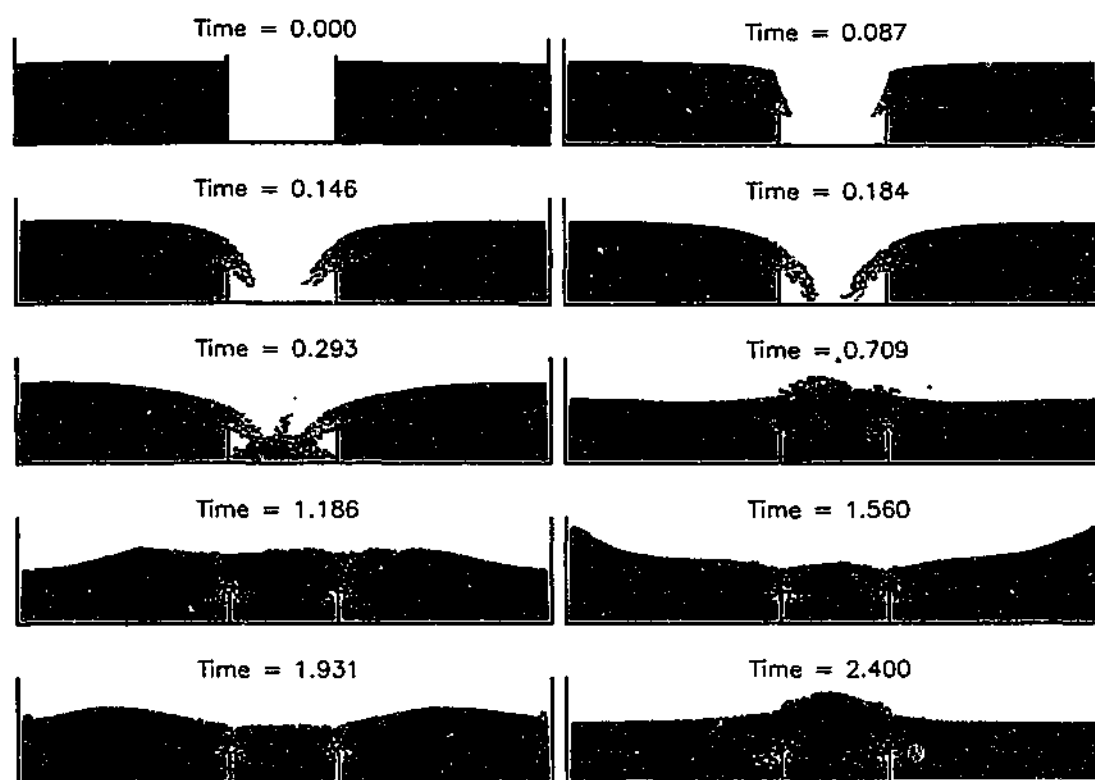
Figure 4.4: *Simulation of experiment shown in figure 4.3 with a boundary force boundary implementation.*

0, 5, 12 and 17cm.

In figure 4.6 we plot the extent of wave runup, R/D at each end of the tank against the dimensionless height of the cavity, D_2/D for these experiments, comparing them to the numerical simulations using ghost particle boundaries. R and D are measured from the bottom of the tank so that in the undisturbed state $R/D = 1$. To ensure that the experimental results were correct, and not merely a result of experimental error, the experiments were conducted three times for each height D_2. The run up on both the left and right hand walls was measured (from still frames taken from the video) giving the six experimental points at each wall height shown in figure 4.6. The measurement error in the computational results is of the order of the particle spacing h.

The SPH simulation using ghost particles was more accurate than those using
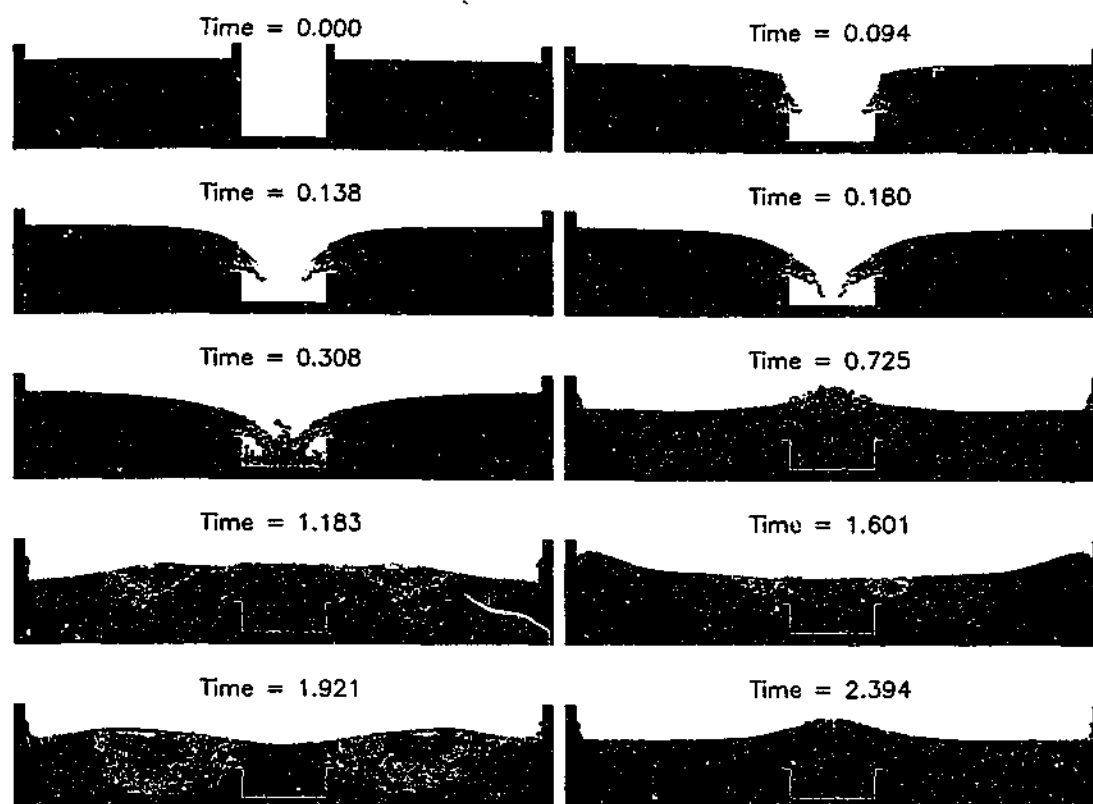
Figure 4.5: *Simulation of experiment shown in figure 4.3 with a ghost particle boundary implementation.*

boundary forces. The reason appears to be that the boundary forces give a poor representation of flow around the top of the fixed boundary. In figure 4.4 this shows up as an asymmetric flow compared to the symmetric flow in figure 4.5.

We note in figure 4.6 that the dimensionless runup R/D is in some cases less than one. This is because the flow into the cavity reduces the depth in the region of the tank outside of the initial cavity. The spread in the experimental results was 40% of the amount of runup above the base water level in each case.

The height of the central column (formed when the two jets projecting out from the wall meet, form a vortex and mix with the trapped air) is underestimated by 10% in the SPH computations. There is a significant amount of splashing produced in the formation of this column that is not present in the computations. This is possibly due to the neglect of air in the computation reducing the mixing and turbulence

Wall Run up for Simple Caldera Model
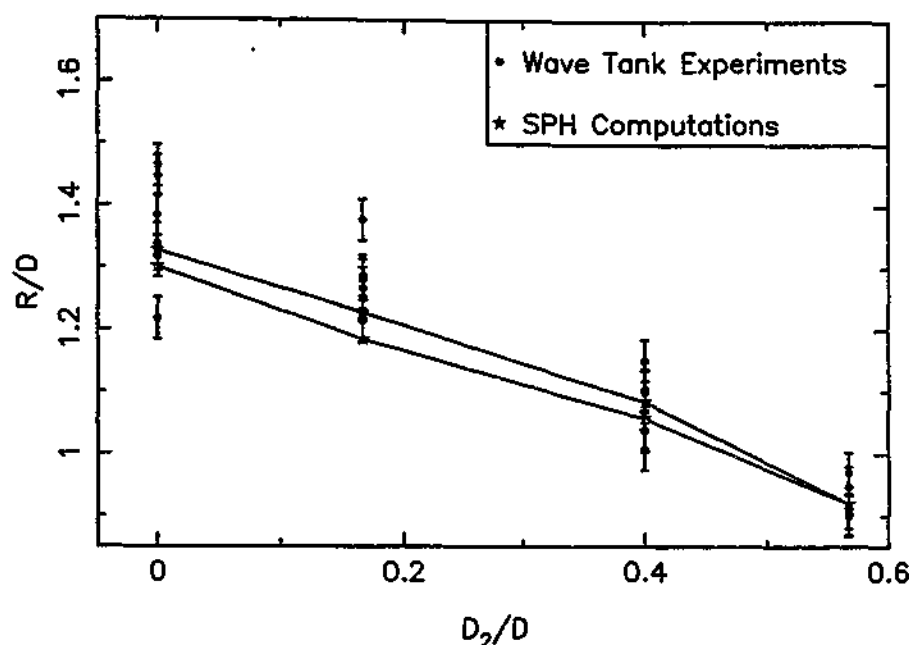
Figure 4.6:   *Comparison of SPH results and experiment of the run up against a wall for the simple caldera model. R is the extent of runup, D is the initial depth of water in the tank and D_2 is the height of the wall that remains in the tank. The solid lines join the points found from our computations. In these experiments $D = 30cm$, and $D_2 = 0cm$, $5cm$, $12cm$ and $17cm$.*

in this central column and may also be due to the amount of numerical viscosity used. The computational results in figure 4.6 appear to be a lower limit of the experimental results due to these factors.

It is interesting to note that in the experiments with $D_2 = 0.12m$ and $D_2 = 0.17m$ the two jets met each other before they hit the floor of the tank. In the $D_2 = 0.05m$ case the jets impact with each other and the tank floor at the same time. To see at which wall heights this should occur we calculate the time taken for the fluid jet to reach the middle of the cavity, τ_M and the time for it to reach the bottom of the tank, τ_B.

A typical horizontal velocity of the jet is given by $V_x^{Jet} = \sqrt{2g(D - D_2)}$, where g is the gravitational acceleration and D_1 is the fluid depth above the wall. Assuming

that V_x^{Jet} is constant as it moves through the air, the time t to travel a distance Δx is given by, $t = \Delta x / \sqrt{2g(D - D_2)}$. In this case $\Delta x = W/2$ is the distance to the middle of the cavity and $\tau_M = W/2\sqrt{2g(D - D_2)}$.

Motion in the vertical direction is governed by the acceleration due to gravity. Assuming the initial vertical motion to be zero, we can show $\tau_B = \sqrt{2D_2/y}$. We plot both of these times against D_2 in figure 4.7. The value of D_2 for $\tau_M = \tau_B$ is $D_2 = D/2 \pm 1/4\sqrt{4D^2 - W^2}$. In the experiments and simulations discussed so far we have $D = 0.3m$ and $W = 0.4m$ so that the two times are equal at $D_2 = 0.04m$ and $D_2 = 0.26m$. For $D_2 < 0.04m$ and $D_2 > 0.26m$ the jet contacts the bottom of the tank before meeting with the opposing jet. These results are consistent with the experimental results which show that the jets meet at the bottom for $D_2 = 0.05m$ when $D = 0.3m$.
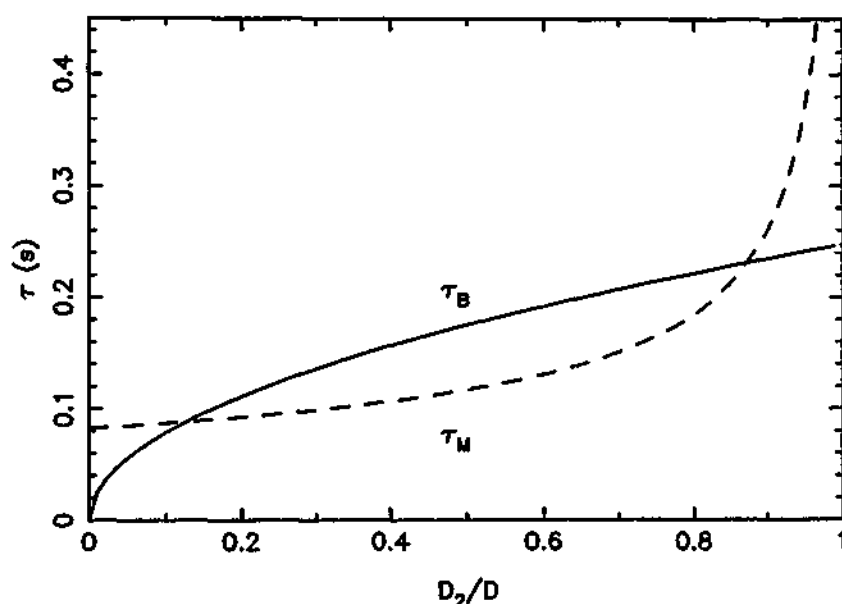
Figure 4.7: *Comparison between times for the jet to reach the middle of the cavity,*
τ_M and the bottom of the tank, τ_B in a cavity of total depth $0.3m$
and width $0.4m$ where D_2/D is the dimensionless height of the lower
interior wall. $D_2/D = 1$ corresponds to the limiting case where no
water is able to flow into the cavity.

For the case considered in figures 4.3-4.5 we find in numerical calculations that when the boundary conditions are implemented with boundary forces that jets do not impact with each other as found in the experiments and expected from our

simple theory. To see this compare the fourth frame of the experimental results in figure 4.3 where the two jets impact with each other before reaching the bottom of the tank with the corresponding frame in the boundary force boundary simulation (figure 4.4) in which the jets touch the bottom of the tank before reaching each other. The problem arises because the boundary particles keep fluid particles from coming within a particle spacing of the boundary. This increases the effective height of the boundary, restricting fluid flow near the top of the central walls. It is known that simulations involving boundary particles lead to a bulging of fluid near the free surface (figure 2.2). The bulging is due to the boundary force being independent of the pressure of the fluid and its effect is more pronounced near a free surface. We note in the simulation performed using ghost particle boundaries (figure 4.5) that this problem is removed and the jets impact in the air before touching the bottom of the tank.

Several rows of particles are used to make up a ghost particle boundary. Only one row is used for our boundary particle implementation. As a result the ghost particle boundaries appear thicker in figure 4.5 than the boundary force boundaries in figure 4.4. However, the two approaches are consistent as the boundary forces keep particles a distance in the order of a particle spacing away from the boundary.

A major difficulty with the experiments is in ensuring that they are symmetrical, so that they can be modelled effectively. If one wall was lifted quicker than the other, the two incoming jets would not necessarily meet in the middle and an asymmetry would result. Our experiments were conducted with different colours in the two compartments, we see in figure 4.8 that the experiments are initially symmetrical. This can be seen by the straight interface between the different coloured bodies of water. Small perturbations are amplified during the splashing of the central column and the experiments become asymmetric after this point.

One notices a few particles breaking away from the bulk of the fluid in the sixth frame of figure 4.4. This asymmetry is in a calculation incorporating boundary force boundary conditions and is more than likely due to slight differences in the particle setup introduced during the damping period, these differences then affect the size of the interaction between particles and lead to an asymmetry. However, as pointed out by Monaghan and Lattanzio (1985) the cubic spline kernel has a continuous second derivative so these variations are small. Simulations employing ghost particle boundary conditions (figure 4.5) have a much greater degree of symmetry after the
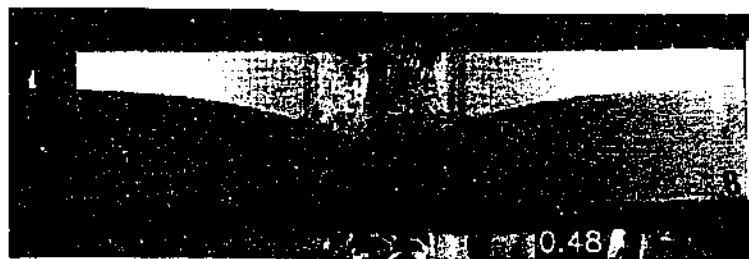
Figure 4.8: Experimental frame indicating the symmetry of the experiments.

damping period and are more symmetrical.

Comparing the numerical and experimental results (figures 4.3 and 4.5) we notice an initial discrepancy of 0.1 seconds in the timing of features of the flow, with events occurring earlier in the simulations. This may be an effect of the wall not being instantaneously removed in the experimental case. However, as this error follows through for the duration of the experiment it is not of serious concern.

In this section we have introduced a simple model of the fluid motions that occur and lead to wave production in caldera collapse. We have presented wave tank experiments and compared them to the results of SPH simulations for varying cavity depths. In the next section we extend the analysis to cover cavities of varying widths.

4.2   Different Cavity Widths

In this section we explore how varying the cavity width affects the size of the waves that are produced. We again use the extent of runup as a measure of the size of a wave. In these calculations we use a ghost particle boundary implementation and make use of symmetry in our model by placing a wall in the middle of the cavity and only following fluid motions in one of the compartments, this allows us to increase the length of the tank without increasing the number of particles in and computational time of the simulation. The advantage of increased tank length is that waves are more able to form unaffected by boundary effects.

One expects that for a very narrow cavity only a small wave will be produced, as only a small amount of water is disturbed, meaning only a small amount of water can form into the wave. Alternatively, if we have a wide cavity we again expect

only minimal amplitude waves. In this case the energy released by a large fraction of water falling into the cavity is dissipated by a disordered flow.

For cavity widths in between we get significant waves. Taking a narrow cavity and increasing the width, we find the extent of runup to increase until the jet impacts the bottom of the side wall. When the width is increased further the jet strikes the floor first, then breaks into two flows which move in opposite directions, rebound of the sides of the cavity and run back into each other producing disordered motion and reducing the runup.

We conducted a series of numerical simulations in a $200cm$ long tank, which included a cavity of width W at one end of the tank. The simulations were carried out for different widths, $2.5cm \leq W \leq 75cm$ for a range of cavity depths, $5cm \leq D_2 \leq 20cm$. The depth of the water was $D = 30cm$ with the removable wall of height $D_1 = D - D_2$ being instantaneously removed.

In figures 4.9-4.12 we show a series of simulations of the waves produced with different cavity widths. All of these simulations were carried out with $D_2 = 12.5cm$, water depth $D = 30cm$ and tank length $L = 200cm$. As L is fixed as we vary the width of the cavity we find that differences arise in the average water level in the tank due to the flow of water into the cavity. If the cavity width is much smaller than the length of the tank, $W \ll L$ the water level outside the cavity is not significantly affected by the flow of water into the cavity, as only a small percentage of the total amount of water is required to fill the cavity. As the cavity width increases, the amount of water required to fill the cavity increases and the average water level outside the cavity decreases. Eventually we find that when $W \simeq L$, there is insufficient water in the tank to fill the cavity, and the flow will largely be contained inside the cavity.

We begin in figure 4.9 with the case of a very thin cavity, $W = 5cm$. (Note that as we have included a wall in the middle of our cavity the equiv... ent width of the cavity for the models presented in section 4.1 is $W = 10cm$.) When the wall is removed fluid flows into the cavity, the jet impacts with the side wall long before fluid reaches the bottom of the cavity by essentially sliding down the side wall. As only a small amount of fluid is required to fill the cavity the majority of fluid in the tank is undisturbed by the filling process. A small column of water forms above the cavity and forms a small amplitude wave which travels across the tank followed by a secondary wave. The maximum runup on the right hand wall had $R/D = 1.07$ in

this case i.e. $2.1cm$ above the initial water level.

The next simulation we present (figure 4.10) has $W = 15cm$ and turns out to give the wave of maximum amplitude for $D_2 = 12.5cm$. The maximum runup in this case had the value $R/D = 1.17$, $5.1cm$ above the initial reference level, and $7.4cm$ above the average (reduced by flow into the cavity) water level. The outpouring jet impacts towards the bottom of the side wall near the junction with the tank bottom, a vortex forms, the cavity fills and a column forms above the cavity. A much higher amplitude wave develops than in the $W = 5cm$ case followed by a smaller secondary wave. We found in the previous case that there was only a minimal effect on the average water level in the tank. In this case the effects of a larger amount of water flowing into the cavity are more dramatic. The opening of the cavity leads to a rush of water to the left side of the tank, by the time the wave has reached the middle of the tank, the depth at the right hand side of the tank is significantly less than the initial depth.

In the case of $W = 25cm$ (figure 4.11) we find that the jet reaches the bottom of the tank before impacting with the side wall, a vortex still forms with a dimension similar to that of the cavity as the cavity is filled. Although the jet is broken up into two streams, one running towards the left hand wall with the other moving to the right towards the right side of the cavity. The competition between these two jets means that some of the energy that was previously transferred into the wave is now trapped in the cavity, the effects of the lowering of the water depth are again increased over the previous two cases. The maximum runup of $R/D = 1.09$ is subsequently decreased. R is now equal to $32.7cm$ while the actual (average) water depth over which the wave propagates has dropped to $26.3cm$. Therefore the wave runup above the actual water depth is $6.4cm$.

We now discuss the $W = 40cm$ case depicted in figure 4.12. The maximum value of runup was $R/D = 1.0$, however this does not mean that no wave was produced because, as mentioned above the average water level in the tank is reduced as water flows into the large cavity. In this case the cavity is so wide that the vortex formed as the cavity fills is on a length scale much less than the width. A column of water builds up over the cavity and forms a wave before the cavity is filled, this wave is unable to propagate out of the cavity. Eventually a second column builds up over the cavity (although not as high as the previous cases) and develops into a low amplitude long wavelength wave.

The factors described above are illustrated in the results of the numerical simulations shown in figure 4.13 where each line represents a different cavity height, D_2. We find that initially the extent of runup increases with increasing cavity width up to the point where energy is trapped in the cavity and the size of the runup decreases. The hypothesis breaks down at the lowest cavity height ($D_2 = 5cm$) where violent disorder dissipates a large proportion of the energy. For a cavity of zero width there is no displacement of the water and we expect $R/D = 1$ indicating that the maximum runup height is the initial depth. We also note that R/D may be less than 1 due to a decrease in the initial depth of the water as fluid flows into the cavity.

As in section 4.1 we find that the amplitude of the waves increases as D_2 decreases and more water is allowed to flow into the cavity at a higher initial velocity (due to the larger hydrostatic pressure with smaller D_2). We find that the variations in the parameter space of D_2 and W are ordered and that it is theoretically possible to define a scaling relation for the variation in runup height R, in terms of the water depth D, cavity width W, cavity height D_2 and the length of the tank L. We do not present a scaling relation that picks out all the features in figure 4.13, but do present one that explains some of the features.

We find from figure 4.13 that, in general, as the height D_2 decreases, there is an increase in the cavity width at which the maximum runup occurs W^{Max}. We find that W^{Max} is approximately given by,

$$W^{Max} = \frac{D^2}{6D_2}. \tag{4.1}$$

In general the extent of runup can be given by the function,

$$\frac{R}{D} = F\left(\frac{D}{L}, \frac{D_2}{L}, \frac{W}{L}\right). \tag{4.2}$$

However, the simulations we have conducted in this section are conducted in a tank of fixed length, L. We also note that the curves for each cavity height can be approximated by a parabola with a maximum given by (4.1). We find the results in figure 4.13 can be fitted by an approximate relation between R, W and D_2,

$$\frac{R}{D} = 1 + \frac{W}{D}\left(\frac{D}{3D_2} - \frac{W}{D}\right). \tag{4.3}$$

Substituting (4.1) into (4.3) we find the maximum runup is given by,

$$\frac{R^{Max}}{D} = 1 + \left(\frac{D}{6D_2}\right)^2 . \tag{4.4}$$

The scaling relation (4.3) predicts minimal runup $R/D = 1$ for the cavity width $W = 0$, which is the case of no cavity. As the cavity width is increased we also expect minimal runup when $W = D^2/(3D_2)$ due to the cavity width being too large for significant wave production, this is an underestimate of the experimental value, but it still gives a reasonable estimate.

A defect of (4.3) is that $R/D \to \infty$ as $D_2 \to 0$, indicating a change in behaviour of the system. In fact the simulations show that as $D_2 \to 0$ complicated breaking waves form and the runup is reduced from that expected from the scaling relation. The scaling relation does give reasonable agreement for larger cavity heights.
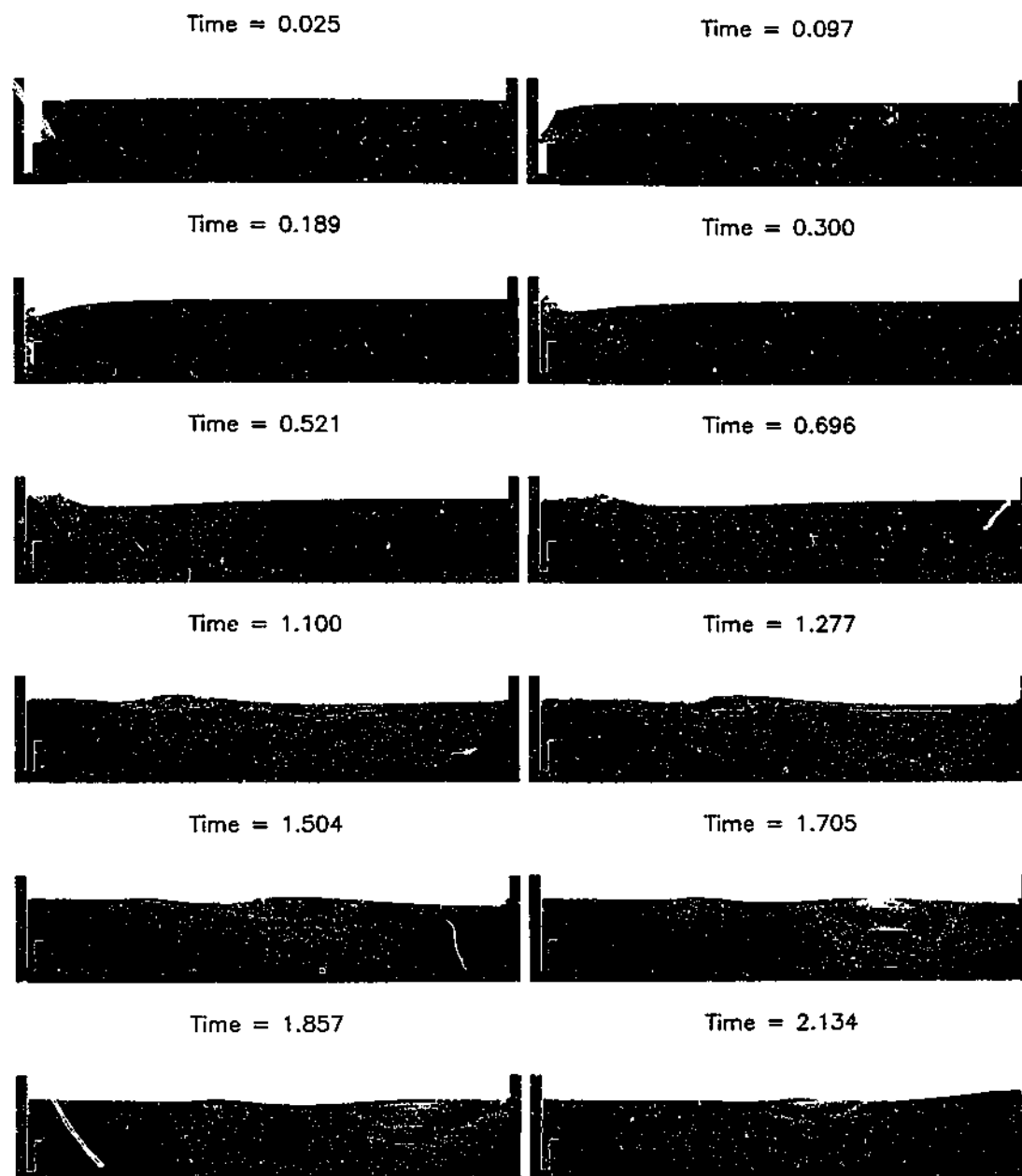
Figure 4.9:   Wave generation in a thin cavity with dimensions $W = 5cm$, $D_2 = 12.5cm$, $D = 30cm$, $L = 200cm$ and parameters $\Delta p = 0.01$, $h/\Delta p = 1.2$, $\alpha = 0.01$, $\xi = 0.5$. A discussion of the amplitude of waves produced is given in the text.

Time = 0.097   Time = 0.165

Time = 0.239   Time = 0.307

Time = 0.515   Time = 0.673

Time = 0.888   Time = 1.063

Time = 1.313   Time = 1.591

Time = 1.966   Time = 2.191
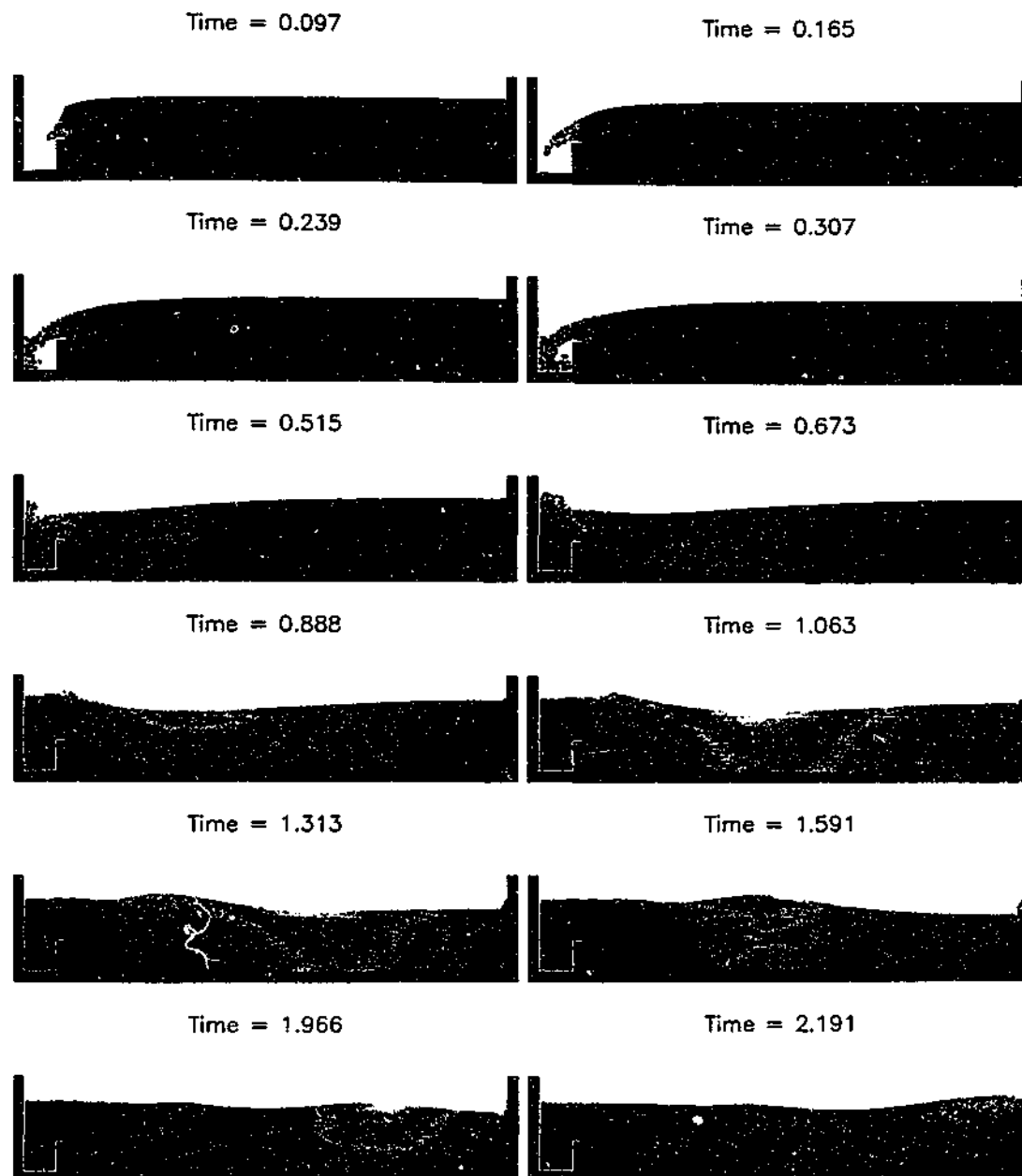
Figure 4.10: Wave generation in a medium width cavity with dimensions $W = 15cm$, $D_2 = 12.5cm$, $D = 30cm$, $L = 200cm$. Other parameters as for figure 4.9. A discussion of the amplitude of waves produced is given in the text.

Time = 0.118   Time = 0.187

Time = 0.229   Time = 0.312

Time = 0.439   Time = 0.568

Time = 0.770   Time = 0.946

Time = 1.641   Time = 1.939

Time = 2.090   Time = 2.290
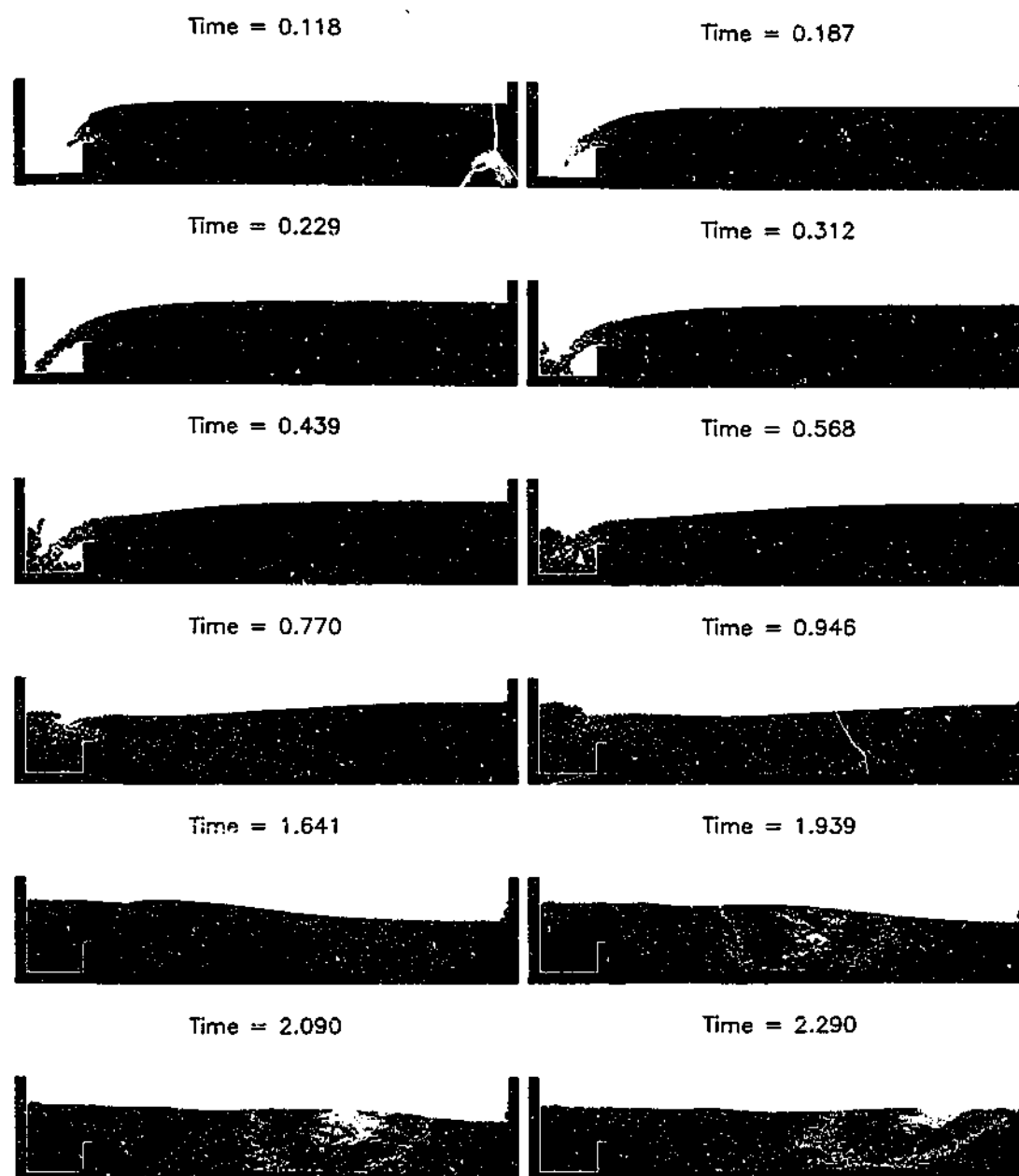
Figure 4.11: *Wave generation in a medium width cavity with dimensions $W =$ 25cm, $D_2 = 12.5cm$, $D = 30cm$, $L = 200cm$. Other parameters as for figure 4.9. A discussion of the amplitude of waves produced is given in the text.*
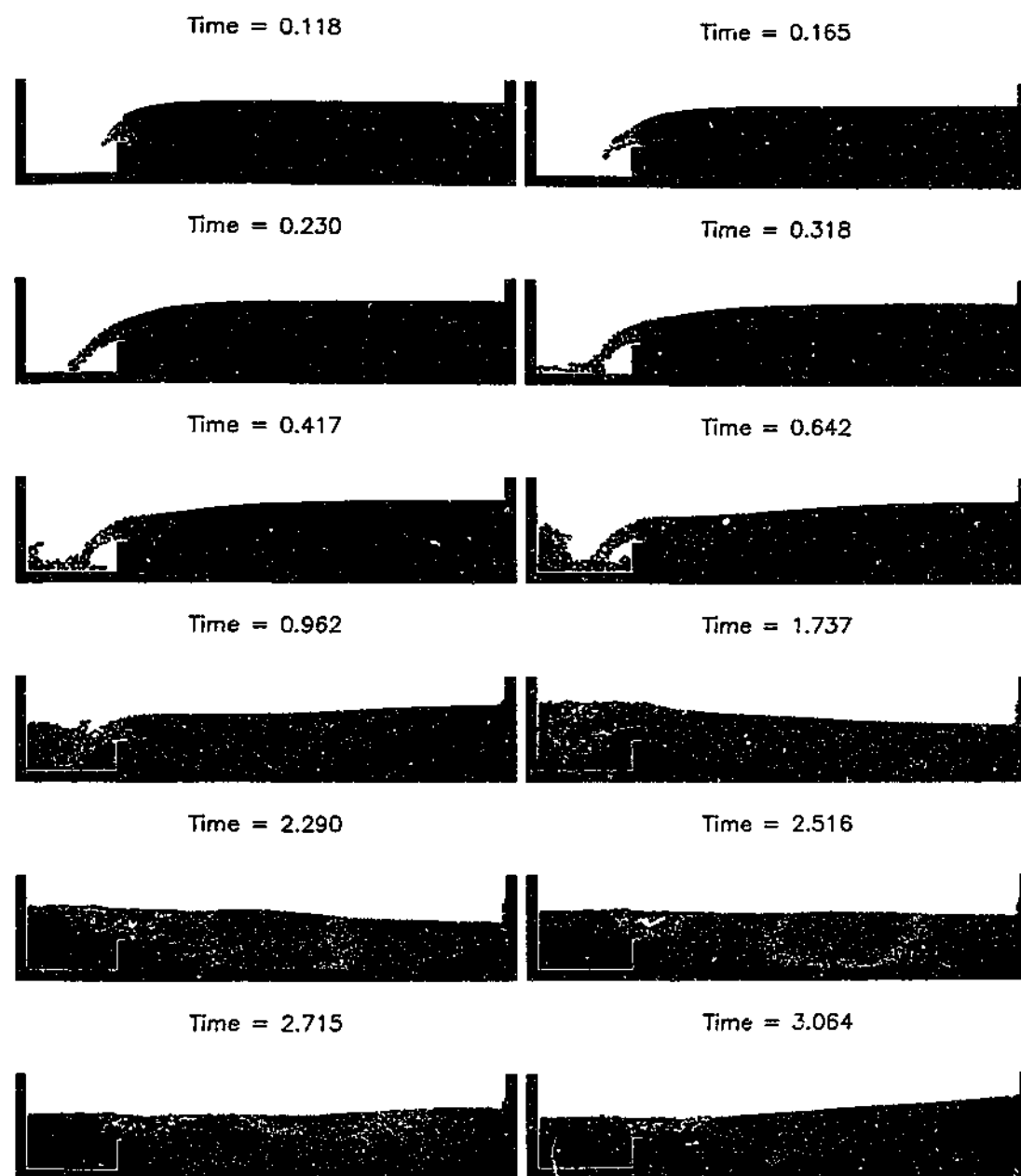
Figure 4.12: *Wave generation in a very wide cavity with dimensions* $W = 40cm$, $D_2 = 12.5cm$, $D = 30cm$, $L = 200cm$. *Other parameters as for figure 4.9. A discussion of the amplitude of waves produced is given in the text.*
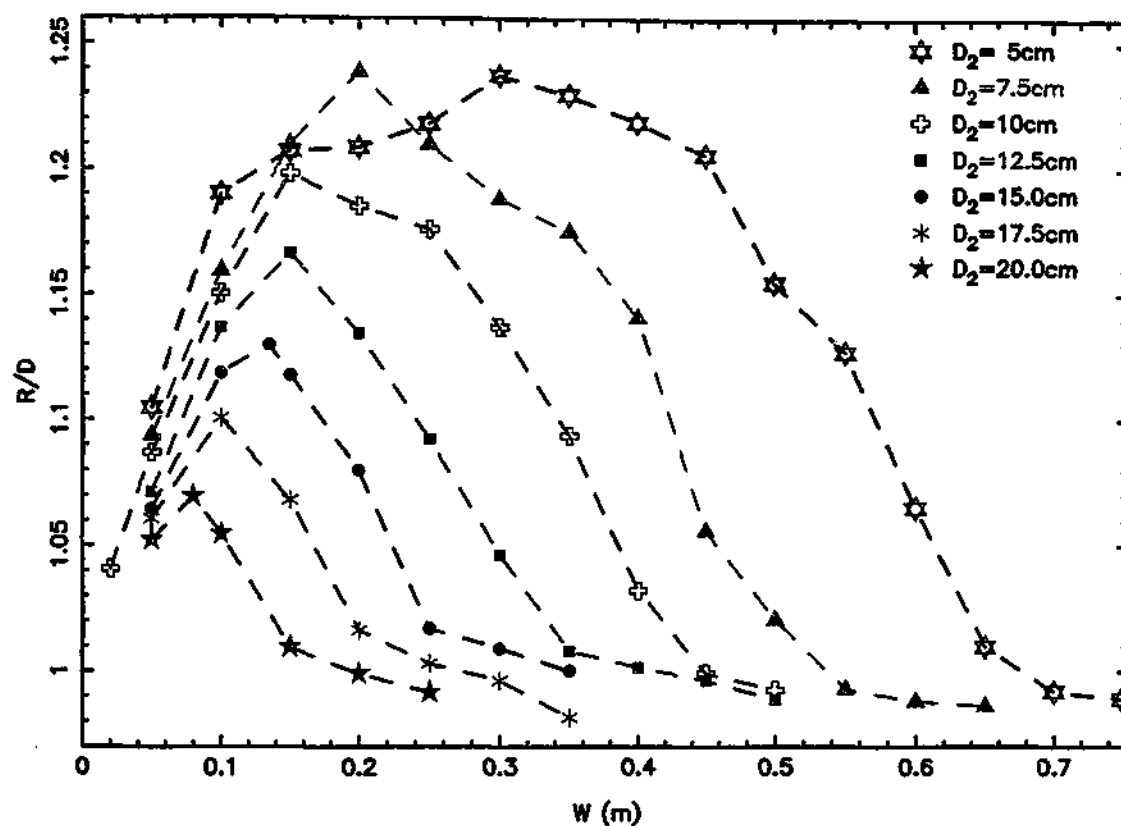
Figure 4.13: *Comparison of the extent of runup (R/D) for different cavity widths W where each line represents a different cavity height D_2. R is the maximum value of runup (measured from the bottom of the tank) and $D = 30cm$ is the initial water depth. These results are obtained from numerical simulations and are consistent with the experimental results in section 4.1.*

4.3   A Train of Waves

The situations we have discussed so far are in tanks with simple geometries involving only square boundaries, one of the advantages of SPH is that it can be easily adapted to complicated terrains and geometries. We now discuss a simulation conducted in a much larger tank that includes a sloping beach on which the waves run up and can break. The bonus in using a larger tank is that we can see the wave motions when they are fully formed and unaffected by reflections from the tank ends.

The bottom of the tank was flat for $3.8m$, after which a sloping beach at an angle of $10°$ from the horizontal was positioned. In figure 4.14 the water was of depth $D = 0.3m$, the cavity width was $W = 0.4m$, with the height of the bottom static wall being $D_2 = 0.05m$. The resolution was given by $\Delta p = 0.5cm$, with $h/\Delta p = 1.2$, $\alpha = 0.01$ and $\xi = 0.5$. The scale of figure 4.14 is exaggerated in the vertical direction. Vertical distances are plotted five times greater than those in the horizontal direction to more clearly show features of the wave.

The mechanism of wave generation is the same as for the cases where the length of the tank was smaller (sections 4.1 and 4.2). An outpouring jet forms a vortex and a column of water is built up over the cavity which is higher than the average water level. We then find that this column breaks up into a series of (at least) four waves, with the later waves being of smaller amplitude.

The speed of the first wave was $1.1m/s$ with the half width and amplitudes having values of $18.6cm$ and $3.9cm$ respectively. The wave train travels across the tank towards the sloping beach. Water withdraws from the beach as the wave approaches. The wave profile steepens as it runs up the beach before it breaks and surges up the beach. The later waves do not break. The present calculation does not contain a high enough resolution to accurately follow the breaking motions of the wave.

Breaking waves have been studied in detail by Grilli, Svensden, and Subramanya (1997) using a Boundary Element Method. However, this technique cannot follow the breaking wave after its tip hits the fluid in front of the wave. The ability of SPH to effortlessly handle the overturning and reconnection of fluid after wave breaking make it a potentially useful method in a comprehensive study of wave breaking.

Time =   0.36   Time =   0.54

Time =   0.98   Time =   1.28

Time =   2.85   Time =   3.59

Time =   4.81   Time =   5.39
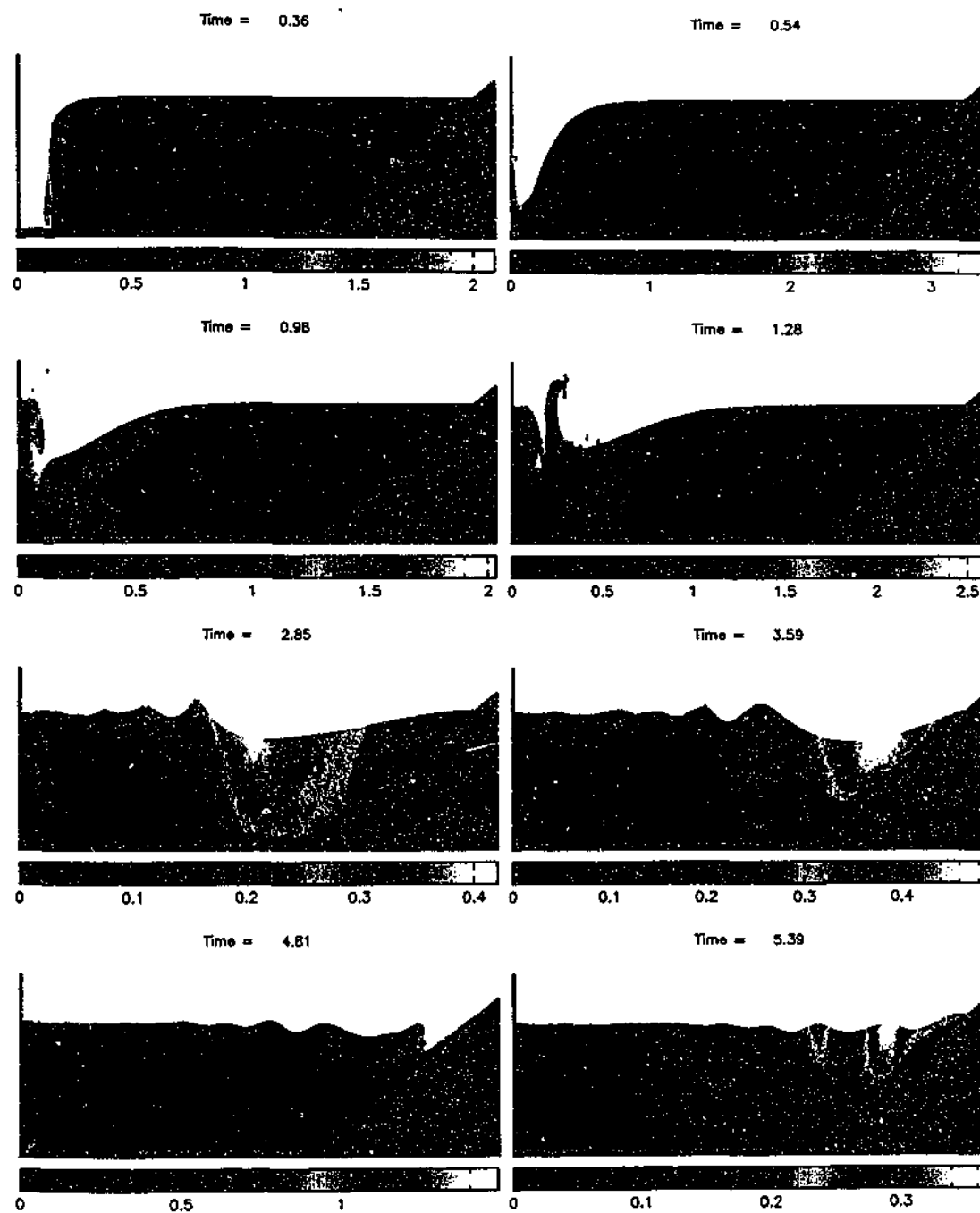
Figure 4.14:   *Wave generation in a tank 6m long with a sloping beach. Vertical lengths are exaggerated and are five times greater than horizontal lengths.*

4.4 Summary and Conclusions

We have reviewed different types of caldera collapse and discussed how caldera collapse may be related to the production of tsunamis when it occurs in a marine environment. We began by introducing a simple model for piston subsidence and presented the results of wave tank experiments conducted using this model. We computed numerical simulations of these experiments and found the features were best represented when a ghost particle boundary implementation was imposed (as opposed to the use of boundary forces). We found the wave amplitude to increase as the cavity height D_2 was decreased and more water was able to flow into the cavity.

The effect of changing the width of the cavity was studied in section 4.2. We found that for each cavity height D_2 there was a certain cavity width at which the maximum runup occurred. Below this width wave production was inhibited as only a small amount of water was disturbed and formed into waves. At higher widths the energy of the incoming water was trapped and dissipated inside the cavity during the filling process, as a result of these losses smaller waves were generated. An approximate scaling relation linking the extent of wave runup at the end of the tank to the cavity width and height was found.

In section 4.3 we followed the production and propagation of waves in a long tank. The advantage of using a long tank is that we are able to view the waves (and their travelling motions) unaffected by wave reflections. A train of waves was seen to develop. The distinction between waves which are affected by boundary reflections and waves that are not is also important in realistic applications.

We can imagine two regimes, one where the tsunami wavelength is approximately the same as the characteristic lengthscale of the environment and boundary effects are important. This situation covers islands $5 - 10km$ from the caldera where the runup and reflection of waves occurs near the source and has an effect on the generation of further waves. This situation is similar to the first set of simulations and experiments (section 4.1) and is what might be expected from the caldera collapse of Santorini.

In the other regime the tsunami wavelength is many times smaller than the distance propagated and wave reflection effects do not affect the generation of waves. This was shown in the simulation of the long tank (section 4.3) where a train of waves was seen to develop. This regime is relevant to those waves produced during the

eruption of Santorini which propagate to the beaches of Crete and other islands.

One of the major achievements of this work has been to benchmark the SPH numerical code for the simulation of the generation and propagation of water waves. This has been done both in the previous chapter by comparing results of the code to a range of test problems and experiments and in the present chapter where we have compared computations to a series of experiments for a simple caldera collapse model. The benchmarking of the code is important as it allows us to apply the code to a range of different problems with confidence in the accuracy of the results.

The problems we have used to benchmark our code have all been on a laboratory lengthscale ($\sim 1m$). In order to be able to apply our results on a larger lengthscale ($\sim 100km$) we must ensure that the important physical phenomena are the same on both length scales. Essentially this means that the test problems were largely unaffected by surface tension and boundary layer effects. We find that both these conditions hold, and that we are able to apply our results.

Another achievement was to obtain a scaling relation for the extent of wave runup between many of the important lengths in our model of wave generation due to caldera collapse. The two dimensional nature of the simulations used to obtain this relation mean that its applicability to the realistic case is limited due to the neglect of the complicated three dimensional geometry. The breadth of the cavity and varying depth of the floor are ignored, even though they have an effect on the volume of water which is displaced and the subsequent size of the waves that are produced.

Before discussing wave amplitudes, we need information on the geometry of Santorini immediately before and after the Minoan eruption. The models we have presented are very simple, they contain flat floors and vertical walls and are almost certainly only an approximation to the realistic situation. The geometry of Santorini is complicated, it has been fashioned by a series of volcanic events spanning $100,000$ years (Heiken and McCoy 1984; Druitt and Francaviglia 1992).

A shallow, flooded caldera fed by a shallow inlet in the south western corner of the island formed during an eruption $21,000$ years ago and was present immediately prior to the Minoan eruption (Druitt and Francaviglia 1992). The Minoan eruption occured $3,500$ years ago and increased both the size and depth of the caldera.

The modern day caldera floor (figure 1.1) consists of a northen basin approximately $370m$ deep, the southern half of the caldera is around $275m$ deep with the

recently formed Kameni islands in the middle of the caldera complex. There is a $20m$ deep inlet on the south western side of the caldera with the surrounding sea having a depth of $370m$. The north eastern inlet is $300m$ deep although the water around this entrance is only $50 - 100m$ deep.

In section 4.2 we found the maximum extent of wave runup to be given by (4.4). To convert from runup to wave amplitude we note from section 3.1 that the extent of runup is approximately twice the amplitude of the initial wave. We assume $H \simeq (R - D)/2$, where H is the wave amplitude and we find,

$$\frac{H}{D} \simeq \frac{W}{2D}\left(\frac{D}{3D_2} - \frac{W}{D}\right). \tag{4.5}$$

During the Bronze age eruption of Santorini reasonable values of the appropriate heights are $D = 370m$ and $D_2 = 270m$ for the northern inlet. For large cavity widths (4.4) and (4.5) do not apply, they predict runups much less than the initial water depth and waves of negative amplitude. The simulations exhibit waves of minimal amplitude at such widths. The relation (4.5) is only valid for $W < D^2/(3D_2)$. Taking a width in the order of $5,000m$ for the northern inlet of Santorini we have $W \gg D^2/(3D_2)$. Either waves were not produced from the collapse or a different wave generation mechanism applies for large cavity widths.

The ratio of height to width of the cavity is significantly lower in the case of Santorini ($H/W \simeq 0.08$), than in our simulations and experiments ($H/W \simeq 1$). It is likely that this difference means that the scaling relation (4.4) is not applicable and may indicate that a different mechanism is involved in the production of waves. Although our initial motivation was to determine the magnitude of waves produced at Santorini, our models do not apply. Further investigation is required to achieve this motivation.

It is theoretically possible to calculate the flow of Santorini with realistic dimensions, although such a calculation is very computationally expensive. The resolution of SPH is determined by the particle spacing, to be able to resolve the amplitude of waves to within a metre we require a particle spacing, $\Delta p = 1m$. In a two dimensional simulation of Santorini we need to model an area at least $400m$ deep by $16,000m$ long. A minimum of $400 \times 16,000 = 6.4 \times 10^6$ particles are required. A typical timestep τ can be found from the Courant condition and is given by $\tau = \Delta p/c_s \simeq \Delta p/(15gD)$ where the soundspeed is given by (2.25). This leads to a timestep $\tau = 1/60000$ seconds.

In comparison, the simulations in section 4.2 involved 6,000 particles and a timestep $\tau = 1/4500$ seconds. These simulations had 20,000 steps and took 15 minutes of computational time on a 466MHZ ev6 Alpha CPU. The increased particle resolution means each timestep will take 1,000 times as long. The increased resolution decreases the size of the timestep by a factor of 10 and the simulation has to be conducted for a longer time due to the longer time it takes for waves to travel over the increased length of the tank. This indictates a simulation using the dimensions of Santorini would be computationally prohibitive as it would take many weeks to complete.

An important factor which will determine whether or not collapse will lead to wave production is the time it takes for subsidence to occur. Instantaneous collapse, (where the rate of collapse is similar to an earthquake) will probably lead to the production of waves of maximum amplitude. Conversely, slow gradual collapse over a timescale of hours or days, will almost certainly lead to smaller waves being produced (probably none). The fundamental question of which timescales and subsidence rates lead to the production of significant waves requires further investigation.

We have shown that it is possible to accurately model the waves produced in a simplified model of caldera collapse on a laboratory scale. The limitations in our model are discussed along with extensions required to obtain an estimation of wave amplitudes. Whilst it is possible to scale our simulations to handle bigger lengths, the geometry and resolution required for the realistic simulation mean that such a simulation is prohibitive in a serial computing environment.

Chapter 5

Solid Body Equations

n this section we outline a way the SPH method for fluid dynamics can be extended to model elastic solid bodies. The essence of the method is to introduce a stress tensor into the equations that account for elastic effects. If we take a gas and pull it apart there is nothing to resist the tensile forces (neglecting self-gravity) so it expands. In a solid, the strong bonds between molecules resist the extension by producing stresses in the solid.

The idea of using hydrocodes for the simulation of elastic-plastic flow has been around since the sixties (Wilkins 1964; Petschek and Hanson 1968) in a finite difference context. In the SPH framework it has been pioneered by Libersky and Petschek (1991), Libersky et al. (1993) and Benz and Asphaug (1994,1995).

5.1 Elastic Material Equations

The stress tensor can be written as,

$$\sigma^{\alpha\beta} = S^{\alpha\beta} - P\delta^{\alpha\beta}, \tag{5.1}$$

where P is the pressure and $S^{\alpha\beta}$ is the deviatoric part of the stress tensor.

The simplified momentum equation (without viscous and forcing terms) then becomes,

$$\frac{dv_\alpha}{dt} = \frac{1}{\rho}\frac{\partial\sigma^{\alpha\beta}}{\partial x^\beta}. \tag{5.2}$$

or in SPH form,

$$\frac{dv_a}{dt} = \sum_b m_b\left(\frac{\sigma_b^{xx}}{\rho_b^2} + \frac{\sigma_a^{xx}}{\rho_a^2}\right)\frac{\partial W_{ab}}{\partial x_b} + \sum_b m_b\left(\frac{\sigma_b^{xy}}{\rho_b^2} + \frac{\sigma_a^{xy}}{\rho_a^2}\right)\frac{\partial W_{ab}}{\partial x_b} \tag{5.3}$$

The SPH equation for density is different to the one we used for water waves (2.20). This form is used as it gives zero divergence at the interface with two different density fluids.

First we write the SPH continuity equation as,

$$\frac{d\rho_a}{dt} = -\rho_a \sum_b \frac{m_b}{\rho_b} \mathbf{v}_b \cdot \nabla_a W_{ab}. \tag{5.4}$$

Then we use the fact that the derivative of a constant is equal to zero. To write,

$$\rho_a \mathbf{v}_a \cdot \nabla(1) = \rho_a \mathbf{v}_a \cdot \sum \frac{m_b}{\rho_b} \nabla_a W_{ab}. \tag{5.5}$$

Adding (5.4) and (5.5) we find that,

$$\frac{d\rho_a}{dt} = -\rho_a \sum_b m_b \frac{1}{\rho_b} (\mathbf{v}_a - \mathbf{v}_b) \cdot \nabla_a W_{ab}. \tag{5.6}$$

The rate of change of the deviatoric stress $S^{\alpha\beta}$ is given by Hooke's Law (Wilkins 1964; Libersky and Petschek 1991). The equations take the form,

$$\begin{aligned}
\frac{dS^{xx}}{dt} &= \frac{2}{3}\mu(2\dot{\epsilon}^{xx} - \dot{\epsilon}^{yy}) + 2\Omega^{xy}S^{xy} \\
\frac{dS^{yy}}{dt} &= \frac{2}{3}\mu(2\dot{\epsilon}^{yy} - \dot{\epsilon}^{xx}) - 2\Omega^{xy}S^{xy} \\
\frac{dS^{xy}}{dt} &= 2\mu\dot{\epsilon}^{xy} + \Omega^{xy}S^{yy} - S^{xx}\Omega^{xy}.
\end{aligned} \tag{5.7}$$

Where, μ is the Shear Modulus, $\Omega^{\alpha\beta}$ are rotation terms,

$$\begin{aligned}
\Omega^{xy} &= \frac{1}{2}\left(\frac{\partial v^x}{\partial y} - \frac{\partial v^y}{\partial x}\right) \\
\Omega^{yx} &= -\Omega^{xy}
\end{aligned} \tag{5.8}$$

and $\dot{\epsilon}^{\alpha\beta}$ are strain rates given by,

$$\begin{aligned}
\dot{\epsilon}^{xx} &= \frac{\partial v_x}{\partial x} \\
\dot{\epsilon}^{yy} &= \frac{\partial v_y}{\partial y} \\
\dot{\epsilon}^{xy} = \dot{\epsilon}^{yx} &= \frac{1}{2}\left(\frac{\partial v_x}{\partial y} + \frac{\partial v_y}{\partial x}\right).
\end{aligned} \tag{5.9}$$

The rotation terms are important as we want our stress rates to be *objective*, which means that they are invariant with respect to rotated observer frames (Atluri 1984). For large deformations alternative rotation terms are required (Dienes 1979; Flanagan and Taylor 1987) to retain objectivity.

The use of (5.7) means that we find natural strains, where the strain of an element corresponds to the current configuration and not the original material configuration. The strain rates are found by the summation,

$$\dot{\epsilon}_a^{\alpha\beta} = \frac{1}{2} \left(\sum_b \frac{m_b}{\rho_b}(\hat{v}_b^\alpha - \hat{v}_a^\alpha)\frac{\partial W_{ab}}{\partial x_b^\beta} + \sum_b \frac{m_b}{\rho_b}(\hat{v}_b^\beta - \hat{v}_a^\beta)\frac{\partial W_{ab}}{\partial x_b^\alpha} \right) \qquad (5.10)$$

where, $\hat{v}$ refers to the XSPH smoothed velocity (2.22). Note that the rotation terms Ω^{xy} are similar to the strain rates $\dot{\epsilon}^{xy}$ with the second derivative being subtracted instead of added.

We follow Melosh, Ryan, and Asphaug (1992) and use a Murnaghan-type equation of state with $n = -1$ (Murnaghan 1951) (pg.68),

$$P = \rho_o c_s^2 \left(\frac{\rho}{\rho_o} - 1 \right). \qquad (5.11)$$

Randles and Libersky (1996) use the Mie-Gruneisen equation for solids, but for the present problem the simplified equation of state (5.11) is sufficient because thermal effects are negligible.

In the present calculations the elastic constant Poisson's ratio ν is determined in terms of the shear modulus μ and the bulk modulus κ according to,

$$\nu = \frac{3\kappa - 2\mu}{6\kappa + 2\mu}. \qquad (5.12)$$

5.2   Plastic Material Equations

In an elastic material, the strain is proportional to the stress (Hookes's law) up until the stress reaches the yield strength of the material, Y_o. After the yield strength has been exceeded plastic (permanent) deformation occurs. Yield strength is both material and condition (e.g. temperature) dependent. Below the yield strength we can remove the stress and the material will return to it's original shape.

Following Libersky and Petschek (1991) and Benz and Asphaug (1994) we introduce the Von Mises yielding criterion to our elastic equations to allow us to account for plastic deformation. The Von Mises criterion is implemented by limiting the deviatoric stress. Limiting the size of the deviatoric stress tensor in the plastic region reduces the resistance of the material to expansion and leads to permanent

deformation. The deviatoric stress tensor for plasticity is given by,

$$S^{\alpha\beta} \Rightarrow f S^{\alpha\beta} \tag{5.13}$$

where f is found from,

$$f = MIN \left(\frac{Y_o^2}{3J_2}, 1 \right). \tag{5.14}$$

The second invariant of the deviatoric stress tensor J_2 is given by

$$J_2 = \frac{1}{2}(S^{xx}S^{xx} + 2S^{xy}S^{xy} + S^{yy}S^{yy}). \tag{5.15}$$

5.3 Artificial Stresses and the Tensile Instability

It has long been known that SPH can become unstable when particles are in tension (Swegle 1992; Morris 1994; Swegle, Hicks, and Attaway 1995; Randles and Libersky 1996). A short wavelength instability also occurs when using SPH for magnetic field problems (Phillips and Monaghan 1985). Here we take the approach of Monaghan (2000) to combat this instability.

The tensile instability occurs when particles acquire negative pressures and begin to clump together. In the context of elastic materials, this leads to premature (numerical) fracturing. A variety of methods have been proposed to remove the tensile instability. Among them is the idea that the stresses can be calculated at different points in space to the other variables, this is known as the *Stress Point* technique (Dyka, Randles, and Ingel 1997; Vignjevic, Campbell, and Libersky 2000). The *Conservative Smoothing* approach is proposed by Swegle, Hicks, and Attaway (1995). The *Moving Least Squares* (MLS) method Dilts (1999,2000) replaces the usual SPH interpolants with moving least square interpolants to slow the growth of the tensile instability.

Monaghan (2000) overcomes the tensile instability problem in the fluid case by adding artificial stress terms which lead to a repulsive force in the momentum equation. The artificial stresses take effect when particles become close together and the stress is positive (in tension). In this section we discuss the implementation of the artificial stress.

For the case of gas dynamics and fluids where the stress tensor consists of just a pressure term on the diagonal Monaghan (2000) takes a repulsive force based on the smoothing kernel,

$$f_{ab} = \frac{W(\mathbf{r}_{ab})}{W(\Delta p)}. \tag{5.16}$$

This force is equal to 1 for two particles the average particle spacing Δp apart and increases for particles which are closer together. This results in the force increasing as particles clump together, resisting the clumping.

The momentum equation is then changed from,

$$\frac{P_b}{\rho_b^2} + \frac{P_a}{\rho_a^2} + \Pi_{ab} \tag{5.17}$$

to

$$\frac{P_b}{\rho_b^2} + \frac{P_a}{\rho_a^2} + \Pi_{ab} + (R_a + R_b)f_{ab}^n. \tag{5.18}$$

Where,

$$R_a = \begin{cases} 0 & \text{if } P \geq 0 \quad \text{(Attraction)} \\ \\ \epsilon P_a/\rho_a^2 & \text{if } P < 0 \quad \text{(Expansion).} \end{cases} \tag{5.19}$$

The artificial stress R_a is only active for negative pressure, which is when the tensile instability becomes a problem, and scales the force (f_{ab}) so that it is smaller than the usual stress terms. The power of n is high which means that the force drops off rapidly for particles further than a particle spacing apart.

Monaghan (2000) shows from an analysis of the dispersion relation that stability can be achieved for $\epsilon = 0.3$ and that by taking, $2 \leq n \leq 6$ the errors in the long wavelength limit are minimized. The dispersion relation for long wavelengths then becomes,

$$\omega^2 = k^2 c_o^2 \left(1 + 0.02\epsilon \left| \frac{\bar{\rho} - \rho_o}{\rho_o} \right| \right). \tag{5.20}$$

Although the error does not vanish in the limit $\Delta p \to 0$, it is negligible in practical applications.

We now express the extension of this artificial stress to elastic bodies. Including the deviatoric stress terms for the solid body case, the momentum equation is then changed from,

$$\frac{\sigma_b^{ij}}{\rho_b^2} + \frac{\sigma_a^{ij}}{\rho_a^2} + \Pi_{ab}\delta^{ij} \tag{5.21}$$

to

$$\frac{\sigma_b^{ij}}{\rho_b^2} + \frac{\sigma_a^{ij}}{\rho_a^2} + \Pi_{ab}\delta^{ij} + (R_a^{ij} + R_b^{ij})f^n. \tag{5.22}$$

Where,

$$R_a^{ij} = \begin{cases} 0 & \text{if } \sigma_a^{ij} \le 0 \quad \text{(Compression)} \\[2ex] \epsilon\sigma_a^{ij}/\rho_a^2 & \text{if } \sigma_a^{ij} > 0 \quad \text{(Tension)}. \end{cases} \tag{5.23}$$

As $\sigma^{ij} = -\delta_{ij}P + \S^{ij}$, negative pressure in this case corresponds to a positive stress tensor. For stability we again take $\epsilon = 0.3$ and $2 \le n \le 6$ to minimise the long wavelength errors.

The question then arises as to the best way to implement this on each of the stress components. The alternatives are to apply the term to each of the stress components as they are or to rotate to a frame where the principal stress occurs. Monaghan (2000) illustrates the colliding ball problem (Swegle 1992) using the former approach. We prefer the latter since the stress component associated with tension is then clear.

It is well known that the angle θ_a required to rotate to a plane of Principal stress is given by,

$$\tan(2\theta_a) = \frac{2\sigma_{xy}}{\sigma_{xx} - \sigma_{yy}}. \tag{5.24}$$

The principal stresses in this rotated frame are given by,

$$\begin{aligned} \bar{\sigma}_a^{xx} &= \sigma_a^{xx}\cos^2\theta_a + \sigma_a^{xy}2\sin\theta_a\cos\theta_a + \sigma_a^{yy}\sin^2\theta_a \\ \bar{\sigma}_a^{yy} &= \sigma_a^{xx}\sin^2\theta_a + \sigma_a^{xy}2\sin\theta_a\cos\theta_a + \sigma_a^{yy}\cos^2\theta_a. \end{aligned} \tag{5.25}$$

In the case $\sigma_{xx} = \sigma_{yy}$ the denominator in (5.24) is zero and care must be taken. In practice this case corresponds to $\cos(2\theta_a) = 0$, and if the two deviatoric stress components are equal we take $\theta_a = 45°$.

If the stress is tensional the correction terms $\bar{R}_a^{xx}$ and $\bar{R}_a^{yy}$ are calculated by,

$$\bar{R}_a^{ii} = -\epsilon \frac{\bar{\sigma}_a^{ii}}{\rho_a^2}. \tag{5.26}$$

These corrections are rotated back to the original coordinates,

$$\begin{aligned}
R_a^{xx} &= \bar{R}_a^{xx} \cos^2 \theta_a + \bar{R}_a^{yy} \sin^2 \theta_a \\
R_a^{yy} &= \bar{R}_a^{xx} \sin^2 \theta_a + \bar{R}_a^{yy} \cos^2 \theta_a \\
R_a^{xy} &= (\bar{R}_a^{xx} - \bar{R}_a^{yy}) \cos \theta_a \sin \theta_a.
\end{aligned} \tag{5.27}$$

Finally, the artificial stress terms are added to the momentum equation,

$$\frac{dv_b^i}{dt} = \sum m_a \left(\frac{\sigma_b^{ij}}{\rho_b^2} + \frac{\sigma_a^{ij}}{\rho_a^2} + \Pi_{ab}\delta^{ij} + (R_a^{ij} + R_b^{ij})f^n \right) \frac{\partial W_{ab}}{\partial x_b}. \tag{5.28}$$

5.4 Solid Body Implementation

The implementation of the solid body code is the same as for the earlier fluid code (section 2.3) except that we do not use damping as in these problems the initial state is in equilibrium. Unlike the fluid problems, boundaries and gravitational forces are not involved an initial readjustment of particle positions does not occur.

Dimensionless Units The solid body calculations in the following sections have been conducted with normalised coordinates, scaled in terms of ρ_o and c_o. We take the unit of length L_o to be $1cm$. In the following a prime refers to a variable in our dimensionless coordinate system.

Velocities are scaled by the soundspeed, $v = c_o v'$. Similarly for density $\rho = \rho_o \rho'$. The scaled time t' is found with a combination of the length scale L_o and speed of sound c_o such that, $t = (L_o/c_o)t'$.

The bulk modulus K is scaled by, $K = -(1/V)(\partial P/\partial V) = \rho\partial P/\partial\rho$. Taking the equation of state (5.11) we have $K = \rho_o c_o^2$. We normalise the elastic moduli and stresses by dividing by $\rho_o c_o^2$ so that $K' = 1$, $\mu' = \mu/(\rho c_o^2)$ and $\sigma' = \sigma/(\rho c_o^2)$.

A drawback of introducing dimensionless units is that there is a loss in any physically intuitive feel one may have for the magnitudes and effects of stresses. For most metals the bulk modulus and Young's modulus are approximately equal. For rocks there may be a factor of two or three difference (Jaeger 1964) (pg.58). We

can gain an understanding of the expected size of our dimensionless stresses if we assume $E \simeq K$. From Hooke's law we then find,

$$\epsilon = \frac{\sigma}{E} \simeq \frac{\sigma}{K} \simeq \sigma'. \tag{5.29}$$

That is our dimensionless stress is also a rough estimate of the strain a material is undergoing.

Another way to quantify the dimensionless stress is to compare it to a materials ultimate tensile strength σ_{TS}, converted into the dimensionless coordinates. We take values of the bulk modulus and tensile strength from (Jaeger 1964) (pg.58,75) and find for steel that $\sigma_{TS}/K = 2.8 \times 10^{-3}$ and granite has a value of $\sigma_{TS}/K = 1.5 \times 10^{-4}$. These are estimates of the strength of the material in the dimensionless coordinates and we conclude that stresses greater than one percent of the materials bulk modulus $(\sigma' = 0.01)$ are very high.

For convenience we remove the primes when referring to the dimensionless coordinates from now on.

Double Precision Variables   It was found that when the axes are rotated to the directions of principal stress computational problems can arise if $\sigma_{xx} \approx \sigma_{yy}$. The equation for the principal axis rotation angle (5.24) will then have a term that is divided by a number that is very close to zero. This has been overcome by using double precision variables. Alternatively a term similar to η in the momentum equation (2.18) that ensures that particles on top of each other do not lead to a singularity can be incorporated. A suitable term is $\Delta\sigma = \pm\rho c_o^2 \times 10^{-6}$ where the sign of $\Delta\sigma$ is taken to be the same as the stress difference $(\sigma^{xx} - \sigma^{yy})$, to ensure that the compressive or tensile state of the particle is retained.

Integration   The same integration scheme as for the fluid calculations is used. With the integration of the stress terms in the present case being treated the same as density in the fluid case. That is a predictor-corrector scheme is again used, writing $dS^{ij}/dt = T^{ij}$ the predictor step is,

$$\begin{aligned}
\mathbf{v}_p &= \mathbf{v}_o + \Delta t\mathbf{F}_o, \\
\rho_p &= \rho_o + \Delta t\mathbf{D}_o, \\
S_p^{ij} &= S_o^{ij} + \Delta t T_o^{ij}.
\end{aligned} \tag{5.30}$$

We now calculate new values of $\mathbf{F}$, $\mathbf{D}$ and T^{ij} before using the corrector step,

$$
\begin{aligned}
\mathbf{v} &= \mathbf{v}_p + \tfrac{1}{2}\Delta t(\mathbf{F} - \mathbf{F}_o), \\
\rho &= \rho_p + \tfrac{1}{2}\Delta t(\mathbf{D} - \mathbf{D}_o), \\
S^{ij} &= S^{ij}_p + \tfrac{1}{2}\Delta t(T^{ij} - T^{ij}_o).
\end{aligned}
\tag{5.31}
$$

5.5   Damage Model and Equations

It was only recently (1821) when Navier gave the equations for the equilibrium and motion of elastic solids (Todhunter and Pearson 1960) (pg.1). However similarities between the basic materials of buildings and tools employed by ancient civilisations and those we use today indicate that much was learned about material strength before this time via trial and error.

Galileo Galilei theorised in the 1630's as to what things affected the strength of solids and their resistance to fracture (a translation of this work is given by Crew and De Salvio (1914)). He proposed that an objects resistance to fracture depended on things like it's composition, shape and size, as well as the magnitude and orientation of applied forces. These macroscopic factors are still considered important today in modern fracture theories, based on the formation of cracks at atomic scales.

The modern idea of material fracture which was developed by Griffith in the 1920's (Sammonds 1999) is that if a large enough force is applied to a material the atoms are no longer able to hold themselves together and the material fails. The theoretical strength of materials is based on the strength of the bonds between atoms and is much larger than the strength found in practice (Ashby and Jones 1980) (pg.86-88). The reason is that bonds between atoms in real materials are not perfect, but instead contain flaws that reduce the strength of the material (Marder and Fineberg 1996). The flaws act like holes and magnify the size of an applied stress near the flaw. The stress near a flaw is able to reach the critical failure stress whilst the remainder of the material is at lower stress. Once a flaw fails, a small crack can develop and grow.

Solid materials can be either brittle or ductile, the distinction between the regimes is temperature dependent and varies for different materials. Materials are brittle at low temperatures and ductile at high temperature. The behaviour of brittle and ductile materials is similar up to the elastic limit. After the elastic limit has

been reached a brittle material will fracture and break, whereas a ductile material will undergo stretching and plastic extension.

We have already outlined the equations which deal with elastic and plastic (ductile) materials. We now turn our attention to a numerical description for brittle fracture. A damage model was first used in SPH by Benz and Asphaug (1994) who implemented a variation of the numerical fracture and fragmentation work of Grady and Kipp (1980). Benz and Asphaug (1994) proposed a model of explicit and implicit flaws. Each particle was assigned an explicit flaw threshold above which damage was allowed to accumulate.

As the resolution of a numerical simulation is not high enough to account for each flaw in the material explicitly, implicit flaws were allowed to accrue damage on a subgrid length scale. The growth of these implicit flaws was based on the statistical approach of Grady and Kipp.

Benz and Asphaug (1995) proceeded in a different way. The implicit flaws were removed, with each particle being given a number of explicit flaws with different failure strains. In this way a larger number of explicit flaws could be introduced at the same spatial resolution. Meaning that the statistics involved larger numbers and were better represented. This approach is also computationally clearer as we do not have to worry about the effects of implicit subgrid scale flaws. It is also similar to the SPH statistical fracture model of Mandell, Wingate, and Schwalbe (1996), although they assign their failure strains differently.

In the above models the amount and shape of the cracks that develop depend on the distribution of flaws in the material and the rate of tensile loading experienced by the material. The model is based on a Weibull distribution of flaws

$$n(\epsilon) = k\epsilon^m, \tag{5.32}$$

where, n is the number of flaws in a unit volume which can activate below a tensile strain of ϵ, k and m are material constants which affect the number of active flaws at a given strain. The value of k can vary largely depending on the type of rock and its history. The constant m typically ranges from 6 to 12. We show in figure 5.1 the Weibull distribution for the case of $k = 1 \times 10^{19}$ and $m = 8.5$, along with some minor variations to these parameters. Higher values of k mean that the material has more flaws and result in a higher number of active flaws for a given strain. An increase in m results in a decrease in the number of active flaws at a given strain.
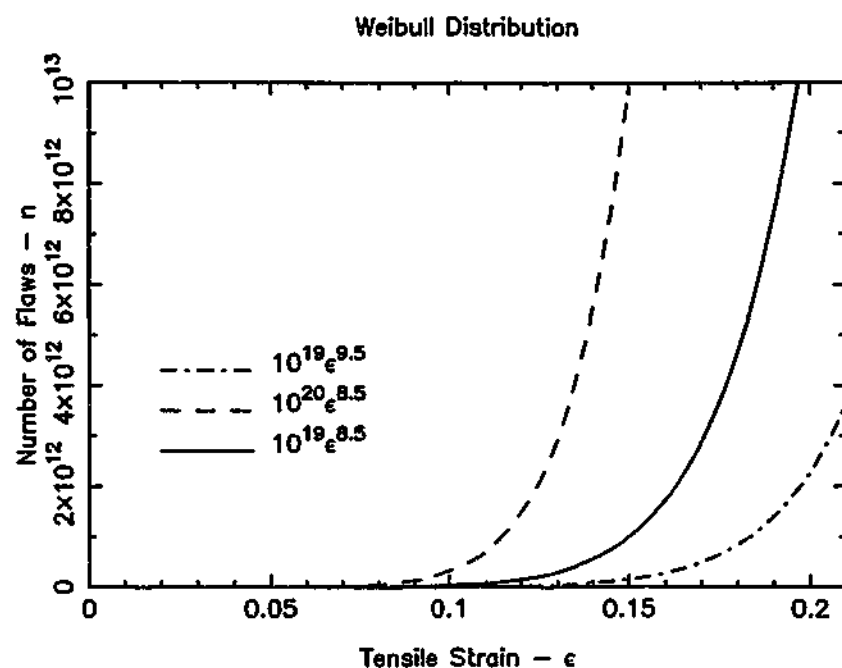
Figure 5.1: *Examples of the Weibull distribution for a range of k and m.*

The basic idea behind the models of Benz and Asphaug is to give each particle a damage variable D, where $0 \leq D \leq 1$. Zero damage means that the particle is undamaged and behaves as a plastic-elastic material. A particle in compression with a damage $D = 1$ feels no stresses and in a sense behaves as a fluid. If a particle is in tension with $D = 1$ the stress is set to zero so that fully damaged particles do not attract each other.

The stress tensor (5.1) is replaced by,

$$\sigma_{ij} = -P^* \delta_{ij} + (1 - D) S_{ij}. \tag{5.33}$$

P^* is defined by,

$$P^* = \begin{cases} P & \text{if } P \geq 0 \\ (1 - D)P & \text{if } P < 0. \end{cases} \tag{5.34}$$

The factor $(1 - D)$ is introduced to account for the reduction in stress as a particle becomes damaged.

Flaws are randomly assigned to particles. Damage begins to accumulate once the strain activation threshold of a flaw has been reached. A series of flaws is assigned

to each particle in the simulation. A flaw is activated and damage is allowed to grow in the particle when the particle undergoes a strain higher than the activation threshold for the flaw. The strain on each particle is found from,

$$\epsilon = \frac{\sigma_{Max}^{ij}}{2\mu(1 - D^2)} \tag{5.35}$$

where σ_{Max}^{ij} is the maximum principal stress for the particle.

If $\epsilon > \epsilon_{flaw}$ damage is allowed to accumulate up to a maximum amount determined by the number of active flaws in the particle. That is,

$$D \leq \frac{N_{active}}{N_{flaws}}, \tag{5.36}$$

where, N_{active} is the number of active flaws, and N_{flaws} is the total number of flaws in the particle. In this way a particle that has one weak flaw and three strong flaws does not have its strength governed by only the weakest flaw.

The half length of a growing crack (initiated at time τ) is,

$$a = c_g(t - \tau) \tag{5.37}$$

where c_g is the crack growth speed ($c_g \sim 0.4c_s$). Walsh (1965) found that cracks had an effect on the compressibility of rock proportional to the cube of their length. It is therefore reasonable to assume that in two dimensions cracks lead to stress relief in a circular area around the crack. Our derivation is slightly different to that of Grady and Kipp (1980) as we are dealing with only two dimensions.

$$D = \frac{\pi}{A}a^2$$
$$D^{1/2} = \left(\frac{\pi}{A}\right)^{1/2} a \tag{5.38}$$
$$\frac{dD^{1/2}}{dt} = \left(\frac{\pi}{A}\right)^{1/2} \frac{da}{dt} = \left(\frac{\pi}{A}\right)^{1/2} c_g$$

For a propagating crack it is shown that damage accrues according to,

$$\frac{dD^{1/2}}{dt} = \frac{c_g}{R_s} \tag{5.39}$$

where R_s is the radius of the circle relieved of stress by the crack. If we look at the Weibull distribution (5.32) the weakest flaw in an area, A will fail at a strain, ϵ_{min},

$$\frac{1}{A} = k(\epsilon_{min})^m$$
$$\epsilon_{min} = \left(\frac{1}{kA}\right)^{1/m} . \tag{5.40}$$

From this we see that the smaller the size, the stronger a piece of material is. This is consistent with real rocks. The larger the material size, the more likely it is to contain a weak flaw and is thus weaker. Smaller volumes are less likely to contain weak flaws and are therefore more likely to be stronger.

Particles are assigned explicit flaws where the strength of the flaw is random. Each flaw is assigned a random number $p(i)$, such that $1 \leq p(i) \leq N \log N$, where N is the number of particles in the simulation. The failure strain of each flaw is then given by,

$$\epsilon_{min}^i = \left(\frac{p(i)}{kA}\right)^{1/m}. \tag{5.41}$$

Flaws are assigned to particles randomly until every particle contains at least one flaw. This means that on average each particle will be assigned $N \log N$ flaws in a simulation. We set the maximum number of allowed flaws per particle to be twenty to conserve memory.

The rate of growth of damage in a particle with active flaws is given by,

$$\frac{dD^{1/2}}{dt} = N_{active}\frac{c_g}{R_s}. \tag{5.42}$$

We remember that there is a limit placed on the maximum damage that can accumulate in a particle that does not have all of its flaws active (5.36).

5.6   Dispersion Relation

The correct propagation of elastic waves is fundamental to the solution of problems in solid body dynamics. It is important that elastic waves are allowed to propagate at the correct velocities and that their propagation is stable. To study the propagation of elastic waves we calculate the dispersion relation for them.

We begin by calculating the dispersion relation for the exact elastic equations. We do this as the long wavelength behaviour of our SPH equations is required to match that of the exact equations. We follow by calculating the dispersion relation for the SPH equations and showing that it agrees with the exact dispersion relation in the long wavelength limit. The tensile instability is a short wavelength instability, we study the short wavelength dispersion relation to gain an understanding of the instability and appropriate ways to remove it.

The derivations in this section are included with more detail in appendix B. The work presented in this section involves work done in conjunction with Joe Monaghan.

5.6.1 Dispersion relation: Exact Equations

In this section we calculate the dispersion relation for waves in an initially uniform, infinite, elastic material with constant initial stress. We choose Cartesian axes to give an initial diagonal stress, and assume that the velocity is small. Variables are in the form,

$$
\begin{aligned}
\mathbf{v} &= \mathbf{V}e^{i(\mathbf{k}\cdot\bar{\mathbf{r}}-\omega t)} \\
\mathbf{r} &= \bar{\mathbf{r}} + \mathbf{R}e^{i(\mathbf{k}\cdot\bar{\mathbf{r}}-\omega t)} \\
\rho &= \bar{\rho} + De^{i(\mathbf{k}\cdot\bar{\mathbf{r}}-\omega t)} \\
P &= \bar{P} + c_o^2 De^{i(\mathbf{k}\cdot\bar{\mathbf{r}}-\omega t)} \\
S^{ij} &= \bar{S}^{ij} + T^{ij}e^{i(\mathbf{k}\cdot\bar{\mathbf{r}}-\omega t)}
\end{aligned}
\tag{5.43}
$$

where overbars refer to unperturbed quantities. The components of $\mathbf{V}$ are V_x and V_y. Components of $\mathbf{R}$ are X and Y.

Substituting these expressions into the equations of motion we find,

$$
\begin{aligned}
\bar{\rho}\omega V_x &= k_x(c_o^2 D - T^{xx}) - k_y T^{xy} \\
\bar{\rho}\omega V_y &= k_y(c_o^2 D - T^{yy}) - k_x T^{xy}.
\end{aligned}
\tag{5.44}
$$

The continuity equation is,

$$
D = \frac{\bar{\rho}}{\omega}(k_x V_x + k_y V_y)
\tag{5.45}
$$

and the rate of change of stress becomes,

$$
\begin{aligned}
T^{xx} &= -\frac{2\mu}{3\omega}(2k_x V_x - k_y V_y) \\
T^{yy} &= -\frac{2\mu}{3\omega}(2k_y V_y - k_x V_x) \\
T^{xy} &= -\frac{\mu}{\omega}(k_x V_y + k_y V_x) + \frac{\zeta}{\omega}(k_y V_x - k_x V_y)
\end{aligned}
\tag{5.46}
$$

where,

$$
\zeta = \frac{1}{2}(\bar{S}^{yy} - \bar{S}^{xx}).
\tag{5.47}
$$

Substituting for T^{ij} and D in (5.44) we find,

$$
\begin{aligned}
\bar{\rho}\omega^2 V_x &= V_x k_x^2(\bar{\rho}c_o^2 + \tfrac{4}{3}\mu) + V_x k_y^2(\mu - \zeta) + V_y k_x k_y(\bar{\rho}c_o^2 + \tfrac{1}{3}\mu + \zeta) \\
\bar{\rho}\omega^2 V_y &= V_y k_y^2(\bar{\rho}c_o^2 + \tfrac{4}{3}\mu) + V_y k_x^2(\mu + \zeta) + V_x k_x k_y(\bar{\rho}c_o^2 + \tfrac{1}{3}\mu - \zeta).
\end{aligned}
\tag{5.48}
$$

The solution of these equations leads to a quartic equation for ω,

$$\omega^4 + \Lambda\omega^2 + \Gamma = 0, \tag{5.49}$$

where,

$$\begin{aligned}
\Lambda &= -\frac{1}{\bar{\rho}}\left(\left(\bar{\rho}c_o^2 + \tfrac{4\mu}{3}\right)k^2 + (\mu + \zeta)\,k_x^2 + (\mu - \zeta)\,k_y^2\right) \\
\Gamma &= -\frac{1}{\bar{\rho}^2}\left(\bar{\rho}c_o^2 + \tfrac{4\mu}{3}\right)k^2\left((\mu + \zeta)\,k_x^2 + (\mu - \zeta)\,k_y^2\right).
\end{aligned} \tag{5.50}$$

This can be solved to give a longitudinal mode with frequency

$$\omega^2 = k^2\left(c_o^2 + \frac{4\mu}{3\bar{\rho}}\right) \tag{5.51}$$

and the propagation speed of longitudinal sound waves is given by

$$v_l = \sqrt{c_o^2 + \frac{4\mu}{3\bar{\rho}}}. \tag{5.52}$$

There is also a (nearly) transverse mode with frequency

$$\omega^2 = \frac{\mu k^2}{\bar{\rho}} + \frac{(k_x^2 - k_y^2)(\bar{S}^{yy} - \bar{S}^{xx})}{2\bar{\rho}} \tag{5.53}$$

and components of velocity

$$\frac{V_x}{V_y} = -\frac{k_y}{k_x}\frac{\left(\bar{\rho}c_o^2 + \tfrac{\mu}{3} + \zeta\right)}{\left(\bar{\rho}c_o^2 + \tfrac{\mu}{3} - \zeta\right)}. \tag{5.54}$$

If the initial deviatoric stresses are zero, this reduces to the standard transverse mode, $\nabla \cdot \mathbf{v} = 0$. The differences from the standard transverse mode arise because of the use of rotation terms to retain *objectivity* in the deviatoric stress rates (5.7).

To test that the long wavelength behaviour of the SPH algorithm is correct we simulate the propagation of the longitudinal mode and check its velocity. This was done by placing a Gaussian velocity distribution onto a periodic two dimensional array of particles and measuring the speed of the waves that are produced. In figure 5.2 we show V_x against x at a range of times in the simulation. The initial disturbance was given by $V_x = 0.05e^{((x-100)/20\Delta x)^2}$ the elastic material was $200cm$ long and $20cm$ high with a resolution of 400×40 particles.

We consider cases with $c_o = 1.0$, $\mu = 0.22$ and $\rho_o = 1.0$ for a range of different values of $h/\Delta p$. For these parameters we find the theoretical longitudinal wave
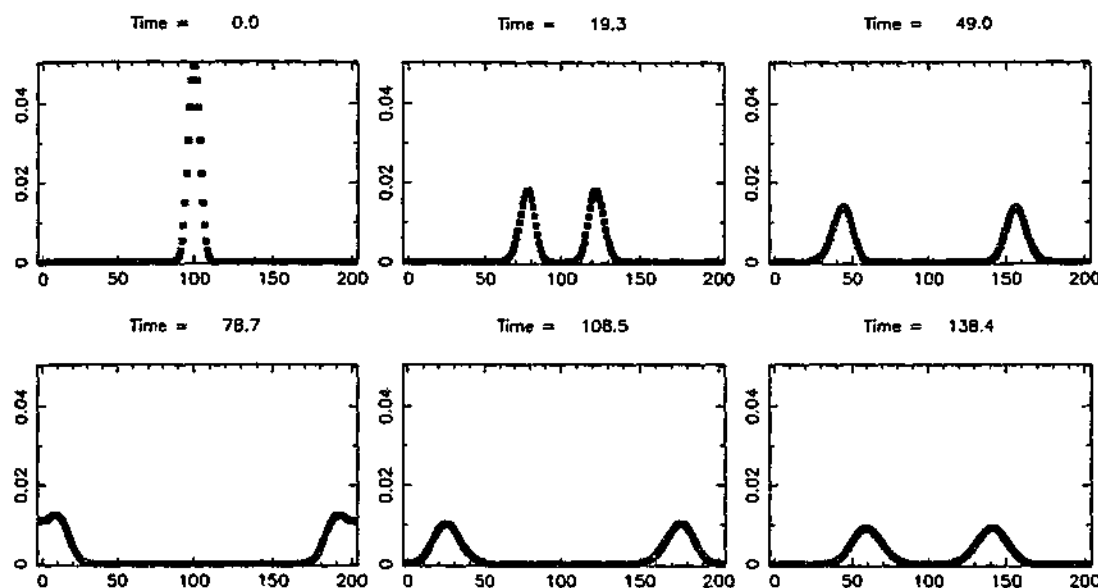
Figure 5.2: *Test of the propagation of longitudinal waves. Frames show the mo-
tions of an initial Gaussian velocity perturbation on a periodic array
of particles with parameters $\epsilon = 0.0$, $\alpha = 0.5$, $\mu = 0.22$, $h/\Delta p = 1.0$,
$\rho_o = 1.0$, $c_o = 1.0$. Further details in the text.*

velocity is, $v_l = 1.137$. The theoretical speed compares well with the measured wave
speeds in the computations of 1.164, 1.148 and 1.131 for the cases $h/\Delta p$ equal to
1.0, 1.3 and 1.5 respectively.

It is clear from figure 5.2 that there is an amount of dissipation and dispersion
as the waves interact. The amplitude of the perturbation decreases by 40% and the
wavelength increases by 40% over the course of the simulation.

5.6.2   SPH Dispersion Relation

In this section we calculate the dispersion relation for the SPH equations. In section
5.6.3 we compare the long wavelength behaviour of this relation to the dispersion
relation of the exact equations. We will also study the short wavelength behaviour
and its stability in section 5.6.5.

We assume the SPH particles are initially placed at the vertices of a regular grid,
for example a grid of square cells each of side Δp. The mass of each particle is then
$\bar{\rho}(\Delta p)^2$. We denote the initial position of particle a by $\bar{r}_a$ and write the perturbed

position as,

$$\mathbf{r}_a = \bar{\mathbf{r}}_a + \mathbf{R}e^{i(\mathbf{k}\cdot\bar{\mathbf{r}}_a - \omega t)}. \tag{5.55}$$

We write the velocity $\hat{\mathbf{v}}_a$ in the form,

$$\hat{\mathbf{v}}_a = \hat{\mathbf{V}}e^{i(\mathbf{k}\cdot\bar{\mathbf{r}}_a - \omega t)} \tag{5.56}$$

and note from XSPH with $\xi = 1/2$ that the relation between the normal velocity $\mathbf{V}$ and the smoothed velocity $\hat{\mathbf{V}}$ is,

$$\hat{\mathbf{V}} = \mathbf{V}\left[1 - \frac{1}{2}(\Delta p)^2 \sum_b (1 - \cos(\mathbf{k}\cdot\mathbf{r}_{ab}))W_{ab}\right]. \tag{5.57}$$

For sufficiently long wavelengths the summation can be replaced by an integral and, in this limit,

$$\hat{\mathbf{V}} = \frac{1}{2}\mathbf{V}(1 + \tilde{W}), \tag{5.58}$$

where $\tilde{W}$ denotes the Fourier transform of W. This expression shows that $\hat{\mathbf{V}}$ introduces additional dispersion coming from the Fourier transform of the kernel. The absence of complex terms show that the XSPH velocity is not dissipative.

All perturbed variables associated with particle a are denoted by a subscript a and they take the same form as those in the continuum case above except that k.r· is replaced by k.$\bar{\mathbf{r}}_a$

It is convenient to begin with the standard SPH equations and include the artificial stress terms later. To simplify the analysis after substituting the perturbation variables into the equations of motion we define the summations,

$$\mathbf{A} = (\Delta p)^2 \sum_b \sin(\mathbf{k}\cdot\mathbf{r}_{ab})\nabla_a W_{ab}$$

$$B_{xx} = (\Delta p)^2 \sum_b (1 - \cos(\mathbf{k}\cdot\mathbf{r}_{ab}))\frac{\partial^2 W_{ab}}{\partial\bar{x}_a^2}$$

$$B_{yy} = (\Delta p)^2 \sum_b (1 - \cos(\mathbf{k}\cdot\mathbf{r}_{ab}))\frac{\partial^2 W_{ab}}{\partial\bar{y}_a^2} \tag{5.59}$$

$$B_{xy} = (\Delta p)^2 \sum_b (1 - \cos(\mathbf{k}\cdot\mathbf{r}_{ab}))\frac{\partial^2 W_{ab}}{\partial\bar{x}_a\partial\bar{y}_a}$$

$$\beta = \xi(\Delta p)^2 \sum_b (1 - \cos(\mathbf{k}\cdot\mathbf{r}_{ab}))W_{ab}.$$

The x component of the acceleration equation becomes,

$$\omega V_x = -2\frac{\bar{P} - \bar{S}^{xx} - \bar{\rho}c_o^2}{\bar{\rho}\omega}(\hat{\mathbf{V}} \cdot \mathbf{A})A_x + 2\frac{\bar{P} - \bar{S}^{xx}}{\bar{\rho}\omega}(B_{xx}\hat{V}_x + B_{xy}\hat{V}_y)$$

$$-\frac{(\Delta p)^2}{\bar{\rho}}(T^{xx}A_x - T^{xy}A_y). \tag{5.60}$$

The equation for the y component is identical except for an interchange of x and y.

Substituting the perturbations into the equations for the rate of change of stress components we find,

$$T^{xx} = -\frac{2\mu}{3\bar{\omega}}(2\hat{V}_x A_x - \hat{V}_y A_y)$$

$$T^{yy} = -\frac{2\mu}{3\bar{\omega}}(2\hat{V}_y A_y - \hat{V}_x A_x) \tag{5.61}$$

$$T^{xy} = -\frac{\mu}{\bar{\omega}}(\hat{V}_x A_y + \hat{V}_y A_x) + \frac{\zeta}{\omega}(\hat{V}_x A_y - \hat{V}_y A_x).$$

Substituting the stress components, replacing $\hat{\mathbf{V}}$ by $\mathbf{V}$ and taking note of β (5.57) in the acceleration equation we find,

$$\frac{\omega^2 \bar{\rho} V_x}{1 - \beta} = -(2(\bar{P} - \bar{S}^{xx}) - \bar{\rho}c_o^2)A_x(\mathbf{A} \cdot \mathbf{V}) + (2\bar{P} - 2\bar{S}^{xx})(B_{xx}V_x + B_{xy}V_y)$$

$$+ \frac{2\mu}{3}(2V_x A_x - V_y A_y)A_x + \mu(V_x A_y + V_y A_x)A_y - \zeta(V_x A_y - V_y A_x)A_y. \tag{5.62}$$

5.6.3 Long Wavelength Limit

For sufficiently long wave lengths we can approximate the summations defining $\mathbf{A}$ and B_{ij} by integrals. We solve the integrals using an integration by parts and find,

$$\begin{aligned}
\mathbf{A} &= -\mathbf{k}\tilde{W} \\
B_{ij} &= k_i k_j \tilde{W} \\
\beta &= \xi(1 - \tilde{W})
\end{aligned} \tag{5.63}$$

where $\tilde{W}$ is the Fourier transform of W which, in the long wave approximation, can be taken as being equal to one. Correspondingly, we can take β as zero and the x component of acceleration becomes,

$$\bar{\rho}\omega^2 V_x = V_x k_x^2(\bar{\rho}c_o^2 + \frac{4}{3}\mu) + V_x k_y^2(\mu - \zeta) + V_y(c_o^2 + \frac{1}{3}\mu + \zeta))k_x k_y \tag{5.64}$$

Which agrees with the continuum equation for the dispersion relation of the exact equations (5.44). This result shows that the SPH perturbation equations are correct in the longwavelength limit and that the dispersion introduced by the SPH formulation can be determined from the Fourier transform of the kernel.

5.6.4   The Artificial Stress

In the present analysis, where the axes have been chosen so that the stress tensor is diagonal, we only need to add a term $(R_a^{xx} + R_b^{xx})f^n$ to the x component of the acceleration and a term $(R_a^{yy} + R_b^{yy})f^n$ to the y component. In general, however, there is a term R_{ab}^{xy} after rotating from the local principal axes to the original axes. Since the initial state is uniform we take,

$$R_a^{xx} = R_b^{xx} = R^{xx} \tag{5.65}$$

so that $R_a^{xx} + R_b^{xx} = 2R^{xx}$, and similarly $R_a^{yy} + R_b^{yy} = 2R^{yy}$.

The right hand side of the x component of the SPH acceleration equation includes a term from the artificial stress,

$$2\bar{\rho}R^{xx}(XF_{xx} + YF_{xy}), \tag{5.66}$$

where,

$$
\begin{aligned}
F_{xx} &= \frac{(\Delta p)^2}{(n+1)W^n(\Delta p)} \sum_b (1 - \cos(\mathbf{k} \cdot \mathbf{r}_{ab})) \frac{\partial^2 W}{\partial x_a^2}^{n+1} \\
F_{yy} &= \frac{(\Delta p)^2}{(n+1)W^n(\Delta p)} \sum_b (1 - \cos(\mathbf{k} \cdot \mathbf{r}_{ab})) \frac{\partial^2 W}{\partial y_a^2}^{n+1} \\
F_{xy} &= \frac{(\Delta p)^2}{(n+1)W^n(\Delta p)} \sum_b (1 - \cos(\mathbf{k} \cdot \mathbf{r}_{ab})) \frac{\partial^2 W}{\partial x_a \partial y_a}^{n+1}.
\end{aligned}
\tag{5.67}
$$

From the velocity equation (2.22) we can show $X = iV_x/\omega$ so that (5.66) becomes,

$$\frac{2i\bar{\rho}R^{xx}}{\omega^2}(\hat{V}_x F_{xx} + \hat{V}_y F_{xy}). \tag{5.68}$$

The dispersion relation (5.62) is now,

$$\frac{\omega^2 \bar{\rho} V_x}{1-\beta} = -\left(2(\bar{P} - \bar{S}^{xx}) - \bar{\rho} c_o^2\right) A_x (\mathbf{A} \cdot \mathbf{V}) + (2\bar{P} - 2\bar{S}^{xx})(B_{xx} V_x + B_{xy} V_y)$$

$$+ \frac{2\mu}{3}(2V_x A_x - V_y A_y)A_x + \mu(V_x A_y + V_y A_x)A_y \tag{5.69}$$

$$- \zeta(V_x A_y - V_y A_x)A_y + 2\bar{\rho}^2 R^{xx}(\hat{V}_x F_{xx} + \hat{V}_y F_{xy}).$$

We now consider how to chose R^{ij} to prevent short wavelength instabilities.

5.6.5   Short Wavelength Limit

The tensile instability is a short wave length instability initiated by the clumping of pairs of particles. The rate of growth of the instability depends on the initial configuration of particles, kernel, smoothing length, and equation of state. See Morris (1996) for the non elastic case. In this section we study the stability of some simple particle configurations.

In the first case particles are placed on the vertices of a grid of square cells of side Δp. The second and third cases involve what we term *face centred* lattices. These *face centred* lattices have a similar configuration to the square cells except that every second row of particles is shifted by a distance $\Delta p/2$ in the x direction, to form an x shifted *face centred* lattice. A slight variation is to form the y shifted *face centred* lattice by shifting alternate columns of particles in the y direction. These lattices are illustrated in figure 5.3.

In each case we consider waves propagating along the x axis with $k_x = \pi/\Delta p$, $k_y = 0$. The dangerous modes are the longitudinal modes with $V_x \neq 0$ and $V_y = 0$ since clumping occurs if these modes are unstable. The transverse modes with $V_x = 0$ and $V_y \neq 0$ are benign because, if they become unstable, they result in lines of particles moving vertically very slowly (Morris 1996).

Square Cells   In the square lattice case we find A_x, A_y, B_{xy} and F_{xy} are all equal to zero. The equations of motion simplify to,

$$\begin{aligned}
\frac{\bar{\rho}\omega^2 V_x}{1-\beta} &= 2(V_x B_{xx}(\bar{P} - \bar{S}^{xx}) - V_x R^{xx}\bar{\rho}^2 F_{xx}) \\
\frac{\bar{\rho}\omega^2 V_y}{1-\beta} &= 2(V_y B_{yy}(\bar{P} - \bar{S}^{xx}) - V_y R^{yy}\bar{\rho}^2 F_{yy}).
\end{aligned} \tag{5.70}$$
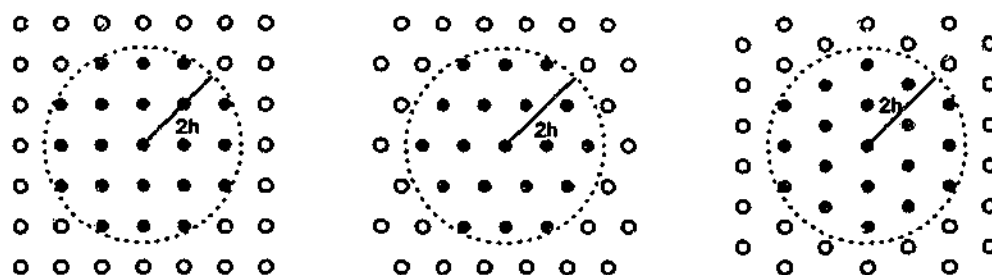
Figure 5.3:   *Particles within the 2h smoothing distance for various initial par-*
ticle placements. The left frame shows the square cell arrangement.
The middle frame shows the case where a face centred arrangement
obtained by shifting every second row of particles a distance $\Delta p/2$ in
the x direction. The frame on the right shows the particles within the
2h smoothing distance in the case where a face centred arrangement is
obtained by shifting every second column of particles a distance $\Delta p/2$
in the y direction.

The first equation in (5.70) specifies the longitudinal mode with $V_x \neq 0$ and frequency given by,

$$\frac{\bar{\rho}\omega^2}{1-\beta} = 2(B_{xx}(\bar{P} - \bar{S}^{xx}) - R^{xx}\bar{\rho}^2 F_{xx}). \tag{5.71}$$

We now calculate the coefficients in the case $h = \Delta p$ and $k_x = \pi/\Delta p$, $k_y = 0$.

$$
\begin{aligned}
B_{xx} &= \frac{30}{7\pi(\Delta p)^2}(10 - 5\sqrt{2}) \\
B_{yy} &= \frac{30}{7\pi(\Delta p)^2}(7 - 5\sqrt{2}) \\
F_{xx} &= \frac{30}{7\pi(\Delta p)^2}(3n + 2) \\
\beta &= \frac{10}{7\pi}\left(1 + 2(2 - \sqrt{2})^3\right)
\end{aligned}
\tag{5.72}
$$

We consider this case as the coefficients are simplified by the fact that only the eight nearest neighbours contribute. The tensile instability involves short wavelength particle clumping, so we chose $k_x = \pi/\Delta p$ to study changes over short wavelengths and $k_y = 0$ so that the analysis is simplified. In any case coefficients for higher values of $h/\Delta p$ are tabulated in appendix B and discussed later in the present section.

Complex values of ω are unstable so for stability we wish to find values of ω^2 which are positive. As Both B_{xx} and $(1 - \beta)$ are positive, the longitudinal mode is stable for $\bar{\sigma}^{xx} < 0$ (recall that $\bar{\sigma}^{xx} = -\bar{P} + \bar{S}^{xx}$) which corresponds to the material

being compressed. Hence if $\bar{\sigma}^{xx} < 0$ we can chose $R^{xx} = 0$ and the system will be stable. If $\bar{\sigma}^{xx} > 0$, the system is in tension and the longitudinal mode is unstable unless we chose,

$$R^{xx} < -\frac{B_{xx}|\bar{P} - \tilde{S}^{xx}|}{F_{xx}\bar{\rho}^2}. \tag{5.73}$$

Which corresponds to,

$$R^{xx} < -\frac{3}{3n+2}\frac{|\bar{P} - \bar{S}^{xx}|}{\bar{\rho}^2}. \tag{5.74}$$

This result agrees in the limit of no deviatoric stress ($\bar{S}^{xx} = 0$), with the results obtained by Monaghan (2000). The limit of no deviatoric stress is the standard SPH for gas dynamics. It is possible to minimise the error in the long wave length dispersion relation due to the artificial stress by taking into account the way F_{xx} varies with n. It is found that for $1 < h/\Delta p < 1.5$ the optimal choice of n has only a slight dependence on h. In the following examples we take $n = 4$ as a suitable value.

Taking $n = 4$ the variation of B_{xx} and F_{xx} with $h/\Delta p$ is shown in the left frame of figure 5.4. The stability criteria is illustrated in the right frame of figure 5.4, the longitudinal mode is stable in compression for positive values of $(1 - \beta)B_{xx}/F_{xx}$. A steady decrease in the coefficient required for stability (when the system is in tension) is clearly seen as smoothing length is increased. The system remains stable up until $h/\Delta p = 1.7$ where it briefly becomes slightly unstable before again becoming stable for higher $h/\Delta p$.

The second equation in (5.70) describes the transverse mode for the case of particles placed on a square cell with $V_y \neq 0$ and frequency found from,

$$\frac{\bar{\rho}\omega^2 V_y}{1 - \beta} = 2(B_{yy}(\bar{P} - \bar{S}^{xx}) - R^{yy}\bar{\rho}^2 F_{yy}). \tag{5.75}$$

When $h = \Delta p$, B_{yy} is negative (figure 5.5) and the mode is unstable when $\sigma^{yy} < 0$ if R^{yy} is zero. This instability causes lines of particles to move in the y direction rather than clump. The effect is generally weak as the particles move slowly to the more stable *face centred* array. The stability of this transverse mode changes as the smoothing length is increased. It becomes stable when $h = 1.2\Delta p$ and unstable
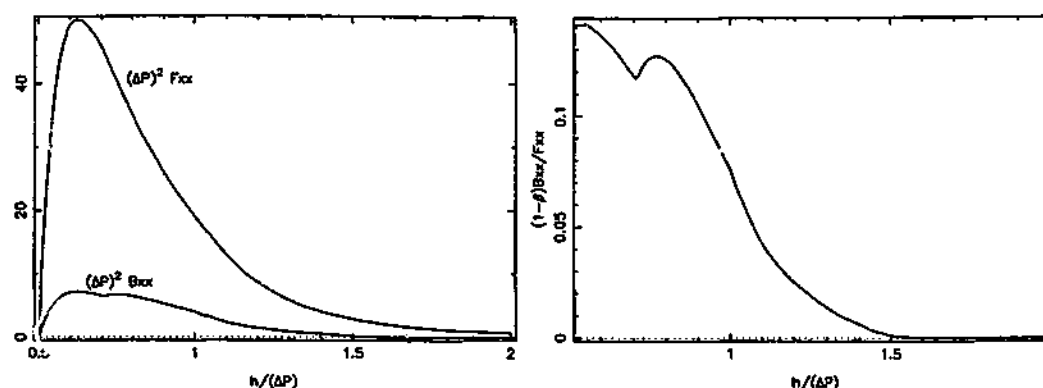
Figure 5.4: Left Frame shows the square cell variations of B_{xx} and F_{xx} with smoothing length. The right frame shows the criterion for stability of the longitudinal mode. The mode will be stable in compression for positive $(1-\beta)B_{xx}/F_{xx}$.

again at $h = 1.0\Delta p$. We do not look for a value of R^{yy} which will stabilise this mode as it doesn't lead to clumping and we instead chose R^{yy} to stabilise the longitudinal mode travelling in the y direction which can lead to the tensile instability.
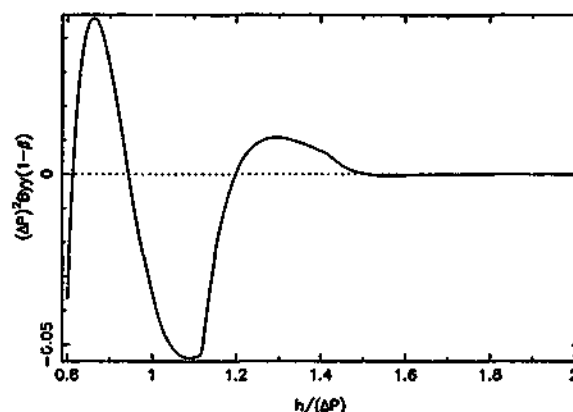
Figure 5.5: Stability of the transverse mode for a square cell particle arrangement.

Swegle, Hicks, and Attaway (1995) looked at the stability properties of SPH by studying a square two dimensional array with fixed particle boundaries to stop wave propagation relieving the initial stress. We now look at similar examples although we incorporate periodic boundary conditions instead of fixed boundaries.

In figure 5.6 we see what happens to a group of particles in compression. Here

we expect the simulation to be stable with no clumping due to the tensile instability. In the left frame we show our initial set up. A $1cm$ square grid where each of the particles have been given a small random velocity. The second frame shows what happens in the case of $h = 1.0\Delta p$, the initial particle velocities settle down before the particles arrange themselves by shifting every second column half a particle spacing vertically to the stable *face centered* arrangement. The final frame shows the motions for the case of $h = 1.5\Delta p$, the final configuration here is much more complicated that the $h = 1.0\Delta p$ case, though it is still stable.
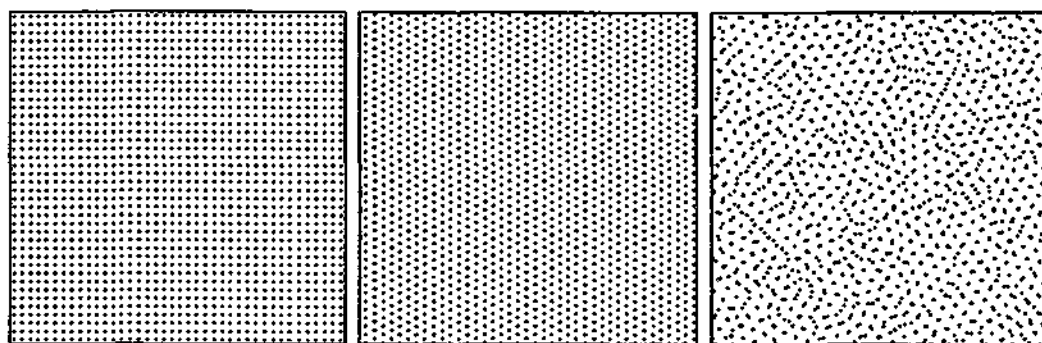
Figure 5.6: *Periodic box of particles in compression $\mu = 0.22, \Delta p = 0.025$, $\epsilon = 0$, $\rho = 1.1\rho_o$. The left frame shows the initial square cell set up. The middle frame shows the particle positions after $10,000$ time steps at $t = 100.1$, for $h = \Delta p$. The right frame shows the particle positions after $10,000$ timesteps at $t = 149.8$, for the case of $h = 1.5\Delta p$.*

We now look at the stability of initially *face centred* arrays. As mentioned earlier these arrays are formed by the displacement of alternate rows by an amount $\Delta p/2$. In the real case where there are waves propagating in both x and y directions the difference is unimportant, however in this analysis we only have waves propagating in the x direction and the results are slightly dependent on the direction of the shift.

Face Centred Cells: y direction shift In this case we again find A_x and A_y equal to zero and the stability criteria is similar to the square cell case. The longitudinal mode is stable in compression and still requires the implementation of an artificial stress for stability in tension.

The stability of the transverse mode oscillates as in the square cell case. However, the move to a *face centred* array means that the transverse mode is now stable in

the $h = \Delta p$ case. This explains why the initially square cell array arranges itself into a stable *face centred* array (figure 5.6).

Face Centred Cells: x direction shift The stability criteria in this case are complicated by the fact that A_x now has a non zero value. The frequency of the longitudinal mode is now described by,

$$\omega^2 = \frac{2(1-\beta)}{\bar{\rho}} \left((B_{xx} - A_x^2)(\bar{P} - \bar{S}^{xx}) + A_x^2 \left(\frac{4}{3}\mu + \bar{\rho}c_o^2 \right) - \bar{\rho}R^{xx}F_{xx} \right). \quad (5.76)$$

As the term $A_x^2 \left(\frac{4}{3}\mu + \bar{\rho}c_o^2 \right)$ is always positive, its contribution is to stabilise the system. The first frame of figure 5.7 shows the weight of the first two terms in (5.76) for a range of smoothing lengths. From figure 5.7 it is clear that for $h < 1.3\Delta p$ the $(\bar{P} - \bar{S}^{xx})$ term will dominate and the stability properties of the longitudinal mode are almost identical to the case of square cells (compare figures 5.7 and 5.4). For larger smoothing lengths the $\frac{4}{3}\mu + \bar{\rho}c_o^2$ term becomes important though the system still retains stability.
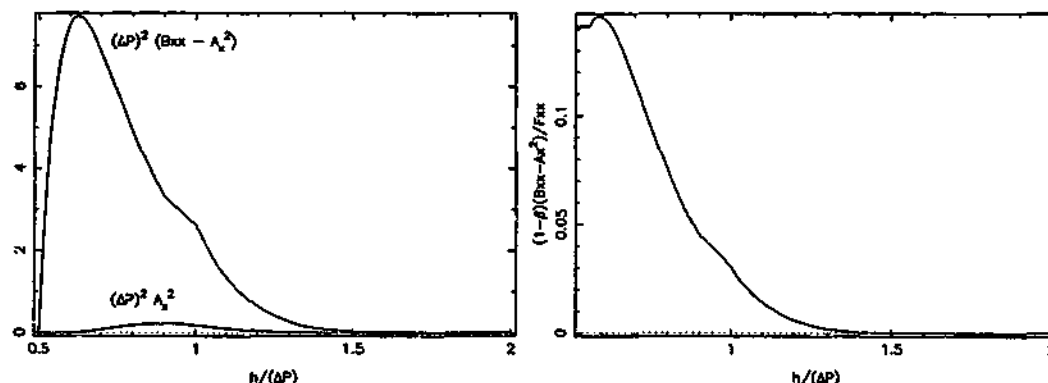
Figure 5.7: *Stability of the x shifted longitudinal mode. Left frame shows the variation of $(\Delta p)^2(B_{xx} - A_x^2)$ and $(\Delta p)^2 A_x^2$ with smoothing length. The right frame shows the stability criterion for the longitudinal mode. Particles will be stable in compression for positive $(1 - \beta)(B_{xx} - A_x^2)/F_{xx}$.*

In this case the transverse mode is described by,

$$\omega^2 = 2\frac{(1-\beta)}{\bar{\rho}}B_{yy}(\bar{P} - \bar{S}^{yy}) + A_x^2(\mu + \zeta). \quad (5.77)$$

For the $h = \Delta p$ case we have $B_{yy} \simeq 5A_x^2$. We find that the transverse mode is stable in compression for both the x and y shifted *face centred* cell cases.

5.6.6   Effect of Artificial Stress in Tension

In this section we study the effects of the tensile instability on a periodic array of particles by initially placing the array particles in a tensile state. Similar calculations have been performed by Swegle, Hicks, and Attaway (1995) and Monaghan (2000) though not on periodic arrays. Particles are given an initial negative pressure by modifying the equation of state (5.11) to,

$$P = \rho_o c_s^2 \left(\frac{\lambda \rho}{\rho_o} - 1 \right). \tag{5.78}$$

The parameter λ is given values of 0.99, 0.95 and 0.90 to simulate different magnitudes of tensile stress. In the following calculations we take $\rho_o = c_s = 1$.

Our first example (figure 5.8) is the case where $\lambda = 0.99$. We show the initial particle set up followed by the particle positions after $10,000$ steps with $\epsilon = 0.0$ and $\epsilon = 0.3$ in the left, middle and right frames respectively. We notice little difference between all three frames. The tensile instability is having minimal effect at this low stress, and the artificial stress terms do not degrade the calculation.
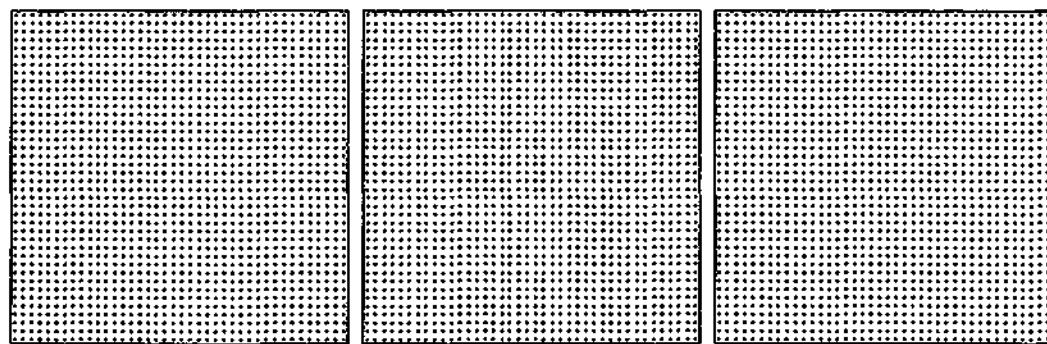
Figure 5.8:   *Periodic array of particles under a small tensile stress, parameters $\lambda = 0.99$, $h/\Delta p = 1.0$ and $\Delta p = 0.025$. The left hand frame shows the initial state. The middle frame shows particle positions after $10,000$ steps when $\epsilon = 0.0$, clumping effects of the tensile instability are not obvious. The right hand frame shows the calculation with epsilon $= 0.3$ at step $10,000$ and is similar to the initial state.*

In figure 5.9 we increase the tensile stress by setting $\lambda = 0.95$. We find that the tensile instability has led to particles beginning to clump together in groups of four in the middle frame where $\epsilon = 0.0$. This particle clumping does not lead to artificial fracturing in this case. We see in the right hand side frame that the inclusion of the artificial stress terms ($\epsilon = 0.3$) in the calculation has resulted in the removal of particle clumping from the simulation, and the particles do not move from the initial square cell state.
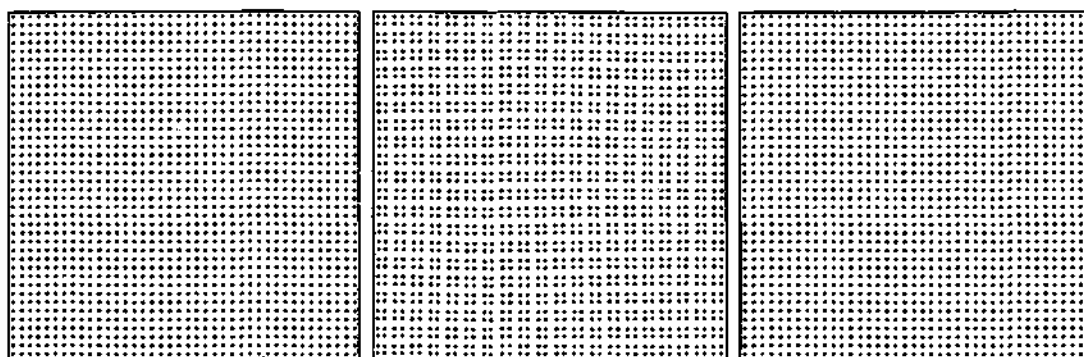
Figure 5.9: Periodic array with parameters and frames as for figure 5.8 except that now $\lambda = 0.95$. The middle frame illustrates the particle clumping which occurs due to the tensile instability. The clumping effects have been stabilised in the right frame which is a calculation with $\epsilon = 0.3$.
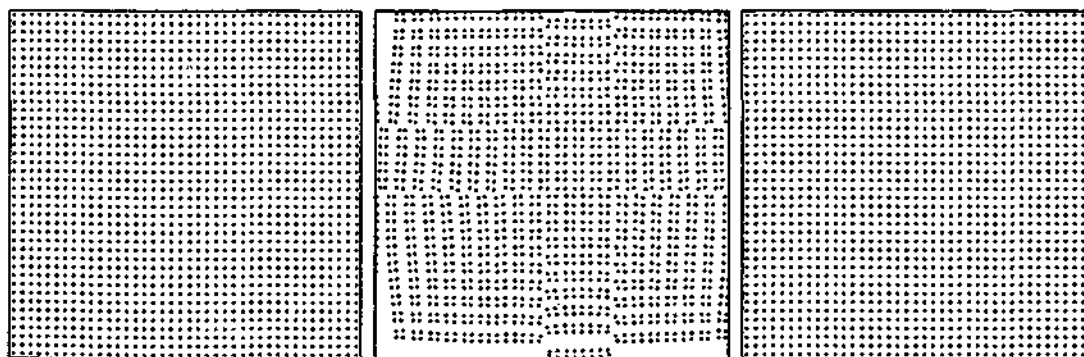
Figure 5.10: Periodic array with parameters and frames as for figure 5.10 except in the case of $\lambda = 0.9$. The tensile instability leads to numerical fracturing (middle frame). The use of artificial stress terms, $\epsilon = 0.3$ (right frame) remove the effects of the tensile instability.

The final example in this section has a much larger tensile stress ($\lambda = 0.9$) and does lead to numerical fracturing at the bottom and left boundaries of our periodic particle array as can be seen in the middle frame of figure 5.10. We again find that effects of the tensile instability can be removed by setting $\epsilon = 0.3$, which leads to the initial particle positions being retained.

In this chapter we have outlined an extension of our free surface fluid dynamics SPH code which enables the modelling of elastic, plastic and brittle materials. The SPH tensile instability has been discussed along with a method which appears to be effective in removing this instability. An analysis of the stability of the solid body SPH method has been conducted and simple calculations on periodic arrays have been presented to illustrate the effects of short wavelength instabilities.

Chapter 6

Solid Body Code Validation

ow we turn our attention to some more practical test problem for elastic materials. Some of these tests have been performed by other authors and as such are good tests cases for our SPH code. We firstly look at the problem of colliding balls, this problem was shown by Swegle (1992) to fail when using SPH due to the tensile instability. We then study the behaviour of oscillating beams, comparing to theory. We look at beams in tension, and then incorporate a damage model to study the brittle fracture of beams in tension. The tests with the damage model are similar to those presented by Benz and Asphaug (1995) although our beams are only two dimensional. Finally we turn our attention to the modelling of stresses around cavities.

6.1 Colliding Balls

Swegle (1992) ran into problems when using SPH to model the collision of two tennis balls. The calculations which we present are two dimensional the balls are really cylinders, though we will refer to them as balls or rings. Physically we expect that the collision of two balls will involve a contraction as the balls slow down before rebounding off each other and travelling in the opposite direction. Finite difference codes are able to model this without difficulty. Swegle (1992) found that effects of the tensile instability when SPH was used to model the collision meant that artificial fracturing of the materials occurred in regions that were in tension. A range of particle configurations and viscosities were tried but the standard SPH was unable to model the collision satisfactorily. Monaghan (2000) simulated the rings with a similar algorithm to prevent the tensile instability as the algorithm described in section 5.3 although he did not rotate to the axes of principal stress before applying the artificial stress.

Vignjevic, Campbell, and Libersky (2000) overcome the problem of tensile in-

stability by using a stress point approach and are able to successfully model the colliding rings. Sulsky, Zhou, and Schreyer (1995) were able to model the collision of a cylinder with a rigid wall using the FLIP technique.

We model the balls as two rings of particles on a square grid. Each of the rings has an inner radius of $3cm$ and an outer radius of $4cm$. They approach each other with a velocity of $50m/s$ which corresponds to a speed of 5.87×10^{-3} in our scaled units. We take $\mu = 0.22$, and the resolution is given by $\Delta p = 0.1$. All calculations in this chapter use the smoothing length $h = 1.5\Delta p$.

In the following pictures (and most pictures in this chapter) the colours refer to the mean stress $(\sigma^{xx} + \sigma^{yy})$ and times are presented in the dimensionless coordinates of section 5.4. It can be shown from linear algebra that the trace (sum of the diagonal elements) of a tensor is invariant to axes rotation. We define the mean stress to be the trace of the stress tensor. The invariance of the mean stress to axis rotation makes it a suitable measure of the stress field.

In figure 6.1 we show the results for when $\epsilon = 0.0$. This is standard SPH without the fix for the tensile instability and we find that artificial fragmentation occurs in regions of tension as the stresses become too large in the collision. The fracturing means that the rings are unable to return their elastic energy back into kinetic energy and the rings do not bounce off each other.

Figure 6.2 shows the rings for the case $\epsilon = 0.3$. Artificial fracturing that occurs due to the tensile instability in the standard SPH case has now been removed. We are able to model the collision, interaction and bounce of the rings without difficulty.

Figure 6.3 shows the rings in the case of zero viscosity. The simulation works reasonably until the cylinders begin to rebound off each other, particles begin to penetrate each other and the simulation becomes extremely disordered and unstable.

Figure 6.4 shows the rings in a format similar to that found in Swegle (1992), Sulsky et al. (1995) and Vignjevic, Campbell, and Libersky (2000). The frames shown are the time of impact and then intervals of approximately $500\mu s$. The colours in figure 6.4 refer to the horizontal particle velocity, so that the results presented are consistent with other authors.

In tables 6.1 and 6.2 we show measurements for the width, height and separation of the elastic rings for our SPH results and the TOODY finite difference results of Swegle (1992) respectively. The results are in excellent agreement for the collision before the rings change direction and begin their bounce ($\sim 500\mu s$). The bounce

Time	Width	Height	Separation
0	8.0	8.0	0.0
507	5.1	9.8	0.0
994	5.8	9.7	0.0
1498	8.0	8.2	0.3
1811	9.2	6.8	1.4

Table 6.1: SPH results for colliding rings. Values of ring width, height and separation in cm at various times in μs. Distances are measured in cm, time is measured in μs.

Time	Width	Height	Separation
0	8.0	8.0	0.0
500	5.1	9.9	0.0
1000	6.4	9.9	0.0
1500	7.2	8.7	1.4

Table 6.2: TOODY results of Swegle (1992) for colliding rings. Values of ring width, height and separation at various times. Distances are measured in cm, time is measured in μs.

occurs quicker in the finite difference calculation. At $1000\mu s$ the qualitative shape is like a D with a flat interface between the balls and *pointed* ends on the opposing sides, the shape is similar for both methods although the width has expanded quicker for the TOODY results. The separation at $1500\mu s$ is greater in the TOODY results $(1.4cm)$ than the SPH results $(0.3cm)$. In both cases the rings are egg shaped although the sharpest point of the egg points inwards in the SPH case and outwards for the TOODY case. In both the SPH and TOODY codes the rings oscillate after the bounce, the difference in direction of the pointed end of the rings are due to the phase of oscillation being different in each of the cases. The SPH case reaches a separation of $1.4cm$ at $t = 1811\mu s$ and the ovals are in the same direction at this point although the width of the rings at this separation is greater in the SPH case.

The SPH calculation is able to follow the collision of rubber rings without difficulty. There are differences in the results when compared to the TOODY results of Swegle (1992), the rings take longer to rebound off each other in the SPH case.
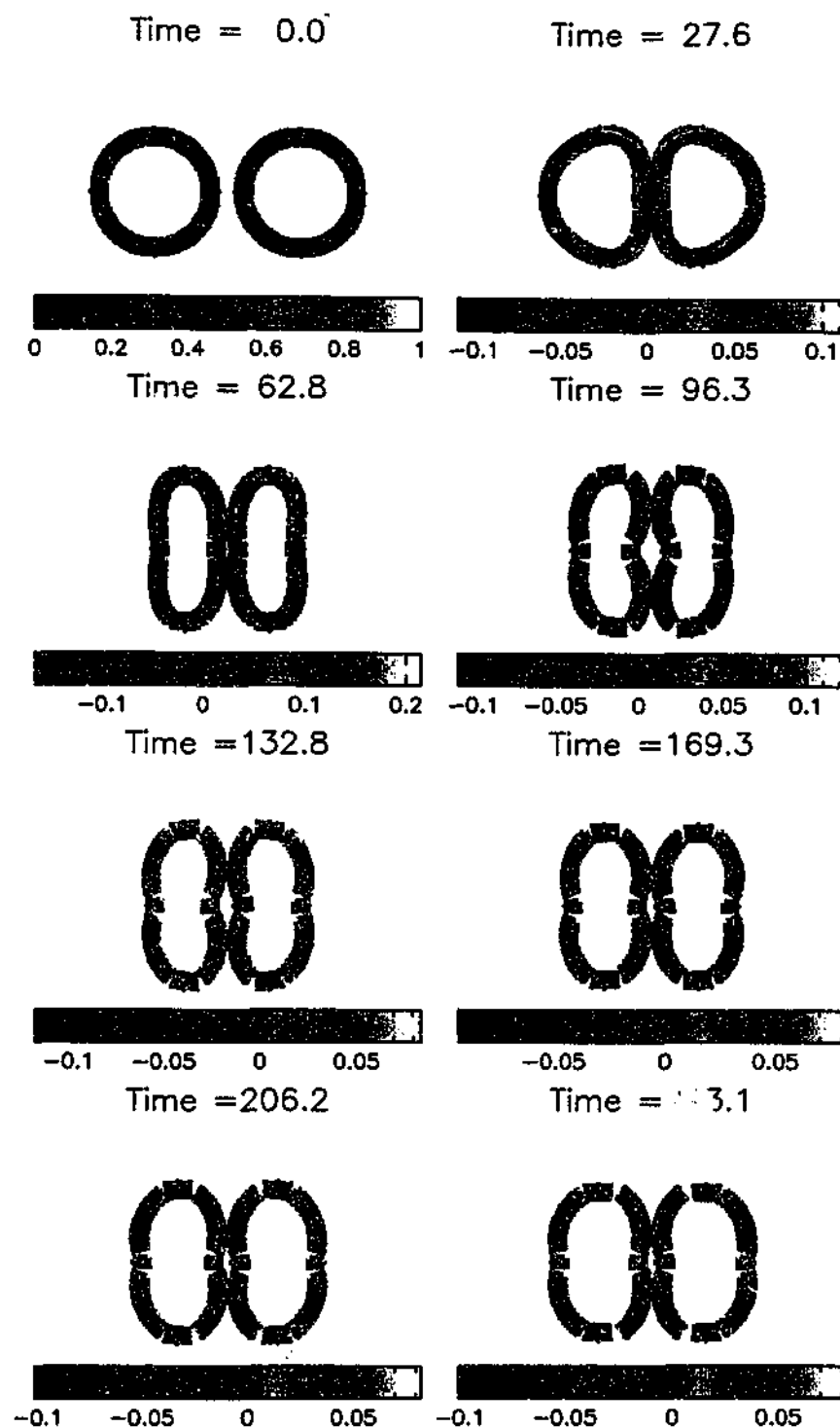
Figure 6.1: *Colliding rings. Standard SPH ($\epsilon = 0.0$) with artificial viscosity ($\alpha = 0.5$) in which artificial fracturing occurs.*
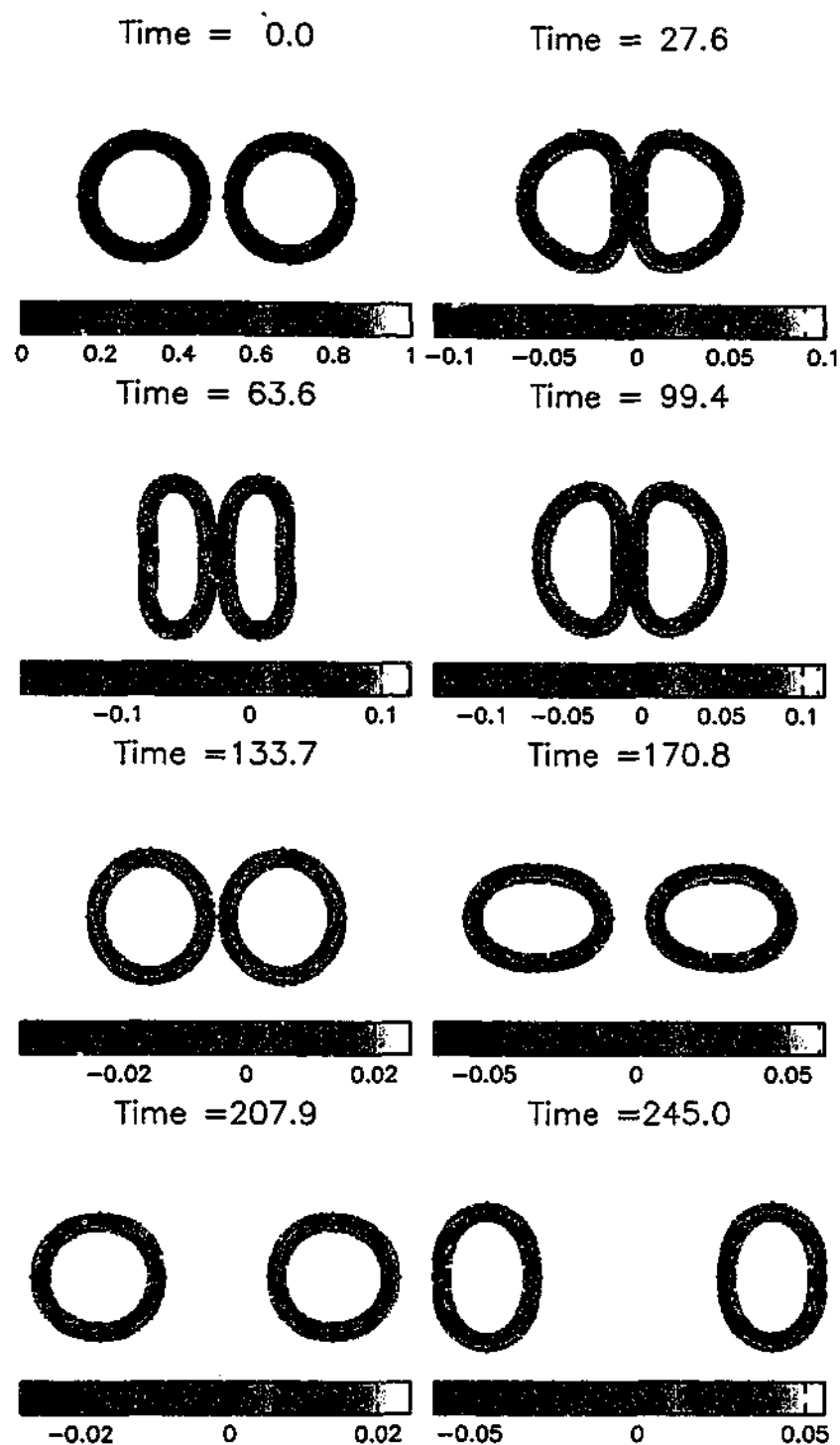
Figure 6.2:   Colliding rings.   SPH with artificial stress ($\epsilon = 0.3$) and artificial viscosity ($\alpha = 0.5$) which simulates the collision without fracturing.
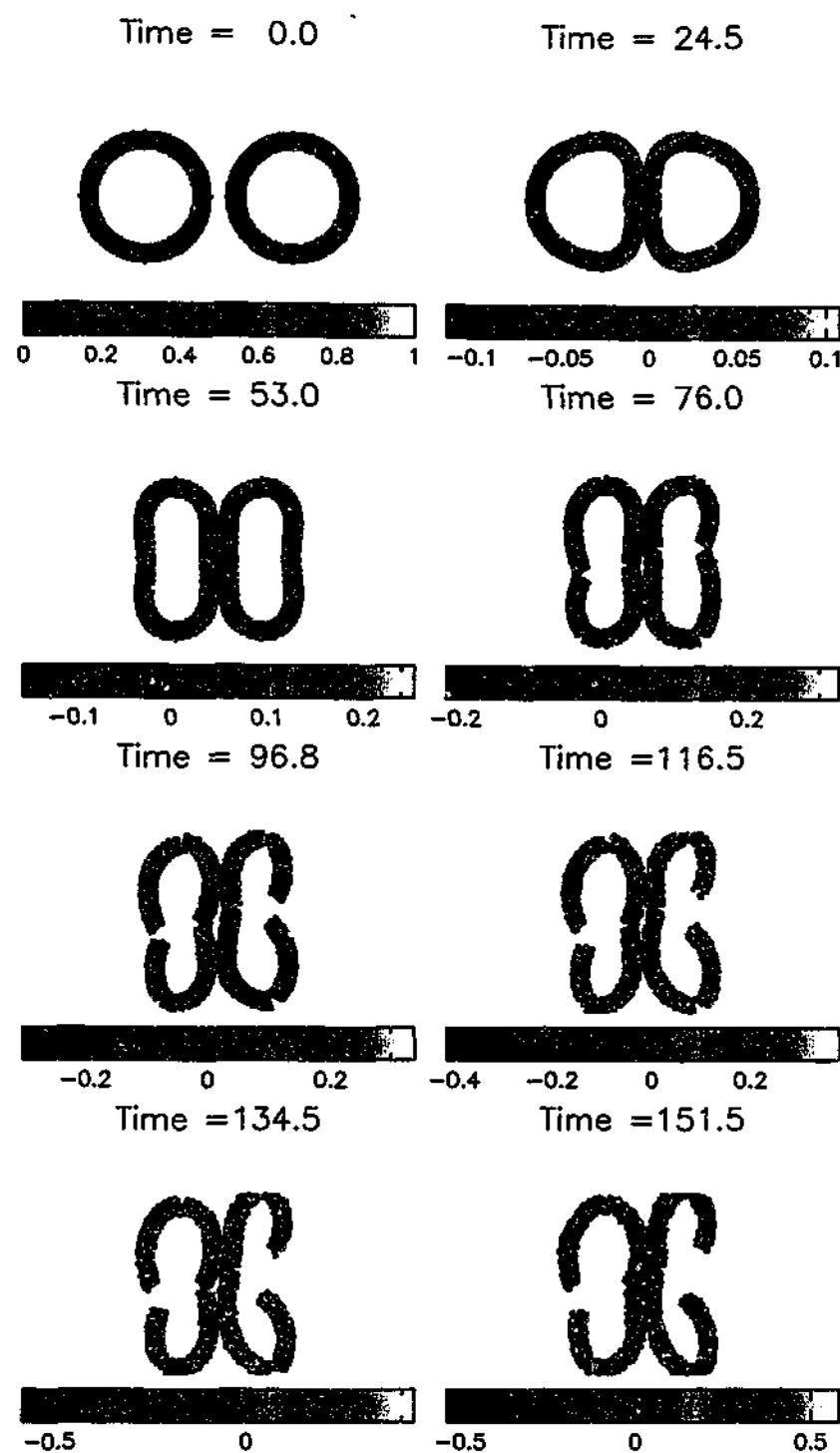
Figure 6.3: Colliding rings. SPH with artificial stress ($\epsilon = 0.3$) but without artificial viscosity ($\alpha = 0.0$).
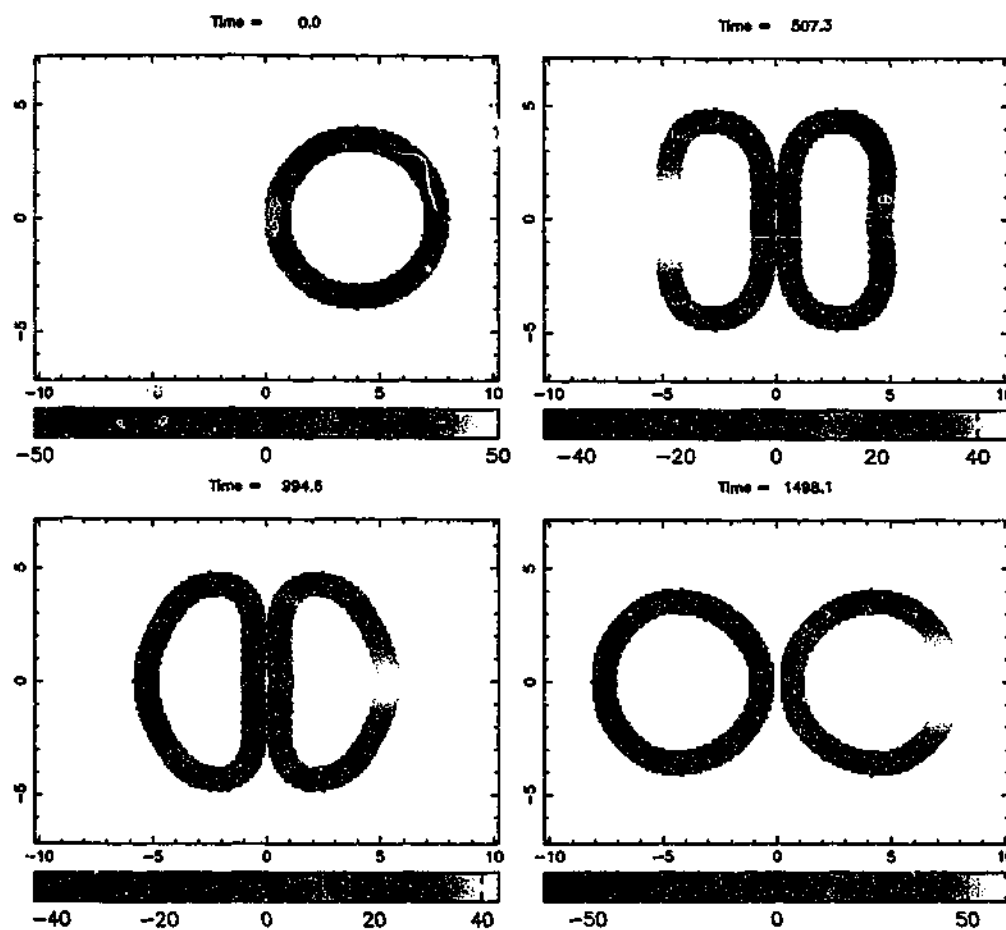
Figure 6.4: *Colliding rings. SPH with artificial stress ($\epsilon = 0.3$). Colours show horizontal velocity. Speeds in m/s, distances in cm, time in μs. The balls are touching at $t = 0$.*

6.2   Bending of a Plate

The next test we undertake is to check the period of the lateral oscillations of a fixed-free plate. We choose this problem as an analytic solution exists and we are able to study the shape and dynamics of the oscillation of the beam in detail. An analytic solution is known from the Euler-Bernoulli thin beam theory and can be found in standard engineering texts, see for example Rao (1990) (pg.394-400), Landau and Lifshitz (1970) (pg.46-51).

It can be shown that the natural frequency of a plate is given by,

$$\omega^2 = \frac{Eh^2\beta^4}{12\rho(1-\nu^2)}. \tag{6.1}$$

Young's modulus is related to the shear modulus by,

$$E = 2\mu(1+\nu), \tag{6.2}$$

so that

$$\omega^2 = \frac{\mu h^2 \beta^4}{6\rho(1-\nu)}, \tag{6.3}$$

where, μ is the shear modulus and $\nu = (3\kappa - 2\mu)/(6\kappa + 2\mu)$ is Poisson's ratio. The height and length of the plate are given by h and L respectively. The parameter β depends on the mode of oscillation.

The assumptions made in arriving at the solution are that the thickness of the plate is thin compared to its length and breadth, and also that the deformations of the plate are small. As our calculations are two dimensional the assumption for the breadth always holds. Further assumptions are that the stresses involving the z direction (σ^{xz}, σ^{yz}, σ^{zz}) are equal to zero.

Boundary conditions on the beam are that the displacement and gradient of the beam are zero at the fixed end. A zero gradient corresponds to the beam remaining horizontal.

For a fixed free-beam β is determined from the equation,

$$\cos(\beta L)\cosh(\beta L) = -1. \tag{6.4}$$

For the fundamental mode,

$$\beta = \frac{1.875}{L}. \tag{6.5}$$

For our simulations we take two beams $28cm$ long, one with a thickness of $1cm$ and the other of thickness $2cm$. As the analytic solution assumes the plate to be thin, we take two different thicknesses to assess the validity of this assumption. We fix the end $8cm$ of the beam two sets of particles which are fixed and do not move. This ensures the boundary conditions for the analytic solution of no deflection, and zero gradient at the fixed end are met.

We then apply a shear force to the beam by setting the velocity to each particle dependent on its horizontal position along the beam. This force sets the beam in oscillation. The initial velocity of a particle at position x is given by,

$$V(x) = \frac{V_f}{2} \frac{(\sin \beta L + \sinh \beta L)(\cos \beta x - \cosh \beta x)}{\cos \beta L \sinh \beta L - \sin \beta L \cosh \beta L}$$
$$- \frac{V_f}{2} \frac{(\cos \beta L + \cosh \beta L)(\sin \beta x - \sinh \beta x)}{\cos \beta L \sinh \beta L - \sin \beta L \cosh \beta L} \tag{6.6}$$

where, L is the length of the beam that is allowed to oscillate ($L_{beam} = 28cm$ is the total length of the beam) and V_f is a parameter which governs the size of the perturbation. This form is based on the analytic solution for the displacement of the beam. We take V_f to be 0.01, 0.03 and 0.05. The beams shown in this section have been run with a smoothing length $h = 1.5\Delta p$. Though the results are consistent with those run with the smaller smoothing length of $h = 1.3\Delta p$.

Our first example (figure 6.5) shows the case where $\epsilon = 0.0$, $V_f = 0.05$, $h = 2cm$ and the tensile instability takes effect. There are 20 particles across the height of the beam. The beam bends upwards, artificial fracturing begins at the bottom of the beam, at the end of the support where tensile stress is at a maximum. This fracture propagates up through the beam.

Figure 6.6 shows the same simulation except that now $\epsilon = 0.3$. The beam no longer fractures and continues to oscillate for many cycles without any artificial fracture. The final frame in figure 6.6 shows the beam after five cycles have been completed, some noise in the stress field of the beam can be seen. The noise in the stress field is less than 10% in an oscillation.

Oscillation periods of the beam simulations are compared with theoretical results in tables 6.3 and 6.4 for the $2cm$ and $1cm$ high beams respectively. The average percentage error in the $2cm$ high beams is 9.5%, compared with 3.2% in the $1cm$ high beams. This improvement is consistent with the assumption of thin beams in the analytic solution.

V_f	μ	T_{sph}	T_{theory}
0.001	0.22	1674.6	1557.0
0.01	0.22	1671.5	1557.0
0.03	0.22	1688.2	1557.0
0.05	0.22	1705.0	1557.0
0.001	0.30	1473.6	1341.9
0.01	0.30	1469.8	1341.9
0.03	0.30	1482.1	1341.9
0.05	0.30	1495.4	1341.9
0.001	0.60	1131.6	1030.4
0.01	0.60	1127.2	1030.4
0.03	0.60	1130.7	1030.4
0.05	0.60	1136.1	1030.4

Table 6.3: *Oscillation periods for a plate with $H = 2cm$ and $L = 20$ for various V_f and μ.*

In figure 6.7 we show that there is good agreement between the actual and theoretical shape of the beam for a given displacement. The blue particles show the numerical position of the beam where the black line indicates the analytic solution for the fundamental mode beam displacement. The analytic solution is given by (6.6) if V_f is taken to be the maximum displacement.

Figure 6.8 shows the convergence of beam oscillations with increased particle resolution. The vertical displacement of the centre of the free end of the beam is plotted against time. The cases shown are of $h = 2cm$, $\mu = 0.22$, $V_f = 0.01$, with resolution $\Delta p = 0.2$, 0.1 and 0.067. Figure 6.9 shows a close up of the initial stages of the simulations. All resolutions agree up to the point where the beam first approaches its maximum displacement. The period of oscillation and maximum displacement decrease as the resolution increases. There is a 13% decrease in the amplitude of the oscillation over the three cycles shown due to dissipation.

In figure 6.10 we see the effects of the artificial stress used to remove the tensile instability in a case that doesn't fracture artificially when using standard SPH ($V_f = 0.01$, $h = 2cm$, $\mu = 0.22$). The dashed line shows the standard SPH case. The solid line the case using the artificial stress with $\epsilon = 0.3$. There are only minimal

V_f	μ	T_{sph}	T_{theory}
0.01	0.22	3333.6	3213
0.03	0.22	3385.7	3213
0.05	0.22	3322.8	3213
0.01	0.30	2902.0	2833
0.03	0.30	2977.7	2833
0.05	0.30	2934.9	2833
0.01	0.60	2214.4	2175
0.03	0.60	2221.7	2175
0.05	0.60	2200.4	2175

Table 6.4: *Oscillation periods for a plate with $H = 1cm$ and $L = 20cm$ for various V_f and μ.*

differences in the period of oscillation. The difference between the two cases first becomes noticeable as the beam is completing it's first upward motion where tensile stresses are at a maximum. The major difference in the two cases is that the standard SPH case contains a much larger decrease in the maximum amplitude of the oscillations. Over three oscillations damping reduces the amplitude by 13% in the case of $\epsilon = 0.3$ compared to a reduction of 53% in the $\epsilon = 0.0$ case. This indicates that even though the simulation doesn't undergo numerical fracturing due to the tensile instability, the initial effects of particle clumping still have an effect on the stresses in the system.

Figure 6.11 shows a beam in a case ($V_f = 0.05$, $h = 1cm$, $\mu = 0.22$, $\epsilon = 0.3$) with a very large deformation. The beam shows no sign of the tensile instability despite the large overturning displacement it is encountering. This shows that the method of using an artificial stress to remove the tensile instability is effective in removing the instability.

Time =   11.9   Time = 107.0
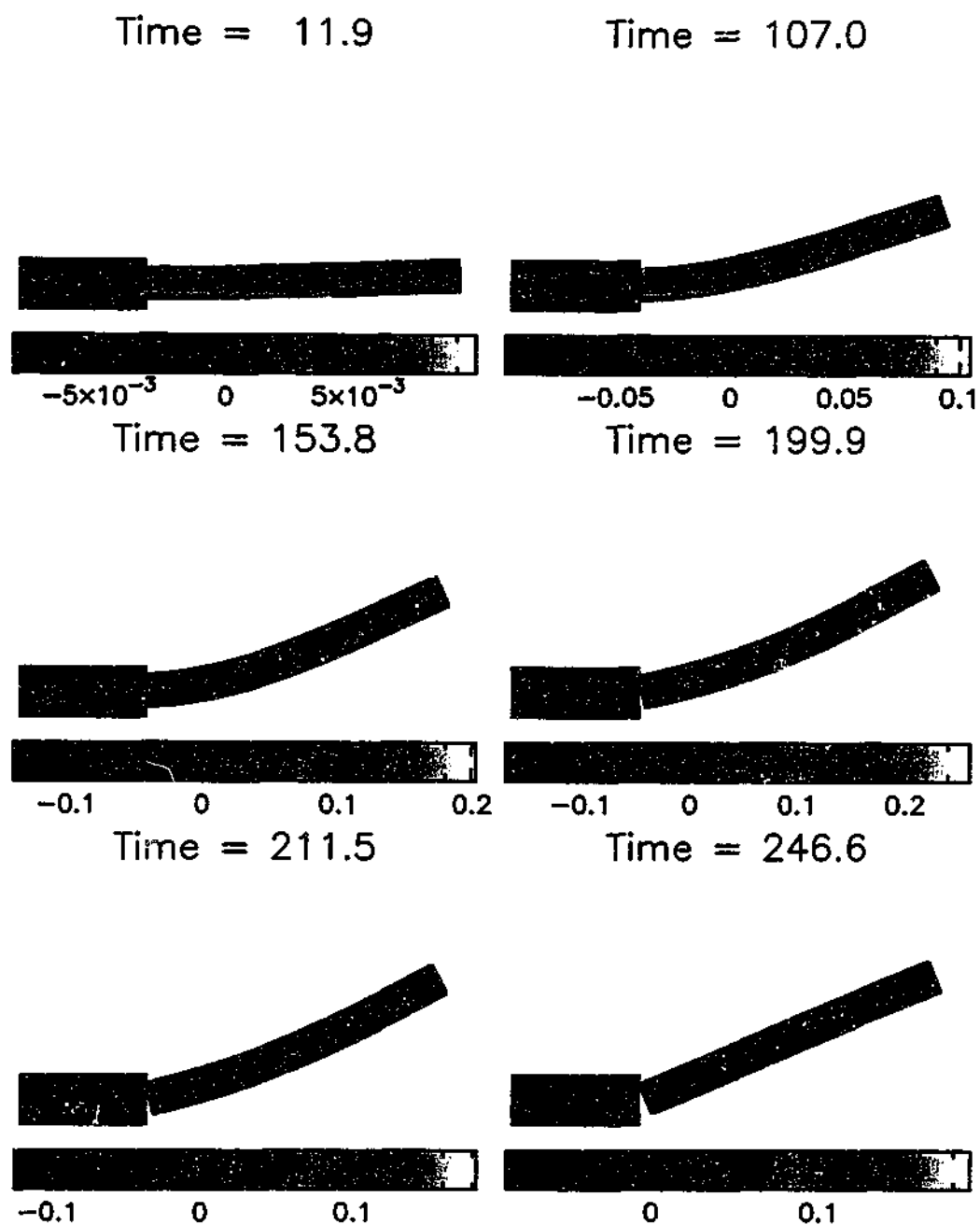
Figure 6.5:   Oscillating plate with parameters $\mu = 0.60$, $V_f = 0.05$, $\Delta p = 0.1$, $\epsilon = 0.0$. Note the clear breakage at $T = 211.5$ due to the tensile instability.

Time =   11.9   Time = 293.9

−5×10⁻³   0   5×10⁻³
Time = 575.8   Time = 870.0

−0.1   0   0.1

−0.01   0   0.01   0.02
Time =1152.4   Time =5687.2

−0.1   0   0.1

−0.02   0   0.02   0   0.05
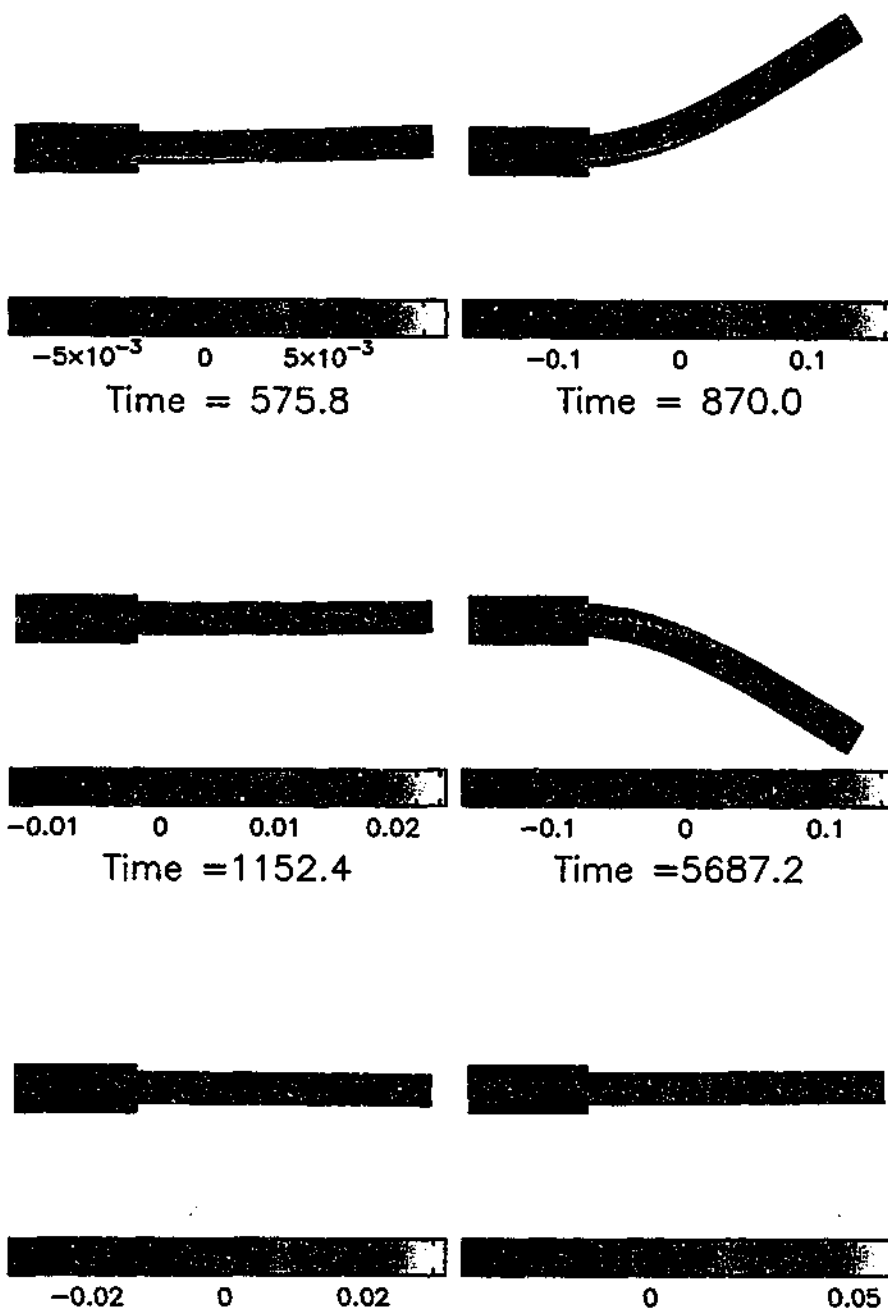
Figure 6.6: *Oscillating plate with parameters* $\mu = 0.60$, $V_f = 0.05$, $\Delta p = 0.1$, $\epsilon = 0.3$. *Note that the breakage caused by the tensile instability in figure 6.5 has been removed with the inclusion of our artificial stress.*
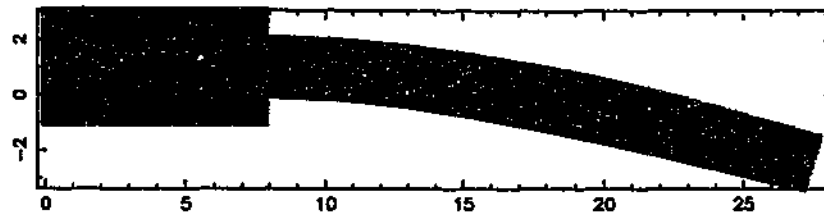
Figure 6.7: Comparison of the beam shape in an SPH simulation with the analytic solution for $\mu = 0.60$, $V_f = 0.05$, $H = 2cm$, $\Delta p = 0.02$. Black line indicates the analytic solution for the shape of the beam. Blue particles are the positions of the SPH particles which make up the beam.
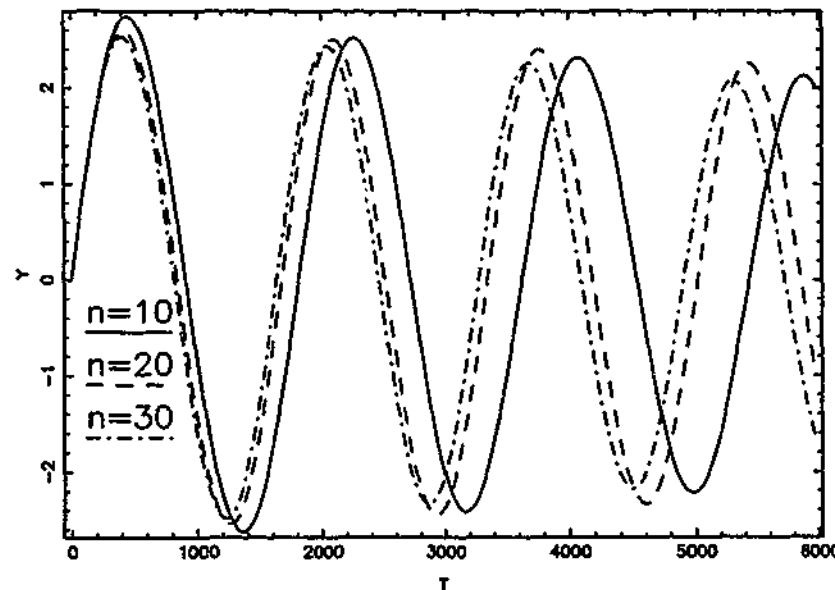
Figure 6.8: Convergence of the vertical position of the middle of the right hand end of a plate for different particle resolutions. The plate had 10, 20 and 30 particles across its height $H = 2cm$. Other parameters were $\mu = 0.22$, $V_f = 0.01$, $\epsilon = 0.3$.
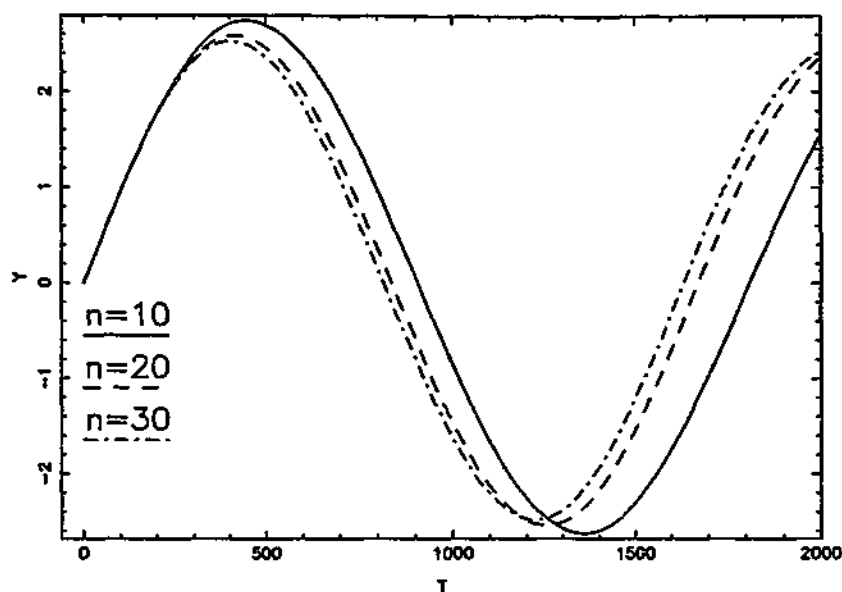
Figure 6.9: *Close up (first period of oscillation) of the convergence of the vertical position of the middle of the right hand end of a plate for different particle resolutions. The plate had 10, 20 and 30 particles across its height $H = 2cm$. Other parameters were $\mu = 0.22$, $V_f = 0.01$, $\epsilon = 0.3$.*
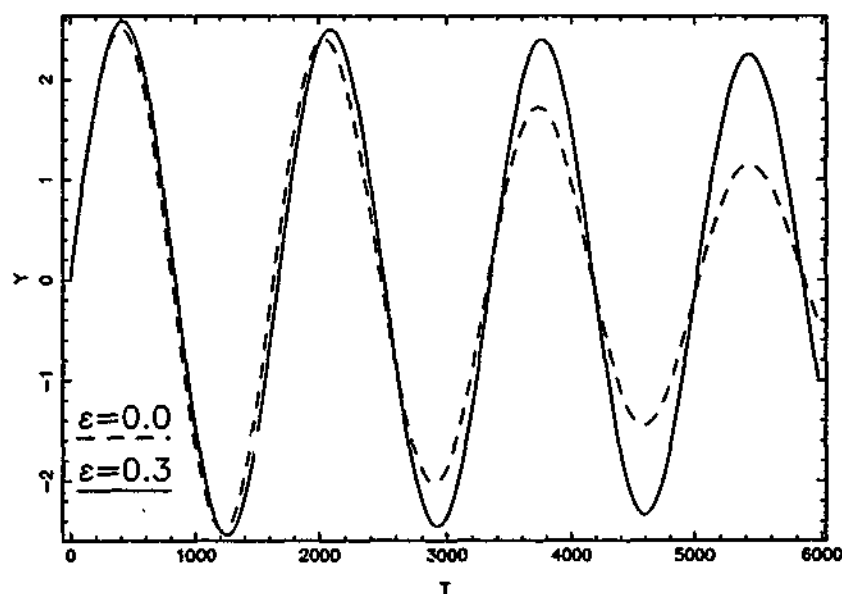
Figure 6.10: *Comparison between the vertical movement of the right hand end of the plate between simulations with $\epsilon = 0.3$ and $\epsilon = 0.0$. Other parameters were $\mu = 0.22$, $V_f = 0.01$, $H = 2cm$, $\Delta p = 0.1$.*

Time = 842.9
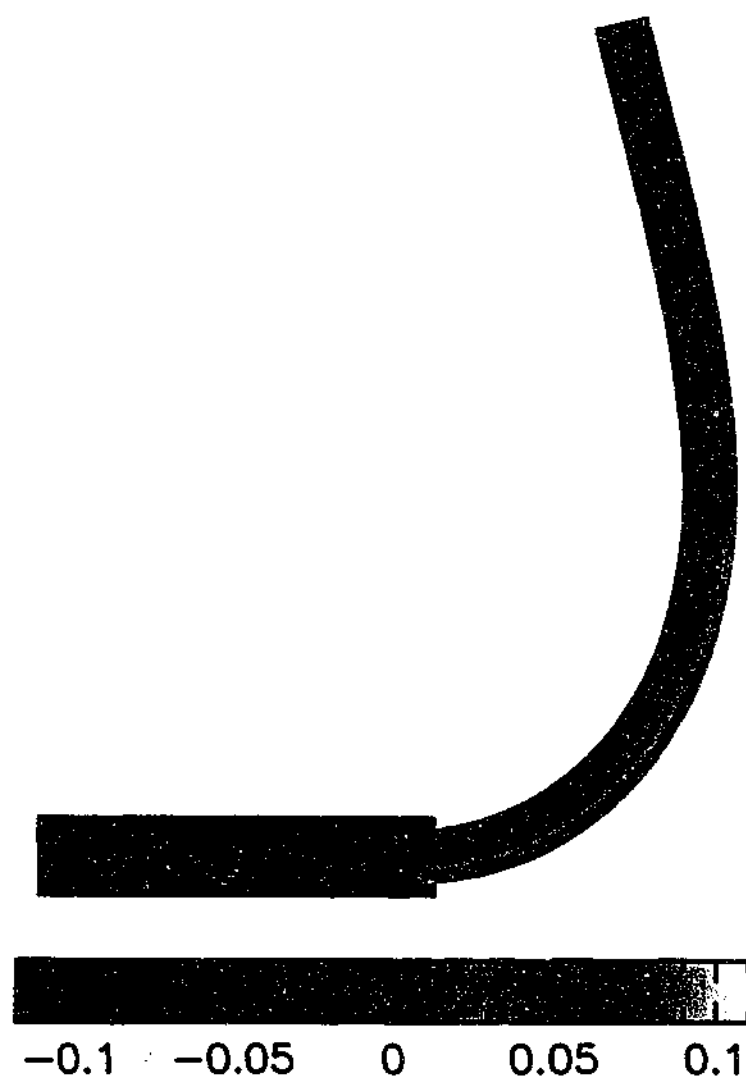
Figure 6.11: Illustration of the large distortions and displacements our beams are able to undergo without the onset of the tensile instability. $\mu = 0.22$, Simulation parameters were $V_f = 0.05$, $H = 1cm$, $\Delta p = 0.05$.

6.3   Plastic Deformation of a Plate

Plastic flow begins to occur in a material when it becomes distorted to such an extent that it can no longer store any elastic energy and the material undergoes a permanent change of shape. In elastic flow the energy used to stretch a material is stored and released when the stretching forces are removed. In plastic flow the stretching energy is used to permanently deform the material and only elastic energy is released when the applied forces are removed.

In figure 6.12 we illustrate the effects of plasticity on the oscillation of the elastic beams in the previous section. We take a shear modulus $\mu = 0.60$, with the parameter determining the size of the initial velocity $V_f = 0.05$, and a yield strength one tenth of the shear modulus $Y_o = 0.06$. We take a plate height $H = 2cm$ and resolution $\Delta p = 0.2$.

As in the case of elastic beams the initial condition for the movement of the beam is upwards. The plastic effects first take hold on the bottom of the beam near the support where the tensile stresses are highest. The material here becomes permanently deformed as the beam reaches the top of its oscillation. As the beam attempts to swing back down to the starting position, the plastic extension at the base means that it is unable to reach its original position. The beam does not sweep down below the support as in the purely elastic case as the boundary condition at the support has changed. Plastic effects mean material at the base of the beam near the support does not return to its original position and the remainder of the beam cannot swing down lower than the support.

The maximum amplitude of vertical oscillation of the plastic beam is larger than the elastic case and there is a corresponding increase in the period of oscillation. This can be seen in figure 6.13 where we compare the vertical displacement of the right hand end of the beam with a purely elastic case with the same parameters. The increase in the maximum vertical displacement is due to the material being less able to resist the tensile stresses it is encountering. One can think of the forces in an elastic material being in competition, a tensile force extending the material and an elastic force to resist the extension. A reduction in this resistive force (due to plasticity) means that the material is stretched further for the same applied force.
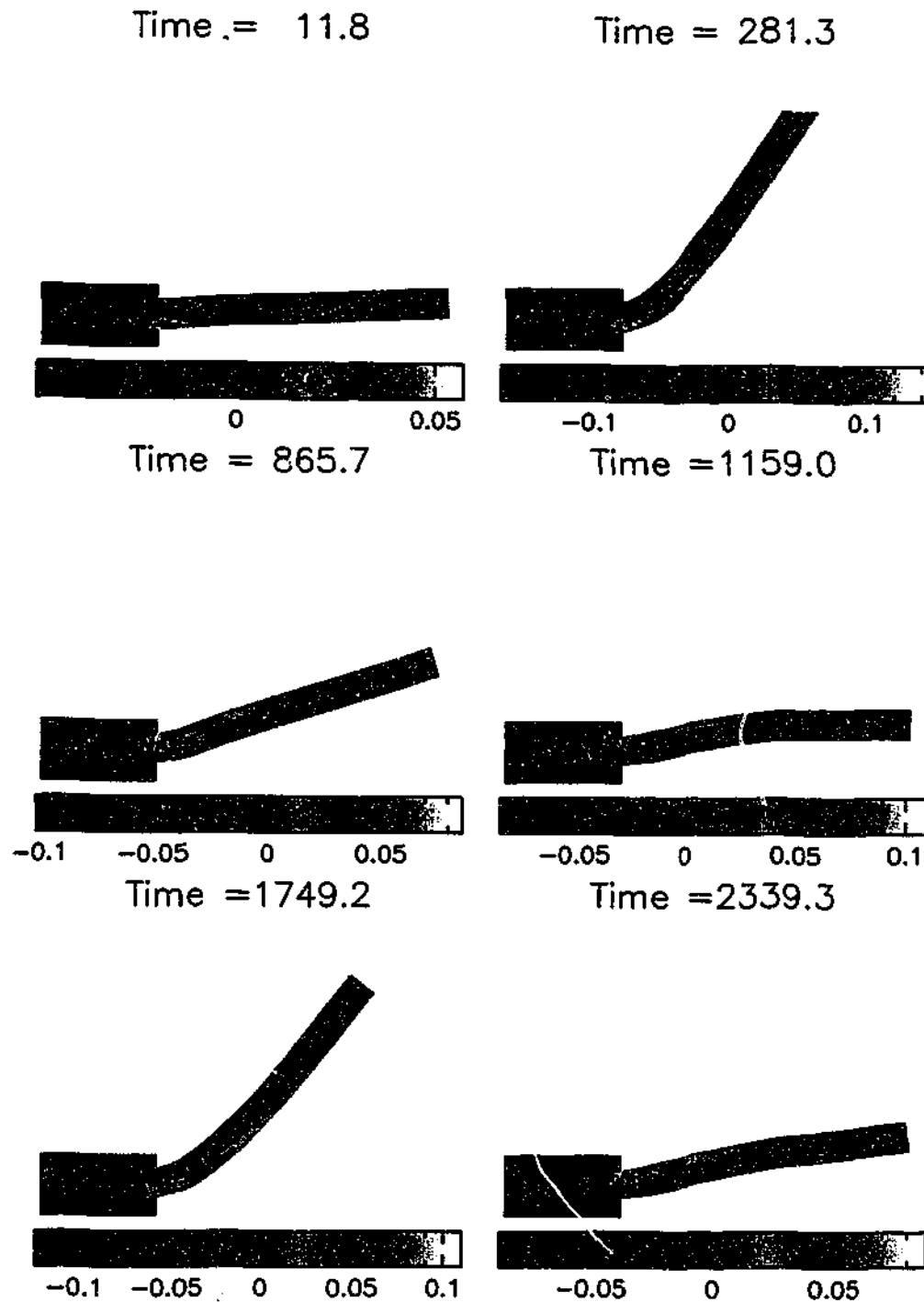
Figure 6.12: The effect of including plasticity using a Von Mises yielding criterion on the oscillating beams of section 6.2. This is the case of $\mu = 0.60$, $V_f = 0.05$, $H = 2$, $\Delta p = 0.2$, $Y_o = 0.06$.
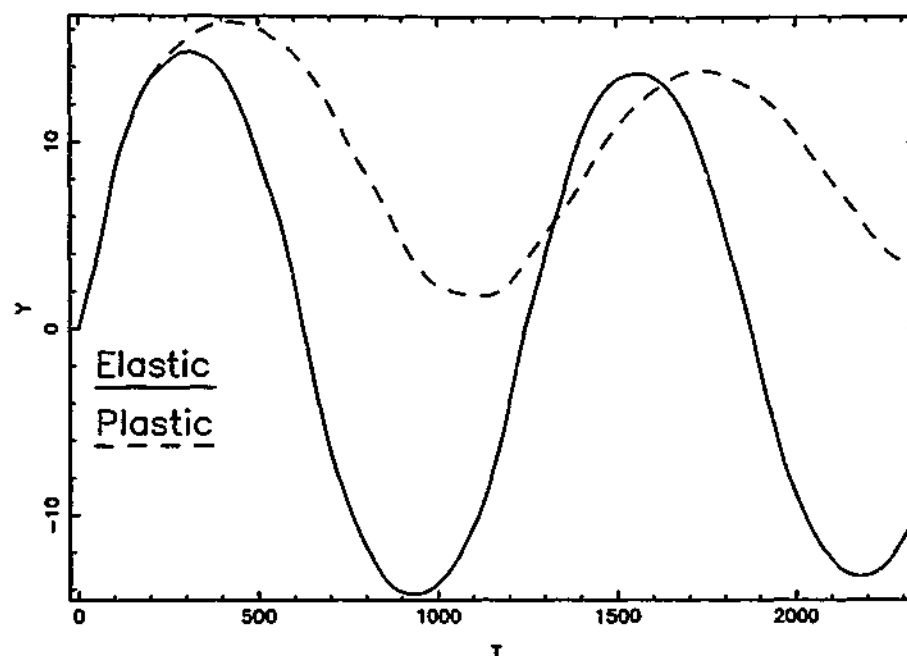
Figure 6.13: *Comparison between vertical position at the end of beams with and without plastic effects. The beam that has plastic effects has a yield strength $Y_o = 0.06$. Both the elastic and plastic cases have parameters $\mu = 0.60$, $V_f = 0.05$, $H = 2$, $L = 20$, $\Delta p = 0.2$.*

6.4   Plates in Simple Tension

As the short wavelength instability in SPH manifests itself when an elastic body is in tension perhaps the most instructive test case to study is that of plates in simple tension. We begin with a purely elastic-plastic beam, which means a damage model is not included in the calculations. We see how this beam is seriously affected by the tensile instability when using standard SPH. We then show that by adding artificial stress terms with $\epsilon = 0.3$ the effects of the tensile instability are removed, the beam in SPH calculation undergoes necking, ductile extension and finally failure.

After studying the elastic-plastic case we add flaws to the material and include a Benz-Asphaug damage model (section 5.5) to investigate the brittle failure of beams in tension. We see that an effect of the formation of cracks is to relieve the stress in an area local to the crack, that brittle behaviour is largely unaffected by the SPH

tensile instability and that our damage model converges with increasing resolution.

6.4.1 Pure Elasticity-Plasticity: No Flaws

The example in figure 6.15 is of a rectangular plate under tension, without the artificial stress fix for the tensile instability, that is $\epsilon = 0.0$. The block is $1cm$ high by $3cm$ long. Tension is applied by moving the particles within $0.2cm$ at each end with the constant horizontal acceleration $A_f = 5 \times 10^{-6}$ in the x direction. In the case shown $\mu = 0.3$ and plasticity is modelled using a yield strength of $Y_o = 0.03$, we take a resolution of $\Delta p = 0.0167$ and $h = 1.5\Delta p$.

In this case as we include only elastic and plastic effects and we expect behaviour similar to a ductile material. The plate is stretched without the appearance of artificial fracturing up until the dimensionless time $t = 110$ (the dimensionless time is defined in section 5.4). After this time the tensile instability takes hold and artificial fractures can be seen at each end of the plate. The distance moved in a time t is given by $2.5 \times 10^{-6}t^2$ cm, so at the time $t = 110$ the horizontal strain on the plate is 0.01. We illustrate the tensional extension of the same plate, with $\epsilon = 0.3$ in figures 6.16 and 6.17. The first five frames of figure 6.16 correspond to the same times as the first five frames in the $\epsilon = 0$ case (figure 6.15). The two cases are similar up until $t = 110$ where the tensile instability takes effect. Unlike the standard SPH case (shown in figure 6.15) the $\epsilon = 0.3$ calculation is able to sustain a strain of 0.15 without difficulty. As the strain is increased the material begins to neck and then fractures consistent with a real ductile material.

Continuity implies that the volume of material in the plate is conserved as it undergoes extension. An increase in the length of our two dimensional material is accompanied by a decrease in its height (cross sectional area). A tensile force applied to the ends of the plate must be supported by each cross section through the plate. Necking occurs when one of the cross sections develops an area less than the rest of the material, leading to an increase in the stress and longitudinal extension in this area. An instability develops as the increased extension leads to a further decrease in the height of the material at the point of necking and eventually leads to fracture of the material. This fracture is a result of the physical geometry and not the tensile instability.

Ductile extension occurs by shear and is a result of plastic flow (Ashby and Jones

1980) (pg.103). Applying a tensile stress to a plate results in the material feeling a shear stress at some angle to the applied stress.

Materials fail in tension when adjacent atoms become too far apart and the bonds between them break. Large strains (without fracture) are possible if plastic flow occurs and the extension results in adjacent planes of atoms sliding over each other. Plastic strain is accommodated by the permanent deformation of the atomic lattice structure.

The Lagrangian nature of SPH particles mimic the slip over adjacent planes without difficulty. We see in figure 6.17 that necking results in an increasingly thin region at the centre of the beam as the longitudinal strain increases.

Eventually the particulate nature of the material (SPH algorithm) takes over when there are no longer any particles which are able to slip and the material breaks. This is what occurs in real materials, although our current SPH algorithm results in fracture that is not quite realistic. Shear fractures are expected to result in a *cup and cone* fracture (see figure 6.14 (Jaeger 1964) (pg.74)). It would be interesting to include a description of damage in shear to the computations (Randles and Libersky 1996) to see if it results in more realistic failure during the final stages of the simulation.
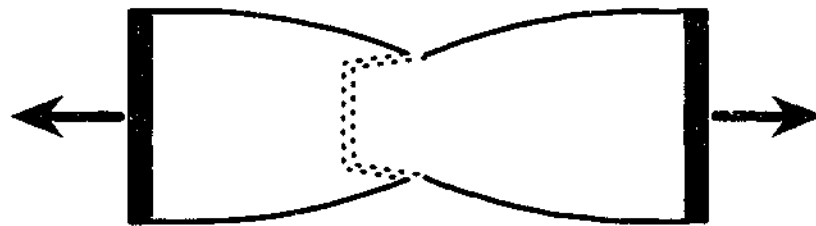
Figure 6.14: *Schematic diagram of a cup and cone fracture that results from the shear fracture of a ductile plate undergoing simple tension. Necking occurs as the material becomes thinner at the middle. This region experiences higher stresses due to the necking and thins further. Eventually the material fails due to shear, with one piece resembling a cone which fits into a cup at the other side of the fracture.*

Time =   0.0   Time = 95.0

Time =110.0   Time =120.0

Time =144.8   Time =194.4
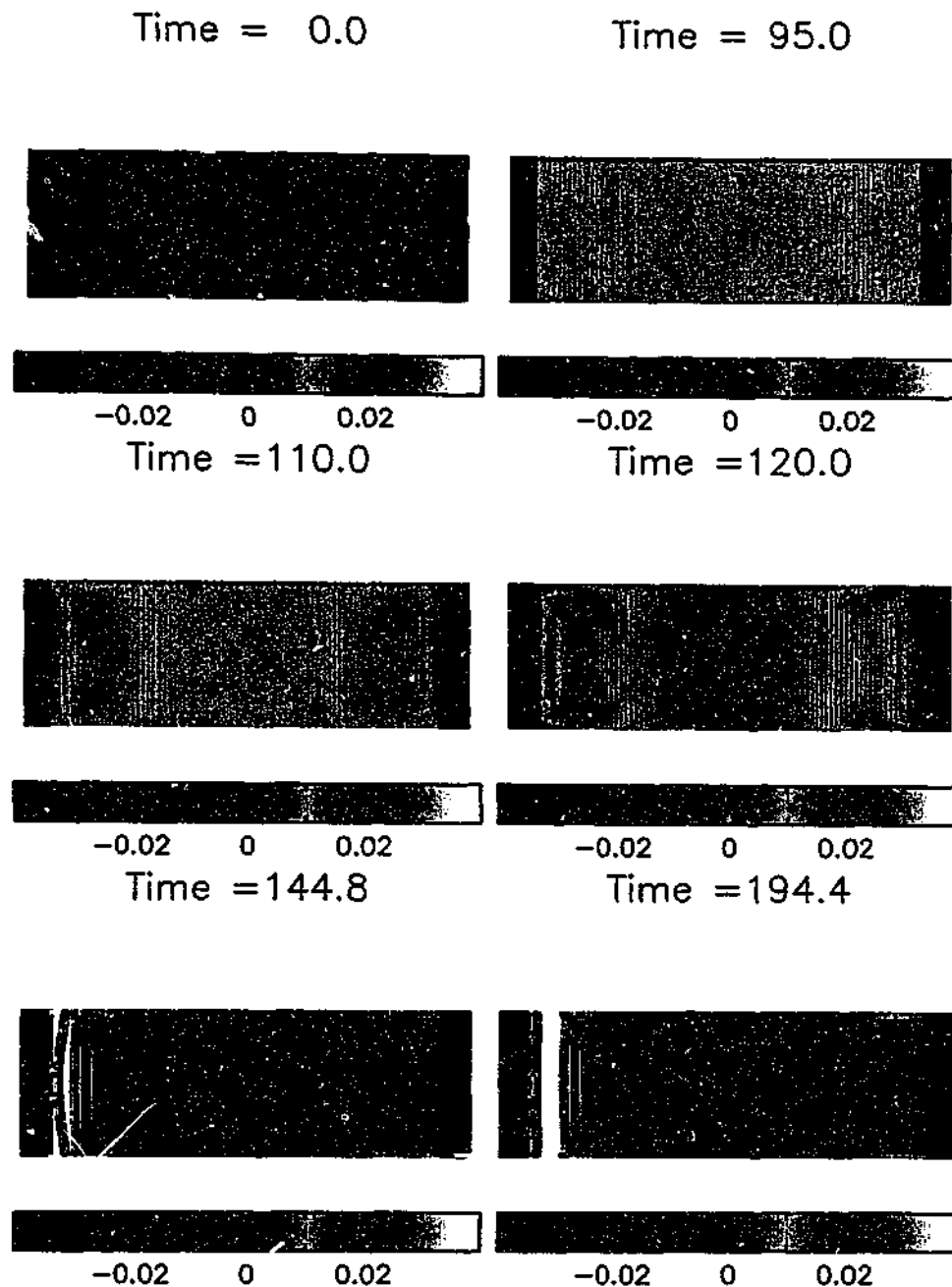
Figure 6.15:   *Tensional extension of a material with $\mu = 0.3$, $Y_o = 0.03$ using the standard SPH algorithm $\epsilon = 0.0$. The dark band of particles at each end indicate the edge particles which apply the extension to the material, these particles are moved with the constant acceleration $A_f = 5 \times 10^{-6}$. Artificial fracturing begins to occur at $T = 120.0$ near the left hand interface between the material and the edge particles.*

Time = 0.0   Time = 95.0

Time =110.0   Time =120.0

Time =145.0   Time =294.8
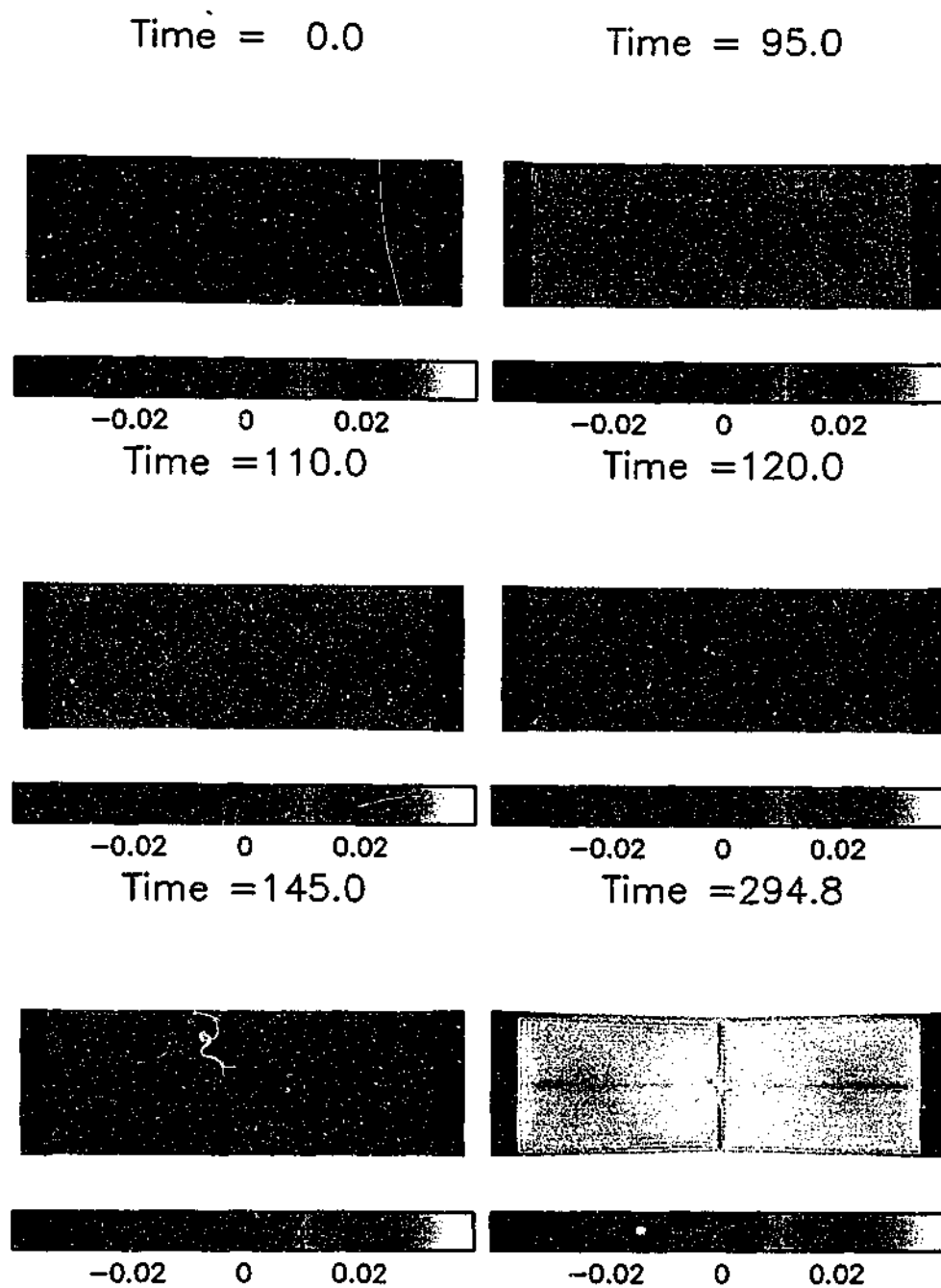
Figure 6.16: *Tensional extension of a material with $\mu = 0.3$, $Y_o = 0.03$ using SPH with an artificial stress ($\epsilon = 0.3$) to remove the effects of the tensile instability. Edge particles are again moved with a constant acceleration $A_f = 5 \times 10^{-6}$. Artificial fracturing no longer occurs, the material begins to neck at the time $T = 294.8$.*

Time =344.8   Time =394.7

−0.02   0   0.02   −0.02   0   0.02
Time =444.0   Time =493.1

−0.02   0   0.02   −0.02   0   0.02
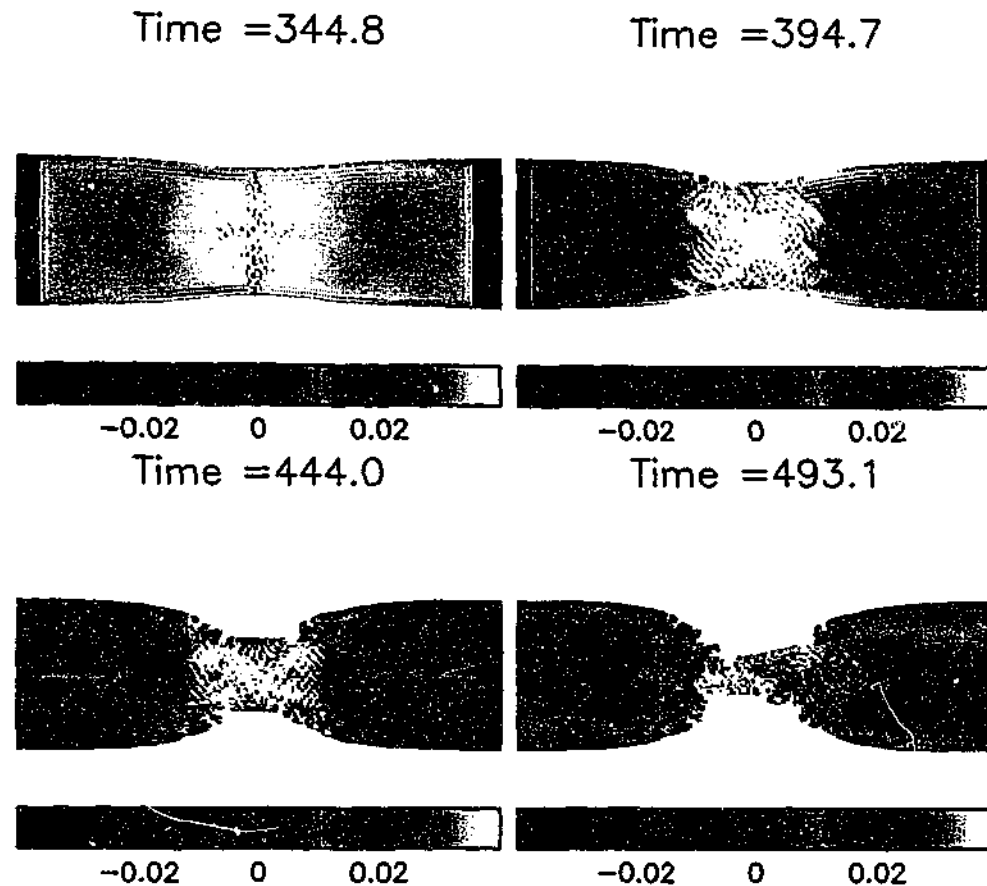
Figure 6.17: Continuation of the simulation figure 6.16. The material undergoes ductile extensional behaviour and continues to neck. Necking continues until the middle region is stretched to an extent that the resolution is such that the particle nature of the SPH algorithm takes over and the material breaks. A real material is expected to eventually break in a similar way, there is stress relief in the material as fracture occurs. Note that artificial fracturing caused by the tensile instability is not present and the addition of the artificial stress terms mean that the material can undergo large strains without difficulty.

6.4.2 Elasticity-Plasticity: With Flaws

The Benz-Asphaug damage model with a Weibull distribution of flaws as described in section 5.5 is now included in to the simulations. We take the material parameters in our Weibull distribution m and k to be 8.5 and 1.4×10^{19} respectively. The value of k is chosen as a two dimensional value for basalt. Benz and Asphaug (1995) take $k_{3D} = 5 \times 10^{28}$ in their three dimensional calculations. As strain is a dimensionless quantity, k has units of the number of flaws per unit volume. A one dimensional line of particles contains $k_{3D}^{1/3}$ flaws. A two dimensional cross section will then contain $k_{3D}^{2/3}$ flaws. For our two dimensional calculations we take $k = k_{3D}^{2/3} = 1.4 \times 10^{19}$.

We now study the behaviour of brittle plates in tension by including a Benz-Asphaug damage model into the calculations. In the previous subsection (without the damage model) we applied a strain to the material by moving the end $0.2cm$ of particles at a specified rate. When we did this in calculations with the damage model we found that the initial stress wave quickly damaged and fractured the particles directly adjacent to the ends, relieving the applied stress, the remainder of the plate was never able to sustain damage. The applied boundary conditions make the calculations inconsistent with experiment and must be improved.

To remove this inconsistency we assigned the end $0.2cm$ of the beam to have no flaws and moved only those particles on the edge of the beam at the prescribed strain rate. This allowed for the stress waves to travel into the plate without causing catastrophic failure at the edge of the domain. We also moved the ends with a constant strain rate in these calculations (by defining the velocity at which the ends were moved, V_f) to allow a comparison with the statistics of fragment size given by Grady and Kipp (1980).

Crack Propagation Velocity The tests we present in this subsection are similar to ones given by Benz and Asphaug (1995). We begin with a test of the crack propagation velocity. We expect cracks to grow at the velocity $c_g = 0.4$ in our scaled coordinates. In figure 6.19 we show the case of a beam with $\epsilon = 0.3$, $\mu = 0.3$, $Y_o = 0.03$ and $\Delta p = 0.033$. The beam is shown at three times, the frames on the left are coloured by the mean stress $(\sigma^{xx} + \sigma^{yy})$. In the frames on the right the colours of the particles refer to the value of the damage variable. A blue particle is undamaged, with yellow corresponding to a fully damaged particle.

A crack first appears in the middle of the beam. The stress in the area around this beam is relieved. The crack then grows until the beam is broken into two pieces. Some of the flaws were activated in other areas of the beam although the beam is otherwise largely unaffected by damage in these areas as it is only the weakest flaws which have been activated. As expected the crack grew in a straight line perpendicular to the applied stress.

We measured the crack velocity to be $c_g^{meas} = 0.381$, this compares well with the expected value of $c_g = 0.4$. The difference is within the measurement error which is limited by the particle resolution of the calculation.

Artificial Stress As cracks in a brittle material are expected to form at low strains and long before the critical onset of the tensile instability, we expect that the results of simulations without the artificial stress terms used to remove the tensile instability should be similar to those in which the terms are included.

In our next example figure 6.20, we illustrate a simulation with the Benz-Asphaug damage model and without the artificial stress terms ($\epsilon = 0.3$), strain is applied to the plate by moving the ends with the constant horizontal velocity $V_f = 1 \times 10^{-4}$. The first crack to be initiated is at the centre of the beam at the scaled time $T = 11.5$, as this crack grows a second crack forms on the right hand side of the plate. Both cracks propagate through the beam until it adjusts itself to the relieved state of stress and the accumulation of damage ceases. The fractures formed in the simulation including the artificial stress terms are almost identical although there are some minor differences in the timing of crack initiation and growth. These small discrepancies are likely effects (of small amounts) of non-disruptive particle clumping in the $\epsilon = 0.0$ case. Remember the oscillating beam (figure 6.10) had an amplitude that was damped more strongly in the $\epsilon = 0.0$ case, even though it did not crack under the instability, we propose that similar differences also occur here.

Effect of Particle Resolution As with all numerical calculations it is important that the resolution used is sufficient to gain a clear understanding of the physical processes under investigation, and also that changes in the resolution do not change the results of the simulation. In the present case flaws are assigned randomly, so that changing the resolution also means changing the flaw assignment and the positions of weaknesses in the material.

In figure 6.22 we show the extent of damage at the scaled time of $t = 4.2$ for resolutions of 20, 40 and 60 particles across the height of the beam. We apply a higher strain rate to the beam in this case by using a larger velocity parameter ($V_f = 5 \times 10^{-3}$) than the previous cases. The agreement between all three cases is good, with finer detail being found at the higher resolutions. The majority of the fracturing occurs around the centre of the beam, when the stress waves applied at each end first meet.

All three cases have cracks through the middle of the plate. A series of smaller fractures has developed out towards each end. Large cracks also form a distance of approximately one quarter of the beams length from each end. Minimal damage has been accumulated between these cracks and the ends of the beam. Except for the lowest resolution where damage began to accumulate at the interface between the beam and boundary particles which apply the stress.

Higher Strain Rates   The quicker a mate! .a) .s pulled apart the greater the number of cracks are expected to develop. The reason for this is that cracks propagate at a finite velocity, at low stresses a single crack is able to develop and relieve the stress applied to the plate. As the stresses increase a single crack is unable to relieve the stress quickly enough (due to the finite velocity of its growth) so that more flaws become active and more cracks grow in the material (Grady and Kipp 1980).

In figures 6.21 and 6.22 the plate of figure 6.19 is pulled apart with a strain rate 2 and 10 times greater respectively. The increased amount of cracks and damage are clear to see. We find at the lowest strain rate that the plate is split in two by a single crack. The average fragment size is $1.5cm$. At the next highest strain rate (figure 6.21) two cracks form, one in the centre and one at the right hand edge, but again the average fragment size is around $1.5cm$ long. At the highest strain rate in our calculations (figure 6.22) the beam is broken into four pieces with the average fragment size close to $0.7cm$. We now follow Grady and Kipp (1980) and Benz and Asphaug (1994) and statistically determine the most likely expected fragment size.

Grady-Kipp Fragment Statistics   In the Grady-Kipp model the effects of flaws are accounted for with a damage parameter D. At a time t the damage in the

material is given by a superposition of all of the active cracks.

$$D = \int_0^t \frac{\partial n(\tau)}{\partial t} v(t - \tau) d\tau \tag{6.7}$$

where, $\partial n(\tau)/\partial t$ is the rate of increase in the number of active flaws, and $v(1 - \tau)$ describes the growth in the volume of material in which the stress is affected by the cracks. As our calculations are two dimensional, we take v to be the area affected by the cracks.

The rate of increase of active flaws is given by,

$$\frac{\partial n(\tau)}{\partial t} = \frac{\partial n(\epsilon)}{\partial \epsilon} \frac{\partial \epsilon(\tau)}{\partial t} (1 - D) \tag{6.8}$$

where, $\partial n(\epsilon)/\partial \epsilon$ is the increase in the number of active flaws, $\partial \epsilon(\tau)/\partial t$ is the strain rate over time, and the factor $(1 - D)$ accounts for the reduction in stress bought about by damage.

The area of material that is relieved of stress by a crack is given by πr_g^2 where r_g is the length of the crack. The Grady-Kipp model assumes that once active cracks grow at a constant velocity c_g. So that the length of the crack is given by $r_g = c_g \Delta t$. If a crack becomes active at a time τ, the area relieved of stresses by a crack is given by,

$$v(t - \tau) = \pi c_g^2 (t - \tau)^2. \tag{6.9}$$

Combining (6.7), (6.8) and (6.9) together Grady-Kipp arrived at an integral equation for the damage,

$$D(t) = \pi c_g^2 \int_0^t \frac{\partial n(\epsilon)}{\partial \epsilon} \frac{\partial \epsilon(\tau)}{\partial t} (1 - D)(t - \tau)^2 d\tau. \tag{6.10}$$

Grady and Kipp then assume that a constant strain rate, $\partial \epsilon/\partial t = \dot{\epsilon}_o$ is applied to the material so that,

$$\epsilon(t) = \dot{\epsilon}_o t. \tag{6.11}$$

Then from the Weibull distribution (5.32) we find,

$$\frac{\partial n(\epsilon)}{\partial \epsilon} = mk\epsilon^{m-1} = mk\dot{\epsilon}_o^{m-1} t^{m-1}. \tag{6.12}$$

Substituting into (6.10) the integral equation for damage becomes,

$$D(t) = \pi c_g^2 m k \dot{\epsilon}_o^m \int_0^t \tau^{m-1}(1 - D(\tau))(t - \tau)^2 d\tau. \tag{6.13}$$

Grady and Kipp then obtain a first order series solution to this equation. This solution is found by setting $D(\tau) = 0$ in (6.13),

$$
\begin{aligned}
D(t) =& \pi c_g^2 m k \dot{\epsilon}_o^m \int_0^t \tau^{m-1}(t - \tau)^2 d\tau \\
=& \pi c_g^2 m k \dot{\epsilon}_o^m \left[\frac{t^2 \tau^m}{m} - \frac{2t \tau^{m+1}}{m+1} + \frac{\tau^{m+2}}{m+2} \right]_0^t \\
=& \frac{2\pi c_g^2 k \dot{\epsilon}_o^m t^{m+2}}{(m+1)(m+2)} \\
D(t) =& \alpha \dot{\epsilon}_o^m t^{m+2}
\end{aligned}
\tag{6.14}
$$

where,

$$\alpha = \frac{2\pi c_g^2 k}{(m+1)(m+2)}. \tag{6.15}$$

To find the most likely fragment size, Grady and Kipp assume that fragmentation occurs when $D(t_f) = 1$. Taking the solution to the integral equation for damage (6.14) this corresponds to,

$$
\begin{aligned}
1 =& \alpha \dot{\epsilon}_o^m t_f^{m+2} \\
t_f =& \alpha^{-\frac{1}{m+2}} \dot{\epsilon}_o^{-\frac{m}{m+2}}.
\end{aligned}
\tag{6.16}
$$

The fragment distribution is given by,

$$F(L) = \frac{\pi m k}{8 c_g} L^2 (t_f - L/2c_g)^{m-1} \dot{\epsilon}_o^m. \tag{6.17}$$

We plot the most likely fragment distribution for the case of $k = 1.4 \times 10^{19}$, $m = 8.5$ and strain rates of $\dot{\epsilon}_o$ equal to 3.33×10^{-3}, 6.66×10^{-4} and 3.33×10^{-4} in figure 6.18. The peak of the distribution occurs at lower fragment lengths and becomes sharper as the strain rate is increased.

We set $\partial F/\partial L = 0$ to find the likely maximum fragment size,

$$L_M = \frac{4c_g}{m} \alpha^{-1/(m+2)} \dot{\epsilon}_o^{-m/(m+2)}. \tag{6.18}$$
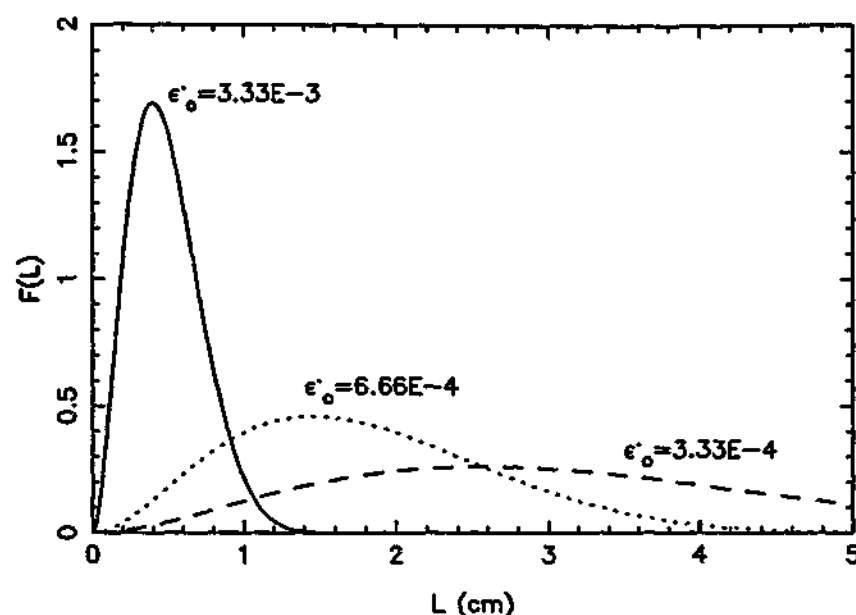
Figure 6.18: *The likely distribution of fragment size from Grady-Kipp statistics for constant strain rates $\dot{\epsilon}_o$ of 3.33×10^{-3}, 6.66×10^{-4} and 3.33×10^{-4} with $k = 1.4 \times 10^{19}$ and $m = 8.5$. The distribution is more strongly peaked at a lower maximum for the higher strain rate.*

We find that $L_M = 0.44cm$ for $\dot{\epsilon}_o = 3.33 \times 10^{-3}$, this is compared to $0.7cm$ in our simulation. At the lower strain rate of $\dot{\epsilon}_o = 6.66 \times 10^{-4}$, $L_M = 1.63cm$ using Grady-Kipp statistics and $1.5cm$ in our computation. At our lowest strain rate $\dot{\epsilon}_o = 3.33 \times 10^{-4}$ (seen in figure 6.19) the expected fragment size is $L_M = 2.87cm$. As our beam is of a similar length we cannot expect fragments of this size in the computation which provided two fragments $1.5cm$ long. The computations agree qualitatively with the Grady-Kipp statistics, the computed fragment sizes are of the same order of magnitude as the statistically expected sizes and decrease with increasing strain rates.

Time = 22.750   Time = 22.750

Time = 23.491   Time = 23.491

Time = 24.726   Time = 24.726
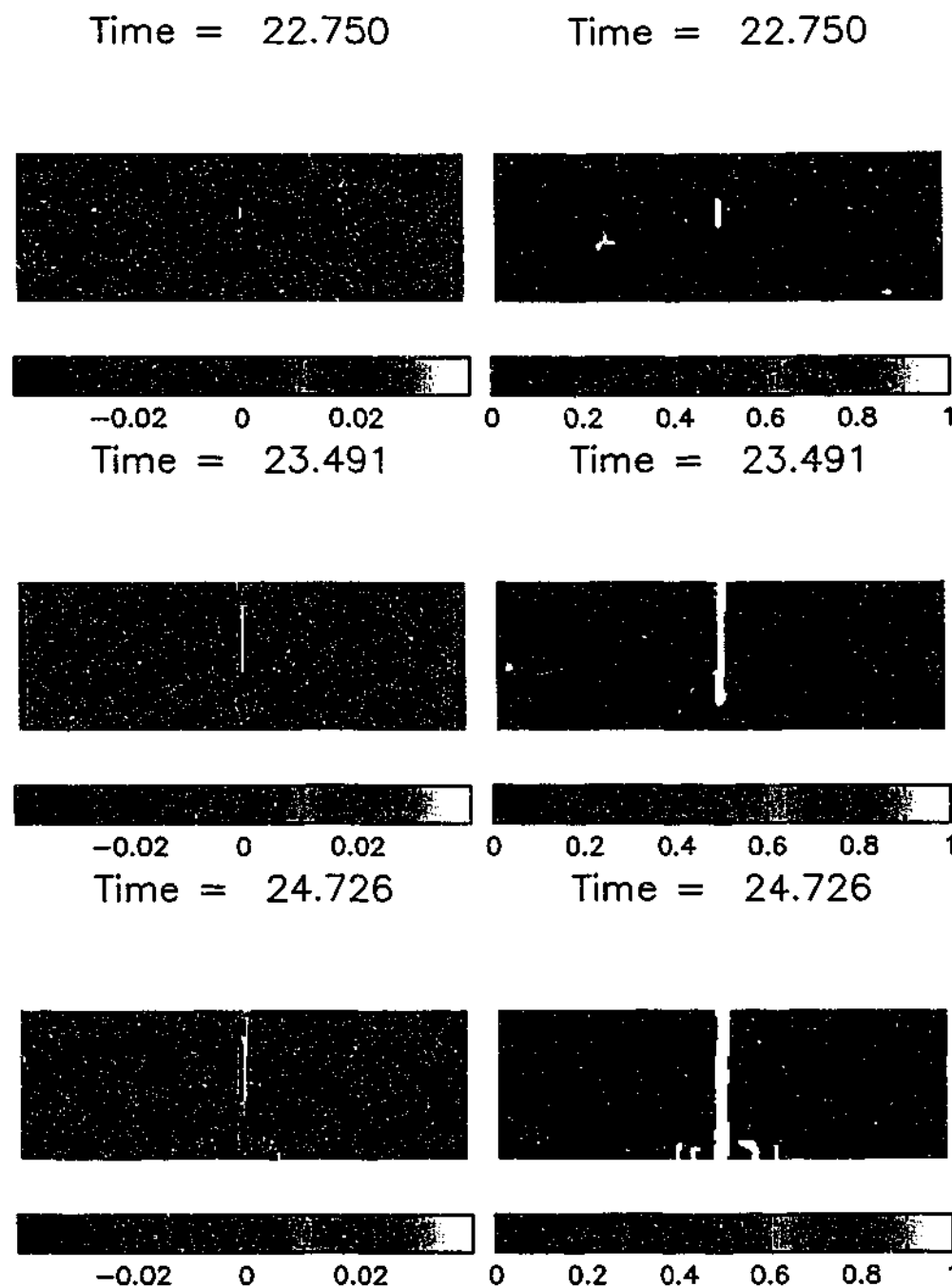
Figure 6.19: Tensile extension of a brittle beam. Frames of left side indicate the evolution of the mean stress. Frames on right show the build up of damage. Parameters of the simulation were $\epsilon = 0.3$, $V_f = 5 \times 10^{-4}$, $\mu = 0.3$, $Y_o = 0.03$, $k = 1.4 \times 10^{19}$, $m = 8.5$, $H = 1.0$, $L = 3.0$, $\Delta p = 0.0167$.

Time = 9.744   Time = 11.495

Time = 12.235   Time = 13.219

Time = 13.712   Time = 14.698
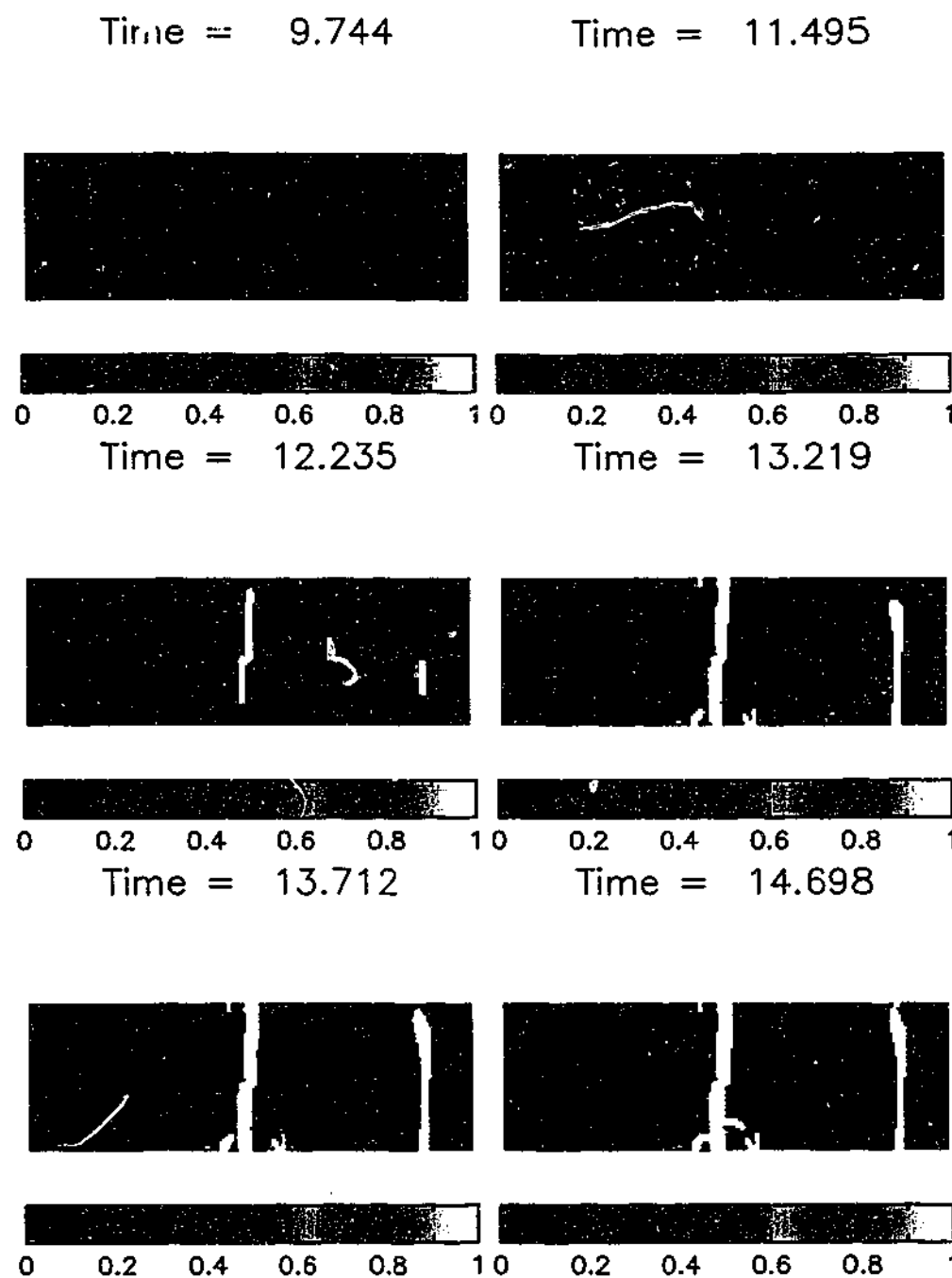
Figure 6.20:   *Tensile extension of a brittle beam, standard SPH case ($\epsilon = 0.0$).*
All frames show the build up of damage. Beam ends are moved with
a higher velocity than figure 6.19, note the more extensive fracture
development. Simulation parameters were $V_f = 1 \times 10^{-4}$, $\mu = 0.3$,
$Y_o = 0.03$, $k = 1.4 \times 10^{19}$, $m = 8.5$, $H = 1.0$, $L = 3.0$, $\Delta p = 0.0167$.
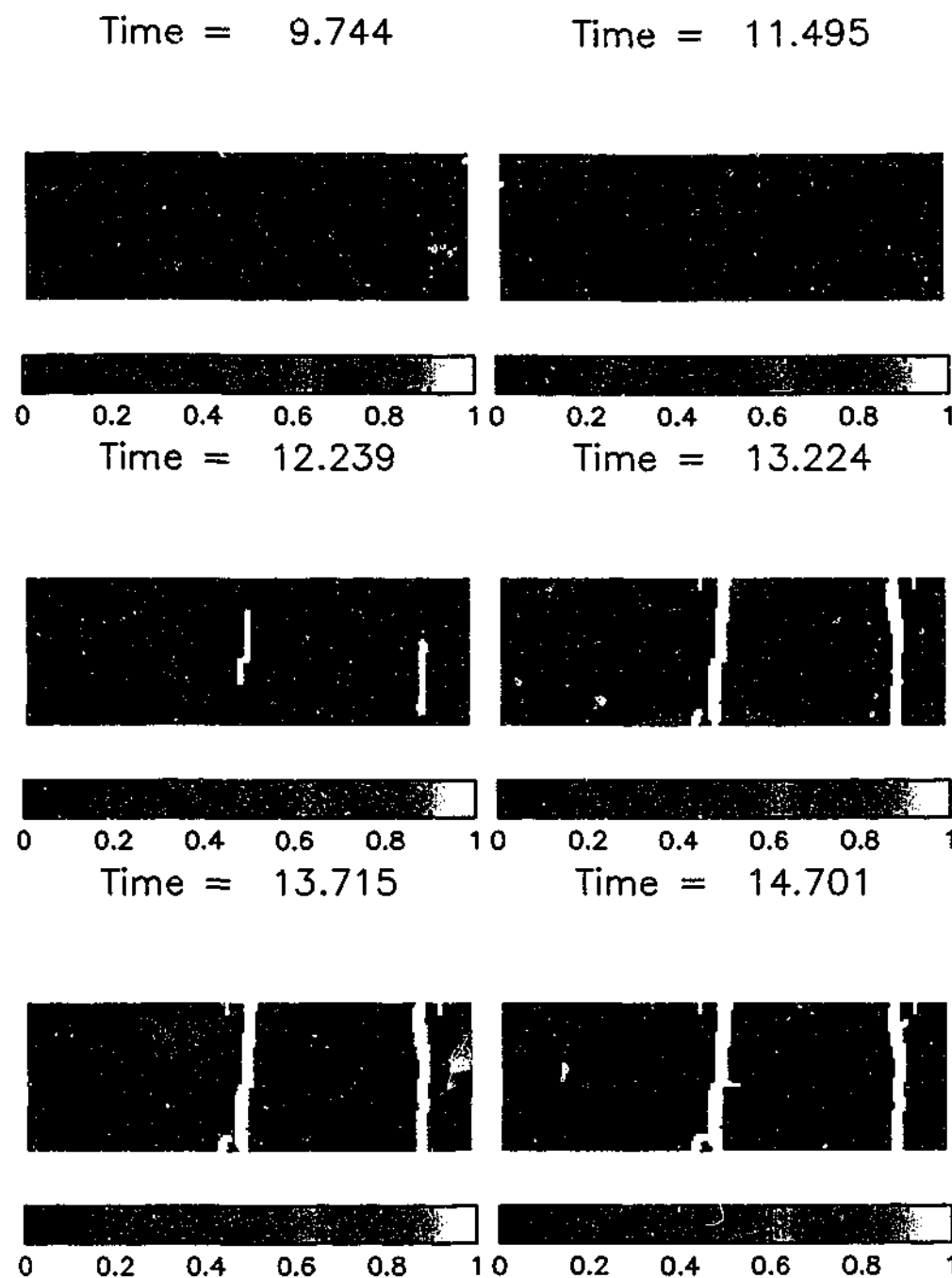
Figure 6.21:   Tensile extension of a brittle beam with artificial stress terms. All
frames show the build up of damage. Unlike the ductile beam (fig-
ures 6.15 and 6.16), brittle beam calculations have only minimal dif-
ferences when the artificial stress is employed. Parameters of the
simulation as for figure 6.20 except that $\epsilon = 0.3$ in this case.
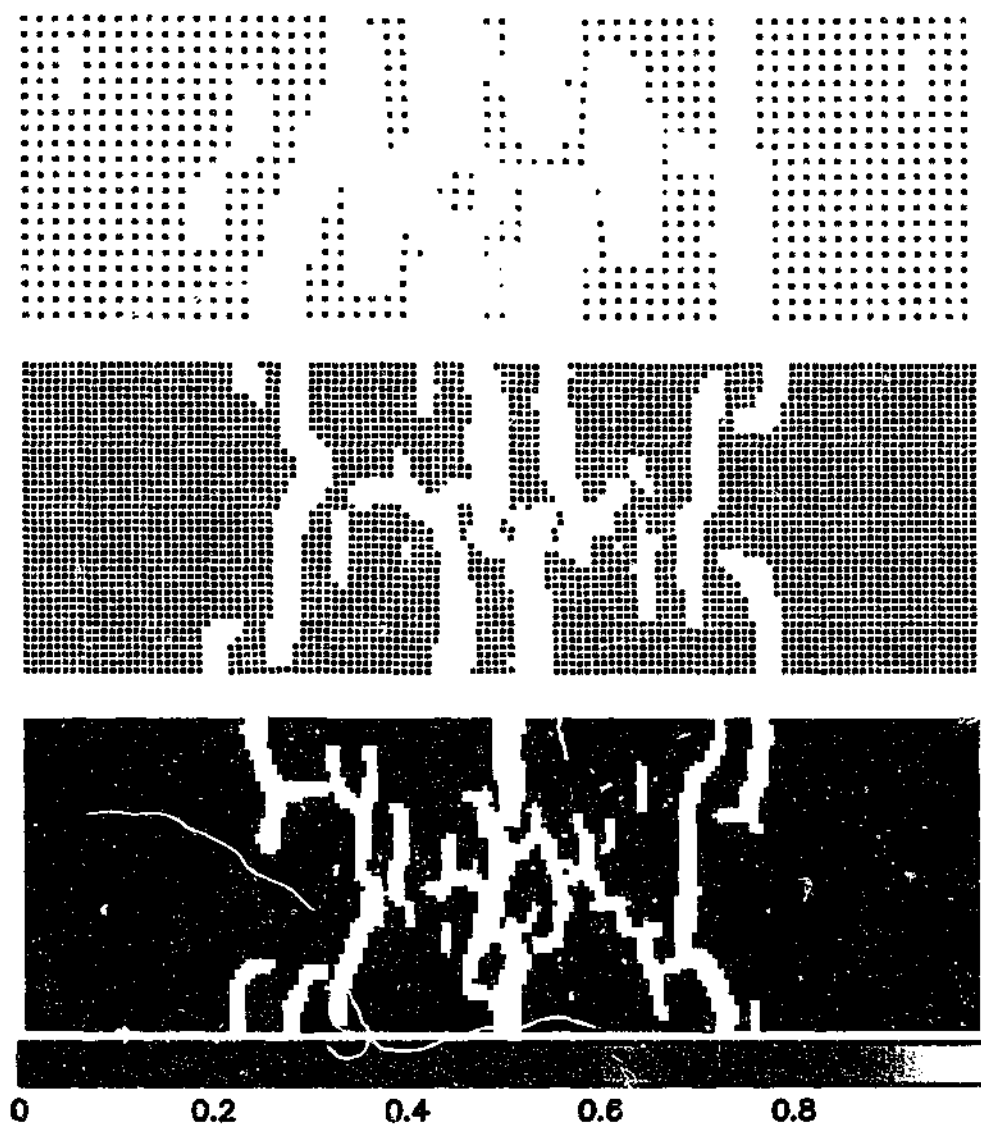
Figure 6.22: *Tes. of different particle resolutions. Material parameters of $\mu =$ 0.3, $Y_o = 0.03$, $k = 1.4 \times 10^{19}$ and $m = 8.5$. Simulation includes an artificial stress with $\epsilon := 0.3$, and beam ends ar: stretched with the constant velocity $V_f = 5 \times 10^{-3}$, $\Delta p = 0.05$, 0.025 and 0.0167, at the scaled times of 4.208, 4.228 and 4.201 respectively from the top to bottom frame. Note the much more extensive crack patterns due to a larger strain rate.*

6.5   Stress Concentration Around Holes

As we wish to investigate the fracture around chambers, the correct modelling of the stress fields around holes is vital. The stresses around a circular hole of radius a, with a tensile stress at infinity of p_1 in the x direction and no stress at infinity in the y direction are given by Jaeger (1964) (pg.187).

$$\sigma_{rr} = \frac{1}{2}p_1 \left(\left(1 - \frac{a^2}{r^2} \right) + \left(1 - \frac{4a^2}{r^2} + \frac{3a^4}{r^4} \right) \cos 2\theta \right)$$

$$\sigma^{\theta\theta} = \frac{1}{2}p_1 \left(\left(1 + \frac{a^2}{r^2} \right) - \left(1 + \frac{3a^4}{r^4} \right) \cos 2\theta \right) \tag{6.19}$$

$$\sigma^{r\theta} = -\frac{1}{2}p_1 \left(1 + \frac{2a^2}{r^2} - \frac{3a^4}{r^4} \right) \sin 2\theta$$

We saw earlier (in section 6.1) that the sum of the diagonal elements of a stress tensor, is invariant to a rotation of axes and is thus an appropriate measure of the stress field. We refer to this as the *mean stress* field.

$$\sigma_{mean} = Trace(\sigma^{ij}) = \sigma^{rr} + \sigma^{\theta\theta} = p_1 \left(1 - 2\frac{a^2}{r^2}\cos 2\theta \right). \tag{6.20}$$

Far away from the hole ($a^2 \ll r^2$) we find $\sigma_{mean} = p_1$, this corresponds to the applied boundary condition. For the boundary of the cavity ($a^2 = r^2$) the mean stress oscillates, it is a minimum of $-p_1$ when $\theta = 0$. When $\theta = \pi/4$ the mean stress is equal to the applied stress. The maximum stress concentration occurs when $\theta = \pi/2$ where $\sigma_{mean} = 3p_1$.

These qualitative effects are seen in figure 6.23 where we compare the analytic result (6.20) with the results of an SPH calculation (right frame). The stresses have been normalised by dividing by the stress at infinity p_1, so that the colours in the figure illustrate the areas of stress concentration.

The SPH calculation was performed on a grid $7cm \times 7cm$, with resolution of 140×140 particles. The stress is applied by moving the ends of the block at a constant strain rate as with the beams in section 6.4.2. The ends of the block were moved with a velocity $V_f = 5 \times 10^{-6}$ in the horizontal direction. The radius a of the circle was such that $a^2 = 0.3125cm^2$.

Stress is relieved on either side of the hole in the horizontal direction, with a high stress concentration perpendicular to the applied stress. This is consistent with the
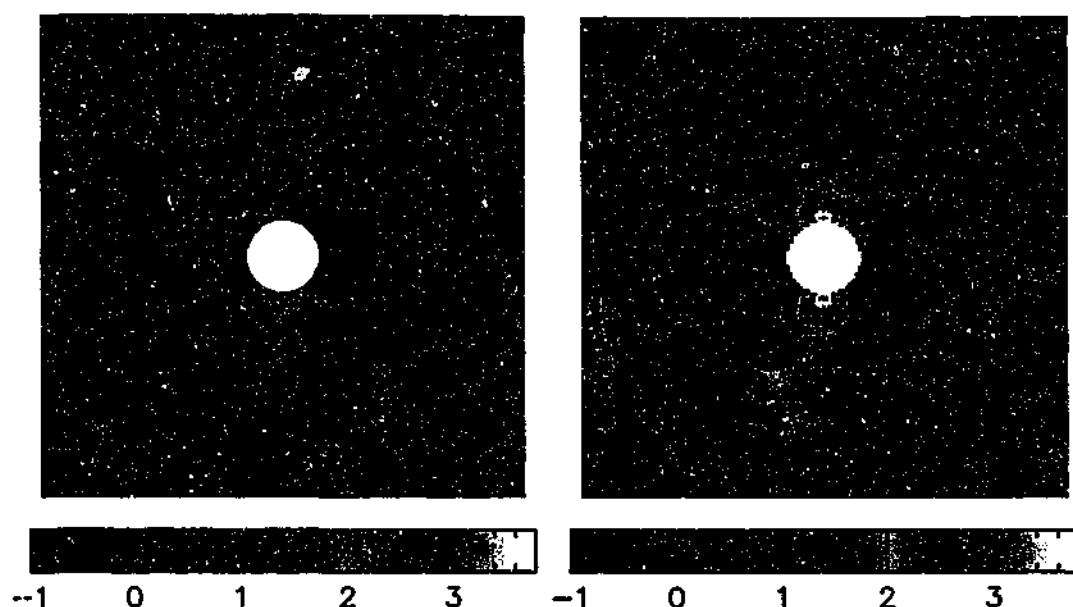
Figure 6.23: *Comparison to analytic solution on the left and and SPH simulation on the right for the mean stress concentration around a circular hole.*

idea that active flaws in a material relieve the stress in a circular area around the collection of flaws (section 5.5).

The major difference from the analytic result is that there is some noise at the point of maximum stress concentration and the maximum numerical stress concentration (3.8) is slightly higher than the analytic result (3.0) in part due to this.

We do not expect an exact comparison as our numerical discretisation of the circular cavity is arranged on a Cartesian grid and the edges of our numerical cavity do not agree exactly with those in the analytic solution.

One of the assumptions of the analytic solution is that the hole is in an *infinite* material. Increasing the size of the numerical domain to place these boundaries further away from the cavity has minimal effect on the computations. It appears then that the boundaries are sufficiently far away from the cavity to fulfill this assumption.

6.6   Solid Body Code Summary

In this chapter we have tested our code to model the dynamics of solid bodies using the method of adding an artificial stress to remedy the tensile instability for a range of problems. We started with the problem of colliding rubber balls and showed that artificial fracturing occurred in the standard SPH case. We have further shown that this artificial fracturing can be removed with the addition of an artificial stress (5.3) that prevents the clumping of particles which leads to an instability for particles that are in tension. The SPH results are also compared to the TOODY finite difference results of Swegle (1992).

In section 6.2 we look at the shape and dynamics of oscillating beams, comparing SPH results tu those of the Euler-Bernoulli theory. In section 6.3 we introduce plasticity to these oscillating beams. We show that permanent deformation can be modelled using the Von Mises yielding criterion.

This is followed by a look at plates being stretched in tension in section 6.4. We begin by illustrating the effects of the tensile instability in standard SPH. The beam is seen to fracture due to this numerical instability in a non-physical way. This numerical instability is then removed with an artificial stress. The material necks and fractures at a much later time and at a much larger strain. Although the final stages are not consistent with the continuum equations (pure elasticity/plasticity, no fracture model), the fracture can be understood from the numerical resolution being such that the particle nature of the SPH code takes over. The particles making up the beam are eventually drawn so far apart that they lose contact and break.

Our attention is turned to incorporating the fracture model of Benz and Asphaug (1994) into our code to handle brittle fracture. Cracks are seen to form and propagate realistically. We compare our results with the fragment size distribution of the Grady-Kipp statistical model. We find qualitative agreement with the statistical distribution. Fractures become more disordered and the fragment size decreases as the strain rate increases. The predicted fragment sizes agree with our computations.

The correct calculation of the concentration of stress bought about by cavities and cracks is vital for the simulation of fracture around magma chambers. In section 6.5 we find good agreement between the SPH calculation of the stress concentration field around a circular cavity and the analytic solution.

As in the fluid dynamics case we have seen that the SPH algorithm and our

computer programs are able to properly simulate some simple test problems and we can be confident that they will be suitable to handle the magma chamber fracture problems in the next chapter.

Chapter 7

Magma Chambers and Fracture

n this chapter we investigate the formation of cracks around magma chambers and the relation of these cracks to caldera collapse. A complete analysis and solution of the broad problem of rock fracture during caldera collapse is beyond the scope of this work and is not presented here. The suitability of the SPH method for these applications is examined by studying simple two dimensional systems.

The literature on volcanic eruptions and caldera collapse is large and we do not aim to give a complete account. In this chapter we discuss the basic background of the physics and cause of caldera collapse events and illustrate the possible areas to which the SPH numerical method can be applied. A more complete account of the caldera collapse problem remains to be completed as further work.

7.1 Background

We discuss some of the issues related to the eruption of volcanoes and caldera collapse. A general text such as Francis (1993) gives a basic understanding of many of the issues discussed in this section. The paper by Smith and Bailey (1968) gives a good description of the basic events that are associated with caldera forming eruptions. Most of the discussion in this section relates to the simple case of piston subsidence, even though other more complicated collapse forms can also occur (Lipman 1997).

In figure 7.1 we show a schematic illustration of a normal ring fault bound caldera. Normal faults are inward dipping faults that occur in tensional environments. Fractures form in the country rock that lead to the formation of ring faults surrounding a central block. The central block then subsides into the chamber.

The first step in determining the crack patterns that occur around magma chambers is to know the appropriate stresses which lead to their formation. Once we know
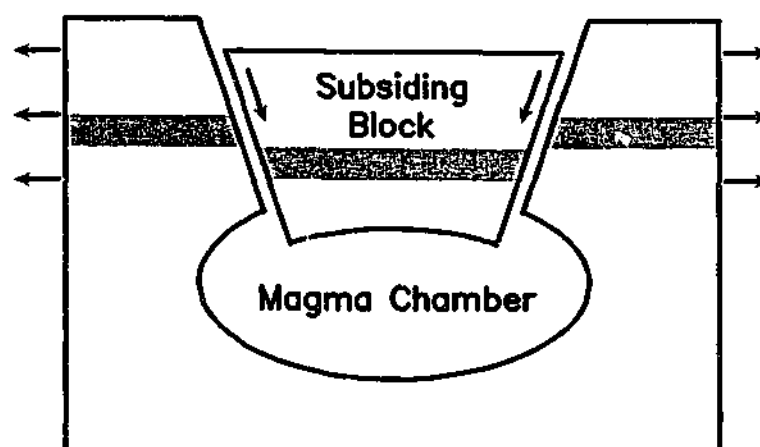
*Figure 7.1: Schematic diagram of a normal fault caldera. A tensional environ-
ment in the country rock leads to the occurrence of inward dipping ring
faults and the subsidence of a central piston of rock into the magma
chamber.*

these stresses we can define suitable boundary conditions for our numerical models.

7.1.1 Appropriate Boundary Stress Conditions

The mechanisms of collapse are complicated. The specific conditions and mechanism
of one particular case may be completely different to the conditions and mechanisms
of other calderas. A common feature of many calderas are the formation of ring
fractures around a block of material. This central block becomes detached from
surrounding rock and then subsides into the magma chamber which has become
partially evacuated due to the eruption of magma (Smith and Bailey 1968; Druitt
and Sparks 1984).

One theory for the development of ring type fractures is that they occur in
situations where the extension of the country rock surrounding a magma chamber
leads to a concentration of stress at the Earth's surface above the magma chamber
(Gudmundsson 1998). Faults form at places where the stress is large and propagate
down to the chamber, if these faults bound a block of material above the magma
chamber it is able to subside into the chamber. The tensional extension of the
country rock may be due to inflation of the magma chamber (Smith and Bailey 1968;
Druitt and Sparks 1984) or extension at a divergent plate boundary (Gudmundsson

1988).

Intrusions occur when magma moves into pre-existing rock. Dykes form when the pressure of a magma body leads to cracks forming in the rock around the magma chamber and magma is injected into these cracks. These dykes are known as ring dykes if they take on a roughly circular shape at the surface. They can occur along vertical or conical lines. They also occur in cases where the magma is pushed up into previously formed tensile fractures.

An alternative explanation for the development of ring fractures is that a ring dyke may propagate from the magma chamber to the Earth's surface detaching the block from its surroundings and allowing it to subside. A combination of the two regimes is also possible, an upward moving ring dyke may intersect with a downward moving fault. Likewise an older fault in the rock (unrelated to collapse causing volcanism) may be intercepted and lead to subsidence.

The doming of the surface of the Earth has been proposed (Smith and Bailey 1968; Komuro, Fujita, and Kodama 1984; Komuro 1987) as another possible cause of fractures. Doming refers to an uplift of the Earth's surface, possibly due to the rise and thermal expansion of underground magma (Komuro, Fujita, and Kodama 1984). The uplift is in someways analogous to the bending of a plate. We saw in section 6.2 that the bending of a plate leads to a tensional environment on one side of the plate and compression on the other. Tensile fractures at the Earth's surface can form if doming is sufficiently large. From field evidence the doming has to occur over a region much larger than that of the caldera that undergoes collapse for ring faults to form (Smith and Bailey 1968; Druitt and Sparks 1984; Komuro, Fujita, and Kodama 1984).

Our next question is *What are the conditions inside a magma chamber that lead to dyke injection?* High pressures are able to accumulate inside magma chambers. Explosive eruptions occur when the pressure inside a magma chamber exceeds the tensile strength of the overlying rock (Francis 1993) (pg.167). The magma pressure leads to fracturing of the rock, magma breaks through the rock and is ejected at high speed. Lava forming eruptions also involve an internal magma chamber pressure greater that the strength of the overlying rock though the magma is ejected at much lower speeds.

The pressure can be a result of the exsolution of volatiles from a rising magma (Sparks 1978; Wilson 1980) or an injection of extra magma into the chamber from

another source. The mechanism of the exsolution of volatiles is complicated. A magma contains an amount of volatile gases such as water and carbon dioxide, as the magma rises and/or lithostatic pressure decreases volatile liquids become exsolved (separated) from the magma, gas bubbles are produced through boiling. The gas bubbles grow, leading to a volume and pressure increase in the magma. Exsolution may also occur when a cooling magma crystallises, leading to volatile saturation in the residual magma.

In appendix A we have shown that the thermodynamic effects of magma on a large amount of water are minimal, because an insulating skin of solid material forms around the magma. However, large explosive effects are possible if small amounts of ground water mix with magma (Colgate and Sigurgeirsson 1973; Sheridan and Wohletz 1983). Self sustaining mixing of magma and water can lead to a pressure increase via the vaporisation of water under certain conditions.

Thermodynamic considerations are important in both the determination of the correct boundary conditions that should be applied to the rock and the effects that temperature has on crack propagation. The exsolution of gas from magma (Turcotte et al. 1990) and explosions caused in the interaction between water and magma that can lead to violent self sustaining mixing (Colgate and Sigurgeirsson 1973) are events which are heavily reliant on the physics of thermodynamics. As we presently only wish to model the effects of the thermodynamics (which applies pressure to the boundary of the rock) we simplify our analysis and computations by neglecting thermodynamic effects

The stress concentration at the very tip of a sharp crack are high and lead to further crack propagation (Ashby and Jones 1980) (pg.130). The stress concentration around a blunt or rounded tip is much lower and cracks are less likely to propagate. A hot magma that has propagated to the tip of a crack in a rock of low melting temperature may lead to the melting and blunting of the tip leading to a lower stress concentration, inhibiting crack growth. Rock properties such as ductility and ultimate strength are also known to be temperature and pressure dependent (Handin and Hager 1958; Griggs, Turner, and Heard 1960). We acknowledge that these factors can be important though we do neglect them in our computations.

Just as a column of water attains hydrostatic balance to give equilibrium between gravitational and pressure forces, the pressure of rock in the Earth's crust acquires what is known as lithostatic balance. We have conducted tests that show that in the

cases we present the inclusion of gravitational effects lead to only minimal differences in the crack patterns that form.

In our two dimensional calculations we expect ring faults to occur as two vertical or angled fractures a distance apart. If the faults are close together they are then more like a central vent from which magma can erupt but caldera collapse is unlikely to occur.

In the next two subsections we review the results of previous experimental and numerical studies into the mechanisms of caldera collapse.

7.1.2   Previous Experimental Studies

Many experimental investigations into the mechanisms of caldera collapse have been conducted (see Komuro 1987, Marti et al. 1994, Roche, Druitt, and Merle 2000). The experiments in these investigations are all based along similar lines, and while conceptually simple they are able to provide good results. The basic idea is to model the brittle rock with a tank full of a powder such as sand. Forces are applied to the sand to simulate events such as pre-collapse doming and collapse caused by the withdrawal of magmatic support. The method of applying the forces varies for each study.

While the use of a material such as sand to model solid brittle rock may seem inappropriate, these are scaled experiments and the strength of the sand turns out to be approximately appropriate for rocks on a larger scale (Marti et al. 1994).

Komuro (1987) looked at the doming effects of an ascending magma body by moving a ball of clay up through the sand. Uplift (doming) of the sand occurs above the ball and surface fractures develop radially from the centre of the dome. These radial fractures are then intersected by the development of fractures which form perpendicular to the radial fractures and eventually form a polygonal ring fracture (a ring fracture made up of a series of short straight fractures).

Komuro (1987) also modelled the withdrawal of magmatic support with the evaporation of dry ice under the sand. The evaporation leaves a cavity and a collapse structure develops. The structure collapses by a ring fault moving upwards to the surface boundary from the magma chamber.

The investigations of Marti et al. (1994) involved balloons covered by sand, the balloons were able to be inflated and deflated. Adjustments in balloon pressure

simulate doming and collapse. A significant difference from the experiments of Komuro (1987) is that the powder consists of layers of sand of different colours and cross sections are viewed to analyse the subsurface movement and fracture patterns.

Pre-collapse doming is again seen to lead to the formation of radial fractures at the surface, although they do not propagate very deeply. Doming leads to a series of inward dipping faults that do not quite reach the surface. These faults propagate from the magma chamber and may be analogous to the formation of ring dykes. Subsequent collapse leads to the reactivation of and subsidence along these faults.

The fracture structures that form when doming is not simulated before the collapse are different, primarily because there are no pre-existing faults along which the subsiding block can slip. The confining faults of the subsiding block are much clearer and more vertical, the extent of subsidence is also larger with the block subsiding to deeper levels.

Roche, Druitt, and Merle (2000) present a series of two and three dimensional experiments using sand and silicon to model the formation of a caldera. They use silicon to model the magma instead of a balloon. The pressure of the silicon is reduced and the sand subsides into the silicon cavity. These experiments indicate differences in the ways that fractures develop dependent on the aspect ratio of the chamber. For low aspect ratio roofs, where the depth of overlying rock is less than the width of the magma chamber, one set of ring faults develop propagating upwards from the magma chamber. Higher aspect ratios subside through a series of faults. As one set of fractures is unable to fracture the entire depth of overlying rock, the subsiding block is delineated from its surroundings by a series of upward moving faults.

7.1.3   Previous Numerical Studies

Using a boundary element method Gudmundsson, Marti, and Turon (1997) and Gudmundsson (1998) studied the stress fields generated around a simplified magma chamber and implications of these stresses on the formation of ring fractures. The volcano is modelled as a two dimensional structure containing a hole (magma chamber) to which external stresses are applied. Fracturing is inferred to occur at regions of high stress, but the fractures and their growth are not explicitly modelled.

Doming caused by a large scale magma reservoir underneath the chamber is

modelled by applying a vertical stress to the base of the plate modelling the rock surrounding the chamber. This configuration was found to lead to the initiation of ring fractures at the surface. The points of maximum stress can occur at the surface at points horizontally removed from the point directly above the centre of the chamber. Fractures at these points can propagate down to the chamber as ring faults.

Ring faults may also develop when fractures caused by an extension at the surface propagate down towards the chamber. Extension of the country rock is handled by applying a horizontal tensile stress to the ends of the rock. This configuration can also lead to surface stresses which are conducive to the formation of ring fractures.

Ring faults are presumed to be unable to be generated at the rock/magma chamber interface as the injection of magma into dykes leads to a pressure decrease and the dykes may not reach the surface. Gudmundsson (1998) infers that as ring faults which lead to subsidence are not initiated at the magma chamber, (due to these forming intrusions which do not reach the surface) the internal pressure of the magma chamber cannot lead to ring fault production. This is because in this case the maximum surface stress and displacement occurs at the centre of the chamber and is unlikely to lead to fractures forming far enough apart to lead to ring faulting.

7.2 Basic Model Features

In the previous section we have described the features that are important to the formation of fractures in the rock surrounding magma chambers. In this section we present a numerical investigation of these features. The important factors are:

- **Tensional extension of country rock** It is well established that many volcanoes exist near the boundaries of crustal plates (Francis 1993) (pg.17), which means that the tension or extension of country rock can play an important role in the development of volcanoes.

- **Large scale doming caused by an underground magma reservoir** We have also previously noted that the doming caused by a magma reservoir of a scale around three times greater than the magma chamber is a possible cause of the formation of ring faults. We do not investigate it here although its effects could be modelled with the SPH technique.

- **Internal pressure from magma inside chamber** Although Gudmundsson (1998) believes that ring dykes are unable to lead to ring faults we investigate the possibility here. Wisser (1927) studied the subsidence and fracturing in limestone overlaying ore bodies that have shrunk due to oxidation and the fractures propagate up from the cavity. The experimental studies we discussed in the previous section found that in general collapse occurred on faults that had propagated upwards from the chamber.

- **Stress concentration around magma chamber** Another important factor is the concentration of applied stresses caused by the shape and positioning of the magma chamber. This is important as the stress concentration means that fracture can occur at lower strains.

In this section we numerically investigate the effects of these features. The simulations are set up similar to those for the stress concentration around a hole (section 6.5) except that these calculations now incorporate the Benz-Asphaug damage model (section 5.5). The damage model is used to simulate the initiation and propagation of fractures in the rock.

Flaws are assigned randomly to each particle but in each of the examples in this section each particle has the same flaw assignment. This ensures that weak spots in the material are the same in each case and that differences are due to the applied boundary conditions. Tension is placed on the material by moving the horizontal ends of the material with the dimensionless velocity $V_f = 1 \times 10^{-5}$ in the dimensionless units described in section 5.4. The model block had dimensions $7cm \times 7cm$, with a hole of radius a at its centre in the two cases were cavities where included. The radius a is determined from $a^2 = 0.3125cm^2$.

The lengthscale over which these computations are conducted ($\sim 10cm$) is much smaller than the lengthscale appropriate for actual caldera events ($\sim 10km$). As the primary purpose of this section is to illustrate the effects of stress concentrators and internal magmatic pressure on the fracture of a material structure, the actual size of the block is somewhat unimportant. It is important however that the calculations can be scaled up to the larger geological lengthscale.

The major problem in scaling the present calculations up to a larger lengthscale is to be able to sufficiently resolve the formation of cracks. The small scale calculations in this section have the advantage that they are able to resolve the formation of

smaller cracks for an equal number of particles in the simulation. In the present cases we have a particle spacing of $0.05cm$, and are able to resolve cracks in the order of this size. In a simulation of a larger block $7km \times 7km$ with the same number of particles we can only resolve cracks in the order of $50m$ wide (which is still a reasonable lengthscale for some flaws). Ideally, we would increase the number of particles used in the larger lengthscale case to obtain better resolution, although this quickly becomes computationally prohibitive when using a serial code. We do note that as the results of later calculations (section 7.4) on a geological lengthscale are qualitatively similar to the present case that it does appear to be possible to scale the present calculations up to a larger lengthscale.

In figure 7.2 we see the case of a block of material without a stress concentrating chamber present. In the first frame the block is in tension and no significant damage has been accumulated. Cracks have developed by the second frame, one crack near the centre of the block and another in the top right hand corner. The reduction of stress in an approximately circular area around these cracks can be clearly seen (note the discussion preceding (5.38)).

The crack initiated near the middle propagates through the block. The crack from the top is allowed to travel half way through the block before stopping when the stress has been relieved by the other crack. A crack also forms as an offshoot of this upper crack propagating parallel to the applied stress. This is likely to be due to the stress field being disrupted by the formation of the cracks.

Particles in this section are coloured by the mean stress $(\sigma^{xx} + \sigma^{yy})$. Note that the colour scale representing stress is the same for each example in this section although the stress concentration at the very tip of the cracks can exceed the given range and has not been plotted to allow more detail of the stress field to be shown in the remainder of the material.

We introduce a circular cavity which has the effect of concentrating the stress in figure 7.3, otherwise conditions are as for figure 7.2. Fracture first occurs at the base of the chamber where the stress concentration is largest (section 6.5). The stress concentration is also the same at the top of the chamber and the reason for a crack not being initiated here at the same time is that flaws are distributed at random and by chance there are weaker flaws in the material at the bottom of the chamber. A crack is initiated shortly afterwards at the top of the chamber and the block is quickly split into two pieces by two straight fractures originating at the

cavity. Notice that in this case the fractures occurred at a much earlier time in this case ($T \sim 105$) than in the case with no cavity present in the material ($T \sim 250$). This is due to the cavity being a stress concentrator leading to higher stresses for the same applied strain. As with most of the quantities in this chapter the units of time are given in the dimensionless units of section 5.4.

We also recall from (6.20) that the perturbation to the applied mean stress caused by a circular hole scales as ($1/r^2$). We therefore expect that at large distances from the hole that the stress field will be largely unchanged and (as the top surface of the material is far from the hole) it follows that we expect cracks to be first initiated near the stress concentration and not at the surface of the block.

In the final case for this section we investigate the effects of internal pressure inside the cavity. We place a gas in the chamber with the equation of state

$$P = \rho c_{gas}^2 \tag{7.1}$$

where we take $c_{gas} = c_s/80$. This is equivalent to an overpressure of the magma inside a chamber i.e. it applies a pressure to the surface of the chamber.

As we can see from figure 7.4 the internal pressure increases the stresses around the cavity. It is not surprising then that the fractures are initiated earlier ($T \sim 80$) than the case with no pressure in the cavity. The cracks then propagate and relieve the tensile stress in much the same way as the previous case. We next find that several small cracks originate around the internal cavity due to the internal pressure

In summary, the computations in this section appear to exhibit sensible behaviour, in particular the simulations have shown:

- The block without a cavity to concentrate the stress undergoes fractures in essentially random places.

- The inclusion of a cavity means that fracture first occurs at points of highest stress concentration. The stress concentration caused by a cavity is seen to focus the areas in which fractures occur.

- The inclusion of internal pressure in this cavity leads to higher stresses around this cavity and fracture being initiated at lower tensile strains. It also leads to a series of fractures in radial directions being initiated at the cavity. It is possible that these radial fractures represent ring dykes in a volcanic system.

Time =237.0   Time =252.0

−5×10⁻³ 0   5×10⁻³ 0.01   −5×10⁻³ 0   5×10⁻³ 0.01

Time =257.9   Time =266.9

−5×10⁻³ 0   5×10⁻³ 0.01   −5×10⁻³ 0   5×10⁻³ 0.01
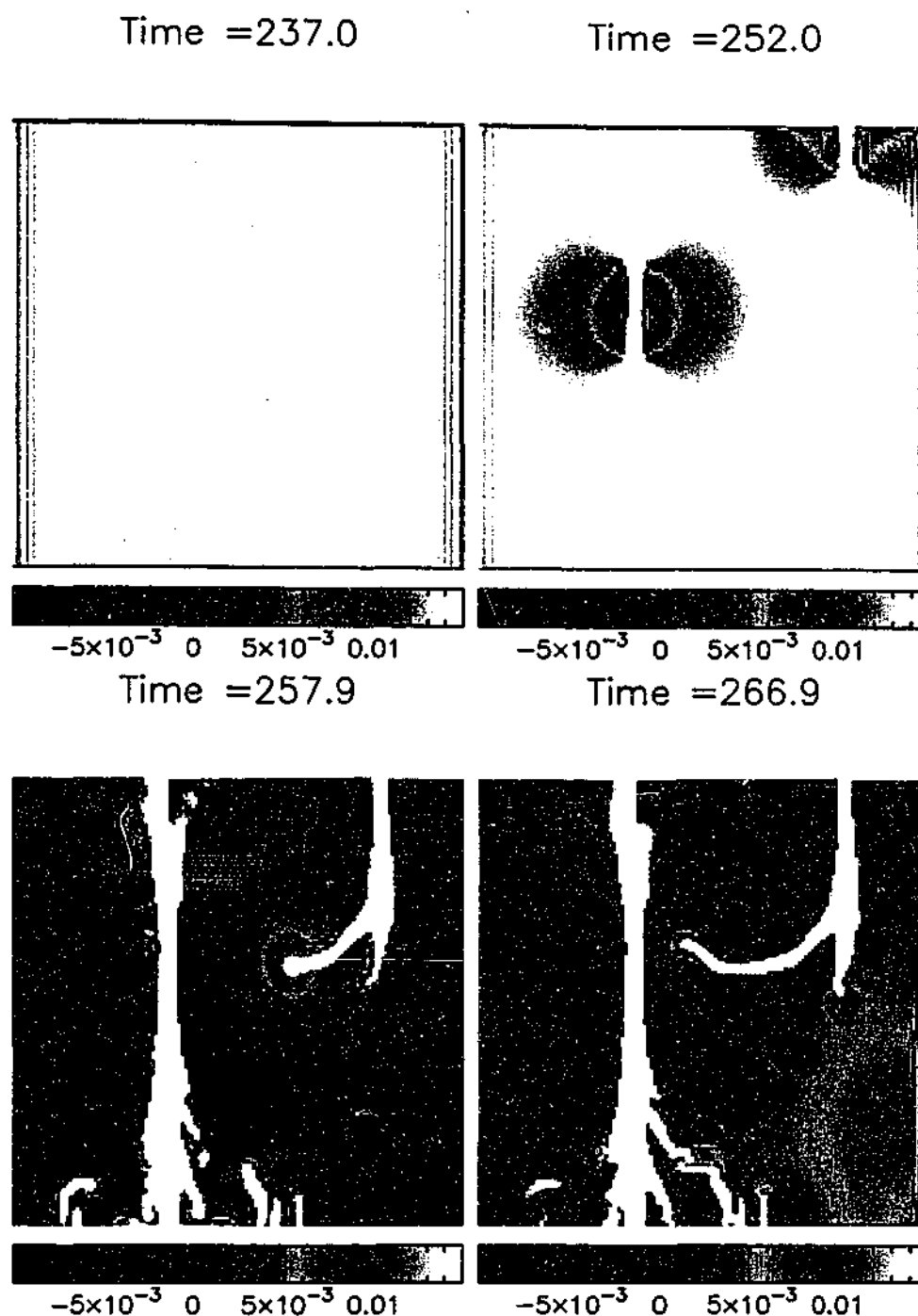
Figure 7.2: *Effect of tensile strain on a block of material containing flaws. A vertical cross section is shown of dimension 7.0cm×7.0cm. The tensile strain is applied by moving the ends with the velocity $V_f = 1 \times 10^{-4}$. Fractures develop in weak spots in the material. $\mu = 0.85$, $Y_o = 0.01$, $k = 1.4 \times 10^{19}$, $m = 8.5$, $\Delta p = 0.05$.*

Time =101.9   Time =104.9

−5×10⁻³ 0   5×10⁻³ 0.01   −5×10⁻³ 0   5×10⁻³ 0.01

Time =110.9   Time =116.8

−5×10⁻³ 0   5×10⁻³ 0.01   −5×10⁻³ 0   5×10⁻³ 0.01
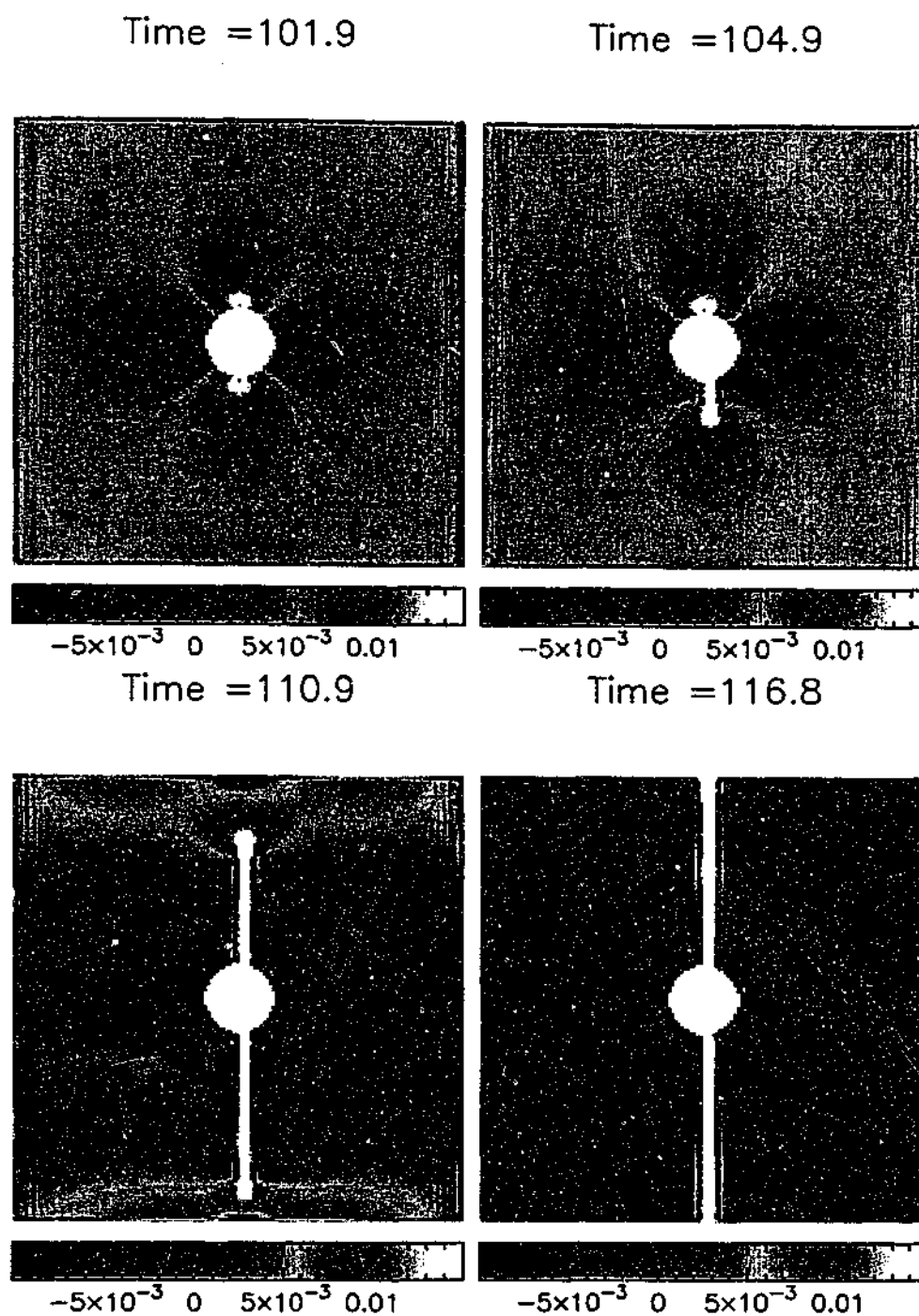
Figure 7.3: *Effect of introducing a hole as a stress concentration on the block*
of figure 7.2. Fracture is initiated earlier due to the concentration
of stress and fractures occur at points of highest stress concentration.
Radius of hole $a = \sqrt{0.3125}$ otherwise parameters as for figure 7.2.

Time = 77.9   Time = 80.9

-5×10^{-3} 0 5×10^{-3} 0.01 -5×10^{-3} 0 5×10^{-3} 0.01

Time = 98.8   Time =176.5

-5×10^{-3} 0 5×10^{-3} 0.01 -5×10^{-3} 0 5×10^{-3} 0.01
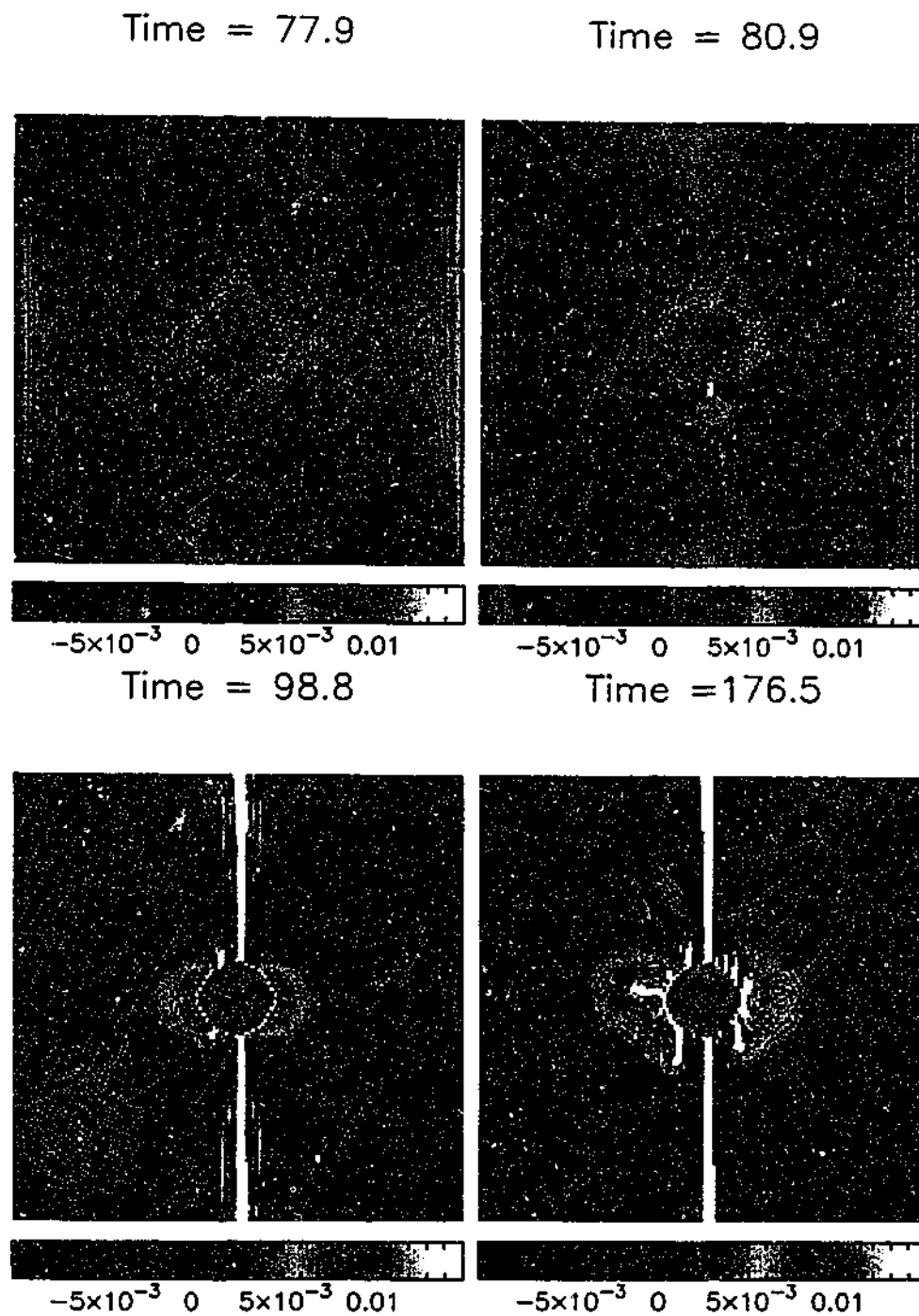
Figure 7.4: *Effect of introducing an internal pressure into the stress concentrating hole of figure 7.3. Fracture is again initiated at points of highest stress concentration. Internal pressure leads to several small fractures occurring near the hole. Parameters as for figure 7.3.*

7.3   Effect of Magma Chamber Depth

Here we investigate the effect of surface stresses for an elliptical chamber placed at varying depths below the surface. We consider an elliptical magma chamber with a horizontal semi-major axis $1.3a$ and a vertical semi-minor axis a placed in a block of material which is horizontally stretched in tension. We place the chamber at three different depths below the surface. The chamber is empty, and the only applied stress is tension.

Gudmundsson, Marti, and Turon (1997) and Gudmundsson (1998) assumed that ring faults were caused by tensional fractures being produced at the surface and propagating down to the chamber. The main criteria used for the initiation of a ring fault is that the maximum surface stress concentration must occur at a radial distance away from the free surface point above the centre of the cavity, otherwise fracturing will lead to a central vent instead of a ring fracture. We investigate the stress fields here using SPH calculations.

In figure 7.5 we illustrate the change in surface stress concentration for an elliptical magma chamber at three different depths. We find that there are two maximums of the surface mean stress concentration which occur a distance from the centre of the chamber. The minimum occurs at a point above the centre of the chamber at which point the stress is less than the applied stress. This is consistent with the results of Gudmundsson, Marti, and Turon (1997).

We find that as the depth at which the chamber is situated is increased the surface stress concentration decreases. This is not all that surprising. In section 6.5 we studied the stress concentration around a circular hole and saw in (6.20) that in an infinite medium the deviation in the applied stress decreased proportional to $1/r^2$, where r is the distance from the centre of the hole. A similar proportional decrease is to be expected in this case.

We do not expect exact agreement with a $1/r^2$ decrease as our boundaries are at a finite distance. We do find that the surface stress concentration increases with decreasing chamber depth and that the rate of this increase is larger for smaller depths. This is consistent with a law of the type $1/r^2$ decrease.

We find the maximum surface stress concentration to have values of 2.19, 1.24 and 1.02 for depths of the centre of the ellipse of $1.9a$, $3.1a$ and $4.4a$ below the surface. The distance that the maximum occurs from the surface point directly above the

centre of the chamber increases with increasing chamber depth. This implies that the greater the depth of a chamber, faults propagating from the surface are more likely to be produce ring faults, as the propagating faults are a significant distance apart. However, the magnitude of the surface stress concentration and likelihood of fault formation decreases with increasing magma chamber depth. These findings are consistent with the boundary element models of Gudmundsson (1998).
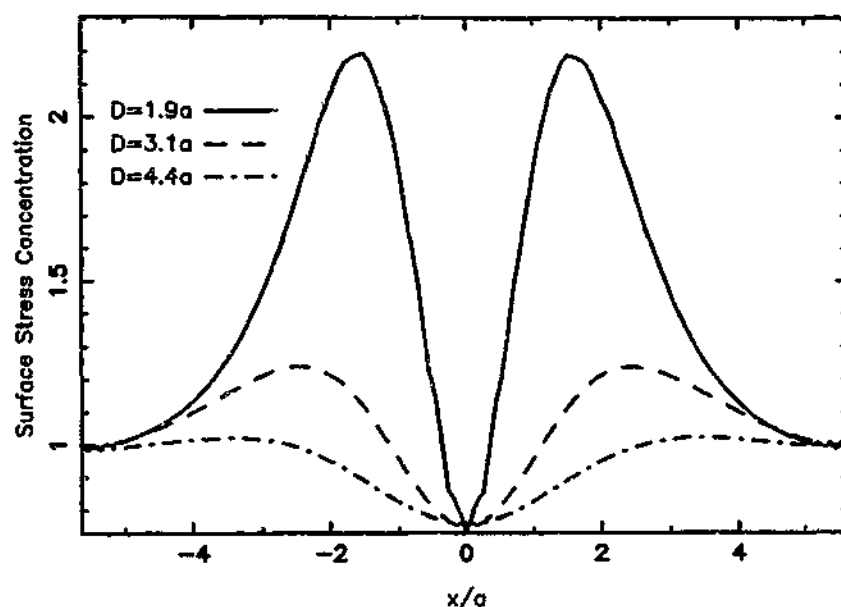
Figure 7.5: *Surface stress concentration above an elliptical cavity at varying depths (D) of the centre of the ellipse below the surface, where the country rock is stretched in tension. A scaled measure (x/a) of horizontal distance is used, x/a = 0 refers to the point at the surface directly above the centre of the cavity. The cavity has a vertical semi minor axis of height a and horizontal semi major axis of length 1.3a. The surface stress concentration has two maximums away from the cavity centre. The distance between these maximums increases and the stress concentration decreases with increasing cavity depth.*

7.4   Caldera Models

In this section we illustrate the suitability of the SPH method to handle the problems of the initiation and propagation of fractures and faults around magma chambers.

As we have remarked earlier we do not present a complete account of the problem and the relevance of our numerical results to field studies, but do show the potential for its use in these areas.

We model a rectangular area of rock $7km$ wide by $4.9km$ high. With an elliptical magma chamber centered at a point $3.5km$ from the bottom in the middle of the chamber. We take $k = 1.4 \times 10^{19}$ and $m = 8.5$, flaws have a radius of $75m$, the weakest flaws are activated at strains exceeding 6×10^{-4}. Our ellipses each have semi-major axis of $1.75km$ in the horizontal direction. Our first examples contain ellipses with semi-minor axis $0.8km$ high in the vertical direction. The final ellipse has a semi-minor axis of $1.12km$ which gives both a bigger ellipse and an edge which is closer to the surface.

We begin by placing the rock into tension. Stretching each end with the velocity V_f in the horizontal direction up until the dimensionless time $T = 1 \times 10^7$ after which the ends are kept stationary. We stop the stretching at this time as we want to include the effects of a tensional environment, but also wish to be able to differentiate between fractures caused by a tensional environment and those due to internal pressure in the chamber and doming above the chamber.

We fill the elliptical chamber with a gas which exerts pressure on the rock. The equation of state of the gas is given by (7.1). Initially we take $c_{gas}^2 = 5 \times 10^{-5}c_s^2$, at the time $T = 1 \times 10^7$ we increase the pressure by setting $c_{gas}^2 = 1 \times 10^{-4}c_s^2$. The gas is representative of the pressure exerted by magma. The sudden increase in pressure is due to causes such as the exsolution of gas or steam eruptions. We find that the stress induced around a chamber with internal pressure, stretched with the velocity $V_f = 1 \times 10^{-5}$ is typically 5×10^{-4} in our dimensionless coordinates when $T = 10^7$. A typical stress before $T = 10^7$ in the case of no strain but with internal pressure is $\sigma_{typ} = 4 \times 10^4$ increasing to $\sigma_{typ} = 10^{-3}$ after the pressure has been increased.

We consider calculations similar to those found in Gudmundsson (1998), we do not consider the eruption of the magma and collapse of the chamber although these effects can be incorporated using the SPH method. Our calculations also neglect thermodynamic effects.

Simplifications have been made in these models so that we can gain an understanding of the effect of stress and fracture alone on collapse mechanisms. The models presented here are initially stretched in the horizontal direction. When the stretching is finished, pressure inside the chamber is increased. The stretching leads

to the rock accumulating damage and fractures. This leads to it being easier for effects local to the chamber to initiate fault formation and caldera collapse.

In our first example (figure 7.6) we take V_f equal to zero, there is no tension and the effects are only those due to the internal pressure. Minimal damage has occurred up until the time at which the pressure is increased. After this time we see fractures developing towards the upper edge of the chamber. These fractures grow and move upwards, they do not quite reach the surface. They can be considered to be similar to ring dykes. Doming of the surface means that the highest pressure is over the centre on the chamber. We notice an amount of damage accumulating there and a ring fault develops down towards the chamber, like the upward moving dykes, this fault does not quite reach the surface. We note that the upward moving dykes occur largely symmetrical.

In figure 7.7 we see an example with the country rock being in a tensional environment. We find the tension introduces a degree of asymmetry (with the two upward moving dykes propagating at different angles) even though tension has ceased before the fracturing begins. A dyke appears on the left moving upwards from the chamber. It develops at a more vertical angle (than the $V_f = 0.0$ case) and does reach the surface. A downward fracture develops down from the surface above the centre of the chamber. Again this fracture is vertical. Finally a fracture develops up from the chamber on the right hand side. Although this fracture grows at an angle much less than vertical. The strain rate of the material when it is being stretched in tension is 1.43×10^{11}, meaning that it has undergone strain of 1.43×10^{-4} when the velocity is set to zero.

A horizontal tensile strain rate of 1.43×10^{10} is used in figure 7.8. At this strain rate the material has undergone a strain of 1.43×10^{-3} before the tensile stress is removed and the internal pressure is increased. Unlike the previous cases (with lower strain rates) significant fractures have formed by this stage. A large degree of asymmetry has resulted from the higher strain rate. There are fractures originating from the cavity which have moved up towards the top surface and one down towards the bottom, these fractures are largely vertical. The strain has also lead to the formation of an upward moving dyke, this dyke halts its progression when the tensile strain rate is set to zero, but is reactivated on a shallower angle by the higher internal pressure.

Our final example uses the higher magma chamber which is also closer to the

surface (figure 7.9). The first fracture to develop is a downward moving fault from the centre of the chamber, not unsurprising as doming is much more prominent with the chamber being closer to the surface. A set of ring dykes appear at an almost vertical angle, quickly followed by a second set. The faults are then almost met by faults coming down from the surface which form due to doming and the damage surrounding the two sets of ring faults increases widening the area of the faults.

7.5   Summary and Conclusions

Cavities and cracks in a material lead to a distortion of an applied stress field, with a concentration of stress in particular areas and stresses being relieved in other areas. In section 7.2 we investigated the effects of stress concentrations due to a circular hole in a brittle material. These calculations are similar to those in section 6.5 where we compared the stress concentration around a hole in an elastic material with an analytic result, except that they incorporate a damage model. The introduction of a cavity is clearly shown to have a dramatic effect on the fracture mechanics, the stress concentration around the cavity focussing fractures to form in areas of high stress concentration.

We remarked earlier in this chapter that our aim is not to present an exhaustive investigation into the mechanisms of collapse, though we can still make some comments on these mechanisms. In section 7.3 we compare the SPH method to boundary element results of Gudmundsson, Marti, and Turon (1997) and Gudmundsson (1998) for the surface stress concentration above an elliptical chamber in an elastic material. In agreement with the results of Gudmundsson we found that for a shallow elliptical magma chamber (close to the free surface) that the surface stress concentration was high, however the maximum concentration occurs towards the centre of the chamber and is unlikely to lead to ring fault formation. As the depth of the chamber below the free surface is increased the maximum stress concentration occurs at distances away from the centre, faults initiated here are then likely to lead to the formation of ring faults as the fractures form a radial distance apart, with the drawback being that the amount of stress concentration at the surface is lower and a higher applied stress is required for faults to form.

The major problem with the analysis in section 7.3 is that there is an assumption

that fractures are initiated at a point of high stress and travel from the Earth's surface down to the magma chamber. An advantage of the SPH calculations in section 7.4 is that they incorporate a damage model which is able to explicitly follow crack formation and growth. The damage model is able to account for weaknesses in the rock which may lead to failure at points that may not necessarily correspond to the point of maximum stress.

We investigated the fracture around a chamber that was in placed in tension and was also subject to internal pressure. We found that as the strain rate (tensional stress) was increased faults were likely to occur at a more vertical angle. This is particularly important for piston type collapse events as subsidence is inhibited if normal faults occur at angles which are far from vertical. The positioning of the chamber closer to the surface was again seen to lead to a higher degree of fracturing due to a higher stress concentration.

The calculations we have conducted have shown that the mechanism of caldera collapse due to the initiation of ring faults at the Earth's surface does not on its own appear to be a likely mechanism. Fractures formed in this way usually occurred over the centre of the chamber and are unable to lead to ring faults, they may still possibly lead to collapse in conjunction with an upward moving dyke (figure 7.7). This is somewhat different to the work of Gudmundsson, Marti, and Turon (1997) and Gudmundsson (1998) who assumed that any fractures forming at the magma chamber would only lead to dyke formation and not ring faults. Although our study is not comprehensive and we cannot say so with certainty.

What we can conclude is that the mechanisms of collapse are complicated and is likely due to a range of different factors including chamber geometry, internal magmatic pressure, previous tectonic faults and regional doming. We further conclude that the SPH method has been shown to be able to handle the problem of caldera collapse with relative ease and is a suitable tool for further work in the area.

Time =1.08E+07   Time =1.11E+07

Time =1.17E+07   Time =1.32E+07
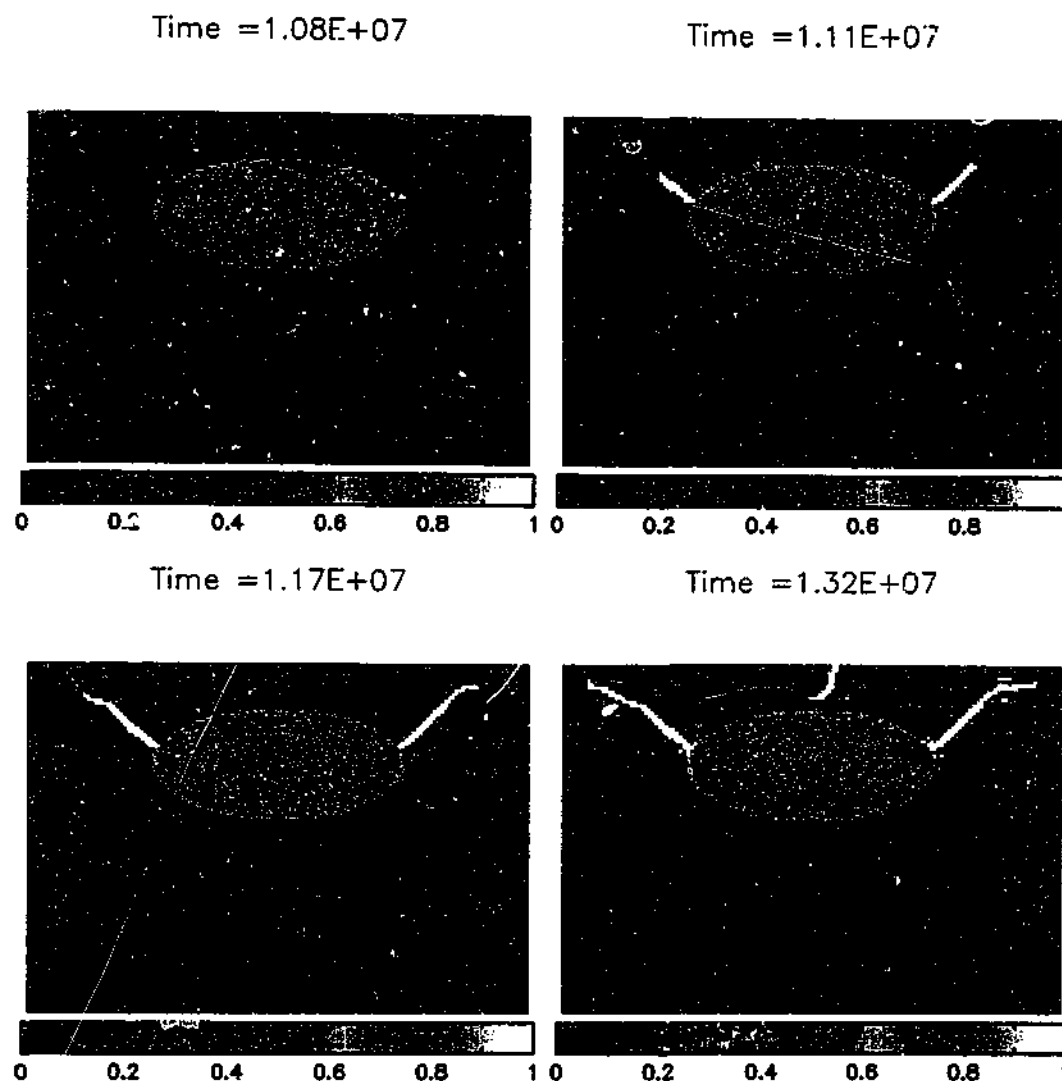
Figure 7.6: Effect of internal pressure with no extension of the country rock. Shortly the gas pressure is increased a fracture appears on the upper right surface of the cavity and propagates upwards, a similar fracture also quickly develops from the left side of the cavity. These fractures do not reach the surface. Finally a fracture develops at the surface close to the centre of the chamber and propagates down towards the chamber although it doesn't quite reach the chamber. Parameters used in the simulation are $V_f = 0$, $\Delta p = 5,000$, $k = 1.4 \times 10^{19}$, $m = 8.5$, $\mu = 0.85$, $Y_o = 0.01$.

Time =1.05E+07   Time =1.08E+07

Time =1.11E+07   Time =1.26E+07
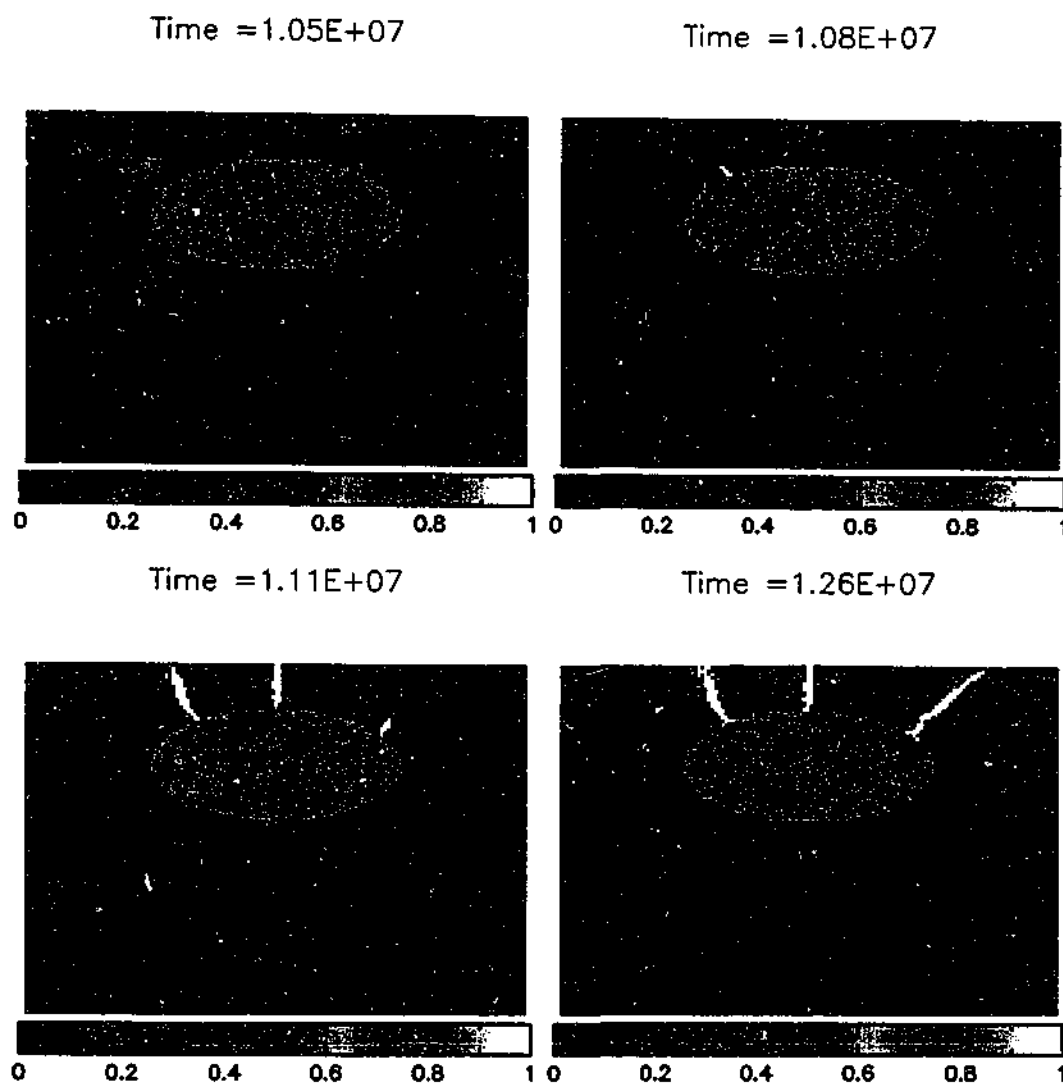
Figure 7.7: *We now investigate the effect of applying a tensional strain to our model. The fractures that develop are now more vertically aligned and do reach the surface. The downward propagating fracture reaches the chamber. Parameters used in the simulation are $V_f = 5 \times 10^{-6}$, $\Delta p = 5,000$, $k = 1.4 \times 10^{19}$, $m = 8.5$, $\mu = 0.85$, $Y_o = 0.01$.*

Time =8.70E+06   Time =9.59E+06

Time =1.02E+07   Time =1.23E+07
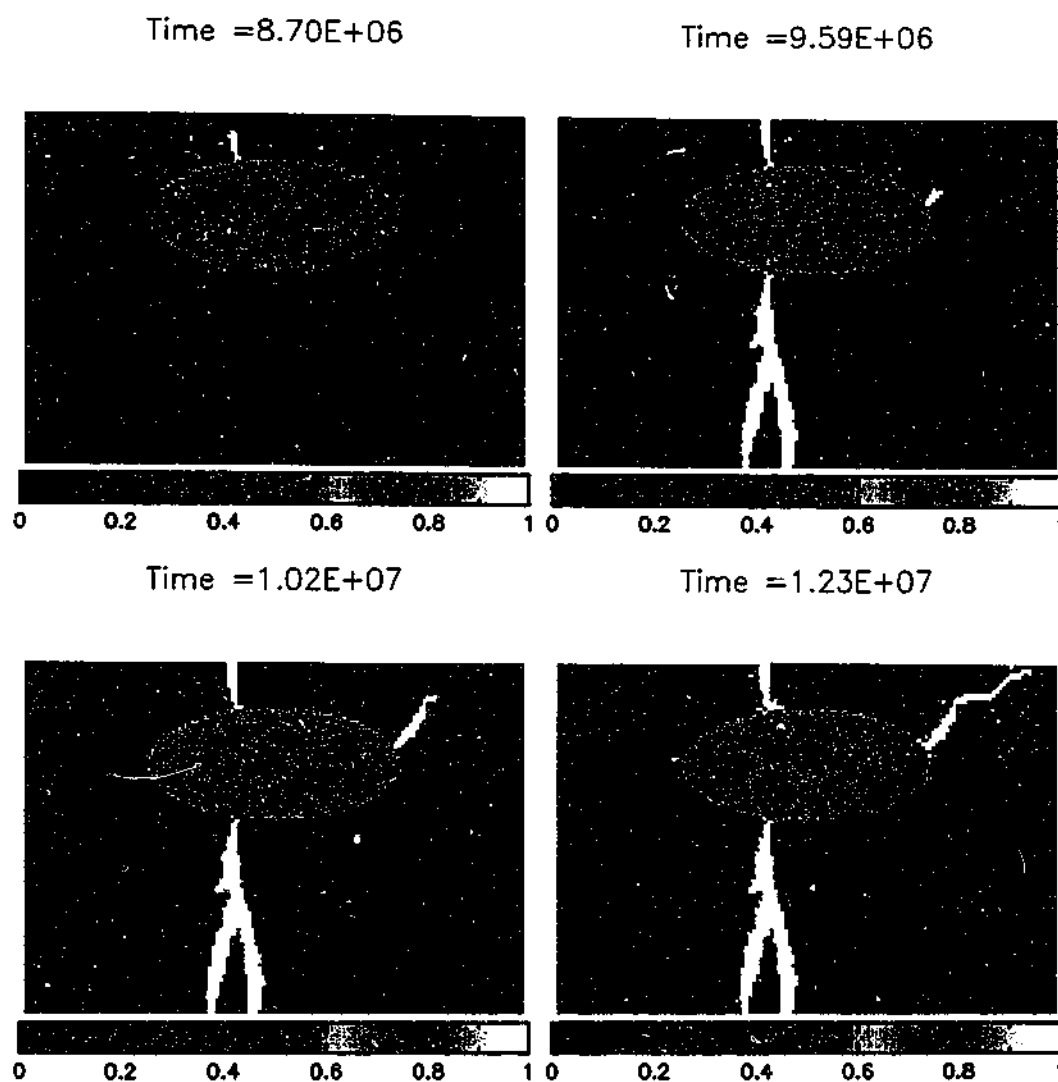
Figure 7.8:   *This case involves a tensional strain rate ten times greater than the strain rate in figure 7.7. Fractures develop before the point where the internal pressure is decreased, the higher strain rate is large enough for a fracture to develop all the way through the block. A dyke is formed and grows upwards on the left side of the material. Parameters used in the simulation are $V_f = 1 \times 10^{-5}$, $\Delta p = 5,000$, $k = 1.4 \times 10^{19}$, $m = 8.5$, $\mu = 0.85$, $Y_o = 0.01$.*

Time =1.20E+06

Time =5.70E+06

Time =1.17E+07

Time =1.77E+07
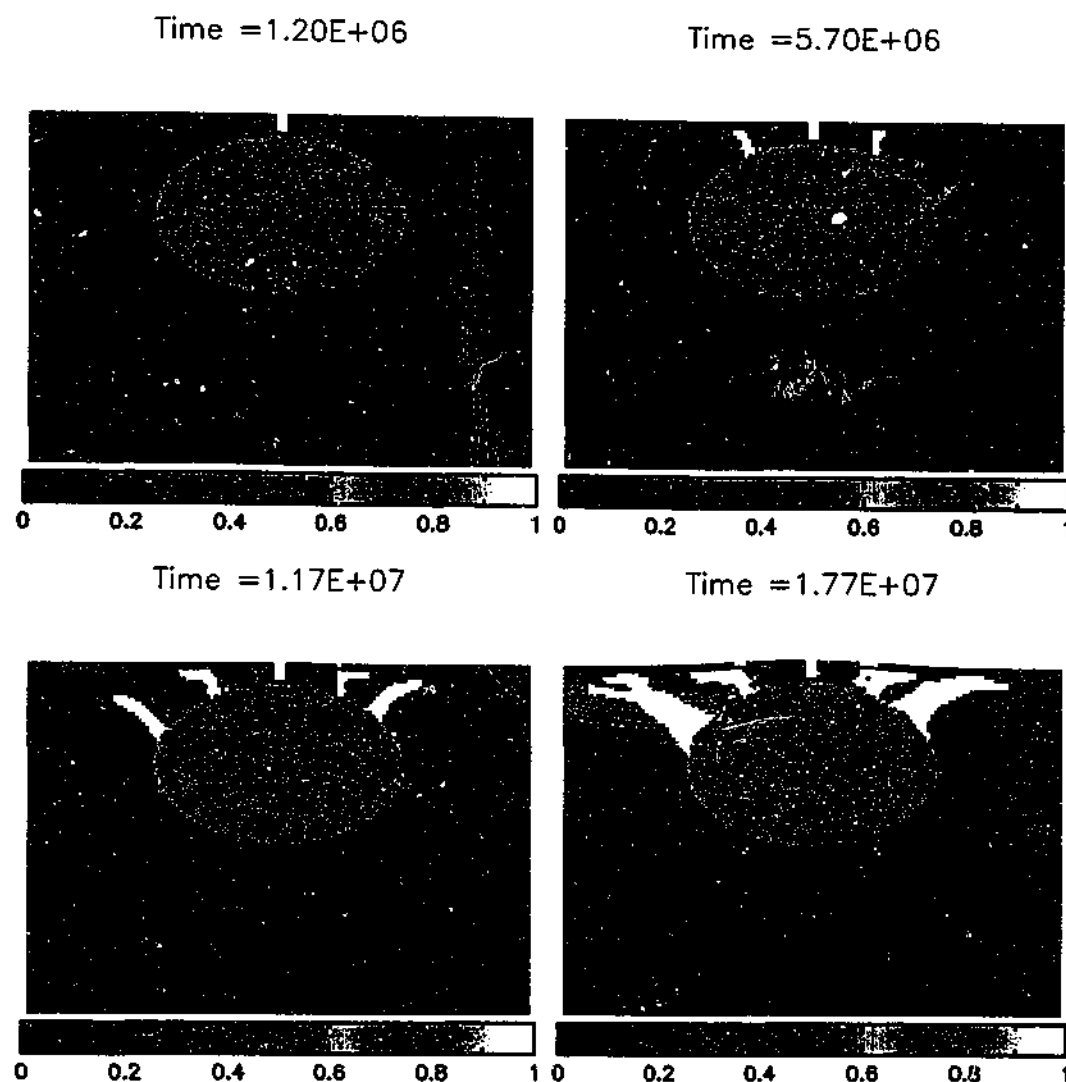
Figure 7.9: *Effect of a cavity with a greater ratio of semi-minor to semi-major axes, placing the top of the cavity closer to the surface. The tensile strain rate of $V_f = 5 \times 10^{-6}$ is the same as the case shown in figure 7.7. Fractures develop at lower strains than the case in figure 7.7 with a fracture propagating vertically down from the surface over the centre of the cavity. This is followed by a set of upward moving vertical dykes which are followed by a second set of dykes which occur more distant from the centre. A significant amount of doming occurs as the cavity is nearer the surface, fractures develop at the surface and propagate down towards the first set of dykes. Simulation parameters are $\Delta p = 5,000$, $k = 1.4 \times 10^{19}$, $m = 8.5$, $\mu = 0.85$, $Y_o = 0.01$.*

Chapter 8

Concluding Remarks

The basic aim of this thesis was to gain an understanding of some of the phenomena associated with caldera collapse. We conclude with a discussion on our success in meeting this aim and remarks concerning further directions in which work should proceed. This discussion is kept brief as a result of summaries being provided throughout this thesis.

8.1 Discussion

In chapter four we have considered the problem of waves produced during caldera collapse eruptions. Although there are several possible mechanisms for the initiation of waves by these eruptions (pyroclastic flows, earthquakes, submarine explosions Latter (1981)), we concentrated on the collapse of an island into the sea as the source mechanism.

We developed a simple model for the waves produced by piston subsidence and conducted a series of wave tank experiments to benchmark our numerical code. Further simulations were conducted which enabled an approximate scaling relation for the extent of wave runup (size of waves) to be developed. Unfortunately, we could not apply our results to the realistic case of Santorini. The ratio of cavity height to width is much smaller in the case of Santorini than in our simulations and it is likely a different mechanism for the generation of waves applies. The resolution and time required for a realistic simulation of Santorini call for a parallel SPH implementation. Areas of further investigation which would enable a realistic estimation of the wave amplitudes on Santorini are addressed below.

The problem of how fractures form in the country rock around magma chambers was examined in chapter seven. A range of simulations were conducted to determine appropriate stress conditions that may lead to the formation of ring faults and possibly result in caldera collapse.

Magma chambers in a two dimensional structure were seen to act as stress concentrators of applied stresses, locally increasing the size of an applied stress and focussing fractures to occur in the regions of high stress. Internal magmatic pressure was seen to lead to the formation of ring dykes. Preliminary models of realistic situations were presented although further work is required to pinpoint the exact mechanisms and critical stresses which lead to the formation of ring faults and subsequent collapse.

8.2 Further Work

This thesis could be divided into two areas, fluid mechanics and solid body dynamics. Some of the directions for further work we now discuss are interlinked and are appropriate improvements to both of these areas. One important improvement would be the parallelisation of the SPH numerical code. There are two main advantages that this would bring.

Firstly, it would enable the simulation of two dimensional calculations involving a larger number of particles. As mentioned in section 4.4 the lengthscales involved and resolution required in a realistic simulation of Santorini mean that such a calculation would take many weeks to run on a serial computer, a time that can be greatly reduced by parallelisation.

Simulations with a larger number of particles would also enable the accurate computation of phenomena on a larger scale. Instead of modelling only the generation of waves, it would be possible to follow the waves that are produced large distances over the sea and their runup on the beaches of Crete. The forms and amplitudes that the waves take are important in assessing how their effects on civilisation when they reach land.

Allowing the efficient computation of higher numbers of particles would also be useful in increasing resolution and accuracy in the simulations, which would be particularly useful in computations involving breaking waves (section 4.3). In the context of our models of the fracturing of magma chambers an increased number of particles would allow us to increase the resolution of the fractures that are formed. It would also enable us to increase the domain over which the simulation is conducted and allow the effects of other physical boundary conditions to be examined.

The second advantage of a parallel code would be that it would enable three dimensional calculations to be performed efficiently. Three dimensional calculations have the obvious improvement that the physical processes that are being modelled are much closer to those found in the realistic situation. Simplifications are not made in reducing to a two dimensional system. We remarked in section 4.4 that the neglect of the cavity breadth in our simulations of wave production limited the applicability of our computations. This limitation can be overcome with the use of a three dimensional code.

The pleasing thing about the parallelisation of SPH is that the algorithm is well suited to parallel computation. Essentially, as particles need only know about particles in their own neighbourhood it is easy to split different sections of a computation onto different computational nodes (of course one also has to consider how to treat interactions between the boundary of each section). Using a parallel implementation such as MPI on a Beowulf type cluster is an economical way of conducting parallel SPH computations.

Another area where the computations in chapter four were unrealistic was that they assumed a simple flat, right angled geometry which is vastly different to the complicated geometry found in realistic situations. It would be interesting to see what effects the more complicated geometry, along with including a slower timescale over which collapse occurs has on the final results of wave amplitude.

Possible extensions of the work on magma chamber fracture are many and varied, increases inresolution and the extension to three dimensions have already been discussed. In the simplest cases more simulations need to be conducted to highlight the dominant physical processes. We have seen that t. . stress concentration is important in determining fracture formation. Changes in the formation of cracks due to chambers of different geometries (sizes, shapes and positions) leading to different stress fields is worthy of further study. An indepth look at changes in physical parameters such as strength and the applied pressures and tensile strains would also be appropriate.

The final avenue for further work we discuss is to combine the two areas of this thesis together so that we can model the effects that the collapsing chamber has on surrounding water as the chamber is subsiding. This is not an overly difficult task as the implementation of both the codes is very similar.

Appendix A

Thermodynamic Effects

We outline a series of calculations in this appendix which quantify the size of the thermodynamic effects that occur in the mechanics of the generation of waves by caldera collapse.

We begin by assuming we have a rectangular cavity of dimension $5km \times 5km \times 400m$ deep. This is a reasonable size for a caldera cavity. At the base of the cavity we assume to have lava and rock at $1,000°C$. We allow water to flow into the cavity and be heated by the caldera floor. The conditions we describe may not be exactly those which occur in reality but they are sufficient to give a reasonable estimate as to the size of the thermodynamic effects.

For thermodynamic effects to outweigh mechanical motion of the water an appreciable amount of the water would be required to be converted into steam. We thus look at the energy required to vaporise the water. As we are only looking for a simple estimate we take physical values appropriate for fresh water, ignoring the minor differences that are present in a salt water environment.

First we require the volume of water which will fill our cavity,

$$
\begin{aligned}
V &= 5 \times 10^3 m \times 5 \times 10^3 m \times 4 \times 10^2 m \\
&= 10^{10} m^3.
\end{aligned}
\tag{A.1}
$$

A one cubic metre volume of water corresponds to one thousand litres, we then have a volume of water $V = 10^{13}$ litres, and mass $M = 10^{13} kg$.

The heat required to vaporise water consists of the heat to raise the water from it's initial temperature to boiling temperature Q_h plus the heat required to vaporise the water Q_v.

We take $C_w = 4190 J/(kgK)$ to be the specific heat of water, the amount of heat required to heat the water from an initial temperature T_i to a final temperature T_f is given by,

$$
Q_h = C_w M (T_f - T_i).
\tag{A.2}
$$

We assume an initial water temperature of $20°C$ and atmospheric pressure so that the boiling point is $100°C$ we find the energy required for heating is,

$$
\begin{aligned}
Q_h &= 4.19 \times 10^3 \times 10^{13}(100 - 20) \\
&= 3.35 \times 10^{18} J.
\end{aligned}
\tag{A.3}
$$

If we take $L_v = 2.3 \times 10^6 J/kg$ to be the latent heat of vaporisation of water we find the energy required to vaporise the water is,

$$
\begin{aligned}
Q_v &= L_v M \\
&= 2.3 \times 10^6 \times 10^{13} \\
&= 2.3 \times 10^{19} J.
\end{aligned}
\tag{A.4}
$$

The total energy required to convert the water at $20°C$ into steam is then $Q = Q_h + Q_v = 2.6 \times 10^{19} J$.

Similarly, we can look at the amount of energy that it takes to cool the lava down to $100°C$. For this calculation we assume equal volumes of lava and water so that the mass of the lava is then $2.6 \times 10^{13} kg$.

The values of the physical constants we use for lava are typical of the values found in Höskuldsson and Sparks (1997). We take the specific heat of lava to be $C_l = 1200 J/(kgK)$, the amount of thermal energy lost as the lava cools from an initial temperature T_i to a final temperature T_f is given by,

$$
Q_c = C_l M(T_f - T_i).
\tag{A.5}
$$

We assume lava with an initial temperature of $1,000°C$ which is cooled down to the boiling point of water $100°C$ we find the energy released during cooling is,

$$
\begin{aligned}
Q_c &= 1.2 \times 10^3 \times 2.6 \times 10^{13} \times (1000 - 100) \\
&= 2.8 \times 10^{19} J.
\end{aligned}
\tag{A.6}
$$

We take $L_f = 2.1 \times 10^5 J/kg$ to be the latent heat of fusion of lava and the energy released as the lava solidifies is,

$$
\begin{aligned}
Q_f &= L_f M \\
&= 2.1 \times 10^5 \times 2.6 \times 10^{13} \\
&= 5.5 \times 10^{18} J.
\end{aligned}
\tag{A.7}
$$

The total energy released as the molten lava at $1,000°C$ cools to rock at $100°C$ is then $Q = Q_c + Q_f = 3.4 \times 10^{19} J$. This is sufficient energy to vaporise the water, provided the energy can be efficiently transferred from the lava to the water.

As lava begins to cool an insulating skin appears at its surface. We now calculate the amount of heat that is able to conduct through this skin. Colgate and Sigurgeirsson (1973) define the effective *skin depth* δ from the error function solution to the thermal diffusion boundary value problem (Carslaw and Jaeger 1959) as,

$$\delta = \sqrt{\frac{kt}{\rho C_l}}. \tag{A.8}$$

Where k is the thermal conductivity, which we take as $4.9W/(mK)$. The *skin depth* is the length scale over which cooling occurs,

$$\delta = \sqrt{\frac{4.9t}{(2.6 \times 10^3) \times (1.2 \times 10^3)}} \tag{A.9}$$
$$= 1.25 \times 10^{-3}\sqrt{t} \ m$$

After one week $(t = 6 \times 10^5 s)$, $\delta = 0.97m$.

We now look at the heat flux of conduction, F_c,

$$\begin{aligned} F_c &= k\frac{\partial T}{\partial y} \\ &\simeq k\frac{\Delta T}{\delta} \\ &\simeq \frac{4.9 \times 900}{0.97} \\ &\simeq 4.546 \times 10^3 W/m^2 \end{aligned} \tag{A.10}$$

The energy that passes through the bottom of a caldera per second is then $F_c \times A = 1.14 \times 10^{11} J/s$. In one week the heat energy lost by the cooling magma is then $6.9 \times 10^{16} J$. This corresponds to 0.3% of the energy required to vaporise the water. The water is only heated to $21.6°C$. We can therefore conclude that over the short timescale of caldera collapse that is able to produce waves, thermodynamic effects are unimportant. Note that this analysis does not mean that phreatomagmatic eruptions will not occur when lava and water interact by mixing (Colgate and Sigurgeirsson 1973).

Appendix B

Dispersion Relation

In this appendix we derive the dispersion relations of section 5.6 in more detail. We assume plane waves in an infinite, initially uniform, elastic material with constant initial stress and further assume that the perturbations to velocity and position are small. We choose Cartesian axes which are aligned so that the initial stress tensor is diagonal, that is $\bar{S}^{xy} = 0$.

We begin by undertaking an analysis to find the dispersion relation of the exact elastic equations and later compare this result to the dispersion relation of the SPH equations for long wavelengths. Finally we calculate values of the coefficients in the SPH dispersion relation for short wavelengths to assist in a discussion of stability properties. Morris (1996) has undertaken a similar analysis for the dispersion relation in the case of isothermal gas dynamics.

Dispersion relation: Exact equations

We assume waves with small perturbations which are of the form,

$$
\begin{aligned}
\mathbf{v} &= & & \mathbf{V}e^{i(\mathbf{k}\cdot\bar{\mathbf{r}}-\omega t)} \\
\mathbf{r} &= \bar{\mathbf{r}} &+& \mathbf{R}e^{i(\mathbf{k}\cdot\bar{\mathbf{r}}-\omega t)} \\
\rho &= \bar{\rho} &+& De^{i(\mathbf{k}\cdot\bar{\mathbf{r}}-\omega t)} \\
P &= \bar{P} &+& c_o^2 De^{i(\mathbf{k}\cdot\bar{\mathbf{r}}-\omega t)} \\
S^{ij} &= \bar{S}^{ij} &+& T^{ij}e^{i(\mathbf{k}\cdot\bar{\mathbf{r}}-\omega t)}
\end{aligned}
\tag{B.1}
$$

where overbars refer to the initial unperturbed quantities, the other terms referring to the perturbations. The components of $\mathbf{V}$ are V_x and V_y. Components of the position perturbation $\mathbf{R}$ are X and Y. The wave number $\mathbf{k}$ has components k_x and k_y.

Our first step is to substitute these waveforms (B.1) into the equations of motion.

Continuity Equation

We first take the continuity equation,

$$\frac{d\rho}{dt} = -\rho \nabla \cdot \mathbf{v} \tag{B.2}$$

substitute in for the perturbations,

$$-\imath\omega D e^{\imath\phi} = -\imath(\bar{\rho} + D e^{\imath\phi})(k_x V_x + k_y V_y)e^{\imath\phi}) \tag{B.3}$$

linearise (remove second order terms),

$$-\imath\omega D e^{\imath\phi} = -\imath\bar{\rho}(k_x V_x + k_y V_y)e^{\imath\phi} \tag{B.4}$$

and divide each side by $\imath\omega e^{\imath\phi}$ to give,

$$D = \frac{\bar{\rho}}{\omega}(k_x V_x + k_y V_y). \tag{B.5}$$

Deviatoric Stress Rates

The equation for the rate of change of deviatoric stress in the horizontal direction is,

$$\frac{dS^{xx}}{dt} = \frac{2}{3}\mu(2\dot{\epsilon}^{xx} - \dot{\epsilon}^{yy}) + 2\Omega^{xy}S^{xy} \tag{B.6}$$

where,

$$\dot{\epsilon}^{ij} = \frac{1}{2}\left(\frac{\partial v_i}{\partial x_i} + \frac{\partial v_j}{\partial x_j}\right). \tag{B.7}$$

Inserting the perturbations,

$$-\imath\omega T^{xx}e^{\imath\phi} = \imath\frac{2}{3}\mu(2k_x V_x - k_y V_y)e^{\imath\phi} + \imath(k_y V_x - k_x V_y)e^{\imath\phi}(\bar{S}^{xy} + T^{xy}e^{\imath\phi}) \tag{B.8}$$

linearising (removing terms of order $e^{2\imath\phi}$),

$$-\imath\omega T^{xx}e^{\imath\phi} = \imath\frac{2}{3}\mu(2k_x V_x - k_y V_y)e^{\imath\phi} + \imath(k_y V_x - k_x V_y)e^{\imath\phi}\bar{S}^{xy}e^{\imath\phi} \tag{B.9}$$

dividing by $-\imath\omega e^{\imath\phi}$ and recalling that we choose initial coordinates with $\bar{S}^{xy} = 0$ we find,

$$
\begin{aligned}
T^{xx} &= -\frac{2\mu}{3\omega}(2k_x V_x - k_y V_y) \\
T^{yy} &= -\frac{2\mu}{3\omega}(2k_y V_y - k_x V_x).
\end{aligned}
\tag{B.10}
$$

where the component T^{yy} is found in the same way with a coordinate transfer. The equation for the diagonal deviatoric stress is slightly different,

$$\frac{dS^{xy}}{dt} = 2\mu\dot{\epsilon}^{xy} + \Omega^{xy}S^{yy} - S^{xx}\Omega^{xy}. \tag{B.11}$$

Substituting for the perturbations and linearising,

$$-\imath\omega T^{xy}e^{\imath\phi} = \mu\imath e^{\imath\phi}(k_xV_x + k_yV_y) + (\bar{S}^{yy} + T^{yy}e^{\imath\phi} - \bar{S}^{xx} - T^{xx}e^{\imath\phi})\frac{\imath}{2}(k_xV_x - k_yV_y)e^{\imath\phi}$$

$$-\imath\omega T^{xy}e^{\imath\phi} = \mu\imath e^{\imath\phi}(k_xV_x + k_yV_y) + \frac{\imath}{2}e^{\imath\phi}(\bar{S}^{yy} - \bar{S}^{xx})(k_yV_x - k_xV_y)$$

$$T^{xy} = -\frac{\mu}{\omega}(k_xV_x + k_yV_y) + \frac{1}{2\omega}(\bar{S}^{yy} - \bar{S}^{xx})(k_yV_x - k_xV_y).$$

$$\tag{B.12}$$

Which we express as,

$$T^{xy} = -\frac{\mu}{\omega}(k_xV_y + k_yV_x) + \frac{\zeta}{\omega}(k_yV_x - k_xV_y) \tag{B.13}$$

where,

$$\zeta = \frac{1}{2}(\bar{S}^{yy} - \bar{S}^{xx}). \tag{B.14}$$

Momentum Equations

Morris (1996) looked at the effect of viscosity in the case of one dimensional SPH gas dynamics and found that while viscosity was effective in reducing the growth rate of the short wavelength instability, it was unable to stabilise it. As we are undertaking this analysis to eventually stabilise the tensile instability we do not consider the effects of viscosity here.

The momentum equations for elastic bodies in the absence of viscosity are,

$$\frac{\partial V_x}{\partial t} = -\frac{1}{\rho}\left(\frac{\partial P}{\partial x} - \frac{\partial S^{xx}}{\partial x} - \frac{\partial S^{xy}}{\partial y}\right)$$
$$\frac{\partial V_y}{\partial t} = -\frac{1}{\rho}\left(\frac{\partial P}{\partial y} - \frac{\partial S^{yy}}{\partial y} - \frac{\partial S^{xy}}{\partial x}\right). \tag{B.15}$$

The perturbations (B.1) are placed into the momentum equations (B.15). Putting $\phi = \mathbf{k}\cdot\mathbf{r} - \omega t$ we find,

$$-\imath\omega V_xe^{\imath\phi}(\bar{\rho} + c_o^2De^{\imath\phi}) = -\imath k_xc_o^2De^{\imath\phi} + \imath k_xT^{xx}e^{\imath\phi} + \imath k_yT^{xy}e^{\imath\phi}$$
$$-\imath\omega V_ye^{\imath\phi}(\bar{\rho} + c_o^2De^{\imath\phi}) = -\imath k_yc_o^2De^{\imath\phi} + \imath k_yT^{yy}e^{\imath\phi} + \imath k_xT^{xy}e^{\imath\phi} \tag{B.16}$$

linearising we have,

$$
\begin{aligned}
-\imath\omega V_x e^{\imath\phi}\bar{\rho} &= -\imath k_x c_o^2 D e^{\imath\phi} + \imath k_x T^{xx} e^{\imath\phi} + \imath k_y T^{xy} e^{\imath\phi} \\
-\imath\omega V_y e^{\imath\phi}\bar{\rho} &= -\imath k_y c_o^2 D e^{\imath\phi} + \imath k_y T^{yy} e^{\imath\phi} + \imath k_x T^{xy} e^{\imath\phi}
\end{aligned}
\tag{B.17}
$$

dividing by $-\imath e^{\imath\phi}$ gives equations for the two wave velocity components,

$$
\begin{aligned}
\bar{\rho}\omega V_x &= k_x(c_o^2 D - T^{xx}) - k_y T^{xy} \\
\bar{\rho}\omega V_y &= k_y(c_o^2 D - T^{yy}) - k_x T^{xy}.
\end{aligned}
\tag{B.18}
$$

Finding the dispersion relation

We now substitute the values for T^{ij} (B.10,B.13) found from the time rate of change of deviatoric stress and continuity D (B.5) into the equations for the velocity components (B.18) derived from the momentum equations and find,

$$
\begin{aligned}
\bar{\rho}\omega^2 V_x &= V_x k_x^2(\bar{\rho}c_o^2 + \frac{4}{3}\mu) + V_x k_y^2(\mu - \zeta) + V_y k_x k_y(\bar{\rho}c_o^2 + \frac{1}{3}\mu + \zeta) \\
\bar{\rho}\omega^2 V_y &= V_y k_y^2(\bar{\rho}c_o^2 + \frac{4}{3}\mu) + V_y k_x^2(\mu + \zeta) + V_x k_x k_y(\bar{\rho}c_o^2 + \frac{1}{3}\mu - \zeta).
\end{aligned}
\tag{B.19}
$$

We arrange each of these equations to find V_x/V_y,

$$
\frac{V_x}{V_y} = \frac{k_x k_y(\bar{\rho}c_o^2 + \frac{1}{3}\mu + \zeta)}{\bar{\rho}\omega^2 - k_x^2(\bar{\rho}c_o^2 + \frac{4}{3}\mu) - k_y^2(\mu - \zeta)},
\tag{B.20}
$$

and

$$
\frac{V_x}{V_y} = \frac{\bar{\rho}\omega^2 - k_y^2(\bar{\rho}c_o^2 + \frac{4}{3}\mu) - k_x^2(\mu + \zeta)}{k_x k_y(\bar{\rho}c_o^2 + \frac{1}{3}\mu - \zeta)}.
\tag{B.21}
$$

The solution of these equations found by equating (B.20) and (B.21) leads to the quartic equation for ω,

$$
\omega^4 + \Lambda\omega^2 + \Gamma = 0,
\tag{B.22}
$$

where,

$$
\begin{aligned}
\Lambda &= -\frac{1}{\bar{\rho}}\left(k^2\left(\bar{\rho}c_o^2 + \frac{4\mu}{3}\right) + (\mu + \zeta)k_x^2 + (\mu - \zeta)k_y^2\right) \\
\Gamma &= \frac{1}{\bar{\rho}^2}k^2\left(\bar{\rho}c_o^2 + \frac{4\mu}{3}\right)\left((\mu + \zeta)k_x^2 + (\mu - \zeta)k_y^2\right)
\end{aligned}
\tag{B.23}
$$

and $k^2 = k_x^2 + k_y^2$.

We note similarities in these two terms and write,

$$\Psi = \frac{k^2(c_o^2\bar{\rho} + \frac{4}{3}\mu)}{\bar{\rho}}$$

$$\Omega = \frac{k_x^2(\mu + \zeta) + k_y^2(\mu - \zeta)}{\bar{\rho}} \tag{B.24}$$

so that the quartic equation for ω becomes,

$$\omega^4 - (\Psi + \Omega)\omega^2 + \Psi\Omega = 0$$

$$(\omega^2 - \Psi)(\omega^2 - \Omega) = 0. \tag{B.25}$$

Which has two solutions,

$$\begin{aligned}\omega^2 &= \Psi = k^2(c_o^2\bar{\rho} + \tfrac{4}{3}\mu)/\bar{\rho} \\ \omega^2 &= \Omega = (k_x^2(\mu + \zeta) + k_y^2(\mu - \zeta))/\bar{\rho}. \end{aligned} \tag{B.26}$$

Elastic waves (Landau and Lifshitz 1970) (pg.102) consist of two waves which travel independently of each other. A longitudinal wave which travels in the direction of propagation of the elastic wave and a transverse wave in which the particle displacements are perpendicular to the direction of propagation. The longitudinal wave velocity $\mathbf{v}_l$ is such that it's curl is zero ($\nabla \times \mathbf{v}_l = 0$). The transverse mode is in a form such that the divergence of its velocity, $\mathbf{v}_t$ is zero ($\nabla \cdot \mathbf{v}_t = 0$).

The first solution (found in (B.26)) gives a mode with frequency,

$$\omega^2 = k^2 \left(c_o^2 + \frac{4\mu}{3\bar{\rho}}\right). \tag{B.27}$$

Substituting back into the equation for V_x/V_y (B.20) we find that most terms cancel,

$$\frac{V_x}{V_y} = \frac{k_x k_y(\bar{\rho}c_o^2 + \frac{1}{3}\mu + \zeta)}{(k_x^2 + k_y^2)(\bar{\rho}c_o^2 + \frac{4}{3}\mu) - k_x^2(\bar{\rho}c_o^2 + \frac{4}{3}\mu) - k_y^2(\mu - \zeta)} = \frac{k_x}{k_y}. \tag{B.28}$$

The requirement for a longitudinal mode is that the curl of the velocity is zero.

$$\nabla \times \mathbf{v} = \begin{vmatrix} \mathbf{i} & \mathbf{j} & \mathbf{k} \\ \frac{\partial}{\partial x} & \frac{\partial}{\partial y} & \frac{\partial}{\partial z} \\ V_x e^{\imath\phi} & V_y e^{\imath\phi} & 0 \end{vmatrix} \tag{B.29}$$

Evaluating the curl we find,

$$
\begin{aligned}
\nabla \times \mathbf{v} &= \mathbf{k} \left(\frac{\partial}{\partial x} \left(V_y e^{\imath \phi} \right) - \frac{\partial}{\partial y} \left(V_x e^{\imath \phi} \right) \right) \\
&= \imath k_x V_y e^{\imath \phi} - \imath k_y V_x e^{\imath \phi} \\
&= k_x V_y - k_y V_x.
\end{aligned}
\tag{B.30}
$$

Equating to zero we find that the ratio of velocities is the same as (B.28), $V_x/V_y = k_x/k_y$. So $\nabla \times \mathbf{v} = 0$ and this solution is the longitudinal mode.

The propagation speed of longitudinal sound waves $(\partial \omega / \partial k)$ is given by,

$$
\frac{\partial \omega}{\partial k} = v_l = \sqrt{c_o^2 + \frac{4\mu}{3\bar{\rho}}}.
\tag{B.31}
$$

Taking the second solution of the quartic equation (B.26) we find,

$$
\begin{aligned}
\omega^2 &= \frac{\mu k^2}{\bar{\rho}} + \frac{(k_x^2 - k_y^2)\zeta}{\bar{\rho}} \\
&= \frac{\mu k^2}{\bar{\rho}} + \frac{(k_x^2 - k_y^2)(\bar{S}^{yy} - \bar{S}^{xx})}{2\bar{\rho}}
\end{aligned}
\tag{B.32}
$$

and

$$
\begin{aligned}
\frac{V_x}{V_y} &= \frac{k_x k_y (\bar{\rho} c_o^2 + \frac{1}{3}\mu + \zeta}{(k_x^2 + k_y^2)\mu + (k_x^2 - k_y^2)\zeta - k_x^2(\bar{\rho} c_o^2 + \frac{4}{3}\mu) - k_y^2 \mu + k_y^2 \zeta}) \\
&= -\frac{k_y}{k_x} \frac{\bar{\rho} c_o^2 + \frac{\mu}{3} + \zeta}{\bar{\rho} c_o^2 + \frac{\mu}{3} - \zeta}.
\end{aligned}
\tag{B.33}
$$

If the initial deviatoric stresses are zero or the diagonal components of the deviatoric stress are equal $(\zeta = 0)$ this is the standard transverse mode $(\nabla \cdot \mathbf{v} = 0)$.

$$
\begin{aligned}
\nabla \cdot \mathbf{v} &= \frac{\partial}{\partial x} \left(V_x e^{\imath \phi} \right) + \frac{\partial}{\partial y} \left(V_y e^{\imath \phi} \right) \\
&= \imath e^{\imath \phi} (k_x V_x + k_y V_y) \\
&= (k_x V_x + k_y V_y).
\end{aligned}
\tag{B.34}
$$

Equating this to zero, we find it can be expressed as $V_x/V_y = -k_y/k_x$ so this is the transverse mode. Again assuming $\zeta = 0$, we find the standard transverse wave velocity,

$$
\frac{\partial \omega}{\partial k} = \frac{\mu k}{\rho \omega} = \sqrt{\frac{\mu}{\rho}}.
\tag{B.35}
$$

Dispersion relation: SPH equations

We now look at the dispersion relation for the SPH equations. We assume the SPH particles are initially placed at the vertices of a regular grid, that is a grid of square cells each of side Δp. The mass of each particle is then $\bar{\rho}(\Delta p)^2$. We denote the initial position of particle a by $\bar{\mathbf{r}}_a$ and write the perturbation to it's position in the form,

$$\mathbf{r}_a = \bar{\mathbf{r}}_a + \mathbf{R}e^{i(\mathbf{k}\cdot\bar{\mathbf{r}}_a-\omega t)}. \tag{B.36}$$

Our calculations are performed using the XSPH velocity equation (2.22) where the velocity of a particle is found by using an average velocity over neighbouring particles. For simplicity we derive our equations using the standard equation for velocity and include the effect of XSPH later. We denote the XSPH smoothed velocity by a hat and write the velocity $\hat{\mathbf{v}}_a$ in the form,

$$\hat{\mathbf{v}}_a = \hat{\mathbf{V}}_a e^{i(\mathbf{k}\cdot\bar{\mathbf{r}}_a-\omega t)}. \tag{B.37}$$

Again for simplicity we start with the standard SPH equations and include the terms associated with the artificial stress later. We begin by defining the following summations which are used later to simplify our expressions. These summations depend on the wave velocity and particle positions.

$$
\begin{aligned}
\mathbf{A} &= (\Delta p)^2 \sum_b \sin(\mathbf{k}\cdot\mathbf{r}_{ab})\nabla_a W_{ab} \\
B_{xx} &= (\Delta p)^2 \sum_b (1-\cos(\mathbf{k}\cdot\mathbf{r}_{ab}))\frac{\partial^2 W_{ab}}{\partial\bar{x}_a^2} \\
B_{yy} &= (\Delta p)^2 \sum_b (1-\cos(\mathbf{k}\cdot\mathbf{r}_{ab}))\frac{\partial^2 W_{ab}}{\partial\bar{y}_a^2} \\
B_{xy} &= (\Delta p)^2 \sum_b (1-\cos(\mathbf{k}\cdot\mathbf{r}_{ab}))\frac{\partial^2 W_{ab}}{\partial\bar{x}_a\partial\bar{y}_a} \\
\beta &= \xi(\Delta p)^2 \sum_b (1-\cos(\mathbf{k}\cdot\mathbf{r}_{ab}))W_{ab}
\end{aligned}
\tag{B.38}
$$

We assume waves similar to those used in the exact case.

$$
\begin{aligned}
\hat{\mathbf{v}}_a &= & \hat{\mathbf{V}} e^{i(\mathbf{k}\cdot\bar{\mathbf{r}}_a - \omega t)} \\
\mathbf{r}_a &= \bar{\mathbf{r}} &+& \mathbf{R} e^{i(\mathbf{k}\cdot\bar{\mathbf{r}}_a - \omega t)} \\
\rho_a &= \bar{\rho} &+& D e^{i(\mathbf{k}\cdot\bar{\mathbf{r}}_a - \omega t)} \\
P_a &= \bar{P} &+& c_o^2 D e^{i(\mathbf{k}\cdot\bar{\mathbf{r}}_a - \omega t)} \\
S_a^{ij} &= \bar{S}^{ij} &+& T^{ij} e^{i(\mathbf{k}\cdot\bar{\mathbf{r}}_a - \omega t)}
\end{aligned}
\tag{B.39}
$$

For efficiency we sometimes use the notation $\delta\rho_a = D e^{i(\mathbf{k}\cdot\bar{\mathbf{r}}_a - \omega t)}$, $\delta P_a = c_o^2 \delta\rho_a$, and $\delta S_a^{ij} = T^{ij} e^{i(\mathbf{k}\cdot\bar{\mathbf{r}}_a - \omega t)}$, $\delta x_a = X e^{i(\mathbf{k}\cdot\bar{\mathbf{r}}_a - \omega t)}$.

Below we note a few details which we use in the following derivations.

As each particle is of the same mass we can write,

$$
\sum_b m_b = \bar{\rho}(\Delta p)^2.
\tag{B.40}
$$

Using laws for exponentials we can write,

$$
\frac{e^{i\mathbf{k}\cdot\bar{\mathbf{r}}_b}}{e^{i\mathbf{k}\cdot\bar{\mathbf{r}}_a}} = e^{i(\mathbf{k}\cdot\bar{\mathbf{r}}_b - \mathbf{k}\cdot\bar{\mathbf{r}}_a)} = e^{i(\mathbf{k}\cdot(\mathbf{r}_b - \mathbf{r}_a))} = e^{-i\mathbf{k}\cdot\bar{\mathbf{r}}_{ab}}.
\tag{B.41}
$$

To find the effect that a perturbation of the particle positions has on the kernel derivatives we look at a Taylor Series expansion for the kernel derivatives.

$$
\begin{aligned}
\frac{\partial W}{\partial x} &= \frac{\partial W}{\partial \tilde{x}_a} + \frac{\partial^2 W}{\partial \tilde{x}_a^2}(\delta\tilde{x}_a - \delta\tilde{x}_b) + \frac{\partial^2 W}{\partial \tilde{x}_a \partial \tilde{y}_a}(\delta\tilde{y}_a - \delta\tilde{y}_b) \\
\frac{\partial W}{\partial y} &= \frac{\partial W}{\partial \tilde{y}_a} + \frac{\partial^2 W}{\partial \tilde{y}_a^2}(\delta\tilde{y}_a - \delta\tilde{Y}_b) + \frac{\partial^2 W}{\partial \tilde{x}_a \partial \tilde{y}_a}(\delta\tilde{x}_a - \delta\tilde{x}_b)
\end{aligned}
\tag{B.42}
$$

In some of the derivations we require a relationship between position and velocity. The standard equation (excluding XSPH) for velocity is,

$$
\frac{d\mathbf{r}_a}{dt} = \mathbf{v}_a.
\tag{B.43}
$$

Inserting the position and velocity we show,

$$
\begin{aligned}
-i\omega X e^{i(\mathbf{k}\cdot\bar{\mathbf{r}}_a - \omega t)} &= V_x e^{i(\mathbf{k}\cdot\bar{\mathbf{r}}_a - \omega t)} \\
X &= \frac{-V_x}{i\omega} \\
&= \frac{i V_x}{\omega}.
\end{aligned}
\tag{B.44}
$$

Continuity Equation

As with the exact equations we again begin with the continuity equation, which in SPH form is given by,

$$
\begin{aligned}
\frac{d\rho_a}{dt} &= \sum_b m_b (\mathbf{v}_a - \mathbf{v}_b) \cdot \nabla_a W_{ab} \\
&= \sum_b m_b (v_a^x - v_b^x) \frac{\partial W_{ab}}{\partial x} + \sum_b m_b (v_a^y - v_a^y) \frac{\partial W_{ab}}{\partial y}.
\end{aligned}
\tag{B.45}
$$

Substituting for the perturbations (B.39,B.42) and linearising we have,

$$
\begin{aligned}
-\imath\omega D e^{\imath(\mathbf{k}\cdot\bar{\mathbf{r}}_a - \omega t)} = \quad & \sum_b m_b V_x (e^{(\imath\mathbf{k}\cdot\bar{\mathbf{r}}_a - \omega t)} - e^{(\imath\mathbf{k}\cdot\bar{\mathbf{r}}_b - \omega t)}) \frac{\partial W}{\partial \tilde{x}} \\
& + \sum_b m_b V_y (e^{(\imath\mathbf{k}\cdot\bar{\mathbf{r}}_a - \omega t)} - e^{(\imath\mathbf{k}\cdot\bar{\mathbf{r}}_b - \omega t)}) \frac{\partial W}{\partial \tilde{y}}
\end{aligned}
\tag{B.46}
$$

We make use of (B.41) when we divide by $e^{\imath(\mathbf{k}\cdot\bar{\mathbf{r}}_a - \omega t)}$,

$$
-\imath\omega D = \bar{\rho}(\Delta p)^2 \sum_b \left(V_x (1 - e^{-\imath\mathbf{k}\cdot\bar{\mathbf{r}}_{ab}}) \frac{\partial W}{\partial \tilde{x}} + V_y (1 - e^{-\imath\mathbf{k}\cdot\bar{\mathbf{r}}_{ab}}) \frac{\partial W}{\partial \tilde{y}} \right)
\tag{B.47}
$$

As $e^{\imath\phi} = \cos(\phi) + \imath\sin(\phi)$ we write,

$$
\begin{aligned}
-\imath\omega D = &+\bar{\rho}(\Delta p)^2 \sum_b V_x \left(1 - \cos(\mathbf{k}\cdot\bar{\mathbf{r}}_{ab}) + \imath\sin(\mathbf{k}\cdot\bar{\mathbf{r}}_{ab})\right) \frac{\partial W}{\partial \tilde{x}} \\
&+ \bar{\rho}(\Delta p)^2 \sum_b V_y \left(1 - \cos(\mathbf{k}\cdot\bar{\mathbf{r}}_{ab}) + \imath\sin(\mathbf{k}\cdot\bar{\mathbf{r}}_{ab})\right) \frac{\partial W}{\partial \tilde{y}}
\end{aligned}
\tag{B.48}
$$

The $(1 - \cos(\mathbf{k}\cdot\bar{\mathbf{r}}_{ab}))$ terms do not contribute to the summations as they form an *ODD* function when multiplied by the kernel derivatives, they disappear as the summation is taken over all space. We have,

$$
\begin{aligned}
-\imath\omega D &= \bar{\rho}(\Delta p)^2 \sum_b \left(\imath V_x \sin(\mathbf{k}\cdot\bar{\mathbf{r}}_{ab}) \frac{\partial W}{\partial \tilde{x}} + \imath V_y \sin(\mathbf{k}\cdot\bar{\mathbf{r}}_{ab}) \frac{\partial W}{\partial \tilde{y}} \right) \\
&= \imath\bar{\rho}(V_x A_x + V_y A_y).
\end{aligned}
\tag{B.49}
$$

Dividing by $-\imath\omega$ we are left with,

$$
D = -\frac{\bar{\rho}}{\omega}(\mathbf{V} \cdot \mathbf{A})
\tag{B.50}
$$

where $\mathbf{A}$ is defined in (B.38). If we compare this expression to the one obtained from the continuity equation in the dispersion relation of the exact equations (B.5) we notice a correspondence between the summation $\mathbf{A}$ and the wave number $\mathbf{k}$.

Deviatoric Stress Terms

Taking the equations for rate of change of deviatoric stress,

$$\begin{aligned}
\frac{dS^{xx}}{dt} &= \frac{2}{3}\mu(2\dot{\epsilon}^{xx} - \dot{\epsilon}^{yy}) + 2\Omega^{xy}S^{xy} \\
\frac{dS^{xy}}{dt} &= 2\mu\dot{\epsilon}^{xy} + \Omega^{xy}S^{yy} - S^{xx}\Omega^{xy}.
\end{aligned} \tag{B.51}$$

With the rotation terms defined by,

$$\Omega^{xy} = -\Omega^{yx} = \frac{1}{2}\left(\frac{\partial v_x}{\partial y} - \frac{\partial v_y}{\partial x}\right). \tag{B.52}$$

We express the rate of change of velocity as,

$$\frac{\partial v}{\partial x} = \frac{1}{\rho}\left(\frac{\partial}{\partial x}(\rho v) - v\frac{\partial \rho}{\partial x}\right), \tag{B.53}$$

so that the summations for the velocity derivatives in SPH form are symmetric,

$$\frac{\partial v}{\partial x} = -\frac{1}{\rho}\sum_b (v_a^x - v_b^x)\frac{\partial W}{\partial x}. \tag{B.54}$$

As we require only linear terms in the analysis we expand the inverse of the density using a Taylor series.

$$\frac{1}{\rho} = \frac{1}{\bar{\rho} + D\delta\rho} = \frac{1}{\bar{\rho}} - \frac{D}{\bar{\rho}^2}\delta\rho + \cdots \tag{B.55}$$

The $1/\bar{\rho}$ is the only term in (B.55) that survives linearisation when we substitute into (B.54) as the velocity terms are of the order $e^{i(\mathbf{k}\cdot\bar{\mathbf{r}}-\omega t)}$. This means that the higher order terms of the Taylor series for the density generate second order terms when multiplied by the velocities and can be neglected.

We write the linearised form of the SPH velocity equation,

$$\frac{\partial v_x}{\partial x} = -\frac{1}{\bar{\rho}}\sum_b m_b V_x\big(e^{i(\mathbf{k}\cdot\bar{\mathbf{r}}_a-\omega t)} - e^{i(\mathbf{k}\cdot\bar{\mathbf{r}}_b-\omega t)}\big)\frac{\partial W}{\partial \tilde{x}}. \tag{B.56}$$

Substituting into the equation for the rate of change of deviatoric stress (B.51).

$$-\imath\omega T^{xx}e^{\imath(\mathbf{k}\cdot\bar{\mathbf{r}}_a-\omega t)} = -\frac{1}{\bar{\rho}}\frac{4}{3}\mu\sum_b m_b V_x(e^{\imath(\mathbf{k}\cdot\bar{\mathbf{r}}_a-\omega t)} - e^{\imath(\mathbf{k}\cdot\bar{\mathbf{r}}_b-\omega t)})\frac{\partial W}{\partial\tilde{x}}$$
$$+\frac{1}{\bar{\rho}}\frac{2}{3}\mu\sum_b m_b V_y(e^{\imath(\mathbf{k}\cdot\bar{\mathbf{r}}_a-\omega t)} - e^{\imath(\mathbf{k}\cdot\bar{\mathbf{r}}_b-\omega t)})\frac{\partial W}{\partial\tilde{y}}$$
$$-\imath\omega T^{xx} = -(\Delta p)^2\frac{4}{3}\mu\sum_b V_x(1 - e^{-\imath\mathbf{k}\cdot\bar{\mathbf{r}}_{ab}})\frac{\partial W}{\partial\tilde{x}}$$
$$+(\Delta p)^2\frac{2}{3}\mu\sum_b V_y(1 - e^{-\imath\mathbf{k}\cdot\bar{\mathbf{r}}_{ab}})\frac{\partial W}{\partial\tilde{y}}$$
$$= -(\Delta p)^2\frac{4}{3}\mu\sum_b m_b V_x(1 - \cos(\mathbf{k}\cdot\bar{\mathbf{r}}_{ab}) + \imath\sin(\mathbf{k}\cdot\bar{\mathbf{r}}_{ab}))\frac{\partial W}{\partial\tilde{x}}$$
$$+(\Delta p)^2\frac{2}{3}\mu\sum_b m_b V_y(1 - \cos(\mathbf{k}\cdot\bar{\mathbf{r}}_{ab}) + \imath\sin(\mathbf{k}\cdot\bar{\mathbf{r}}_{ab}))\frac{\partial W}{\partial\tilde{y}}$$

$$(B.57)$$

Dividing by $-\imath\omega$ and removing the *EVEN* terms which do not contribute in the summation as the kernel is an *ODD* function.

$$T^{xx} = \frac{2\mu}{3\omega}(\Delta p)^2\sum_b\left(2V_x\sin(\mathbf{k}\cdot\bar{\mathbf{r}}_{ab})\frac{\partial W}{\partial\tilde{x}} - V_y\sin(\mathbf{k}\cdot\bar{\mathbf{r}}_{ab})\frac{\partial W}{\partial\tilde{y}}\right)$$
$$= \frac{2\mu}{3\omega}(2V_xA_x - V_yA_y)$$

$$(B.58)$$

and similarly

$$T^{xx} = -\frac{2\mu}{3\omega}(2V_xA_x - V_yA_y)$$
$$T^{yy} = -\frac{2\mu}{3\omega}(2V_yA_y - V_xA_x)$$
$$T^{xy} = -\frac{\mu}{\omega}(V_xA_y + V_yA_x) + \frac{\zeta}{\omega}(V_xA_y - V_yA_x).$$

$$(B.59)$$

We again note (in a comparison with the results from the exact equations of the deviatoric stress tensor (B.10, B.13)) a correspondence between $\mathbf{A}$ in the SPH dispersion relation and $\mathbf{k}$ in the dispersion relation of the exact equations.

Momentum Equation

To linearise the momentum equation (B.61) we use a Taylor series.

$$\frac{1}{\rho^2} = \frac{1}{(\bar{\rho} + \delta\rho)^2} = \frac{1}{\bar{\rho}^2} - \frac{2\delta\rho}{\bar{\rho}^3} + \frac{\delta\rho^2}{\bar{\rho}^4} + \cdots \tag{B.60}$$

The SPH form of the momentum equation in the absence of viscosity is,

$$\frac{\partial v_x}{\partial x} = \sum_b m_b \left(\left(\frac{S_a^{xx} - P_a}{\rho_a^2} + \frac{S_b^{xx} - P_b}{\rho_b^2} \right) \frac{\partial W}{\partial x} + \left(\frac{S_a^{xy}}{\rho_a^2} + \frac{S_b^{xy}}{\rho_b^2} \right) \frac{\partial W}{\partial y} \right). \tag{B.61}$$

Substituting for perturbations and linearising, we find that second order derivatives of the kernel appear.

$$\begin{aligned}
\frac{\partial v_x}{\partial x} = \ & \sum_b m_b \left(2\frac{-\bar{P} + \bar{S}^{xx}}{\bar{\rho}^2} \right) \left(\frac{\partial W}{\partial \tilde{x}} + \frac{\partial^2 W}{\partial \tilde{x}_a^2}(\delta x_a - \delta x_b) + \frac{\partial^2 W}{\partial \tilde{x}_a \partial \tilde{y}_a}(\delta y_a - \delta y_b) \right) \\
& + \sum_b m_b \left(2\frac{(\bar{P} - \bar{S}^{xx}) - \bar{\rho}c_o^2}{\bar{\rho}^3}(\delta\rho_a + \delta\rho_b) + \frac{\delta S_a^{xx} + \delta S_b^{xx}}{\bar{\rho}^2} \right) \frac{\partial W}{\partial \tilde{x}} \\
& + \sum_b m_b \frac{2\bar{S}^{xy}}{\bar{\rho}^2} \left(\frac{\partial W}{\partial \tilde{y}} + \frac{\partial^2 W}{\partial \tilde{y}_a^2}(\delta y_a - \delta y_b) + \frac{\partial^2 W}{\partial \tilde{x}_a \partial \tilde{y}_a}(\delta x_a - \delta x_b) \right) \\
& + \sum_b m_b \left(-\frac{2\bar{S}^{xy}}{\bar{\rho}^3}(\delta\rho_a + \delta\rho_b) + \frac{\delta S_a^{xy} + \delta S_b^{xy}}{\bar{\rho}^2} \right) \frac{\partial W}{\partial \tilde{y}_a}
\end{aligned}$$
$$\tag{B.62}$$

To avoid a long string of complicated equations we handle each line in (B.62) separately. The left hand side yields,

$$\frac{\partial v_x}{\partial x} = -\imath \omega V_x e^{\imath(\mathbf{k} \cdot \bar{\mathbf{r}}_a - \omega t)}. \tag{B.63}$$

As we eventually wish to find V_x we divide the terms on the right hand side of the following derivations by $\chi = -\imath \omega e^{\imath(\mathbf{k} \cdot \bar{\mathbf{r}}_a - \omega t)}$, leaving V_x on the left hand side.

We consider the first line of (B.62) and eliminate the $(2(-\bar{P} + \bar{S}^{xx})/\bar{\rho}^2)(\partial W/\partial \tilde{x})$ term as the first derivative of the kernel is an *ODD* function and this term disappears when the summation is taken over all space.

Then the first term becomes,

$$\frac{1}{\chi}\sum_b m_b \frac{2(-\bar{P}+\bar{S}^{xx})}{\bar{\rho}^2}\left(\frac{\partial^2 W}{\partial \tilde{x}_a^2}X(e^{i(\mathbf{k}\cdot\bar{\mathbf{r}}_a-\omega t)}-e^{i(\mathbf{k}\cdot\bar{\mathbf{r}}_b-\omega t)})\right)$$

$$+\frac{1}{\chi}\sum_b m_b \frac{2(-\bar{P}+\bar{S}^{xx})}{\bar{\rho}^2}\left(\frac{\partial^2 W}{\partial \tilde{x}_a \partial \tilde{y}_a}Y(e^{i(\mathbf{k}\cdot\bar{\mathbf{r}}_a-\omega t)}-e^{i(\mathbf{k}\cdot\bar{\mathbf{r}}_b-\omega t)})\right)$$

$$=\frac{i}{\omega}\sum_b \frac{m_b}{\bar{\rho}}\frac{2(-\bar{P}+\bar{S}^{xx})}{\bar{\rho}}\left(X(1-e^{-i\mathbf{k}\cdot\bar{\mathbf{r}}_{ab}})\frac{\partial^2 W}{\partial \tilde{x}_a^2}+Y(1-e^{-i\mathbf{k}\cdot\bar{\mathbf{r}}_{ab}})\frac{\partial^2 W}{\partial \tilde{x}_a \partial \tilde{y}_a}\right)$$

$$=+\frac{i}{\omega}\sum_b (\Delta p)^2 \frac{2(-\bar{P}+\bar{S}^{xx})}{\bar{\rho}}\left(X(1-\cos(\mathbf{k}\cdot\bar{\mathbf{r}}_{ab})+i\sin(\mathbf{k}\cdot\bar{\mathbf{r}}_{ab}))\frac{\partial^2 W}{\partial \tilde{x}_a^2}\right)$$

$$+\frac{i}{\omega}\sum_b (\Delta p)^2 \frac{2(-\bar{P}+\bar{S}^{xx})}{\bar{\rho}}\left(Y(1-\cos(\mathbf{k}\cdot\bar{\mathbf{r}}_{ab})+i\sin(\mathbf{k}\cdot\bar{\mathbf{r}}_{ab}))\frac{\partial^2 W}{\partial \tilde{x}_a \partial \tilde{y}_a}\right)$$

$$=\frac{i}{\omega}\sum_b (\Delta p)^2 \frac{2(-\bar{P}+\bar{S}^{xx})}{\bar{\rho}}\left(X(1-\cos(\mathbf{k}\cdot\bar{\mathbf{r}}_{ab}))\frac{\partial^2 W}{\partial \tilde{x}_a^2}+Y(1-\cos(\mathbf{k}\cdot\bar{\mathbf{r}}_{ab}))\frac{\partial^2 W}{\partial \tilde{x}_a \partial \tilde{y}_a}\right)$$

$$=\frac{2}{\omega^2}\left(\frac{(\bar{P}-\bar{S}^{xx})}{\bar{\rho}}\right)(B_{xx}V_x+B_{xy}V_y).$$

$$(B.64)$$

The X is changed to a V_x in the second last line subject to $V_x = iX/\omega$ (B.56). The second term becomes,

$$\frac{1}{\chi}\sum_b m_b \left(\frac{2(\bar{P}-\bar{S}^{xx})-\bar{\rho}c_o^2}{\bar{\rho}^3}(\delta\rho_a+\delta\rho_b)+\frac{1}{\bar{\rho}^2}(\delta S_a^{xx}+\delta S_b^{xx})\right)\frac{\partial W}{\partial x}$$

$$=\frac{1}{\chi}\sum_b (\Delta p)^2 \left(\frac{2(\bar{P}-\bar{S}^{xx})-\bar{\rho}c_o^2}{\bar{\rho}^2}(D(e^{i(\mathbf{k}\cdot\bar{\mathbf{r}}_a-\omega t)}+e^{i(\mathbf{k}\cdot\bar{\mathbf{r}}_b-\omega t)}))\right)\frac{\partial W}{\partial x}$$

$$+\frac{1}{\chi}\sum_b (\Delta p)^2 \left(\frac{1}{\bar{\rho}}T^{xx}(e^{i(\mathbf{k}\cdot\bar{\mathbf{r}}_a-\omega t)}+e^{i(\mathbf{k}\cdot\bar{\mathbf{r}}_b-\omega t)})\right)\frac{\partial W}{\partial x}$$

$$=\frac{i}{\omega}\sum_b (\Delta p)^2 \left(\frac{2(\bar{P}-\bar{S}^{xx})-\bar{\rho}c_o^2}{\bar{\rho}^2}D(1+e^{-i\mathbf{k}\cdot\bar{\mathbf{r}}_{ab}})+\frac{1}{\bar{\rho}}T^{xx}(1+e^{-i\mathbf{k}\cdot\bar{\mathbf{r}}_{ab}})\right)\frac{\partial W}{\partial x}$$

$$=\frac{i}{\omega}\sum_b (\Delta p)^2 \left(\frac{2(\bar{P}-\bar{S}^{xx})-\bar{\rho}c_o^2}{\bar{\rho}^2}(-Di\sin(\mathbf{k}\cdot\bar{\mathbf{r}}_{ab}))-\frac{1}{\bar{\rho}}T^{xx}i\sin(\mathbf{k}\cdot\bar{\mathbf{r}}_{ab})\right)\frac{\partial W}{\partial x}$$

$$=\frac{1}{\omega}\left(\frac{2(\bar{P}-\bar{S}^{xx})-\bar{\rho}c_o^2}{\bar{\rho}^2}D+\frac{T^{xx}}{\bar{\rho}}\right)A_x.$$

$$(B.65)$$

The third term is derived in the same way as (B.64) without the pressure term,

$$
\frac{1}{\chi} \sum_b m_b \frac{2\bar{S}^{xy}}{\bar{\rho}^2} \left(\frac{\partial W}{\partial \tilde{y}_a} + \frac{\partial^2 W}{\partial \tilde{y}_a^2} Y (e^{\imath(k \cdot \bar{r}_a - \omega t)} - e^{\imath(k \cdot \bar{r}_b - \omega t)}) \right)
$$
$$
+ \frac{1}{\chi} \sum_b m_b \frac{2\bar{S}^{xy}}{\bar{\rho}^2} \left(\frac{\partial^2 W}{\partial \tilde{x}_a \partial \tilde{y}_a} X (e^{\imath(k \cdot \bar{r}_a - \omega t)} - e^{\imath(k \cdot \bar{r}_b - \omega t)}) \right) \qquad \text{(B.66)}
$$
$$
= \frac{2}{\omega^2} \left(-\frac{\bar{S}^{xy}}{\bar{\rho}} \right) (B_{yy} V_y + B_{xy} V_x).
$$

This term ends up being equal to zero as we choose our initial coordinates so that $\bar{S}^{xy} = 0$.

The fourth term of (B.62) is similar to the second term (B.65), we find,

$$
\frac{1}{\chi} \sum_b m_b \left(-\frac{2\bar{S}^{xy}}{\bar{\rho}^3} (\delta \rho_a + \delta \rho_b) + \frac{1}{\bar{\rho}^2} (\delta S_a^{xy} + \delta S_b^{xy}) \right) \frac{\partial W}{\partial y}
$$
$$
= \frac{1}{\omega} \left(-\frac{2\bar{S}^{xy}}{\bar{\rho}^2} D + \frac{T^{xy}}{\tilde{\rho}} \right) A_y \qquad \text{(B.67)}
$$
$$
= \frac{T^{xy}}{\bar{\rho}\omega} A_y.
$$

Putting this together we find that the equations for V_x and V_y are given by,

$$
V_x = \left(\frac{DA_x}{\bar{\rho}^2 \omega} \right) \left(2(\bar{P} - \bar{S}^{xx}) - \bar{\rho} c_o^2 \right) + \frac{2(B_{xx} V_x + B_{xy} V_y)}{\bar{\rho}\omega^2} (\bar{P} - \bar{S}^{xx}) + \frac{A_x T^{xx}}{\bar{\rho}\omega} + \frac{A_y T^{xy}}{\bar{\rho}\omega}
$$
$$
V_y = \left(\frac{DA_y}{\bar{\rho}^2 \omega} \right) \left(2(\bar{P} - \bar{S}^{yy}) - \bar{\rho} c_o^2 \right) + \frac{2(B_{yy} V_y + B_{xy} V_x)}{\bar{\rho}\omega^2} (\bar{P} - \bar{S}^{yy}) + \frac{A_y T^{yy}}{\bar{\rho}\omega} + \frac{A_x T^{xy}}{\bar{\rho}\omega}.
$$
$$
\text{(B.68)}
$$

XSPH Smoothed Velocity

Our calculations use a smoothed particle velocity to prevent particle penetration. We now determine the effects of this smoothing on the dispersion relation. When using XSPH a smoothed velocity is calculated by,

$$
\hat{\mathbf{v}}_a = \mathbf{v}_a + \xi \sum_b \frac{m_b}{\bar{\rho}_{ab}} (v_b - v_a) W_{ab}. \qquad \text{(B.69)}
$$

Substituting the velocity perturbation (B.37) into the XSPH velocity equation (B.69).

$$\hat{\mathbf{V}}e^{i(\mathbf{k}\cdot\bar{\mathbf{r}}_a-\omega t)} = \mathbf{V}e^{i(\mathbf{k}\cdot\bar{\mathbf{r}}_a-\omega t)} + \xi\sum_b \frac{m_b}{\bar{\rho}_b}(\mathbf{V}e^{i(\mathbf{k}\cdot\bar{\mathbf{r}}_b-\omega t)} - \mathbf{V}e^{i(\mathbf{k}\cdot\bar{\mathbf{r}}_a-\omega t)})W_{ab}$$

$$\hat{\mathbf{V}} = \mathbf{V}\left[1 - \xi(\Delta p)^2\sum_b(1 - \mathbf{V}e^{i\mathbf{k}\cdot\bar{\mathbf{r}}_{ab}})W_{ab}\right]$$

$$= \mathbf{V}\left[1 - \xi(\Delta p)^2\sum_b(1 - \cos(\mathbf{k}\cdot\bar{\mathbf{r}}_{ab}) + i\sin(\mathbf{k}\cdot\bar{\mathbf{r}}_{ab}))W_{ab}\right] \qquad \text{(B.70)}$$

$$\hat{\mathbf{V}} = \mathbf{V}\left[1 - \xi(\Delta p)^2\sum_b(1 - \cos(\mathbf{k}\cdot\mathbf{r}_{ab}))W_{ab}\right].$$

As we take the summation over all space and the kernel is an *EVEN* function, any *ODD* terms cancel themselves out (i.e. $\sin(\mathbf{k}\cdot\bar{\mathbf{r}}_{ab})$) and we note that for XSPH the relation between $\mathbf{V}$ and $\hat{\mathbf{V}}$ is

$$\hat{\mathbf{V}} = \mathbf{V}(1 - \beta) \qquad \text{(B.71)}$$

with β defined in (B.38).

This smoothed velocity is used in the calculation of position, density and stress. When applying this to our dispersion relation for the SPH equations each of the velocities on the right hand side of (B.68) is multiplied by the factor $(1 - \beta)$. This is equivalent to dividing the left hand side by $(1 - \beta)$.

Substituting for continuity (B.50), the stress components (B.59), and XSPH (B.71) into the momentum equations (B.68) we find,

$$\frac{\omega^2\bar{\rho}V_x}{1-\beta} = -(2(\bar{P} - \bar{S}^{xx}) - \bar{\rho}c_o^2)A_x(\mathbf{A}\cdot\mathbf{V}) + (2\bar{P} - 2\bar{S}^{xx})(B_{xx}V_x + B_{xy}V_y)$$
$$+ \frac{2\mu}{3}(2V_xA_x - V_yA_y)A_x + \mu(V_xA_y + V_yA_x)A_y - \zeta(V_xA_y - V_yA_x)A_y$$

$$\frac{\omega^2\bar{\rho}V_y}{1-\beta} = -(2(\bar{P} - \bar{S}^{yy}) - \bar{\rho}c_o^2)A_y(\mathbf{A}\cdot\mathbf{V}) + (2\bar{P} - 2\bar{S}^{yy})(B_{yy}V_y + B_{xy}V_x)$$
$$+ \frac{2\mu}{3}(2V_yA_y - V_xA_x)A_y + \mu(V_yA_x + V_xA_y)A_x + \zeta(V_yA_x - V_xA_y)A_x,$$

$$\text{(B.72)}$$

with the y component is derived in a similar way to the x component.

The Artificial Stress

In this section we calculate the contribution of our artificial stress terms to the numerical dispersion relation. We calculate these contributions so we can later study the effect that these artificial stress terms have on the short wavelength tensile instability.

We begin by finding $\partial^2 W^{n+1}/\partial x^2$ as we make use of it shortly.

$$
\begin{aligned}
\frac{\partial W^{n+1}}{\partial x} &= (n+1)W^n\frac{\partial W}{\partial x} \\
\frac{\partial^2 W^{n+1}}{\partial x^2} &= (n+1)\left(W^n\frac{\partial^2 W^n}{\partial x^2} + nW^{n-1}\left(\frac{\partial W}{\partial x}\right)^2\right)
\end{aligned}
\tag{B.73}
$$

We can then say that,

$$
\begin{aligned}
\frac{1}{n+1}\frac{\partial^2 W^{n+1}}{\partial x^2} &= W^n\frac{\partial^2 W^n}{\partial x^2} + nW^{n-1}\left(\frac{\partial W}{\partial x}\right)^2 \\
\frac{1}{n+1}\frac{\partial^2 W^{n+1}}{\partial y^2} &= W^n\frac{\partial^2 W^n}{\partial y^2} + nW^{n-1}\left(\frac{\partial W}{\partial y}\right)^2 \\
\frac{1}{n+1}\frac{\partial^2 W^{n+1}}{\partial x\partial y} &= W^n\frac{\partial^2 W^n}{\partial x\partial y} + nW^{n-1}\left(\frac{\partial W}{\partial x}\frac{\partial W}{\partial y}\right).
\end{aligned}
\tag{B.74}
$$

In this analysis we have chosen axes so that the stress tensor is diagonal ($T^{xy} = 0$). This means that we only have two artificial stress terms to add to the momentum equations. A term $(R_a^{xx} + R_b^{xx})f^n$ which is added to the x momentum equation component and a term $(R_a^{yy} + R_b^{yy})f^n$ which is added to the y component of the momentum equation. Since the initial state is uniform we can take,

$$
R_a^{ij} = R_b^{ij} = R^{ij}.
\tag{B.75}
$$

So that, $R_a^{ij} + R_b^{ij} = 2R^{ij}$. The right hand side of the x component of the SPH momentum equation will now include a term,

$$
\begin{aligned}
R_a^{xx}\left(f^n\frac{\partial W}{\partial x}\right) = R_a^{xx}\left(f^n\frac{\partial W}{\partial \tilde{x}_a}\right) &+ R_a^{xx}\left(\frac{\partial}{\partial \tilde{x}_a}\left(f^n\frac{\partial W}{\partial \tilde{x}_a}\right)\right)(\delta x_a - \delta x_b) \\
&+ R_a^{xx}\left(\frac{\partial}{\partial \tilde{y}_a}\left(f^n\frac{\partial W}{\partial \tilde{x}_a}\right)\right)(\delta y_a - \delta y_b).
\end{aligned}
\tag{B.76}
$$

The first term of the artificial stress (B.76) consists of an *EVEN* function by an *ODD* function so it will not contribute when the summation is taken over all space. Recall that $f = W(\mathbf{r}_{ab})/W(\Delta p)$ and using (B.74),

$$\frac{1}{\chi}\sum_b m_b \left(R_a^{xx}\left(f^n\frac{\partial W}{\partial x}\right) + R_b^{xx}\left(f^n\frac{\partial W}{\partial x}\right)\right)$$

$$=\frac{1}{\chi}2R^{xx}\bar{\rho}(\Delta p)^2\sum_b\left(f^n\frac{\partial W}{\partial x}\right)$$

$$=\frac{1}{\chi}\frac{2R^{xx}\bar{\rho}(\Delta p)^2}{W(\Delta p)^n}\sum_b\left(\frac{\partial}{\partial\tilde{x}_a}\left(W^n\frac{\partial W}{\partial\tilde{x}_a}\right)(\delta x_a-\delta x_b)+\frac{\partial}{\partial\tilde{y}_a}\left(W^n\frac{\partial W}{\partial\tilde{x}_a}\right)(\delta y_a-\delta y_b)\right)$$

$$=\quad\frac{1}{\chi}\frac{2R^{xx}\bar{\rho}(\Delta p)^2}{(n+1)W(\Delta p)^n}\sum_b\frac{\partial^2 W^{n+1}}{\partial\tilde{x}_a^2}X(e^{\imath(\mathbf{k}\cdot\bar{\mathbf{r}}_a-\omega t)}-e^{\imath(\mathbf{k}\cdot\bar{\mathbf{r}}_b-\omega t)})$$

$$+\frac{1}{\chi}\frac{2R^{xx}\bar{\rho}(\Delta p)^2}{(n+1)W(\Delta p)^n}\sum_b\frac{\partial^2 W^{n+1}}{\partial\tilde{x}_a\partial\tilde{y}_a}Y(e^{\imath(\mathbf{k}\cdot\bar{\mathbf{r}}_a-\omega t)}-e^{\imath(\mathbf{k}\cdot\bar{\mathbf{r}}_b-\omega t)})$$

$$=-\frac{\imath}{\omega}\frac{2R^{xx}\bar{\rho}(\Delta p)^2}{(n+1)W(\Delta p)^n}X\sum_b(1-e^{-\imath(\mathbf{k}\cdot\bar{\mathbf{r}}_{ab})})\frac{\partial^2 W^{n+1}}{\partial\tilde{x}_a^2}$$

$$-\frac{\imath}{\omega}\frac{2R^{xx}\bar{\rho}(\Delta p)^2}{(n+1)W(\Delta p)^n}Y\sum_b(1-e^{-\imath(\mathbf{k}\cdot\bar{\mathbf{r}}_{ab})})\frac{\partial^2 W^{n+1}}{\partial\tilde{x}_a\partial\tilde{y}_a}$$

$$=-\frac{\imath}{\omega}\frac{2R^{xx}\bar{\rho}(\Delta p)^2}{(n+1)W(\Delta p)^n}X\sum_b(1-\cos(\mathbf{k}\cdot\bar{\mathbf{r}}_{ab})+\imath\sin(\mathbf{k}\cdot\bar{\mathbf{r}}_{ab}))\frac{\partial^2 W^{n+1}}{\partial\tilde{x}_a^2}$$

$$-\frac{\imath}{\omega}\frac{2R^{xx}\bar{\rho}(\Delta p)^2}{(n+1)W(\Delta p)^n}Y\sum_b(1-\cos(\mathbf{k}\cdot\bar{\mathbf{r}}_{ab})+\imath\sin(\mathbf{k}\cdot\bar{\mathbf{r}}_{ab}))\frac{\partial^2 W^{n+1}}{\partial\tilde{x}_a\partial\tilde{y}_a}$$

$$=-\frac{\imath}{\omega}\frac{2R^{xx}\bar{\rho}(\Delta p)^2}{(n+1)W(\Delta p)^n}X\sum_b(1-\cos(\mathbf{k}\cdot\bar{\mathbf{r}}_{ab}))\frac{\partial^2 W^{n+1}}{\partial\tilde{x}_a^2}$$

$$-\frac{\imath}{\omega}\frac{2R^{xx}\bar{\rho}(\Delta p)^2}{(n+1)W(\Delta p)^n}Y\sum_b(1-\cos(\mathbf{k}\cdot\bar{\mathbf{r}}_{ab}))\frac{\partial^2 W^{n+1}}{\partial\tilde{x}_a\partial\tilde{y}_a}$$

$$=+\frac{1}{\omega^2}\frac{2R^{xx}\bar{\rho}(\Delta p)^2}{(n+1)W(\Delta p)^n}V_x\sum_b(1-\cos(\mathbf{k}\cdot\bar{\mathbf{r}}_{ab}))\frac{\partial^2 W^{n+1}}{\partial\tilde{x}_a^2}$$

$$+\frac{1}{\omega^2}\frac{2R^{xx}\bar{\rho}(\Delta p)^2}{(n+1)W(\Delta p)^n}V_y\sum_b(1-\cos(\mathbf{k}\cdot\bar{\mathbf{r}}_{ab}))\frac{\partial^2 W^{n+1}}{\partial\tilde{x}_a\partial\tilde{y}_a}$$

$$=+\frac{1}{\omega^2}2R^{xx}\bar{\rho}(V_x F_{xx}+V_y F_{xy}).$$

$$(B.77)$$

Where,

$$F_{xx} = \frac{(\Delta p)^2}{(n+1)W^n(\Delta p)} \sum (1 - \cos(\mathbf{k} \cdot \bar{\mathbf{r}}_a)) \frac{\partial^2 W}{\partial \tilde{x}_a^2}^{n+1}$$

$$F_{yy} = \frac{(\Delta p)^2}{(n+1)W^n(\Delta p)} \sum (1 - \cos(\mathbf{k} \cdot \bar{\mathbf{r}}_a)) \frac{\partial^2 W}{\partial \tilde{y}_a^2}^{n+1} \tag{B.78}$$

$$F_{xy} = \frac{(\Delta p)^2}{(n+1)W^n(\Delta p)} \sum (1 - \cos(\mathbf{k} \cdot \bar{\mathbf{r}}_a)) \frac{\partial^2 W}{\partial \tilde{x}_a \partial \tilde{y}_a}^{n+1} .$$

The equations for the dispersion relation (B.72) now become,

$$
\begin{aligned}
\frac{\omega^2 \bar{\rho} V_x}{1 - \beta} = & -(2(\bar{P} - \bar{S}^{xx}) - \bar{\rho} c_o^2) A_x (\mathbf{A} \cdot \mathbf{V}) + (2\bar{P} - 2\bar{S}^{xx})(B_{xx} V_x + B_{xy} V_y) \\
& + \frac{2\mu}{3}(2 V_x A_x - V_y A_y) A_x + \mu(V_x A_y + V_y A_x) A_y \\
& - \zeta(V_x A_y - V_y A_x) A_y + 2\bar{\rho}^2 R^{xx}(\hat{V}_x F_{xx} + \hat{V}_y F_{xy}) \\
\frac{\omega^2 \bar{\rho} V_y}{1 - \beta} = & -(2(\bar{P} - \bar{S}^{yy}) - \bar{\rho} c_o^2) A_y (\mathbf{A} \cdot \mathbf{V}) + (2\bar{P} - 2\bar{S}^{yy})(B_{yy} V_y + B_{xy} V_x) \\
& + \frac{2\mu}{3}(2 V_y A_y - V_x A_x) A_y + \mu(V_x A_y + V_y A_x) A_x \\
& + \zeta(V_y A_x - V_x A_y) A_x + 2\bar{\rho}^2 R^{yy}(\hat{V}_y F_{yy} + \hat{V}_x F_{xy}).
\end{aligned} \tag{B.79}
$$

Long Wavelength Limit

We now investigate the long wavelength behaviour of the SPH equations, in this limit we expect the SPH dispersion relation to agree with the dispersion relation of the exact equations. For sufficiently long wavelengths we can approximate the summation defining $\mathbf{A}$ (B.38) by an integral. That is,

$$\mathbf{A} = (\Delta p)^2 \sum_b \sin(\mathbf{k} \cdot \mathbf{r}_{ab}) \nabla_a W_{ab} \simeq \int \sin(\mathbf{k} \cdot \mathbf{r}_{ab}) \frac{\partial}{\partial \mathbf{r}_a}(W_{ab}) d\mathbf{r}_b. \tag{B.80}$$

Making use of $e^{\imath \phi} = \cos \phi + \imath \sin \phi$ we express (B.80) as,

$$
\begin{aligned}
\mathbf{A} = & Im \left((\Delta p)^2 \sum_b e^{\imath \mathbf{k} \cdot (\mathbf{r}_a - \mathbf{r}_b)} \frac{\partial}{\partial \mathbf{r}_a} W(\mathbf{r}_a - \mathbf{r}_b) \right) \\
= & Im \left(\int e^{-\imath \mathbf{k} \cdot \mathbf{r}_{ab}} \frac{\partial}{\partial \mathbf{r}_a} W(\mathbf{r}_{ab}) d\mathbf{r}_b \right).
\end{aligned} \tag{B.81}
$$

We express the difference in position of particles a and b by the vector $\mathbf{s}_b$ such that,

$$\mathbf{r}_b = \mathbf{r}_a + \mathbf{s}_b$$
$$\mathbf{r}_{ab} = -\mathbf{s}_b. \tag{B.82}$$

Our first step is to calculate the integral involving the complex exponential, we will later take only the imaginary part. As we use kernels which are even functions we take, $W(\mathbf{s}) = W(-\mathbf{s})$.

$$\int e^{-\imath \mathbf{k} \cdot \mathbf{s}_b} \left(-\frac{\partial}{\partial \mathbf{s}_b} W(-\mathbf{s}_b) \right) d\mathbf{s}_b = -\int e^{-\imath \mathbf{k} \cdot \mathbf{s}_b} \left(\frac{\partial}{\partial \mathbf{s}_b} W(\mathbf{s}_b) \right) d\mathbf{s}_b \tag{B.83}$$

Integrating by parts (B.83) becomes,

$$-We^{-\imath \mathbf{k} \cdot \mathbf{s}_b} + \int W(\mathbf{s}_b)(-\imath \mathbf{k}) e^{-\imath \mathbf{k} \cdot \mathbf{s}_b} d\mathbf{s}_b$$
$$= -We^{-\imath \mathbf{k} \cdot \mathbf{s}_b} - \imath \mathbf{k} \int W(\mathbf{s}_b) e^{-\imath \mathbf{k} \cdot \mathbf{s}_b} d\mathbf{s}_b. \tag{B.84}$$

Taking the imaginary parts, we find that the first term is an ODD function and does not contribute.

$$\mathbf{A} = -\mathbf{k} \int W(\mathbf{s}_b) e^{-\imath \mathbf{k} \cdot \mathbf{s}_b} d\mathbf{s}_b = -\mathbf{k}\tilde{W} \tag{B.85}$$

Where $\tilde{W}$ is the Fourier transform of W. In the long wavelength approximation we can take $\tilde{W} = 1$. This relationship for $\mathbf{A}$ is not surprising considering our previous noted similarities between $\mathbf{A}$ and $\mathbf{k}$ in the results of the continuity and deviatoric stress rate equations. It can be similarly shown that,

$$B_{ij} = k_i k_j \tilde{W}. \tag{B.86}$$

We also calculate the effect of XSPH on the dispersion relation by calculating the value of the summation β. In the second line we make use of the fact that the SPH kernels are normalised (2.3), so that $\int W(\mathbf{r}_{ab}) d\mathbf{r}_{ab} = 1$.

$$\beta = \xi \int (1 - \cos(\mathbf{k} \cdot \mathbf{s}_b)) W(\mathbf{r}_{ab}) d\mathbf{r}_b$$
$$= \xi \int W(\mathbf{r}_{ab}) d\mathbf{r}_{ab} - \xi \int \cos(\mathbf{k} \cdot \mathbf{s}_b) W(\mathbf{r}_{ab}) d\mathbf{r}_b$$
$$= \xi \left(1 - Re \left(\int e^{-\imath \mathbf{k} \cdot \mathbf{s}_b} W(\mathbf{s}_b) d\mathbf{s}_b \right) \right) \tag{B.87}$$
$$\beta = \xi(1 - \tilde{W})$$

Correspondingly, as $\tilde{W}$ is equal to one in the long wavelength limit we can take β as zero and the x component of acceleration becomes,

$$\frac{\omega^2 \bar{\rho} V_x}{1 - \beta} = - (2(\bar{P} - \bar{S}^{xx}) - \bar{\rho} c_o^2) A_x (\mathbf{A} \cdot \mathbf{V}) + (2\bar{P} - 2\bar{S}^{xx})(B_{xx} V_x + B_{xy} V_y)$$

$$+ \frac{2\mu}{3}(2V_x A_x - V_y A_y) A_x + \mu(V_x A_y + V_y A_x) A_y - \zeta(V_x A_y - V_y A_x) A_y$$

$$\bar{\rho} V_x \omega^2 = (-2\bar{P} + 2\bar{S}^{xx} + \bar{\rho} c^2)(k_x^2 V_x + k_x k_y V_y) + (2\bar{P} - 2\bar{S}^{xx})(k_x^2 V_x + k_x k_y V_y)$$

$$+ \frac{2\mu}{3}(2k_x^2 V_x - k_x k_y V_y) + \mu(k_y^2 V_x + k_x k_y V_y) - \zeta(k_y^2 V_x - k_x k_y V_y)$$

$$= + \bar{\rho} c_o^2(k_x^2 V_x + k_x k_y V_y) + \frac{4\mu}{3} k_x^2 V_x - \frac{2\mu}{3} k_x k_y V_y + \mu k_y^2 V_x + \mu k_x k_y V_y$$

$$- \zeta k_y^2 V_x + \zeta k_x k_y V_y$$

$$= V_x \left(\bar{\rho} c_o^2 k_x^2 + \frac{4\mu}{3} k_x^2 + \mu k_y^2 - \zeta k_y^2 \right) + V_y \left(\bar{\rho} c_o^2 k_x k_y - \frac{2\mu}{3} k_x k_y + \mu k_x^2 - \zeta k_x k_y \right)$$

$$\bar{\rho} V_x \omega^2 = V_x \left(k_x^2 \left(\bar{\rho} c_o^2 + \frac{4}{3} \mu \right) + k_y^2 (\cdots \zeta) \right) + V_y \left(\bar{\rho} c_o^2 + \frac{1}{3} \mu + \zeta \right) k_x k_y.$$

$$(B.88)$$

Which agrees with the dispersion relation of the continuum equations. This result shows that the SPH perturbation equations are correct in the long wavelength limit and that the dispersion introduced by the SPH formulation can be determined from the Fourier transform of the kernel. We now consider how to chose R^{ij} to prevent short wavelength instabilities.

Short Wavelength Limit

The tensile instability is a short wave length instability initiated by the clumping of pairs of particles. The rate of growth of the instability depends on the initial configuration of particles, the kernel, the smoothing length, and the equation of state. See Morris (1996) for the non elastic case. In this section we calculate coefficients used in the discussion of the stability of some simple particle configurations in section 5.6.

In the first case particles are placed on the vertices of a grid of square cells of side Δp. The second and third cases involve what we term *face centred* lattices. These *face centred* lattices are similar except that every second row of particles is shifted by a distance $\Delta p/2$ in the x direction, to form a *face centred* lattice. A slight

variation is to form a *face centred* lattice by shifting alternate columns of particles in the y direction. These lattices were illustrated in figure 5.3.

In each case we consider waves propagating along the x axis with $k_x = \pi/\Delta p$, $k_y = 0$. The dangerous modes (which lead to instability) are the longitudinal modes with $V_x \neq 0$ and $V_y = 0$ since clumping occurs if these modes are unstable. The transverse modes with $V_x = 0$ and $V_y \neq 0$ are benign because, if they become unstable, they result in lines of particles moving vertically very slowly (Morris 1996).

The cubic kernel and it's derivatives

Before we calculate values of $\mathbf{A}$, B_{xx}, B_{yy}, B_{xy}, β, F_{xx}, F_{yy} and F_{xy}, we first need to calculate values of the kernel and kernel derivatives.

We use the cubic spline kernel, with $q = r/h$,

$$W(q) = \frac{10}{7\pi h^2} \begin{cases} 1 - \frac{3}{2}q^2 + \frac{3}{4}q^3 & \text{if} \quad 0 \leq q \leq 1 \\ \\ \frac{1}{4}(2-q)^3 & \text{if} \quad 1 \leq q \leq 2. \end{cases} \tag{B.89}$$

The first derivative of the cubic spline kernel is given by,

$$\frac{\partial W}{\partial q} = \frac{10}{7\pi h^2} \begin{cases} -3q + \frac{9}{4}q^2 & \text{if} \quad 0 \leq q \leq 1 \\ \\ -\frac{3}{4}(2-q)^2 & \text{if} \quad 1 \leq q \leq 2. \end{cases} \tag{B.90}$$

Differentiating again we find the second derivative of the kernel,

$$\frac{\partial^2 W}{\partial q^2} = \frac{10}{7\pi h^2} \begin{cases} -3 + \frac{9}{2}q & \text{if} \quad 0 \leq q \leq 1 \\ \\ \frac{3}{2}(2-q) & \text{if} \quad 1 \leq q \leq 2. \end{cases} \tag{B.91}$$

We require derivatives of q,

$$\begin{aligned} q &= \frac{r}{h} = \frac{(x^2+y^2)^{\frac{1}{2}}}{h} \\ \frac{\partial q}{\partial x} &= \frac{x}{h(x^2+y^2)^{\frac{1}{2}}} = \frac{x}{hr} \\ \frac{\partial q}{\partial y} &= \frac{y}{h(x^2+y^2)^{\frac{1}{2}}} = \frac{y}{hr}. \end{aligned} \tag{B.92}$$

Second derivatives of q are obtained using the quotient rule,

$$
\frac{\partial^2 q}{\partial x^2} = \frac{1}{h} \frac{r^2 - x^2}{r^3} = \frac{1}{hr} \left(1 - \frac{x^2}{r^2} \right)
$$
$$
\frac{\partial^2 q}{\partial y^2} = \frac{1}{h} \frac{r^2 - y^2}{r^3} = \frac{1}{hr} \left(1 - \frac{y^2}{r^2} \right) \tag{B.93}
$$
$$
\frac{\partial^2 q}{\partial x \partial y} = -\frac{xy}{hr^3}.
$$

To find derivatives with respect to x and y we make use of the chain rule,

$$
\frac{\partial W}{\partial x} = \frac{\partial W}{\partial q} \frac{\partial q}{\partial x}
$$
$$
\frac{\partial W}{\partial x} = \frac{\partial W}{\partial q} \frac{\partial q}{\partial y}
$$
$$
\frac{\partial^2 W}{\partial x^2} = \frac{\partial W}{\partial q} \frac{\partial^2 q}{\partial x^2} + \frac{\partial^2 W}{\partial q^2} \left(\frac{\partial q}{\partial x} \right)^2 \tag{B.94}
$$
$$
\frac{\partial^2 W}{\partial y^2} = \frac{\partial W}{\partial q} \frac{\partial^2 q}{\partial y^2} + \frac{\partial^2 W}{\partial q^2} \left(\frac{\partial q}{\partial y} \right)^2
$$
$$
\frac{\partial^2 W}{\partial x \partial y} = \frac{\partial W}{\partial q} \frac{\partial^2 q}{\partial x \partial y} + \frac{\partial^2 W}{\partial q^2} \left(\frac{\partial q}{\partial x} \frac{\partial q}{\partial y} \right).
$$

Square Cells

Figure B.1 illustrates the particles that interact in a grid of square cells with particle spacing Δp and smoothing length $h = \Delta p$. The grey particle in the middle interacts with the eight surrounding particles. The particles on the boundary are just outside the interaction zone. Table B.1 shows all the particles that contribute to the summations in this case. We assume a wave of short wavelength travelling in the x direction, the wave numbers are $k_x = \pi/\Delta p$, $k_y = 0$.

In table B.2 we calculate values of the derivatives of each of the particles that interact with the central particle in figure B.1. We write $\psi = 5/14\pi(\Delta p)^2$. The first half of the table shows derivatives of W with respect to q and the derivatives of q with respect to x and y. The second half of the table combines these derivatives using the chain rule (B.94) to give derivatives of the kernel with respect to x and y.

We then calculate the values of the summations (B.38) for the square cell setup using tables B.1 and B.2. We begin by calculating the values of $A_x = (\Delta p)^2 \sum \sin(\mathbf{k} \cdot \mathbf{r}_{ab}) \partial W/\partial x$ and $A_y = (\Delta p)^2 \sum_b \sin(\mathbf{k} \cdot \mathbf{r}_{ab}) \partial W/\partial y$. When the particles are setup on

square cells the value of $\sin(\mathbf{k} \cdot \mathbf{r}_{ab})$ is always zero we find that A_x and A_y are also zero.
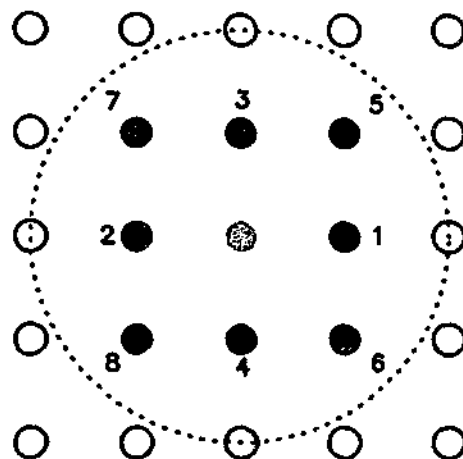
Figure B.1: *Diagram showing particles within the 2h smoothing distance for an initial square cell particle placement for a cubic kernel with $h = \Delta p$. The grey particle at the centre of the circle has interactions with the eight numbered black particles. Dotted line denotes the edge of the circle of influence of the kernel of the grey particle.*

Num	Δx	Δy	$\sin(\mathbf{k} \cdot \mathbf{r})$	$1 - \cos(\mathbf{k} \cdot \mathbf{r})$	q
1	Δp	0	0	2	1
2	$-\Delta p$	0	0	2	1
3	0	Δp	0	0	1
4	0	$-\Delta p$	0	0	1
5	Δp	Δp	0	2	$\sqrt{2}$
6	Δp	$-\Delta p$	0	2	$\sqrt{2}$
7	$-\Delta p$	Δp	0	2	$\sqrt{2}$
8	$-\Delta p$	$-\Delta p$	0	2	$\sqrt{2}$

Table B.1: *Properties of position and wavenumber for particles in the square cell setup of figure B.1 with $h = \Delta p$ and for a wave propagating only in the x direction with wave numbers $k_x = \pi/\Delta p$ and $k_y = 0$. Values of $\sin(\mathbf{k} \cdot \mathbf{r})$ and $1 - \cos(\mathbf{k} \cdot \mathbf{r})$ are used in determining the coefficients (B.38) in the dispersion relation.*

Num	W	$\frac{\partial W}{\partial q}$	$\frac{\partial^2 W}{\partial q^2}$	$\frac{\partial q}{\partial x}$	$\frac{\partial q}{\partial y}$	$\frac{\partial^2 q}{\partial x^2}$	$\frac{\partial^2 q}{\partial y^2}$	$\frac{\partial^2 q}{\partial x \partial y}$
1	ψ	-3ψ	6ψ	$\frac{1}{\Delta p}$	0	0	$\frac{1}{(\Delta p)^2}$	0
2	ψ	-3ψ	6ψ	$-\frac{1}{\Delta p}$	0	0	$-\frac{1}{(\Delta p)^2}$	0
3	ψ	-3ψ	6ψ	0	$\frac{1}{\Delta p}$	$\frac{1}{(\Delta p)^2}$	0	0
4	ψ	-3ψ	6ψ	0	$-\frac{1}{\Delta p}$	$\frac{1}{(\Delta p)^2}$	0	0
5	$\psi(2-\sqrt{2})^3$	$-3\psi(2-\sqrt{2})^2$	$6\psi(2-\sqrt{2})$	$\frac{1}{\sqrt{2}\Delta p}$	$\frac{1}{\sqrt{2}\Delta p}$	$\frac{1}{(\sqrt{2})^3(\Delta p)^2}$	$\frac{1}{(\sqrt{2})^3(\Delta p)^2}$	$\frac{1}{(\sqrt{2})^3(\Delta p)^2}$
6	$\psi(2-\sqrt{2})^3$	$-3\psi(2-\sqrt{2})^2$	$6\psi(2-\sqrt{2})$	$\frac{1}{\sqrt{2}\Delta p}$	$-\frac{1}{\sqrt{2}\Delta p}$	$\frac{1}{(\sqrt{2})^3(\Delta p)^2}$	$\frac{1}{(\sqrt{2})^3(\Delta p)^2}$	$-\frac{1}{(\sqrt{2})^3(\Delta p)^2}$
7	$\psi(2-\sqrt{2})^3$	$-3\psi(2-\sqrt{2})^2$	$6\psi(2-\sqrt{2})$	$-\frac{1}{\sqrt{2}\Delta p}$	$\frac{1}{\sqrt{2}\Delta p}$	$\frac{1}{(\sqrt{2})^3(\Delta p)^2}$	$\frac{1}{(\sqrt{2})^3(\Delta p)^2}$	$-\frac{1}{(\sqrt{2})^3(\Delta p)^2}$
8	$\psi(2-\sqrt{2})^3$	$-3\psi(2-\sqrt{2})^2$	$6\psi(2-\sqrt{2})$	$-\frac{1}{\sqrt{2}\Delta p}$	$-\frac{1}{\sqrt{2}\Delta p}$	$\frac{1}{(\sqrt{2})^3(\Delta p)^2}$	$\frac{1}{(\sqrt{2})^3(\Delta p)^2}$	$\frac{1}{(\sqrt{2})^3(\Delta p)^2}$

Num	W	$\frac{\partial W}{\partial x}$	$\frac{\partial W}{\partial y}$	$\frac{\partial^2 W}{\partial x^2}$	$\frac{\partial^2 W}{\partial y^2}$	$\frac{\partial^2 W}{\partial x \partial y}$
1	ψ	$-\frac{3\psi}{\Delta p}$	0	$\frac{6\psi}{(\Delta p)^2}$	$-\frac{3\psi}{(\Delta p)^2}$	0
2	ψ	$\frac{3\psi}{\Delta p}$	0	$\frac{6\psi}{(\Delta p)^2}$	$-\frac{3\psi}{(\Delta p)^2}$	0
3	ψ	0	$-\frac{3\psi}{\Delta p}$	$-\frac{3\psi}{(\Delta p)^2}$	$\frac{6\psi}{(\Delta p)^2}$	0
4	ψ	0	$\frac{3\psi}{\Delta p}$	$-\frac{3\psi}{(\Delta p)^2}$	$\frac{6\psi}{(\Delta p)^2}$	0
5	$\psi(2-\sqrt{2})^3$	$-\frac{3\psi(2-\sqrt{2})^2}{\sqrt{2}\Delta p}$	$-\frac{3\psi(2-\sqrt{2})^2}{\sqrt{2}\Delta p}$	$\frac{3\psi(3-\sqrt{2})(2-\sqrt{2})}{2(\Delta p)^2}$	$\frac{3\psi(3-\sqrt{2})(2-\sqrt{2})}{2(\Delta p)^2}$	$\frac{3\psi(3-\sqrt{2})(2-\sqrt{2})}{2(\Delta p)^2}$
6	$\psi(2-\sqrt{2})^3$	$-\frac{3\psi(2-\sqrt{2})^2}{\sqrt{2}\Delta p}$	$\frac{3\psi(2-\sqrt{2})^2}{\sqrt{2}\Delta p}$	$\frac{3\psi(3-\sqrt{2})(2-\sqrt{2})}{2(\Delta p)^2}$	$\frac{3\psi(3-\sqrt{2})(2-\sqrt{2})}{2(\Delta p)^2}$	$-\frac{3\psi(3-\sqrt{2})(2-\sqrt{2})}{2(\Delta p)^2}$
7	$\psi(2-\sqrt{2})^3$	$\frac{3\psi(2-\sqrt{2})^2}{\sqrt{2}\Delta p}$	$-\frac{3\psi(2-\sqrt{2})^2}{\sqrt{2}\Delta p}$	$\frac{3\psi(3-\sqrt{2})(2-\sqrt{2})}{2(\Delta p)^2}$	$\frac{3\psi(3-\sqrt{2})(2-\sqrt{2})}{2(\Delta p)^2}$	$-\frac{3\psi(3-\sqrt{2})(2-\sqrt{2})}{2(\Delta p)^2}$
8	$\psi(2-\sqrt{2})^3$	$\frac{3\psi(2-\sqrt{2})^2}{\sqrt{2}\Delta p}$	$\frac{3\psi(2-\sqrt{2})^2}{\sqrt{2}\Delta p}$	$\frac{3\psi(3-\sqrt{2})(2-\sqrt{2})}{2(\Delta p)^2}$	$\frac{3\psi(3-\sqrt{2})(2-\sqrt{2})}{2(\Delta p)^2}$	$\frac{3\psi(3-\sqrt{2})(2-\sqrt{2})}{2(\Delta p)^2}$

Table B.2: Values of kernel derivatives for square cell setup.

Looking at B_{xx} we find that particles numbered *three* and *four* in table B.1, have a value of $1 - \cos(\mathbf{k} \cdot \mathbf{r}_{ab}) = 0$ and do not contribute to the summation. All of the other particles have a contribution of $1 - \cos(\mathbf{k} \cdot \mathbf{r}_{ab}) = 2$. We find that,

$$
\begin{aligned}
B_{xx} &= (\Delta p)^2 \sum_b (1 - \cos(\mathbf{k} \cdot \mathbf{r}_{ab})) \frac{\partial^2 W_{ab}}{\partial \tilde{x}_a^2} \\
&= (\Delta p)^2 2 \sum_b \left. \frac{\partial^2 W_{ab}}{\partial \tilde{x}_a^2} \right|_{1,2,3,4,5,6,7,8} \\
&= (\Delta p)^2 2 \left(2 \left(\frac{6\psi}{(\Delta p)^2} \right) + 2(0) + 4 \left(\frac{3\psi(3 - \sqrt{2})(2 - \sqrt{2})}{2(\Delta p)^2} \right) \right) \quad \text{(B.95)} \\
&= 2 \left(12\psi + 6\psi(3 - \sqrt{2})(2 - \sqrt{2}) \right) \\
&= 12\psi \left(2 + 6 - 3\sqrt{2} - 2\sqrt{2} + 2 \right) \\
&= \frac{30}{7\pi(\Delta p)^2}(10 - 5\sqrt{2}).
\end{aligned}
$$

Similarly, we find the value of B_{yy} to be given by,

$$
\begin{aligned}
B_{yy} &= (\Delta p)^2 \sum_b (1 - \cos(\mathbf{k} \cdot \mathbf{r}_{ab})) \frac{\partial^2 W_{ab}}{\partial \tilde{y}_a^2} \\
&= (\Delta p)^2 2 \sum_b \left. \frac{\partial^2 W_{ab}}{\partial \tilde{y}_a^2} \right|_{1,2,3,4,5,6,7,8} \\
&= (\Delta p)^2 2 \left(-\frac{3\psi}{(\Delta p)^2} - \frac{3\psi}{(\Delta p)^2} + 0 + 0 + 4 \left(\frac{3\psi(3 - \sqrt{2})(2 - \sqrt{2})}{2(\Delta p)^2} \right) \right) \quad \text{(B.96)} \\
&= 2 \left(-6\psi + 6\psi(3 - \sqrt{2})(2 - \sqrt{2}) \right) \\
&= 12\psi(-1 + 6 - 3\sqrt{2} - 2\sqrt{2} + 2) \\
&= \frac{30}{7\pi(\Delta p)^2}(7 - 5\sqrt{2}).
\end{aligned}
$$

In the case of B_{xy} we find that the four nearest neighbours (particles *one*, *two*, *three* and *four*) all have a second derivative $\partial^2 W_{ab}/\partial \tilde{x}_a \partial \tilde{y}_a = 0$ and do not contribute to our summation. We also find that the contributions of the remaining particles cancel with each other so that $B_{xy} = 0$.

$$B_{xy} = (\Delta p)^2 \sum_b (1 - \cos(\mathbf{k} \cdot \mathbf{r}_{ab})) \frac{\partial^2 W_{ab}}{\partial \tilde{x}_a \partial \tilde{y}_a}$$

$$= (\Delta p)^2 2 \sum_b \left. \frac{\partial^2 W_{ab}}{\partial \tilde{x}_a \partial \tilde{y}_a} \right|_{1,2,5,6,7,8}$$

$$= (\Delta p)^2 2 \left(0 + (2 - 2) \left(\frac{3\psi(3 - \sqrt{2})(2 - \sqrt{2})}{2(\Delta p)^2} \right) \right) \qquad \text{(B.97)}$$

$$= 0.$$

The value of β is introduced with our use of the XSPH smoothed velocity. Again particles *three* and *four* have no contribution as they have a value of $1 - \cos(\mathbf{k} \cdot \mathbf{r}_{ab}) = 0$. ξ is the XSPH parameter.

$$\beta = \xi(\Delta p)^2 \sum_b (1 - \cos(\mathbf{k} \cdot \mathbf{r}_{ab})) W_{ab}$$

$$= 2\xi(\Delta p)^2 \sum_b W_{ab}|_{1,2,5,6,7,8}$$

$$= 2\xi(\Delta p)^2 (2\psi + 4(\psi(2 - \sqrt{2})^3) \qquad \text{(B.98)}$$

$$= 4\psi\xi(\Delta p)^2 (1 + 2(2 - \sqrt{2})^3)$$

$$= \frac{10}{7\pi} \xi(\Delta p)^2 (1 + 2(2 - \sqrt{2})^3).$$

The use of our artificial stress introduces the coefficients F_{xx}, F_{yy} and F_{xy} (B.78) into the dispersion relation. We require the value of $\partial^2 W^{(n+1)}/\partial x^2$, which we have shown previously is given by,

$$\frac{\partial}{\partial x} W^{(n+1)} = (n + 1) W^{(n-1)} \left(n \left(\frac{\partial W}{\partial x} \right)^2 + W \frac{\partial^2 W}{\partial x^2} \right). \qquad \text{(B.99)}$$

As the size of our artificial stress is dependent on a high power of the kernel and the value of the kernel is less than one and drops off sharply for particle spacings greater than Δp, particles that are not the nearest neighbours have only a negligible contribution to these summations. We conduct the summation over nearest neighbours (particles *one*, *two*, *three* and *four*), we find that particles *three* and *four* have $1 - \cos(\mathbf{k}.\mathbf{r}_{ab}) = 0$ and do not contribute. We calculate the summation only for particles *one* and *two* which both have $q = 1$ and we find,

$$
\begin{aligned}
F_{xx} &= \frac{(\Delta p)^2}{(n+1)W^n(\Delta p)} \sum (1 - \cos(\mathbf{k} \cdot \tilde{\mathbf{r}}_a)) \frac{\partial^2 W^{n+1}}{\partial \tilde{x}_a^2} \\
&= \frac{(\Delta p)^2}{(n+1)W^n(\Delta p)} 2 \sum \frac{\partial^2 W^{n+1}}{\partial \tilde{x}_a^2} \\
&= \frac{(\Delta p)^2}{(n+1)W^n(\Delta p)} 2 \sum (n+1)W^{n-1} \left(n \left(\frac{\partial W}{\partial x} \right)^2 + W \frac{\partial^2 W}{\partial x^2} \right) \\
&\simeq \frac{(\Delta p)^2}{(n+1)\psi^n} 2(n+1)\psi^{n-1} \left(2n \left(\frac{9\psi^2}{(\Delta p)^2} \right) + 2\psi \frac{6\psi}{(\Delta p)^2} \right) \\
&\simeq \frac{(\Delta p)^2}{\psi} 12 \frac{\psi^2}{(\Delta p)^2} (3n+2) \\
&\simeq 12\psi(3n+2) \\
&\simeq \frac{30}{7\pi(\Delta p)^2} (3n+2).
\end{aligned}
\tag{B.100}
$$

For F_{yy} we find,

$$
\begin{aligned}
F_{yy} &= \frac{(\Delta p)^2}{(n+1)W^n(\Delta p)} \sum (1 - \cos(\mathbf{k} \cdot \tilde{\mathbf{r}}_a)) \frac{\partial^2 W^{n+1}}{\partial \tilde{y}_a^2} \\
&= \frac{(\Delta p)^2}{(n+1)W^n(\Delta p)} 2 \sum \frac{\partial^2 W^{n+1}}{\partial \tilde{y}_a^2} \\
&= \frac{(\Delta p)^2}{(n+1)W^n(\Delta p)} 2 \sum (n+1)W^{n-1} \left(n \left(\frac{\partial W}{\partial y} \right)^2 + W \frac{\partial^2 W}{\partial y^2} \right) \\
&\simeq \frac{(\Delta p)^2}{(n+1)\psi^n} 2(n+1)\psi^{n-1} \left(0 + 2\psi \frac{-3\psi}{(\Delta p)^2} \right) \\
&\simeq -\frac{(\Delta p)^2}{\psi} 12 \frac{\psi^2}{(\Delta p)^2} \\
&\simeq -\frac{30}{7\pi(\Delta p)^2}.
\end{aligned}
\tag{B.101}
$$

As $\partial W/\partial y$ and $\partial^2 W/\partial x\partial y$ are both equal to zero we find that $F_{xy} = 0$. To calculate the values of these summations for different values of h we have resorted to the use of a computer program and obtain numerical values. In table B.3 we show the values of these summations for smoothing lengths $1.0 \leq h/\Delta p \leq 2.0$, we have taken the constant power in the artificial stress to be $n = 4$.

$h/\Delta p$	β	A_{xx}	A_{yy}	B_{xx}	B_{yy}	B_{xy}	F_{xx}	F_{yy}	F_{xy}
1.0	0.6375	0.0	0.0	3.9956	-0.0969	0.0	19.1163	-1.3464	0.0
1.1	0.7607	0.0	0.0	2.3166	-0.2245	0.0	12.9669	-1.1202	0.0
1.2	0.8473	0.0	0.0	1.4234	0.0023	0.0	8.6243	-0.8800	0.0
1.3	0.9086	0.0	0.0	0.8721	0.1169	0.0	5.8022	-0.6508	0.0
1.4	0.9517	0.0	0.0	0.5167	0.1423	0.0	3.9900	-0.4610	0.0
1.5	0.9798	0.0	0.0	0.1655	0.0122	0.0	2.8637	-0.2621	0.0
1.6	0.9940	0.0	0.0	0.0239	-0.0542	0.0	2.0804	-0.1542	0.0
1.7	0.9991	0.0	0.0	0.0004	-0.0315	0.0	1.5383	-0.0866	0.0
1.8	1.0006	0.0	0.0	-0.0203	-0.0238	0.0	1.1528	-0.0471	0.0
1.9	1.0007	0.0	0.0	-0.0080	-0.0110	0.0	0.8727	-0.0260	0.0
2.0	1.0007	0.0	0.0	-0.0048	-0.0078	0.0	0.6657	-0.0158	0.0

Table B.3: *Square cells. Values of the coefficients in the dispersion relation for various $h/\Delta p$.*

Face Centred Cells

We do not evaluate exact values of the summations in the *face centred* case here. These can however be evaluated following the steps previously outlined for the case of *square cells*. Numerical values of the *face centred* summations for a range of smoothing lengths are presented in tables B.4 and B.5 for the x shifted and y shifted cases respectively. We have again assumed a value of $n = 4$. An analysis of the stability of these *face centred* particle arrangements was presented in section 5.6.5. The major difference between the square cell case is that the values of A are no longer equal to zero in the x shifted *face centred* case, these values are equal to zero in the y shifted *face centred* case. This is a result of assuming wavenumbers only in the x direction.

$h/\Delta p$	β	A_{xx}	A_{yy}	B_{xx}	B_{yy}	B_{xy}	F_{xx}	F_{yy}	F_{xy}
1.0	0.7702	-0.4304	0.0	2.8138	0.5162	0.0	19.6767	1.5789	0.0
1.1	0.8621	-0.3323	0.0	1.4554	0.2588	0.0	13.4473	1.7259	0.0
1.2	0.9208	-0.2336	0.0	0.7143	0.1029	0.0	8.9561	1.6295	0.0
1.3	0.9579	-0.1448	0.0	0.3001	0.0091	0.0	5.9602	1.3271	0.0
1.4	0.9805	-0.0777	0.0	0.1127	-0.0399	0.0	4.0013	1.0120	0.0
1.5	0.9928	-0.0392	0.0	0.0282	-0.0685	0.0	2.7169	0.7420	0.0
1.6	0.9984	-0.0184	0.0	0.0253	-0.0496	0.0	1.8668	0.5301	0.0
1.7	1.0005	-0.0082	0.0	0.0147	-0.0313	0.0	1.2975	0.3711	0.0
1.8	1.0006	-0.0017	0.0	0.0042	-0.0090	0.0	0.9117	0.2550	0.0
1.9	0.9998	0.0025	0.0	0.0077	-0.0005	0.0	0.6595	0.1762	0.0
2.0	0.9990	0.0056	0.0	0.0107	0.0043	0.0	0.4780	0.1177	0.0

Table B.4: *Face centred cells - x direction shift. Values of the coefficients in the dispersion relation for various $h/\Delta p$.*

$h/\Delta p$	β	A_{xx}	A_{yy}	B_{xx}	B_{yy}	B_{xy}	F_{xx}	F_{yy}	F_{xy}
1.0	0.6309	0.0	0.0	3.7608	0.1708	0.0	5.8861	1.1561	0.0
1.1	0.7506	0.0	0.0	2.8894	0.2002	0.0	5.8235	1.0718	0.0
1.2	0.8470	0.0	0.0	1.6095	-0.0099	0.0	5.2326	0.8771	0.0
1.3	0.9154	0.0	0.0	0.7964	-0.1320	0.0	4.2707	0.6307	0.0
1.4	0.9573	0.0	0.0	0.3526	-0.0910	0.0	3.3429	0.4194	0.0
1.5	0.9805	0.0	0.0	0.0999	-0.0132	0.0	2.5618	0.2600	0.0
1.6	0.9921	0.0	0.0	0.0295	0.0230	0.0	1.9445	0.1484	0.0
1.7	0.9972	0.0	0.0	0.0087	0.0367	0.0	1.4715	0.0745	0.0
1.8	0.9992	0.0	0.0	0.0236	0.0431	0.0	1.1145	0.0280	0.0
1.9	1.0001	0.0	0.0	0.0014	0.0118	0.0	0.8558	0.0247	0.0
2.0	1.0004	0.0	0.0	-0.0066	0.0000	0.0	0.6560	0.0133	0.0

Table B.5: *Face centred cells - y direction shift. Values of the coefficients in the dispersion relation for various $h/\Delta p$.*

Appendix C

Animations

In addition to presenting images from SPH simulations throughout this thesis we present and describe a series of animations of simulations in this appendix. The animations are provided on an accompanying CDROM. An advantage of viewing animations (instead of a series of still images) is that it is intuitively easier to detect and follow changes over the course of the simulation as we can see more information.

Also contained on the CDROM are electronic versions of this thesis in *PDF* and *postscript* formats. All of these files can be accessed by loading the file *CCAT-GOW.html* (found on the CDROM) into a web browser and following the appropriate links. The animations are provided in the *MPEG* format.

Water Wave Tests

We begin by presenting animations of the tests we conducted in chapter three to validate our code. We demonstrate the runup and generation of solitary waves, the breaking of a dam and an example of an undular bore.

Solitary Wave Run up

Animation:*solwave.mpeg*
Here we present an example of a simulation for the run up of solitary waves against a wall (section 3.1). The colours indicate particle speed, with blue denoting the slowest particles and green denoting the fastest moving particles. We show a solitary wave of amplitude $H/D = 0.5$ and see the wave lose kinetic energy as it climbs the wall (and changes colour from green to blue). The wave reforms as the water falls down the wall and propagates across the tank in the opposite direction.

Solitary Wave Generation

Animation:wavet1.mpeg
Animation:wavet4.mpeg

We show simulations of waves generated by a moving boundary (section 3.2). The first example is the $t_* = 1$ case, the boundary moves only a small distance and the wave that develops from this motion is also only small. The deviation to the water level is minor although the motion of the wave can be seen by the changes in particle speeds (colours) as it propagates along the tank. The second example we show is the $t_* = 4$ case. The wall travels further in this case and displaces a larger amount of water. The wave that develops is clear to see both from its profile and speed (colour variation). The fluid slows down as it runs up the wall, before accelerating down the wall and reforming as a wave.

Breaking Dam

Animation:dambreak.mpeg.

The next test we present is that of a breaking dam, this animation is the $n^2 = 1$ case of Martin and Moyce (1952). Units of time are in the scaled units of (3.5). The animation shows water surging out from the bottom of the column after the wall is removed. The initial sharp and square profile quickly adjusts to a smooth profile as the front surges across the tank.

Tidal Bore

Animation:bore.mpeg

The last animation of our water validation tests that we present is of an undular bore (section 3.4). The bore is pushing water towards the tank wall. After impacting with the wall a splashing motion occurs which forms into the first wave. This wave propagates across the tank followed by two smaller amplitude waves which are also generated.

Caldera Collapse Animations

This series of animations shows some of the simple models of caldera collapse (section 4.1), simulations of different cavity widths and a simulation in a tank with a sloping beach.

Colliding Breaking Dams

Animation:*damcollide.mpeg*

The first animation in this section is for the collision of two collapsing water columns. As expected the initial profile is similar to that of just a single breaking dam (*dambreak.mpeg*). The two surge fronts collide, sending water up in a large column at the centre of the tank. This column disperses away as two breaking waves travelling in opposite directions form. The waves run up the sides of the tank and reform as two non breaking waves, which propagate and meet in the middle of the tank before passing through each other.

Experimental Caldera Model

Animation:*caldexperiment.mpeg*

Here we present an example of one of the wave tank caldera collapse experiments (section 4.1). This is the case of $D_2 = 12cm$, $D = 30cm$, $W = 40cm$ and $L = 200cm$. Two jets are seen to develop when the walls are removed. They meet in the centre of the tank form a vortex and a column of water. The column breaks into waves that propagate across the tank. These waves runup the sides of the tank and reform as waves travelling in the opposite direction towards the centre of the tank.

Boundary Force Caldera Model

Animation:*caldbforce.mpeg*

This animation shows a caldera collapse model with a boundary force implementation of the boundary conditions. The initial part of the animation shows the damping of the system to a relaxed state. There is a lot of noise generated by the tops of the inner walls. The flow is quantitatively similar to the corresponding experiment *caldexperiment.mpeg*.

Ghost Particle Caldera Model

Animation:*caldgpart.mpeg*

The problems with noise at the inner boundaries in the boundary force animation (*caldbforce.mpeg*) have been removed with the use of a ghost particle boundary implementation. Again we see the damping of the system before the wall is removed and two jets are produced. The jets meet before they touch the tank bottom (in agreement with experiment), before forming a head of water which disperses away as waves, which oscillate back and forth across the tank.

Different Cavity Widths

Animation:*wid05.mpeg*
Animation:*wid15.mpeg*
Animation:*wid25.mpeg*
Animation:*wid40.mpeg*

These animations show differences in the mechanism of wave generation as the cavity width is varied (section 4.2). In the first example *wid05.mpeg* the jet contacts the side wall long before reaching the cavity floor, only a small amount of water is displaced and the resulting wave amplitude is also small. The wave amplitude is larger in the next example *wid15.mpeg*, in this case the jet impacts near the bottom of the side wall at the intersection with the floor. As the cavity width is increased further (*wid25.mpeg,wid40.mpeg*) the amplitude of generated waves decreases, the jet impacts with the cavity floor and breaks into two flows.

Waves in a Long Tank

Animation:*longtank.mpeg*

Here we present an animation of the calculation of waves produced in a long tank with a sloping beach. As in section 4.3 the scale is such that the vertical dimension is exaggerated to five times the horizontal scale. This scaling allows us to better view the waves which are produced. Complicated motions can be seen as water fills the cavity. A train of waves develops and propagates across the tank preceded by a drop in the water level. The first wave in the train steepens and breaks as it runs up the beach.

Elastic and Plastic Material Tests

The third set of animations involve test cases of solid bodies. We begin by presenting a test for the propagation of longitudinal waves before demonstrating tests of colliding rings, oscillating plates and the tensional extension of plates.

Longitudinal Waves

Animation: *waveprop.mpeg*

In this animation an initial 5% Gaussian velocity distribution propagates through a periodic block of SPH particles $200cm$ long by $20cm$ wide. See section 5.6 for more details. In this simulation $c_o = 1.0$, $\rho = 1.0$, $\mu = 0.22$, $h = \Delta p$. With these parameters longitudinal waves have a theoretical wave speed (in our dimensionless units) of 1.137, compared to a measured speed of 1.164 for the simulation.

Colliding Rings

Animation: *ringeps0.mpeg*
Animation: *ringeps22.mpeg*

We present animations of the collision of elastic rings of section 6.1. The first animation *ringeps0.mpeg* illustrates how the colliding rings artificially fracture and break up in the standard SPH case. The second animation shows that when the tensile instability is removed (by adding artificial stress terms) SPH is able to model the collision of elastic rings with ease. Particles are now coloured according to the deviatoric stress, lighter colours (yellow) denote tension and darker colours (blue) indicate compression.

Oscillating Plates

Animation: *beamv1.mpeg*
Animation: *beamv5.mpeg*

We demonstrate some of the oscillating plates of section 6.2. Particles are again coloured according to their stress. The first example *beamv1.mpeg* shows a small amplitude oscillation, $V_f = 0.01$. The variation in stress from tension to compression on opposite sides of the plate can be seen as the plate oscillates. The second example

beamv5.mpeg is a case with $V_f = 0.05$, the amplitude of the oscillation is much larger and higher stresses also occur.

Plastic Oscillating Plate

Animation:plasticbeam.mpeg

We introduce the Von-Mises criterion (section 5.2) into our simulations of oscillating plates to model plastic effects. Instead of going through a full oscillation, plasticity takes over, the underside of the plate is stretched past the elastic limit and remains extended. The plate is unable to travel beyond its initial position, instead it pivots at a point along the plate near the support and travels upwards again.

Ductile Plates in Tension

Animation:epbeame0.mpeg

Animation:epbeame3.mpeg

Here we illustrate the effects of the tensile instability in standard SPH on a plate stretched in tension. In epbeame0.mpeg we show the standard SPH case ($\epsilon = 0.0$). Artificial fracturing quickly develops and the plate breaks in an unphysical way. The simulation epbeame3.mpeg employs artificial stress terms with $\epsilon = 0.3$ and illustrates the necking of a ductile plate in tension. The artificial stress terms remove the destructive effects of the tensile instability.

Brittle Plates in Tension

Animation:brittlefrac1.mpeg

Animation:brittlefrac2.mpeg

These animations demonstrate the initiation and growth of cracks of brittle plates in tension with high and low strain rates (section 6.4.2). The first part of the simulation shows the stress waves which develop in the material. In the second half particles are coloured according to their state of damage and the development of cracks can be seen. In agreement with theory the extent of damage is much greater in the higher strain rate case (brittlefrac2.mpeg).

Fracture Around Magma Chambers

In this series of animations we show some of the simple models for the fracture of rock during caldera collapse found in chapter 7. The animations begin with particles coloured according to their mean stress (section 6.1) and conclude by repeating the simulation again, coloured according to damage.

Plate without a Chamber

Animation:*nochamber.mpeg*

Here we show the effect of tensile stress on a material with no stress concentrators. The cracks appear randomly and act to relieve material surrounding them from the applied stress. The cracks are initiated at weaknesses in the material and there is a small amount of damage distributed through the material at the conclusion of the simulation.

Chamber without Internal Pressure

Animation:*chamber.mpeg*

The effect of including a chamber in the material, concentrates the stress in the area directly above and below the chamber. Fracture is initiated earlier (than in the *nochamber.mpeg* simulation) at the points of maximum stress concentration and breaks the material into two clear pieces. Damage is almost only accumulated in the region of highest stress concentration, with few flaws activated elsewhere.

Chamber with Internal Pressure

Animation:*gas.mpeg*

In this simulation we see the effect of including an internal pressure into the chamber. The internal pressure further increases the stress around the chamber (compared to the case with no magmatic pressure (*chamber.mpeg*)). Fracture is again initiated earlier due to this stress concentration which results in radial fractures forming around the cavity due to the internal pressure in addition to the break down the centre of the plate caused by the applied tensile stress.

References

Ashby, M. F. and D. R. H. Jones (1980). *Engineering Materials I: An Introduction to their Properties and Applications*. Pergamon Press.

Atluri, S. N. (1984). On Constitutive Relations at Fiite Strain: Hypo-Elasticity and Elasto-Plasticity with Isotropic or Kinematic Hardening. *Computer Methods in Applied Mechanics and Engineering 43*, 137–171.

Baker, J. A. (1963). *Lattice Theories of the Liquid State*. Pergamon Press.

Batchelor, G. K. (1973). *An Introduction to Fluid Dynamics*. Cambridge University Press.

Benz, W. (1990). Smooth Particle Hydrodynamics : A Review. In J. R. Buchler (Ed.), *The Numerical Modelling of Nonlinear Stellar Pulsations*, pp. 269–288. Kluwer Academic Publishers.

Benz, W. and E. Asphaug (1994). Impact Simulations with Fracture. I. Method and Tests. *Icarus 107*, 98–116.

Benz, W. and E. Asphaug (1995). Simulations of Brittle Solids Using Smooth Particle Hydrodynamics. *Computer Physics Communications. 87*, 253–265.

Camfield, F. E. and R. E. Street (1968). *Journal Waterways and Harbours Division ASCE 95*(WW1). Paper 6380.

Carslaw, H. S. and J. C. Jaeger (1959). *Conduction of Heat in Solids* (2nd ed.). Oxford Science Publications.

Chan, R. K.-C. and R. L. Street (1970). A Computer Study of Finite-Amplitude Water Waves. *Journal of Computational Physics 6*, 68–94.

Chen, G., C. Kharif, S. Zaleski, and J. Li (1999). Two-Dimensional Navier-Stokes Simulation of Breaking Waves. *Physics of Fluids 11*(1), 121–133.

Chorin, A. J. (1967). A Numerical Method For Solving Incompressible Viscous Flow Problems. *Journal of Computational Physics 2*, 12–26. (Reprinted, (1997) *Journal of Computational Physics 135*, 118-125.).

Coleman, C. S. and G. V. Bicknell (1985). Jets with Entrained Clouds - I. Hydrodynamic Simulations and Magnetic Field Structure. *Monthly Notices of the Royal Astronomical Society 214*, 33–355.

Colgate, S. A. and T. Sigurgeirsson (1973). Dynamic Mixing of Water and Lava. *Nature 244*, 552–555.

Cooke, R. J. S., C. O. McKee, V. F. Dent, and D. A. Wallace (1976). Striking Sequence of Volcanic Eruptions In The Bismark Volcanic Arc, Papua New Guinea, In 1972-1975. In R. W. Johnson (Ed.), *Volcanism in Australasia*, pp. 149–172. Elsevier Scientific Publishing Co.

Crew, H. and A. De Salvio (1914). *Dialogues Concerning Two New Sciences*. Dover Publications. English Translation of *Discorsi E Dimostrazioni Matemathice, Intorno á due nucne Scienze* by Galileo Galilei (1638).

Crook, N. A. and M. J. Miller (1985). A Numerical and Anaytical Study of Atmospheric Undular Bores. *Quarterly Journal of the Royal Meterological Society 111*, 225–242.

Cummins, S. J. and M. Rudman (1999). An SPH Projection Method. *Journal of Computational Physics 152*, 584–607.

Curnier, A. (1993). *Computational Methods in Solid Mechanics*. Kluwer Academic Publishers.

Decker, R. W. (1990). How Often Does a Minoan Eruption Occur? In D. A. Hardy (Ed.), *Thera and the Aegean World III*, Volume 2, London, pp. 444–452. The Thera Foundation.

Dias, F., J. B. Keller, and J.-M. Vanden-Broeck (1988). Flows Over Rectangular Weirs. *Physics of Fluids 31*(8), 2071–2076.

Dias, F. and C. Lharif (1999). Nonlinear Gravity and Capillary-Gravity Waves. *Annual Review of Fluid Mechanics 31*, 301–346.

Dias, F. and E. O. Tuck (1991). Weir Flows and Waterfalls. *Journal of Fluid Mechanics 230*, 525–529.

Dienes, J. K. (1979). On the Analysis of Rotation and Stress Rate in Deforming Bodies. *Acta Mechanica 32*, 217–232.

Dilts, G. A. (1999). Moving Least Squares Particle Hydrodynamics - I. Consistency and Stability. *International Journal for Numerical Methods in Engineering 44*, 1115–1155.

Dilts, G. A. (2000). Moving Least Squares Particle Hydrodynamics II: Conservation and Boundaries. *International Journal for Numerical Methods in Engineering 48*, 1503–1524.

Druitt, T. H. and V. Francaviglia (1992). Caldera Formation on Santorini and the Physiography of the Islands in the Late Bronze Age. *Bulletin of Volcanology 54*, 484–493.

Druitt, T. H. and R. S. J. Sparks (1984). On the Formation of Calderas During Ignnimbrite Eruptions. *Nature 310*, 679–681.

Dyka, C. T., P. W. Randles, and R. P. Ingel (1997). Stress Points for Tension Instability in SPH. *International Journal for Numerical Methods in Engineering 40*, 2325–2341.

Ferziger, J. H. and M. Perić (1996). *Computational Methods for Fluid Dynamics.* Springer-Verlag.

Flanagan, D. P. and L. M. Taylor (1987). An Accurate Numerical Algorithm for Stress Integration with Finite Rotations. *Computer Methods in Applied Mechanics and Engineering 62*, 305–320.

Fletcher, C. A. J. (1988). *Computational Techniques for Fluid Dynamics*, Volume II. Springer-Verlag.

Francis, P. (1993). *Volcanoes: A Planetary Perspective.* Oxford University Press.

Gingold, R. A. and J. J. Monaghan (1977). Smoothed Particle Hydrodynamics: Theory and Application to Non-Spherical Stars. *Monthly Notices of the Royal Astronomical Society 181*, 375–389.

Grady, D. E. and M. E. Kipp (1980). Continuum Modelling of Explosive Fracture in Oil Shale. *International Journal of Rock Mechanics and Mining Sciences and Geomechanics Abstracts 17*, 147–157.

Graham, J. W. (1967). The Cretan Palace: Sixty-Seven Years of Exploration. In *A Land Called Crete*, pp. 17–47. Northampton, Mass.: Smith College.

Griggs, D. T., F. J. Turner, and H. C. Heard (1960). Deformation of Rocks at 500° to 800°C. *Geological Society of America Memoir 79*, 39–104.

Grilli, S. T., I. A. Svensden, and R. Subramanya (1997). Breaking Criterion and Characteristics for Solitary Waves on Slopes. *Journal of Waterway, Port, Coastal, and Ocean Engineering 123*(3), 102–112.

Gudmundsson, A. (1988). Effect of Tensile Stress Concentration Around Magma Chambers on Intrusion and Extrusion Frequencies. *Journal of Volcanology and Geothermal Research 35*, 179–194.

Gudmundsson, A. (1998). Formation and Development of Normal-Fault Calderas and the Initiation of Large Explosive Eruptions. *Bulletin of Volcanology 60*, 160–170.

Gudmundsson, A., J. Marti, and E. Turon (1997). Stress Fields Generating Ring Faults in Volcanoes. *Geophysical Research Letters 24*(13), 1559–1562.

Handin, J. and R. V. Hager (1958). Experimental Deformation of Sedimentary Rocks Under Confining Pressure: Tests at High Temperature. *Bulletin of the American Association of Petroleum Geologists 42*, 2892–2934.

Harlow, F. H. (1964). The Particle-in Cell Computing Method for Fluid Dynamics. *Methods in Computational Physics 3*, 319–343.

Harlow, F. H. and J. E. Welch (1965). Numerical Calculation of Time-Dependent Viscous Incompressible Flow of Fluid with Free Surface. *Physics of Fluids 8*, 2182–2189.

Heiken, G. and F. McCoy (1984). Caldera Development During the Minoan Eruption, Thira, Cyclades, Greece. *Journal of Geophysical Research 89*, 8441–8462.

Heiken, G. and F. McCoy (1990). Precursory Activity to the Minoan Eruption, Thera, Greece. In D. A. Hardy (Ed.), *Thera and the Aegean World III*, Volume 2, London, pp. 444–452. The Thera Foundation.

Hirt, C. W. and B. D. Nichols (1980). Adding Limited Compressibility to Incompressible Hydrocodes. *Journal of Computational Physics 34*, 390–400.

Hirt, C. W. and B. D. Nichols (1981). Volume of Fluid (VOF) Method for the Dynamics of Free Boundaries. *Journal of Computational Physics 39*, 201–225.

Hirt, C. W. and J. P. Shannon (1968). Free-Surface Stress Conditions for Incompressible-Flow Calculations. *Journal of Computational Physics 2*, 403–411.

Hockney, R. W. and J. W. Eastwood (1981). *Computer Simulation Using Particles*. McGraw-Hill, New York.

Höskuldsson, A. and R. S. J. Sparks (1997). Thermodynamics and Fluid Dynamics of Effusive Subglacial Eruptions. *Bulletin of Volcanology 59*, 219–230.

Jaeger, C. (1979). *Rock Mechanics and Engineering* (2nd ed.). Cambridge University Press.

Jaeger, J. C. (1964). *Elasticity, Fracture and Flow*. John Wiley and Sons.

Komlós, G., P. Hédervári, and S. Mészáros (1978). A Brief Note on Tectonic Earthquakes Related to the Activity of Santorini from Antiquity to the Present. In C. Doumas (Ed.), *Thera and the Aegean World I*, London, pp. 97–107. Thera and the Aegean World.

Komuro, H. (1987). Experiments on Cauldron Formation: A Polygonal Cauldron and Ring Fractures. *Journal of Volcanology and Geothermal Research 31*, 139–149.

Komuro, H., Y. Fujita, and K. Kodama (1984). Numerical and Experimental Models on the Formation Mechanism of Collapse Basins During the Green Tuff Orogenesis of Japan. *Bulletin of Volcanology 47*, 649–666.

Laitone, E. V. (1960). The Second Approximation to Cnoidal and Solitary Waves. *Journal of Fluid Mechanics 9*, 430–444.

Lamb, H. S. (1932). *Hydrodynamics*. Cambridge University Press.

Landau, L. D. and E. M. Lifshitz (1970). *Theory of Elasticity* (2nd ed.). Pergamon Press.

Lattanzio, J. C., J. J. Monaghan, H. Pongracic, and M. P. Schwarz (1985). Interstellar Cloud Collisions. *Monthly Notices of the Royal Astronomical Society 215*, 124–147.

Latter, J. H. (1981). Tsunamis of Volcanic Origin: Summary of Causes, with Particular Reference to Krakatau, 1883. *Bulletin of Volcanology 44*, 467–490.

Lennard-Jones, J. E. (1931). Cohesion. *Proceedings of the Physical Society 43*, 461–482.

Libersky, L. D. and A. G. Petschek (1991). Smooth Particle Hydrodynamics with Strength of Materials. In H. E. Trease, M. J. Fritts, and W. P. Crowley (Eds.), *Advances in the Free-Lagrange Method*, pp. 248–257. Springer-Verlag.

Libersky, L. D., A. G. Petschek, T. C. Carney, J. R. Hipp, and F. A. Allahdadi (1993). High Strain Lagrangian Hydrodynamics. A Three-Dimensional SPH Code for Dynamic Material Response. *Journal of Computational Physics 109*, 67–75.

Lighthill, J. (1980). *Waves in Fluids*. Cambridge University Press.

Lipman, P. W. (1997). Subsidence of Ash-Flow Calderas: Relation to Caldera Size and Magma-Chamber Geometry. *Bulletin of Volcanology 59*, 198–218.

Luce, J. V. (1970). *The End of Atlantis*. Granada Publishing Limited.

Lucy, L. B. (1977). A Numerical Approach to the Testing of the Fission Hypothesis. *Astronomical Journal 82*, 1013–1024.

Lyard, F. and M. L. Genco (1994). Optimisation Methods for Bathymetry and Open Boundary Conditions in a Finite Element Model of Ocean Tides. *Journal of Computational Physics 114*, 234–256.

Mader, C. L. (1986). *Numerical Modelling of Water Waves*. University of California Press.

Mandell, D. A., C. A. Wingate, and L. A. Schwalbe (1996). Computational Brittle Fracture Using Smooth Particle Hydrodyamics. Technical Report LA-UR 96-2840, Los Alamos National Laboratory.

Marder, M. and J. Fineberg (1996, September). How Things Break. *Physics Today 49*, 24–29.

Marinatos, S. (1939). The Volcanic Destruction of Minoan Crete. *Antiquity 13*, 425–439.

Marti, J., G. J. Ablay, L. T. Redshaw, and R. S. J. Sparks (1994). Experimental Studies of Collapse Calderas. *Journal of the Geological Society, London 151*, 919–929.

Martin, J. C. and W. J. Moyce (1952). Part IV. An Experimental Study of the Collapse of Liquid Columns on a Rigid Horizontal Plane. *Philosophical Transactions of the Royal Society of London 244*, 312–324.

McBirney, A. R. (1990). An Historical Note on the Origin of Calderas. *Journal of Volcanology and Geothermal Research 42*, 303–306.

Melosh, H. J., E. V. Ryan, and E. Asphaug (1992). Dynamic Fragmentation in Impacts: Hydrocode Simulation of Laboratory Impacts. *Journal of Geophysical Research 97*, 14735–14759.

Mészáros, S. (1978). Some Words on the Minoan Tsunami of Santorini. In C. Doumas (Ed.), *Thera and the Aegean World I*, London, pp. 257–291. Thera and the Aegean World.

Miyata, H. (1986). Finite-Difference Simulation of Breaking Waves. *Journal of Computational Physics 65*, 179–214.

Monaghan, J. J. (1985). Particle Methods for Hydrodynamics. *Computer Physics Reports 3*, 71–124.

Monaghan, J. J. (1989). On the Problem of Penetration in Particle Methods. *Journal of Computational Physics 82*, 1–15.

Monaghan, J. J. (1992). Smoothed Particle Hydrodynamics. *Annual Review of Astronomy and Astrophsics 30*, 543–574.

Monaghan, J. J. (1994). Simulating Free Surface Flows with SPH. *Journal of Computational Physics 110*, 399–406.

Monaghan, J. J. (1995). Simulating Gravity Currents with SPH III: Boundary Forces. Technical report, Monash University. Applied Mathematics Reports and Preprints, 95/11.

Monaghan, J. J. (2000). SPH Without a Tensile Instability. *Journal of Computational Physics 159*, 290–311.

Monaghan, J. J., R. A. F. Cas, A. M. Kos, and M. Hallworth (1999). Gravity Currents Descending a Ramp in a Stratified Tank. *Journal of Fluid Mechanics 379*, 39–70.

Monaghan, J. J. and A. Kos (2000). Scott Russell's Wave Generator. *Physics of Fluids 12*(3), 622–630.

Monaghan, J. J., and J. C. Lattanzio (1985). A Refined Particle Method for Astrophysical Problems. *Astronomy and Astrophysics 149*, 135–143.

Morris, J. (1994). A Study of the Stability Properties of SPH. Technical report, Monash University. Applied Mathematics Reports and Preprints, 94/22.

Morris, J. P. (1996). *Analysis of SPH with Applications*. Ph. D. thesis, Monash University.

Morris, J. P., P. J. Fox, and Y. Zhu (1997). Modeling Low Reynolds Number Incompressible Flows Using SPH. *Journal of Computational Physics 136*, 214–226.

Morton, D. E. (1997). *Numerical Simulation of an Impacting Drop*. Ph. D. thesis, G.K. Williams Cooperative Research Centre for Extractive Metallurgy, Department of Chemical Engineering, University of Melbourne.

Murnaghan, F. D. (1951). *Finite Deformation of an Elastic Solid*. John Wiley and Sons.

Nichols, B. D. and C. W. Hirt (1971). Improved Free Surface Boundary Conditions for Numerical Incompressible-Flow Calculations. *Journal of Computational Physics 8*, 434–448.

Page, D. L. (1970). *The Santorini Volcano and the Desolation of Minoan Crete*. London: Society for the Promotion of Hellenic Studies.

Page, D. L. (1978). On the Relation Between the Thera Eruption and the Desolation on Eastern Crete c. 1450 B.C. In C. Doumas (Ed.), *Thera and the Aegean World I*, London, pp. 691–698. Thera and the Aegean World.

Peregrine, D. H. (1966). Calculations of the Development of an Undular Bore. *Journal of Fluid Mechanics 25*(2), 321–330.

Perlin, M. and W. W. Schultz (2000). Capillary Effects on Surface Waves. *Annual Review of Fluid Mechanics 32*, 241–274.

Peskin, C. S. (1972). Flow Patterns Around Heart Valves: A Numerical Method. *Journal of Computational Physics 10*, 252–271.

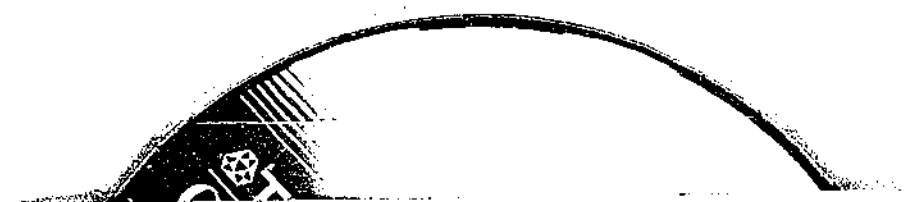Peskin, C. S. (1977). Numerical Analysis of Blood Flow in the Heart. *Journal of Computational Physics 25*, 220–252.

Petschek, A. G. and M. E. Hanson (1968). Difference Equations for Two-Dimensional Elastic Flow. *Journal of Computational Physics 3*, 307–321.

Petschek, A. G. and L. D. Libersky (1993). Cylindrical Smoothed Particle Hydrodynamics. *Journal of Computational Physics 109*, 76–83.

Phillips, G. J. and J. J. Monaghan (1985). A Numerical Method for Three Dimensional Simulations of Collapsing, Isothermal, Magnetic Gas Clouds. *Monthly Notices of the Royal Astronomical Society 216*, 883–895.

Raad, P. E. (1995). Modeling Tsunamis with Marker and Cell Methods. In H. Yeh, P. Liu, and C. Synolakis (Eds.), *Long-Wave Runup Models*, pp. 181–203. World Scientific.

Randles, P. W. and L. D. Libersky (1996). Smoothed Particle Hydrodynamics: Some Recent Improvements and Applications. *Computational Methods in Applied Mechanics and Engineering. 139*, 375–408.

Rao, S. S. (1990). *Mechanical Vibrations* (2nd ed.). Addison-Wesley Publishing Company.

Rayleigh, L. (1908). Note on Tidal Bores. *Proceedings of the Royal Society A. 81*, 448–449.

Rayleigh, L. (1914). On the Theory of Long Waves and Bores. *Proceedings of the Royal Society A. 90*, 324–328.

Roche, O., T. H. Druitt, and O. Merle (2000). Experimental Study of Caldera Formation. *Journal of Geophysical Research 105*, 395–416.

Sammonds, P. R. (1999). Understanding the Fundamental Physics Governing the Evolution and Dynamics of the Earth's Crust and Ice Sheets. *Philosophical Transactions of the Royal Society of London. A. 357*, 3377–3401.

Scardovelli, R. and S. Zaleski (1999). Direct Numerical Simulation of Free-Surface and Interfacial Flow. *Annual Review of Fluid Mechanics 31*, 567–603.

Sheridan, M. F. and K. H. Wohletz (1983). Hydrovolcanism: Basic Considerations and Review. *Journal of Volcanology and Geothermal Research 17*, 1–29.

Simpson, J. E. (1997). *Gravity Currents: In the Environment and the Laboratory* (2nd ed.). Cambridge University Press.

Smith, R. L. and R. A. Bailey (1968). Resurgent Cauldrons. *Geological Society of America Memoir 116*, 613–662.

Sparks, R. S. J. (1978). The Dynamics of Bubble Formation and Growth in Magmas: A Review and Analysis. *Journal of Volcanology and Geothermal Research 3*, 1–37.

Sparks, R. S. J. and C. J. N. Wilson (1990). The Minoan Deposits: A Review of their Characteristics and Interpretation. In D. Hardy (Ed.), *Thera and the Aegean world III*, Volume 2, London, pp. 89–99. The Thera Foundation.

Sulsky, D. and J. U. Brackbill (1991). A Numerical Method for Suspension Flow. *Journal of Computational Physics 96*, 339–368.

Sulsky, D., S.-J. Zhou, and H. L. Schreyer (1995). Application of a Particle-in-Cell Method to Solid Mechanics. *Computer Physics Communications 87*, 236–252.

Swegle, J. W. (1992). SPH Behavior in Tension. Memo, Sandia National Laboratories.

Swegle, J. W., D. L. Hicks, and S. W. Attaway (1995). Smoothed Particle Hydrodynamics Stability Analysis. *Journal of Computational Physics 116*, 123–134.

Symons, G. J. (Ed.) (1888). *The Eruption of Krakatoa and Subsequent Phenomena: Part III. On the Seismic Sea Waves Caused by the Eruption of Krakatoa, August 26th and 27th 1883. Report of the Krakatoa Committee of the Royal Society.* Trübner and Co., London.

Takeda, H., S. M. Miyama, and M. Sekiya (1994). Numerical Simulation of Viscous Flow by Smoothed Particle Hydrodynamics. *Progress of Theoretical Physics 92*(5), 939–960.

Thornton, I. W. (1996). *Krakatau: The Destruction and Reassembly of an Island Ecosystem.* Harvard University Press.

Todhunter, I. and K. Pearson (1960). *A History of the Theory of Elasticity and of the Strength of Materials*, Volume 1. Dover Publications.

Turcotte, D. L., H. Ockendon, J. R. Ockendon, and S. J. Cowley (1990). A Mathematical Model of Vulcanian Eruptions. *Geophysical Journal International 103*, 211–217.

Vanden-Broeck, J.-M. and J. B. Keller (1987). Weir Flows. *Journal of Fluid Mechanics 176*, 283–293.

Verbeek, R. D. M. (1884, May). The Krakatoa Eruption. *Nature 30*, 10–15 and 335–336.

Vignjevic, R., J. Campbell, and L. Libersky (2000). A Treatment of Zero-Energy Modes in the Smoothed Particle Hydrodynamics Method. *Computational Methods in Applied Mechanics and Engineering. 184*, 67–85.

Von Neumann, J. and R. D. Richtmyer (1950). A Method for the Numerical Calculation of Hydrodynamic Shocks. *Journal of Applied Physics 21*, 232–237.

Walker, G. P. L. (1984). Downsag Calderas, Ring Faults, Caldera Sizes, and Incremental Caldera Growth. *Journal of Geophysical Research 89*, 8407–8416.

Walsh, J. B. (1965). The Effect of Cracks on the Compressibility of Rocks. *Journal of Geophysical Research 70*, 381–389.

Wilkins, M. L. (1964). Calculation of Elastic-Plastic Flow. *Methods in Computational Physics 3*, 211–263.

Wilson, L. (1980). Relationships Between Pressure, Volatile Content and Ejecta Velocity in Three Types of Volcanic Explosion. *Journal of Volcanology and Geothermal Research 8*, 291–313.

Wisser, E. (1927). Oxidation Subsidence at Bisbee, Arizona. *Economic Geology 22*(8), 761–790.

Xing, C., H. P. Langtangen, B. F. Nielsen, and A. Tveito (1998). A Finite Element Method for Fully Nonlinear Water Waves. *Journal of Computational Physics 143*, 544–568.

Yeung, R. W. (1982). Numerical Methods of Free-Surface Flows. *Annual Review of Fluid Mechanics 14*, 395–442.

Yokoyama, I. (1978). The Tsunami Caused by the Prehistoric Eruption of Thera. In C. Doumas (Ed.), *Thera and the Aegean World I*, London, pp. 277–283. Thera and the Aegean World.

"You know and I know better"

The Screaming Jets

Caldera Collapse and the Generation of Waves

Time = 0.138   Time = 0.308

Time = 0.725   Time = 1.601

Appendix C: Mpeg Animations